UCRL-LR-121189

RECEIVED
NOV 17 1995
OSTI

Predicting Tropospheric Ozone and Hydroxyl Radical in a Global, Three-Dimensional, Chemistry, Transport, and Deposition Model

Cynthia Shaver Atherton

January 5, 1995

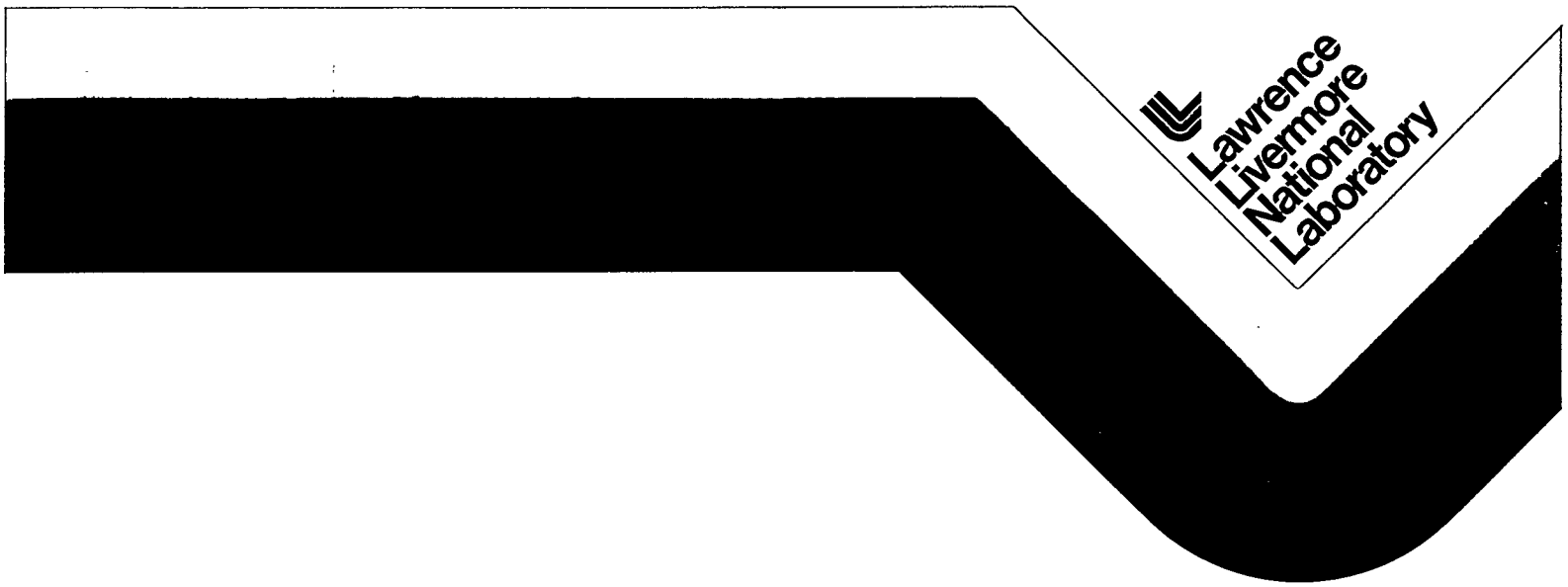

DISCLAIMER

This document was prepared as an account of work sponsored by an agency of the United States Government. Neither the United States Government nor the University of California nor any of their employees, makes any warranty, express or implied, or assumes any legal liability or responsibility for the accuracy, completeness, or usefulness of any information, apparatus, product, or process disclosed, or represents that its use would not infringe privately owned rights. Reference herein to any specific commercial product, process, or service by trade name, trademark, manufacturer, or otherwise, does not necessarily constitute or imply its endorsement, recommendation, or favoring by the United States Government or the University of California. The views and opinions of authors expressed herein do not necessarily state or reflect those of the United States Government or the University of California, and shall not be used for advertising or product endorsement purposes.

This report has been reproduced
directly from the best available copy.

Available to DOE and DOE contractors from the
Office of Scientific and Technical Information
P.O. Box 62, Oak Ridge, TN 37831
Prices available from (615) 576-8401, FTS 626-8401

Available to the public from the
National Technical Information Service
U.S. Department of Commerce
5285 Port Royal Rd.,
Springfield, VA 22161

Work performed under the auspices of the U.S. Department of Energy by Lawrence Livermore National Laboratory under Contract W-7405-Eng-48.

UCRL-LR-121189
Distribution Category UC-702

Predicting Tropospheric Ozone and Hydroxyl Radical in a Global, Three-Dimensional, Chemistry, Transport, and Deposition Model

Cynthia Shaver Atherton

Manuscript date: January 5, 1995

LAWRENCE LIVERMORE NATIONAL LABORATORY
University of California • Livermore, California • 94551

MASTER

DISTRIBUTION OF THIS DOCUMENT IS UNLIMITED

Predicting Tropospheric Ozone and Hydroxyl Radical in a
Global, Three-Dimensional, Chemistry, Transport, and Deposition Model

By

CYNTHIA SHAVER ATHERTON

B.S. (California Institute of Technology) 1983
M.S. (Massachusetts Institute of Technology) 1985

DISSERTATION

Submitted in partial satisfaction of the requirements for the degree of

DOCTOR OF PHILOSOPHY

in

Atmospheric Science

in the

OFFICE OF GRADUATE STUDIES

of the

UNIVERSITY OF CALIFORNIA

DAVIS

Approved:

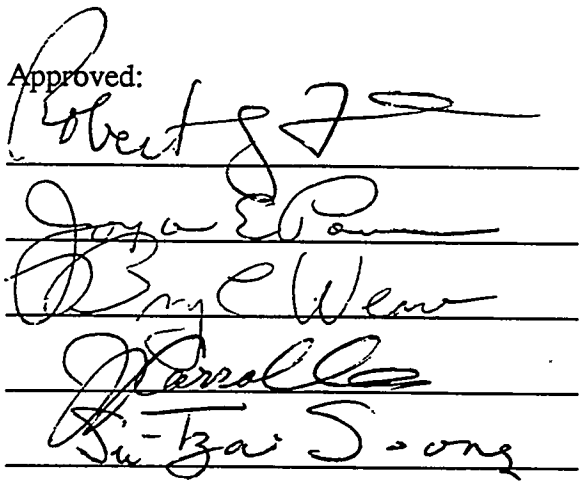

1994

Abstract

PREDICTING TROPOSPHERIC OZONE AND HYDROXYL RADICAL IN A GLOBAL, THREE-DIMENSIONAL, CHEMISTRY, TRANSPORT, AND DEPOSITION MODEL

Two of the most important chemically reactive tropospheric gases are ozone (O_3) and the hydroxyl radical (OH). Although ozone in the stratosphere is a necessary protector against the sun's radiation, tropospheric ozone is actually a pollutant which damages materials and vegetation, acts as a respiratory irritant, and is a greenhouse gas. One of the two main sources of ozone in the troposphere is photochemical production. The photochemistry is initiated when hydrocarbons and carbon monoxide (CO) react with nitrogen oxides ($NO_x = NO + NO_2$) in the presence of sunlight. Reaction with the hydroxyl radical, OH, is the main sink for many tropospheric gases. The hydroxyl radical is highly reactive and has a lifetime on the order of seconds. Its formation is initiated by the photolysis of tropospheric ozone.

Tropospheric chemistry involves a complex, non-linear set of chemical reactions between atmospheric species that vary substantially in time and space. To model these and other species on a global scale requires the use of a global, three-dimensional chemistry, transport, and deposition (CTD) model. In this work, I developed two such three dimensional CTD models. The first model incorporated the chemistry necessary to model tropospheric ozone production from the reactions of nitrogen oxides with carbon monoxide (CO) and methane (CH_4). The second also included longer-lived alkane species and the biogenic hydrocarbon isoprene, which is emitted by growing plants and trees. The models' ability to predict a number of key variables (including the concentration of O_3, OH, and other species) were evaluated. Then, several scenarios were simulated to understand the change in the chemistry of the troposphere since preindustrial times and the role of anthropogenic NO_x on present day conditions.

Acknowledgements

Working on this dissertation has been a wonderful learning process for me. I am especially grateful for the guidance and patience of my advisors, Dr. Joyce Penner and Prof. Su-Tzai Soong, and several faculty members, Prof. Bryan Weare, Prof. Robert Flocchini, and Prof. J.J. Carroll. I have been truly fortunate to have worked very closely with Dr. John J. Walton on this project. I have benefitted from work and discussions with my colleagues, including Dr. Jane Dignon, Dr. Peter Connell, Dr. Doug Kinnison, Dr. Sandy Sillman, Dr. Karl Taylor, Mr. Hal Eddleman, Mr. Dan Bergmann, Mr. John Tamaresis, and Mr. Charlie O'Connor.

This work would not have been possible without further help from my family. My husband, Jeff, has been truly wonderful and supportive in my efforts. My two children, Amy and Jack have given me a far greater appreciation of other pursuits, as well. My parents, Lucy and John Shaver have been avid fans and provided childcare in crunch times. My mother and father-in-law, Jeanne and Larry Atherton, not only helped out, but also provided a sense of humor to make it all bearable. A very special thanks goes to my mother-in-law, Martha Atherton, who not only helped me through, but donated two weeks of her life to care for my family so that I could finish my thesis and turn it in after my son was born early. My friends Carla Ahlstrom, Candy and Dave Roberts, and Lynn and Bob Gatehouse have been my cheering section for years. Gretchen Piscotty pitched in at the end to keep my children alive and well. For all of this support, I am truly grateful.

This research was funded under the auspices of the U.S. Department of Energy by the Lawrence Livermore National Laboratory under contract No. W-7405-Eng-48, and supported in part by the U.S. EPA, NOAA, and the DOE Atmospheric Chemistry Program.

Table of Contents

List of Figures

List of Tables

CHAPTER 1 INTRODUCTION TO TROPOSPHERIC CHEMISTRY

1.1 Chemistry of tropospheric O_3 and OH

1.1.1 Tropospheric O_3

Ozone in the stratosphere is beneficial, as it absorbs a significant fraction of the sun's radiation. However, ozone in the troposphere, which is produced in an entirely different manner, is regarded as an atmospheric pollutant, due to its deleterious effects. Tropospheric ozone is a respiratory irritant for humans (Wayne et al., 1967; Bedi et al., 1988) and animals (Coffin and Stockinger, 1977). It damages crops, vegetation (Heck and Brandt, 1977; Heck et al., 1983), and many materials. For example, ozone cracks rubber (Newton, 1945), fades dyes (Beloin, 1973), and erodes paint (Campbell et al., 1974, Shaver et al., 1983). Additionally, ozone acts as a greenhouse gas, and may contribute to the warming of the earth's atmosphere (Ramanathan et al., 1985; Dickinson and Cicerone, 1986; Wuebbles et al., 1989).

Ozone in the troposphere is believed to be produced via two routes: transport from the stratosphere and in-situ photochemical production. Transport from the stratosphere as an important ozone source was hypothesized in the early 1960s (Junge, 1962). Indeed, in certain regions, tropospheric ozone concentrations peak in the late winter and early spring, when transport from the stratosphere is expected be the strongest (Danielsen, 1968; Singh et al., 1980; Chung and Dann, 1985). Some models indicate that transport plays a major role in tropospheric ozone production (Levy et al., 1985). Danielsen and Mohnen (1977) estimated a flux from the stratosphere to the troposphere of 7.8×10^{10} molecules $cm^{-2}s^{-1}$, while Mahlman et al. (1980) cited a flux of 5.1×10^{10} molecules $cm^{-2}s^{-1}$.

However, photochemical production of ozone in the troposphere has also been effectively argued as the main source. Scientists have long known that the oxidation of species such as CO and CH_4 can produce ozone (Levy, 1972; Levy, 1973; Crutzen, 1973). Model predictions of tropospheric ozone produced from photochemical reactions alone

were sufficient to match actual observations (Chameides and Walker, 1973). Recent model results indicate that photochemical production may be the main source of tropospheric ozone (Logan, 1985; Vukovich et al., 1985). Parrish et al. (1993) measured surface concentrations of CO and O_3 at three North Atlantic Ocean sites during the summer, 1991. They estimated that 110 billion moles of O_3 are transported from the stratosphere each summer over the North Atlantic Ocean, while 100 billion moles of O_3 are transported from the Northeastern United States. Given that much of the O_3 transported from the stratosphere can react before it reaches the surface, they conclude that the bulk of the surface O_3 over the North Atlantic Ocean during the summer is due to in-situ photochemical production over the Eastern U.S., followed by transport to the North Atlantic Ocean.

Ozone is photochemically produced when nitrogen oxides react in the presence of hydrocarbons (and/or CO) and sunlight. There are a variety of hydrocarbons which ultimately lead to ozone production.

They may be divided into three categories. The first category consists of two of the most abundant and chemically simple species, the hydrocarbon methane, CH_4 and carbon monoxide, CO (which is not a hydrocarbon but can lead to O_3 formation). The second group consists of biogenic hydrocarbons such as isoprene and terpenes, which are emitted by vegetation (plants and trees). They are highly reactive and may be responsible for a significant portion of ozone formed near wooded or forested regions (Chameides, et al., 1988). The third group contains many of the hydrocarbons emitted by anthropogenic processes, such as the alkanes, alkenes, aromatics, and aldehydes. Many of these are quite reactive and contribute on a local to regional scale. The alkanes, however, have much longer chemical lifetimes, and may need to be addressed on a global scale. The characteristic lifetime for a species with respect to OH is defined as $\tau_{OH} = 1/\{k_{OH} \times [OH]\}$. For conditions representative of the tropics (T=298K, $[OH] = 2 \times 10^6$ cm^{-3}, $[O_3] = 7.4 \times$

10^{11} cm^{-3} (= 30 ppbv)) and of the globe in general (T=275K, [OH] = 6×10^5 cm^{-3}, [O_3] = 7.4×10^{11} cm^{-3}), Table 1.1 shows the characteristic lifetimes with respect to O_3 and OH for CO and the hydrocarbons used in the model.

Table1.1: Reaction rate coefficients and characteristic lifetimes of CO and non-methane hydrocarbons used in the model

Species	k_{OH}, cm^3 $molecule^{-1}s^{-1}$	k_{O3}, cm^3 $molecule^{-1}s^{-1}$	τ_{OH}, tropics	τ_{O3}, tropics	τ_{OH}, global	τ_{O3}, global
CO	$1.5 \times 10^{-13} \times (1 + (dens \times 2.4 \times 10^{-20}))$	---	24 days	---	78 days	---
CH_4	$2.9 \times 10^{-12} \times \exp(-1820/T)$	---	2.4 years	---	14 years	---
ethane (C_2H_6)	$8.7 \times 10^{-12} \times \exp(-1070/T)$	---	24 days	---	107 days	---
propane (C_3H_8)	$1.1 \times 10^{-11} \times \exp(-700/T)$	---	5.3 days	---	22 days	---
isoprene (C_5H_{10})	$2.55 \times 10^{-11} \times \exp(410/T)$	$1.23 \times 10^{-14} \times \exp(-2013/T)$	80 mins	26 hours	4.2 hours	1.9 days

1.1.2 Tropospheric OH

Reaction with the hydroxyl radical, OH, is the primary sink for virtually every tropospheric species. Formation of the hydroxyl radical is initiated by the photolysis of O_3. The hydroxyl radical is short lived, and remains only a few seconds (Chameides and Davis, 1982). Its concentration is highly spatially variable, and depends on season (due to its photolytic source). The hydroxyl radical concentrations are quite low (on the order of 10^5 to 10^7 molecules/cm^3 during the daytime) and measurements are quite difficult, due to the low detection limits necessary and exceeding short OH lifetime. Limited observations of OH do exist (Felton et al., 1988; Hard et al., 1986; Hewitt and Harrison, 1985; Perner et al., 1987; and Platt et al., 1988). In recent years, a new measurement method has been

developed by Eisele and Tanner (1991) and more measurements should be forthcoming.

1.2 The tropospheric oxidation of CO

Carbon monoxide, CO, is emitted globally in approximately equal amounts by anthropogenic and natural sources (Logan et al., 1981; WMO, 1985). The anthropogenic sources include intentional burning of fossil fuel, wood for fuel, and biomass such as savannas and forests, as well as the oxidation of anthropogenic CH_4 and nonmethane hydrocarbons. The natural sources include the oxidation of naturally emitted CH_4 and other natural hydrocarbons, natural forest fires, and emissions from plants and oceans (Logan et al., 1981; WMO, 1985).

CO has a relatively short atmospheric lifetime with respect to reaction by OH: 0.4 years on a global scale, and as low as 0.1 years in the tropics (WMO, 1985). Consequently, its concentration varies significantly in time and space. There is more CO present in the northern hemisphere than the southern hemisphere. This is not surprising, as the anthropogenic sources are land-based, and the northern hemisphere contains much more land. Also, CO is more prevalent in developed countries, which tend to reside in the Northern Hemisphere. In the Northern Hemisphere, the highest CO concentrations occur in the lowest atmospheric layers of the mid-latitudes, and the seasonally averaged concentration there is 120 parts per billion by volume (ppbv). Also, the CO mixing ratio decreases with altitude. The Southern Hemisphere has a much more uniform CO distribution of around 60 ppbv, and the vertical gradient is not as well defined (Reichle et al., 1986). The major loss for CO is reaction with the hydroxyl radical, OH. Thus, CO experiences a seasonal variation, with highest concentrations during the winter when OH concentrations are low.

Ozone production from CO is initiated by its reaction with hydroxyl radical, OH. The hydroxyl radical is extremely reactive, and acts as the most important sink for many atmospheric species. The hydroxyl radical is initially formed when ozone is photolyzed.

resulting in an oxygen atom, $O(^1D)$, that reacts with water, H_2O:

$$O_3 + h\nu \text{ -----> } O(^1D) + O_2 \quad (1.14)$$

$$O(^1D) + OH \text{ -----> } 2OH. \quad (1.15)$$

The OH species is present at appreciable concentrations during the day. Thus, the CO oxidation process takes place via reactions (1.3) - (1.8).

$$CO + OH \text{ -----> } CO_2 + H \quad (1.16)$$

$$H + O_2 + M \text{ -----> } HO_2 + M \quad (1.17)$$

If enough NO is present, the presence of HO_2 will lead to O_3 production. That is because the HO_2 can convert NO to NO_2:

$$HO_2 + NO \text{ -----> } NO_2 + OH \quad (1.18)$$

and once NO_2 is formed, it then photolyzes to start the cycle in which O_3 is produced and destroyed, shown in reactions (1.6) - (1.8):

$$NO_2 + h\nu \text{ -----> } NO + O \quad (1.19)$$

$$O + O_2 + M \text{ -----> } O_3 + M \quad (1.20)$$

$$NO + O_3 \text{ -----> } NO_2 + O_2. \quad (1.21)$$

Thus, by producing HO_2 radicals, CO leads to the production of ozone. To do so requires an NO concentration of greater than approximately 3 - 10 pptv, in order for the reaction rate of (5) to dominate other competing reactions (Finlayson-Pitts and Pitts, 1986). This condition is probably met for much of the industrialized Northern Hemisphere, but may not hold in the Southern Hemisphere or nonindustrialized Northern Hemisphere (Crutzen, 1979).

If NO concentrations are low enough, then ozone may actually be destroyed, rather

than produced. This happens because reaction (1.5) is so slow that the HO either reacts with itself or ozone:

$$HO_2 + HO_2 \text{ -----> } H_2O_2 + O_2 \qquad (1.22)$$

$$HO_2 + O_3 \text{ -----> } OH + 2\,O_2 \qquad (1.23)$$

The hydrogen peroxide can then photolyze to produce hydroxyl radical, OH.

$$H_2O_2 + h\nu \text{ -----> } 2\,OH \qquad (1.24)$$

1.3 The tropospheric oxidation of CH_4

Methane, CH_4, is produced largely by natural processes, although it does have an anthropogenic contribution, mainly from combustion. The largest natural sources include anaerobic bacterial fermentation (e.g. in rice paddies, swamps, marshes, etc.) and enteric fermentation in cattle and other species (Khalil and Rasmussen, 1983). Perhaps 8 - 15% of the atmospheric CH_4 is released in urban locations (Blake et al., 1984). Because oceans cover more of the Southern Hemisphere, most of the methane production, which is based on land or wetlands, occurs in the Northern Hemisphere. Methane concentrations are typically 7% higher in the Northern Hemisphere compared to the Southern Hemisphere (Blake and Rowland, 1986).

The main sink for methane is also reaction with the hydroxyl radical, OH. Global methane concentrations are steadily increasing: from a global average concentration of 1.52 parts per million by volume (ppmv) in 1978, to 1.625 ppmv in 1983, and up to 1.684 ppmv in 1987 (Blake and Rowland, 1986; Blake and Rowland, 1988). Measurements estimated the global increase in methane concentration to be roughly 1 - 2%/year during the 1960s to early 1980s (Steele et al., 1987; Blake and Rowland, 1988; Khalil et al., 1989). However, the trend appears to have slowed from 13.3 ppbv/year in 1983 to 9.5 ppbv/year in 1990 (Steele et al., 1992). The atmospheric lifetime of methane is estimated

to be 10.1 years (Fung et al., 1991). Thus, its concentration is not as varied in time and space as that of CO.

Like CO, ozone production from CH_4 is initiated by the reaction with hydroxyl radical, OH. Reactions (1.12) and (1.13) show the initial attack of the hydroxyl radical.

$$CH_4 + OH \text{ -----> } CH_3 + H_2O \quad (1.25)$$

$$CH_3 + O_2 + M \text{ -----> } CH_3O_2 + M \quad (1.26)$$

If enough NO is present, NO may be converted to NO_2 by either reaction (1.14) or the reaction sequence of (1.15) and (1.16).

$$CH_3O_2 + NO \text{ ----> } CH_3O + NO_2 \quad (1.27)$$

$$CH_3O + O_2 \text{ -----> } HCHO + HO_2 \quad (1.28)$$

$$HO_2 + NO \text{ -----> } NO_2 + OH \quad (1.29)$$

Thus, both the CH_3O_2 and HO_2 molecules can convert NO to NO_2. The ozone is then formed and destroyed via reactions (1.17) - (1.19):

$$NO_2 + h\nu \text{ -----> } NO + O \quad (1.30)$$

$$O + O_2 + M \text{ -----> } O_3 + M \quad (1.31)$$

$$NO + O_3 \text{ -----> } NO_2 + O_2. \quad (1.32)$$

Additionally, the formaldehyde, HCHO, formed in reaction (1.15) can further contribute to ozone formation. It does so by either reacting with OH or photolyzing, which leads to even more HO_2 in reactions (1.23) and (1.25). The presence of HO_2 means NO may be converted to NO_2, via reaction (1.24), which then leads to reactions (1.26) - (1.28).

$$HCHO + h\nu \text{ -----> } H_2 + CO \quad (1.33)$$

$$HCHO + h\nu \text{ ----> } HCO + H \quad (1.34)$$

$$HCHO + OH \text{ -----> } HCO + H_2O \quad (1.35)$$

$$H + O_2 + M \text{ -----> } HO_2 + M \quad (1.36)$$

$$HO_2 + NO \text{ -----> } NO_2 + OH \quad (1.37)$$

$$HCO + O_2 \text{ -----> } HO_2 + CO \quad (1.38)$$

$$NO_2 + h\nu \text{ -----> } NO + O \quad (1.39)$$

$$O + O_2 + M \text{ -----> } O_3 + M \quad (1.40)$$

$$NO + O_3 \text{ -----> } NO_2 + O_2. \quad (1.41)$$

However, if not enough NO is present, O_3 will be destroyed, rather than created. This causes the reaction of peroxy radicals CH_3O_2 and HO_2 with NO to be slow (reactions 1.14 and 1.25). Competing reactions then lead to O_3 destruction (reactions 1.10, 1.11, and 1.12) as well as:

$$CH_3O_2 + HO_2 \text{ -----> } CH_3OOH + O_2 \quad (1.42)$$

$$CH_3OOH + OH \text{ -----> } CH_2OOH + H_2O \quad (1.43)$$

$$CH_3OOH + OH \text{ -----> } CH_3OO + H_2O \quad (1.44)$$

$$CH_3OOH + h\nu \text{ -----> } CH_3O + OH \quad (1.45)$$

1.4 The tropospheric oxidation of biogenic hydrocarbons

It has long been known that the biogenic hydrocarbons, which are very reactive, can

affect atmospheric photochemistry and eventually produce ozone (Rasmussen, 1972; Graedel, 1979; Dimitriades, 1981). The biogenic hydrocarbons are emitted mainly by vegetation and are, for example, that chemical that gives trees such as pines their "scent". The total biogenic hydrocarbon releases for the U.S. are estimated to be 30 to 65 x 10^9 kg carbon per year (Lamb et al., 1987). This is larger than the estimate for anthropogenic hydrocarbon emissions of 27 x 10^9 kg carbon per year (Altshuller, 1983). Two important biogenic hydrocarbon species are isoprene (C_5H_8) and alpha-pinene ($C_{10}H_{16}$).

Isoprene is released primarily by deciduous trees, such as oak. Its emission rate is temperature- and light-sensitive, and is very low in the dark (Tingey et al., 1979; Lamb et al., 1985). Alpha-pinene (as well as other terpenes) is emitted mainly by coniferous trees, such as pine. Although its emission rate is temperature-dependent, it is less light-sensitive than isoprene, and continues during the dark hours (Lamb et al., 1985; Tingey et al., 1980).

Chemical reaction mechanisms for both isoprene and alpha-pinene have been developed and tested based on laboratory measurements (Lloyd et al., 1983; Killus and Whitten, 1984, Paulson and Seinfeld, 1992). The reaction mechanisms list the reaction steps, product yields, and kinetic rates for the oxidation processes. Since the photochemistry of ozone formation is highly non-linear, a striking conclusion of modeling studies has been that the biogenic hydrocarbons may substantially affect the ozone concentration, particularly near forested or wooded areas, such as those that occur in the southeastern U.S. (Trainer et al., 1987; Chameides et al., 1988).

1.5 The atmospheric chemistry of other anthropogenic species

Nearly 40 years ago, scientists discovered that urban emissions of hydrocarbons and nitrogen oxides, when combined, could lead to the production of ozone (Haagen-Smit, 1952). Since then, an enormous amount of work has been completed on ozone formation in urban environments (Seinfeld, 1986 and references therein; Finlayson-Pitts and Pitts and references therein, 1986). Urban emissions contain a mixture of hydrocarbons such as

alkenes, aromatics, aldehydes, and alkanes. Most of these hydrocarbons are reactive enough that their chemistry involves the production of O_3 on a local to perhaps regional scale. However, the alkanes, particularly the lower weight alkanes, are more chemically stable, have much longer lifetimes, and may be transported far from the urban centers.

Ozone formation from alkanes proceeds via the reaction sequence below, where HC is any hydrocarbon. As with other species, the oxidation sequence is initiated by the reaction of HC with the hydroxyl radical, OH:

$$HC + OH \text{ -----> } R + H_2O \quad (1.46)$$

$$R + O_2 \text{ -----> } RO_2 \quad (1.47)$$

The RO_2 formed is then free to react with many species, including with NO to form NO_2, which then can lead to reactions (1.35) - (1.37):

$$RO_2 + NO \text{ -----> } RO + NO_2 \quad (1.48)$$

$$NO_2 + h\nu \text{ -----> } NO + O \quad (1.49)$$

$$O + O_2 + M \text{ -----> } O_3 + M \quad (1.50)$$

$$NO + O_3 \text{ -----> } NO_2 + O_2. \quad (1.51)$$

A number of other reactions also occur, which can contribute to either the production or loss of ozone. Limited observations of hydrocarbon concentrations have been published (Lonneman et al., 1978; Grosjean and Fung, 1984; Sexton and Westberg, 1984; Rudolph and Khedim, 1985.).

CHAPTER 2 CURRENT THREE-DIMENSIONAL TROPOSPHERIC CHEMISTRY MODELS

2.1 Introduction

Until now, global, three-dimensional models have been used almost exclusively for climate studies. Thus, a number of general circulation models (GCMs) are currently used to predict the effect of increased greenhouse gas concentrations on global warming (e.g. see Cess et al., 1989 and references therein). Because of the enormous computational storage and processing requirements, these GCMs carry only a limited number of variables, such as water mixing ratio, temperature, and wind speed and direction, but do not model atmospheric chemistry.

To model atmospheric chemistry on a global scale entails implementing the chemical sources, sinks, and reactions into an either an Eulerian (grid-based) or Lagrangian (trajectory-based) model, which is then "driven" by the meteorological output of a GCM or actual meteorological measurements. To date, few such models have been developed, and most of the chemistry incorporated in them is fairly simple to allow the models to be computationally viable. The global, three-dimensional tropospheric oxidant chemistry models that have been developed are described below.

2.2 Other global, three-dimensional tropospheric chemistry models

2.2.1 Models calculating OH (with O_3 prescribed)

Logan and co-workers (1981) modeled photochemistry on a global scale which was constrained by observed concentrations of H_2O, O_3, CO, CH_4, NO, NO_2, and HNO_3. (Thus, O_3 was a diagnostic variable, rather than a predictive quantity). They then calculated concentrations of a variety of species versus altitude, latitude, and season to better understand their global budgets.

Spivakovsky et al. (1990a) parameterized the concentration of OH in terms of 13 independent variables that included temperature, concentrations of H_2O, CO, O_3, and NO_y,

solar irradiance, cloud cover, column ozone, latitude, surface albedo, and solar declination. Thus, the concentration of OH was expressed as a high order polynomial, which depended on the 13 input variables.

Their method was then to calculate a global, three-dimensional distribution of OH throughout a year of simulations in a chemical-transport model (CTM) (Spivakovsky et al, 1990b). The global model used the Goddard Institute of Space Studies (GISS) GCM-derived meteorological fields which had been averaged over 8^{o} x 10^{o} and updated every 8 hours. However, the CTM updated fields only every 5 days, using averages of the 8 hour GCM fields. The concentrations of NO_y, CH_4, CO, O_3, and H_2O were specified on a global basis. The CTM then calculated a three-dimensional, global OH field, that was estimated to be 13% too high, based on CH_3CCl_3 observations.

2.2.2 Models of the CO and/or CH_4 cycle (with OH prescribed)

The atmospheric cycle of CO was studied in a general circulation model by Pinto et al. (1983). They examined eight different cases which contained CO from anthropogenic sources, CH_4 oxidation, and the oxidation of non-methane hydrocarbons that are emitted by vegetation. By comparing predicted CO global distributions and seasonal variations with measurements, they were able to infer CO source rates, particularly for the oxidation of NMHCs emitted by vegetation, and a globally averaged hydroxyl radical (OH) concentration.

Fung et al. (1991) used a three-dimensional model of the atmosphere to examine seven different possible CH_4 emission scenarios. Their goal was to back out the most probable emission scenario that could satisfy a list of seven constraints (including being able to reproduce the north-south latitude gradient of approximately 150 ppbv in CH_4 concentrations). They used the three-dimensional OH fields of Spivakovsky et al. (1990), a coarse resolution of the GISS GCM, and ran each scenario for 4 years. Their preferred scenario required a 500 Tg CH_4/year source term. Of this, the CH_4 sink from reaction with

OH was 450 Tg CH_4/year, the sink due to soils accounted for 10 Tg CH_4/year, and the atmospheric accumulation rate was 40 Tg CH_4/year.

Taylor et al. (1991) investigated the sources and sinks of methane using a global, three- dimensional Lagrangian tracer model. Their model had a 2.5^o x 2.5^o grid, and 7 vertical levels. They used wind fields derived from ECMWF wind data. They specified a 2D hydroxyl radical (OH) field which was obtained from the model of Brasseur et al. (1990) and scaled to reproduce methyl chloroform results. The main methane sink was assumed to be reaction with OH. A small term simulating methane transport to the stratosphere was also included. The model then predicted methane concentrations that would result from two different methane source scenarios. They concluded that the source terms necessary to reproduce CH_4 concentrations are 514 - 524 Tg CH_4/year, which gives a CH_4 lifetime of 10.0 - 10.2 years.

Tie et al. (1991) conducted a three-dimensional model study of CH_4. Their model consisted of 4 submodels: (1) a 3D chemical and dynamical model, (2) a quasi-geostrophic spectral dynamical model to supply winds, (3) a 2D model to supply concentration fields (e.g. OH, $O(^1D)$, reaction rate coefficients, etc.), and (4) an estimated source distribution. They prescribed an initial CH_4 distribution, as well as concentration of NO_x, O_3, HNO_3, CO, and H_2O. The methane emissions were then varied until the model predictions could match surface observations. The model-predicted CH_4 source term was 319 Tg CH_4/year, which is on the low side of estimates.

2.2.3 Models of the reactive nitrogen cycle

Penner et al. (1991) used a reactive nitrogen cycle model to study the sources, distributions, and deposition of NO, NO_2, and HNO_3. The model was driven by meteorological fields supplied from NCAR's CCM1 and updated every 12 hours. It included a simple reactive nitrogen cycle, and prescribed OH and O_3 fields from a 2D model. The sources of NO_x included were: fossil fuel combustion- 22.4 Tg N/year,

lightning-3 Tg N/year, soil emissions-10 Tg N/year, stratospheric production-1 Tg N/year, and biomass burning-6 Tg N/year. The model predicted concentration fields generally compared well with observations except over the remote Pacific. The model predicted wet HNO_3 deposition tended to be low, especially in Europe, perhaps due to excessively strong winds from the GCM. Including the fossil fuel combustion and biomass burning sources of NO_x greatly increased the concentrations of NO_x and HNO_3.

Levy and Moxim (1987, 1989) used a global transport model to illustrate how nitrogen emissions from fossil fuel combustion are transported and affect regional acid deposition in rain. Using wind and precipitation fields provided by the Geophysical Fluid Dynamics Laboratory (GFDL) general circulation model, a single species, NO_y, which represents total nitrogen, was transported. Chemical reactions entered the model somewhat indirectly, through the calculation of bulk removal coefficients. The model results showed that dry deposition of HNO_3 could play a major role in acid deposition, particularly in the northeastern U.S. and Canada (Levy and Moxim, 1987). By isolating source regions (Levy and Moxim, 1989), the model also showed that observed nitrate maxima at Mauna Loa could result from US fossil fuel combustion in the summer and autumn, and Asian sources in the springtime.

Kasibhatla et al. (1991) used a version of their reactive nitrogen model to estimate the contributions of fossil fuel combustion and stratospheric production of NO_x to lower tropospheric values. They use a chemical transport model with 265 km horizontal resolution, 11 vertical levels, and 6 hour time averaged winds and precipitation from a parent GCM. Stratospheric NO_x is produced by the reaction:

$$O(^1D) + N_2O \text{ -----> } 2\,NO \qquad (2.52)$$

By specifying concentrations of N_2O, O_3, temperature, and pressure, they calculate a diurnally averaged production rate of NO (total annual source strength: 0.64 Tg N/year). They also include fossil fuel combustion (21 Tg N/year) in their model simulations.

Reactive nitrogen is partitioned into soluble (HNO_3) and insoluble (NO_x) species. Two cases are considered: (1) No peroxyacetyl nitrate (PAN) formation occurs, and (2) PAN formation occurs because ethane concentrations are specified to be 2 ppbv in the northern hemisphere and 0.4 ppbv in the southern hemisphere, and a simplified chemistry creates PAN. The model results show that PAN formation suppresses NO_x formation in the middle and upper troposphere, and can cause NO_x levels to be underpredicted by a factor of 1.5 to 5. However, the stratospheric NO_x source does not appear to contribute significantly to tropospheric NO_x concentrations. (For example, at remote marine locations, fossil fuel combustion accounted for 40 - 50% of nitrate concentrations, but the stratosphere accounted for only 2%.)

Kasibhatla et al. (1993) used their reactive nitrogen model, including the nonmethane hydrocarbons ethane and propane, to study global cycles of NO_x, HNO_3, PAN, and NO_y. The only source of nitrogen was fossil fuel combustion. Whereas their previous study lumped soluble and insoluble nitrogen species, this version considered soluble (HNO_3), insoluble (NO_x), and reservoir species (PAN). As before, meteorological fields were supplied from a parent GCM every 6 hours at 66 vertical levels. Chemical production and loss rates were calculated off-line by specifying 1D CO and NO_x profiles, 2D concentrations of CH_4, O_3, H_2O, temperature, and total column O_3, and 2D ethane and propane fields (which had been multiplied by a factor of 1.5 in the winter and 3.0 in the summer in certain subregions to simulate the presence of isoprene).

Kasibhatla et al. (1993) considered two cases: a standard scenario, and one in which HNO_3 wet deposition was halved. They found that PAN could account for an appreciable amount of the total nitrogen. Of the sources emitted, roughly 30% were wet deposited in the source region, ~40-45% were dry deposited, and 25-30% were exported to oceanic regions. However, the contribution of fossil fuel combustion to nitrate levels over the oceans was much higher over the Atlantic Ocean than over the Pacific Ocean. Very striking

were the results over the Pacific Ocean and surface SEAREX sites (Prospero and Savoie, 1989). At these locations, surface annual average observations ranged from 39-76 pptv HNO3, but model results showed that (except for two sites) fossil fuel combustion could only account for 1-5 pptv, typically. Even if all nitrogen sources were included, the model results might not match observations.

2.2.4 Models with higher oxidant photochemistry (OH, O_3 calculated)

Crutzen and Zimmermann (1991) used a three-dimensional, global model to calculate the concentrations of O_3 and OH in preindustrial and current atmospheres. They used monthly average winds and a chemistry that included the oxidative cycle of CO, CH_4, and NO_x. The lower boundary conditions included the concentration of CO and CH_4, and NO_x emissions. CO was then prescribed an emission rate that reproduced surface concentration observations for current atmospheres. The total present-day NO_x emissions were 40 Tg N/ year and were split into four categories: (1) industry-20 Tg N/year, (2) lightning-5 Tg N/ year, (3) soils-10 Tg N/year, and (4) biomass burning-5 Tg N/year. Ozone concentrations were prescribed at 100 mb based on observations. Photolysis rates were obtained from a 2D model. The preindustrial scenario had only CO and NO_x emissions from natural sources and specified preindustrial values for the surface concentration of CH_4.

Crutzen and Zimmerman's model (1991) found that O_3 concentrations have increased over the entire globe since preindustrial times. However, the modeled OH concentrations increased in the northern hemisphere since preindustrial times, but decreased in the southern hemisphere. The decrease in OH concentrations in the southern hemisphere was large enough that the total global OH concentration decreased by 10-20% from their current global tropospheric average concentration estimate of 7×10^5 molecules/cm^3.

Kanakidou and Crutzen (1993) used a global, three-dimensional model that included the oxidative cycles of CO, CH_4, C_2H_6, and C_3H_8 to understand the effect that

longitudinally averaged emissions (versus longitudinally varying emissions) have on predicted fields of O_3 and OH. Their model resolution was 10^o x 10^o, with 10 vertical levels, and used a 2 hour timestep. They incorporated 100 reactions, with roughly 50 species. Surface concentrations of CH_4 were prescribed. Emissions of CO, NO_x, C_2H_6, and C_3H_8 varied monthly. The total annual global emissions were: 35 Tg N/year emitted as NO_x, 13.8 Tg C_2H_6/year, and 17 Tg C_3H_8/year.

Two cases were compared. In Case A (3D), all emissions varied in both longitude and latitude. In Case B (quasi-2D), emissions were longitudinally averaged over 10^o latitude bands. The two cases showed how results from a 3D model might vary from a 2D model. In a 2D model in which the emissions of NO_x are longitudinally averaged, NO_x concentrations tend to increase over the ocean, and decrease over land areas. Because O_3 production per unit NO_x consumed is much more efficient at lower NO_x values (Liu et al., 1987; Lin et al. 1988), the quasi-2D model predicts higher O_3 concentrations, especially in the lower troposphere tropics and northern mid-latitudes. The effect is not as pronounced during the wintertime, when photochemistry is suppressed. The lower troposphere OH concentrations predicted by the quasi-2D case were a factor of 2 higher than the 3D case in June and September in the tropics, and a factor of 1.6 higher in the northern mid-latitudes.

2.3 Current applications of the GRANTOUR model

The GRANTOUR model of Walton et al. (1988), which is used in this work, has been applied to several atmospheric chemistry and physics topics. Past and current model studies include the climatic response to large scale smoke injections (Ghan et al., 1988), the global reactive nitrogen cycle (Penner et al., 1991; Atherton et al., 1990), the global sulfur cycle (Erickson et al., 1991; Erickson et al., 1990), and the global cycle of radon and lead (Dignon et al., 1989).

CHAPTER 3 - DESCRIPTION OF THE GRANTOUR MODEL

The chemistry-transport-deposition model, GRANTOUR, is described in detail in Walton et al. (1988). It can simulate the important physical (advection, diffusion, dry deposition and wet deposition) and chemical processes of the atmosphere, and has been used to study important tropospheric species (see Section 2.3). Many of the previous GRANTOUR applications were either for chemically inert species, or very simple (e.g. 3 or 4 chemical reactions) chemical cycles. In this work, a much more complex chemical reaction scheme was added to the model. This work entailed, therefore, developing appropriate chemical reaction schemes (including both the reactions and appropriate reaction rate and photolysis rate coefficients), developing appropriate input concentration fields and source emissions, and determining wet and dry deposition parameters.

3.1 Model characteristics

GRANTOUR is a Lagrangian parcel model, typically run with 50,000 parcels using a 6-hour operator-split time step. The actual spin-up to equilibrium may use 25,000 parcels and a 12 hour operator-split time step. The parcels are constrained to have constant mass and are advected by winds on an Eulerian grid. Concentrations at any location are calculated by mapping the parcel concentrations onto the grid. Typically, the GRANTOUR model is run for either a perpetual month or over an annual cycle.

3.2 Meteorological fields

The wind, precipitation, and other meteorological fields that "drive" GRANTOUR are calculated using the Lawrence Livermore National Laboratory (LLNL) version (Cess et al., 1989) of NCAR's CCM1(Community Climate Model). The meteorological fields are updated every 12 hours. In this version of the CCM, the winds are resolved at twelve different levels (sigma = 0.009, 0.025, 0.06, 0.11, 0.165, 0.245, 0.355, 0.500, 0.664, 0.811, 0.926, and 0.991), and have a horizontal resolution or roughly 4.4 degrees latitude by 7.5

degrees longitude. Although the winds and precipitation fields are defined on this coarse grid, using 50,000 parcels, the parcel horizontal resolution is roughly 330 km x 330 km. (Using more parcels yields smaller typical parcel sizes.)

3.2.1 Wind fields

The GRANTOUR model updates the wind fields every 12 hours using the CCM1-calculated wind fields. Using the LLNL CCM, model studies showed time-average zonal winds tended to be within 5 m/s of observations, although they were slightly high for the winter hemisphere.

3.2.2 Temperature fields

The CCM1 temperatures are supplied to GRANTOUR every 12 hours. The predictor-corrector version of GRANTOUR then uses a monthly average temperature field to calculate reaction rate coefficients at grid locations. Parcels are advected for 12 hours, at which point their reaction rate coefficients are updated by interpolating from the monthly grid-based values.

The non-methane hydrocarbon version of GRANTOUR, which uses the Sillman solution technique, calculates reaction rate coefficients directly on the parcels. The reaction rate coefficients are updated every 12 hours on the parcels, when a new temperature is interpolated based on updated CCM1 values.

3.2.3 Precipitation fields

Precipitation fields are updated every 12 hours in GRANTOUR. The precipitation rate in GRANTOUR is equal to the rate of condensation of water vapor in CCM1. Precipitation fields obtained from CCM1 tended to be located correctly, but had a higher intensity than measurements (Penner et al., 1991).

Monthly average water vapor fields obtained from CCM1 were compared to monthly average observations compiled by Oort (1983). The data were obtained over the period 1963-1973. Zonal average precipitation (that is, the rate of water vapor condensation) was available for pressures of 50, 100, 200, 300, 400, 500, 700, 850, 900, 950, and 1000 mbars

Month-by-month zonal average comparisons were made of the CCM1 water vapor and Oort data at various levels. At 500 mb, CCM1 values were less than Oort's in polar regions by a large amount, and by a factor of 1.2 - 1.8 in other regions. At 1000 mb, CCM1 values were often similar or slightly larger than Oort's, especially in the tropics where CCM1 peak values were approximately 1.5 times that of Oort. If CCM1-generated precipitation rates are too high, wet deposition in GRANTOUR will be overestimated.

3.3 Model processes

The processes treated in GRANTOUR include chemical source emissions, chemical reactions, dry deposition, precipitation scavenging (wet deposition), and transport by advection, diffusion, and convection.

3.3.1 Chemical sources

Chemical sources may be injected for a grid box at the appropriate sigma level (although many are surface- or near-surface-based). For the model runs presented, the sources consist of NO_x, isoprene, ethane, and propane emissions. They are presented in more detail in Chapter 8. The ground based NO_x sources include fossil fuel combustion, biomass burning, and soil activity. The elevated NO_x sources include aircraft emissions, lightning (both cloud-cloud and cloud-ground) and a source due to N_2O in the stratosphere. The NMHC emissions are all surface-based.

3.3.2 Chemical reaction mechanism

The chemical reaction mechanisms previously incorporated in the GRANTOUR model have been fairly simple (five or fewer reactions). The ozone chemical reaction mechanisms used in this work are much more complex and are described in more detail in Chapter 6 and 10. The chemical reaction mechanism contains all of the chemical reactions and their appropriate reaction rate coefficients. Two different chemical reaction mechanisms were used in this study. One chemical reaction mechanism treated the cycles of CO and CH_4 (and was solved using a predictor-corrector numerical technique). It

included 47 different reactions, and predicted the concentrations of 17 different species. The version of the chemical reaction mechanism associated with the non-methane hydrocarbon version of the model contained 287 reactions and calculated the concentrations of 76 species. It was numerically integrated using the method introduced by Sillman (1991). Both chemical reaction mechanisms are presented in Chapter 6.

3.3.3 Dry deposition

The process of dry deposition is assumed to occur whenever the centroid of an air parcel passes within 50 mb of the surface. For those parcels, the diffusion equation is solved with the boundary condition that the surface flux of species i is equal to the deposition velocity of i times its surface concentration (Penner et al., 1991). The predictor-corrector version of GRANTOUR calculates the dry deposition of O_3, NO, NO_2, H_2O_2, HNO_3, NO_3, N_2O_5, HCHO, and CH_3OOH. Additionally, the non-methane hydrocarbon version of the model also includes the dry deposition of PAN and PAN-analogues.

Although data is sparse, deposition velocities have been measured for a variety of different species in limited applications (e.g., see Sehmel, 1980; Voldner et al., 1986). The predictor-corrector and non-methane hydrocarbon GRANTOUR models use the deposition velocities detailed in Chapter 4.

3.3.4 Wet scavenging

Precipitation scavenging is accounted for in both stratiform and convective events for a number of species: H_2O_2, HNO_3, N_2O_5, HNO_4, HCHO, CH_3OOH, HONO, and ROOH (Sillman version only). Wet deposition of nitrate, NO_3^- (which comes from HNO_3), was first prescribed in the simple NO_x version of GRANTOUR (Penner et al., 1991) based on the work of Sperber and Hameed (1986). All of the currently deposited species use the same equation to calculate their removal due to wet scavenging. In the model the rate of removal of species i from level k by precipitation type j is defined as:

$$R_{ij}(k) = S_{ij}(k) \times p_j(k) \times f_j \qquad (3.53)$$

where S_{ij} is the species-specific rate coefficient in units of cm^{-1}, p is the rate of precipitation in cm/hr (equal to the rate of condensation of water vapor in the GCM), and f is the fraction of the grid box covered by precipitation. For stratiform precipitation, f = 1 and for convective precipitation, f = 0.3.

In the GCM, precipitation is assumed to occur when saturation ratios reach 1.0. Further details of the scavenging processes may be found in Walton et al. (1988). A literature review of wet scavenging parameterizations and the choice of scavenging coefficients for GRANTOUR are presented in Chapter 5.

3.3.5 Convective mass flux

Vertical mixing due to convective motion is calculated in GRANTOUR as described by Walton et al. (1988). The convective mass flux rates are prescribed based on diagnosed convection in CCM1. Convective mixing is treated as a diffusive process in GRANTOUR. Penner et al. (1991) performed sensitivity studies with the NO_x version of GRANTOUR in which convective mass flux rates were doubled and halved. The resulting NO_x and HNO_3 profiles did not change significantly.

3.3.6 Diffusion

3.3.6.1 Interparcel mixing

As parcels advect throughout the atmosphere, they will influence each other due to concentration gradients between two parcels. The concentration gradient gives rise to a flux from one parcel to another. This interparcel mixing is calculated as a diffusion process, as given in Walton et al. (1988). The diffusion is calculated in both the vertical and horizontal directions by using a shear-dependent formulation of eddy diffusion. However, the interparcel mixing is turned off in the stratosphere, as earlier studies showed that including it led to excessive mixing between the troposphere and the stratosphere (Penner et al., 1991).

3.3.6.2 Large-Scale diffusion

Large scale diffusion is calculated in GRANTOUR as described in Walton et al. (1988). The horizontal diffusion coefficients K_x and K_y are 1.0×10^8 cm^2/s at all vertical levels. The vertical diffusion coefficient is specified as 1.0×10^4 cm^2/s in the troposphere and 1.0×10^2 cm^2/s in the stratosphere.

3.4 Model development for this work

In this work, I have developed two versions of a global, three-dimensional, chemistry-transport-deposition model that can simulate tropospheric O_3 and OH production. The first model version incorporated the chemistry necessary to model tropospheric O_3 production from the reactions of CO, CH_4, and NO_x. The second model version also included longer-lived alkane species and the biogenic hydrocarbon isoprene, which is emitted by live plants and trees.

The development of a GRANTOUR version for photooxidant studies included choosing an appropriate chemical reaction mechanism (a subset of all possible chemical reactions) and a numerical solution technique for the chemistry integration. A predictor-corrector method was used in the CO/CH_4/NOx model version. A tropospheric-specific technique (Sillman, 1991) was used in the CO/CH_4/NMHC/NO_x model version. Numerical experiments were performed to further decrease the models' computational time.

Additionally, appropriate dry deposition velocities and wet deposition parameters were chosen. A number of source emission inventories were developed and/or obtained for NO_x and NMHCs. The important NO_x sources include: fossil fuel combustion, biomass burning, lightning, soil emissions, and transport from the stratosphere. The sources of NMHCs include biomass burning and industrial sources of alkanes and biogenic emissions of isoprene. The concentrations of CO and CH_4 were specified based on values published in the literature.

CHAPTER 4 DRY DEPOSITION

4.1 Introduction to dry deposition

Dry deposition is an important loss for many tropospheric species. For example, Logan (1983) estimated global loss rates of nitrate to be 12-22 Tg N/yr by dry deposition and 12-42 Tg N/yr by wet deposition. Based on field measurements, Huebert and Robert (1985) estimated a dry deposition flux of 24.4-31.1 kg N/km^2 for gaseous HNO_3 in the month of June in an Illinois pasture. For that same month, the nearby National Acid Deposition Program (NADP) site recorded a wet-nitrate deposition rate of 33.9kg N/km^2. Thus, wet and dry deposition of HNO_3 were comparable in magnitude.

Although dry deposition can be significant, it is a complex process. Measurements are sparse and limited in their applicability because dry deposition varies with, among other conditions, the depositing chemical species, prevailing meteorology, and the deposition surface. Sehmel (1980) devotes an entire table to factors that influence dry deposition removal rates.

Dry deposition for a species i is characterized by a deposition velocity, v_d (cm/s). The deposition velocity is expressed in terms of the dry deposited flux, Q (molecules/cm^2-s), and the concentration of i at a reference height, c_i (molecules/cm^3):

$$v_d = \frac{Q}{c_i} \qquad (4.1)$$

To use (4.1) without modification, the species flux should be entirely downward (the surface must not be a source of the chemical species) (Hicks and Matt, 1988).

The deposition velocity may also be thought of in terms of a series of resistances having units of s/cm:

$$v_d = \frac{1}{(r_a + r_b + r_c)} = \frac{1}{r_t} \qquad (4.2)$$

In (4.2), r_a is the atmospheric resistance to micrometeorological transport across the

boundary layer to a laminar sublayer, r_b is the resistance to molecular diffusion across the laminar sublayer, r_c is a resistance to interaction (biological, chemical) between the pollutant and deposition surface, and r_t is the total resistance (Wesely and Hicks, 1977; Huebert and Robert, 1985; Voldner et al., 1986). These resistances are functions of the depositing species, meteorological parameters (such as wind speed, solar heating, stability, wetness, etc.), and the deposition surface (including its biological functions such as stomatal openeings and closings).

Measurements of the total dry deposition flux are used in either equation (4.2) to estimate deposition velocity, or to compare with total wet depostion. To use (4.2), the dry deposited flux, Q, and ambient reference height concentration, [i], are measured (or estimated) and v_d calculated. Two common methods used in the field and lab are to measure the dry depostion flux to surrogate surfaces (e.g., buckets, petri dishes, plates, filters, foil, etc) or to a plant itself (Dasch, 1983; Lindberg and Lovett, 1983, Sickles et al., 1983). The deposition to a plant surface is measured by a foliar wash: the plant is rinsed with water, and the aqueous solution is then analyzed. Alternatively, deposition fluxes may be measured using micrometeorological techniques such as the gradient and eddy correlation methods (Hicks, 1986). Many of the dry deposition measurement techniques were studied in a field intercomparison study during 1981 and 1982 (Dolske and Gatz, 1985 and references therein).

All of the above methods have limitations. Surrogate species are not alive and may not reproduce the deposition to a plant (recall the final resistance, r_c, which incorporates plant biological functions). Dry deposition also varies between surrogate species. Also, in the field, samples may be contaminated by debris such as dust and bird droppings (Hicks, 1986). The foliar wash technique also has drawbacks. Deposited material may be taken up by the plant. An accidental exposure to slight rain or dew can either intensify the deposition amount (due to chemicals in the water) or rinse the plant off. Additionally, the plant could emit the species of interest, which would artificially increase the amount deposited.

Finally, micrometeorological techniques provide relatively precise values, but require fast instruments and are fairly labor intensive and expensive (Sehmel, 1980; Dolske and Gatz, 1985). Thus, network measurements, such as those for wet deposition, which provide widespread data for model verification, are not yet available.

4.2 Parameterization of dry deposition in global models

Generally, global models parameterize the dry deposition of species i at reference height h using an equation similar to the one below:

$$F_{z,i} = -K_{zz} \times \frac{\partial c_i(z,t)}{\partial z} = -v_d \times c_i(z,t)\Big|_{z=h} \tag{4.3}$$

where $F_{z,i}$ is the flux of species i, K_{zz} is the diffusion coefficient, c_i is the concentration of species i, z is height, and v_d is the deposition velocity. In GRANTOUR, the reference height, h, is defined to be the surface. Then, any parcel whose centroid comes within 50 mbar of the surface experiences dry deposition. The diffusion equation is thus solved using the above flux condition as the boundary condition at the surface.

However, in other global models, the reference height, h, is often defined to be higher, perhaps 250m to 2 km (Rodhe and Isaksen, 1980; Isaksen et al., 1985; Hough, 1991). These models invoke an equation that relates the deposition velocity at the reference height, $v_{d,h}$ to the deposition velocity at an elevation of 1 meter, $v_{d,0}$:

$$v_{d,h} = v_{d,0} \times \frac{1}{1 + \frac{v_{d,0}\Delta z}{K_{zz}}} \tag{4.4}$$

where Δz is the vertical grid spacing of the model, and the vertical diffusion coefficient, K_{zz} is assumed to be constant in the boundary layer.

For example, Isaksen et al. (1985) present in their Table III, the deposition velocities used in the model, $v_{d,h}$ (assuming a vertical spacing, Δz = 500m) and their reference

deposition velocities, $v_{d,0}$. The $v_{d,h}$ are alowed to vary with latitude (because K_{zz} varies with latitude) and season (both K_{zz} and $v_{d,0}$ vary with season). Table III of Isaksen et al. (1985) is reproduced below.

Table 4.1 Deposition velocities, $v_{d,h}$ (cm/s) used by Isaksen et al. (1985)

	S U M M E R					W I N T E R				
Latitude (N)		80	70	60	50		80	70	60	50
K_{zz}, 10^4 cm^2/s		0.5	2.0	5.0	5.0		0.125	0.5	1.25	5.0
Species	$v_{d,0}$	$v_{d,h}$	$v_{d,h}$	$v_{d,h}$	$v_{d,h}$	$v_{d,0}$	$v_{d,h}$	$v_{d,h}$	$v_{d,h}$	$v_{d,h}$
O_3	0.5	0.08	0.22	0.33	0.33	0.1	0.01	0.01	0.01	0.33*
NO_2, PAN	0.2	0.07	0.13	0.17	0.17	0.01	0.01	0.01	0.01	0.17*
HNO_3, SO_2	0.7	0.09	0.26	0.41	0.41	0.1	0.02	0.05	0.07	0.41*

*same v_0 as for summer

For reference, Table 4.2 below gives either the surface or 1 m land-based, dry deposition velocities used by global models. Those models which use a 1m dry deposition velocity use equation (4.4) above to calculate actual dry deposition at a reference height. With the exception of GRANTOUR and Crutzen and Zimmermann (1991), which are three-dimensional models, all of the listed models are two-dimensional. .

Table 4.2 Land-based surface deposition velocities, v_d (cm/s) used in global models

Species	GRAN - TOUR	Crutzen & Zimmer-mann (1991)	Kana-kidou et al. (1991)	Hough (1991) *	Isaksen et al. (1985)* (Summer/ Winter)	Gidel et al. (1983)	Rodhe & Isaksen (1980)*
O_3	0.3	0.4	calc	0.6	0.5/0.1	0.25	0.4
NO	0.05	---	0.1	---	---	---	---
NO_2	0.25	1.0	0.5	0.1	0.2/0.01	---	0.2
HNO_3	0.5	1.0	1.0	4.0	0.7/0.1	1.0	0.7
$_2O_2$	0.5	1.0	0.5	1.0	---	---	---
CH_3OOH	0.5	---	0.1	0.5	---	---	---
NO_3	0.2	---	0.1	---	---	---	---
N_2O_5	0.2	---	0.1	---	---	---	---
HCHO	0.1	---	0.2	---	---	---	---
Organic nitrates	---	---	0.1	---	---	---	---
Alde-hydes	0.1	---	0.1	---	---	---	---
Acetic acid	---	---	0.5	---	---	---	---
PAN	0.1	---	0.1?	0.2	0.2/0.01	---	0.2
ROOH	0.5	---	0.1	---	---	---	---

*Models using 1m reference $v_{d,0}$ and equation (4.4) to calculate $v_{d,h}$

Table 4.3 below lists the water-based surface deposition velocities used in global models. For many of the models, the water-based deposition velocity does not differ from the land-based. The highlighted coefficients are those which do actually vary from the model's land-based values.

4.3 Dry deposition velocities used in GRANTOUR

Based on the information above, and available literature on deposition velocities, Table 4.4

lists the deposition velocities used in the predictor-corrector and Sillman versions of GRANTOUR.

Table 4.3 Water-based surface deposition velocities, v_d (cm/s) used in global models

Species	GRAN - TOUR	Crutzen & Zimmer-mann (1991)	Kana-kidou et al. (1991)	Hough (1991)*	Isaksen et al. (1985)* (Summer/ Winter)	Gidel et al. (1983)	Rodhe & Isaksen (1980)*
O_3	**0.03**	**0.1**	calc	**0.1**	0.5/0.1	0.05	**0.1**
NO	0.05	---	**0.05**	---	---	0.1	---
NO_2	**0.05**	**0.1**	**0.5**	**0.05**	0.2/0.01	0.1	0.2
HNO_3	0.5	1.0	1.0	**1.0**	0.7/0.1	2.0	0.7
H_2O_2	0.5	**2.0**	0.5	1.0	---	---	---
CH_3OOH	0.5	---	0.1	0.5	---	---	---
NO_3	0.2	---	**0.05**	---	---	---	---
N_2O_5	0.2	---	**0.05**	---	---	---	---
HCHO	0.1	---	0.2	---	---	---	---
Organic nitrates	---	---	0.1	---	---	---	---
Alde-hydes	0.1	---	0.1	---	---	---	---
Acetic acid	---	---	0.5	---	---	---	---
PAN	0.1	---	0.05	---	0.2	---	0.6
ROOH	0.5	---	0.1	---	---	---	---

*Models using 1m reference $v_{d,0}$ and equation (4.4) to calculate $v_{d,h}$

Table 4.4 Dry deposition velocities, v_d (cm/s) used in GRANTOUR

Species	v_d, land (cm/s)	v_d, water (cm/s)
O_3	0.3	0.03
NO	0.05	0.05
NO_2	0.25	0.05
HNO_3	0.5	0.5
H_2O_2	0.5	0.5
CH_3OOH	0.5	0.5
NO_3	0.2	0.2
N_2O_5	0.2	0.2
PAN	0.1	0.1
ROOH	0.5	0.5
HCHO	0.1	0.1
Other aldehydes	0.1	0.1

CHAPTER 5 WET SCAVENGING PARAMETERIZATIONS

5.1 Introduction to scavenging rates, λ, s^{-1}

Typically, wet removal for species i is parameterized in terms of a scavenging rate, λ_i, s^{-1}, where:

$$\frac{dC_i}{dt} = -\lambda_i \times C_i \tag{5.1}$$

Note that models either use climatological average precipitation, with rain continuously falling through the time period, or event precipitation, which allows for periods of wet and dry. In theory, GRANTOUR uses the latter, but its meteorological variables are only updated every 12 hours.

In GRANTOUR, $\lambda_{ij}(k)$, the rate of removal of species i from level k by precipitation type j is defined as:

$$\lambda_{ij}(k) = S_{ij}(k) \times p_j(k) \times f_j \tag{5.2}$$

where S_{ij} is the species-specific rate coefficient in units of cm^{-1}, p is the rate of precipitation in cm/hr (equal to the rate of condensation of water vapor in the GCM), and f is the fraction of the grid box covered by precipitation. For stratiform precipitation, f = 1 and for convective precipitation, f = 0.3.

5.2 Current GRANTOUR scavenging coefficients

In GRANTOUR, the rate of removal of species i from level k by precipitation type j is given by equation 5.2 above. The species specific rate coefficients, $S_{ij}(k)$ were derived with consideration of the Henry's Law Coefficient for species i, $K_{H,i}$. For species i, K is defined as:

$$K_{H,i} = \frac{C_i(aq)}{P_i(g)} \tag{5.3}$$

where $C_i(aq)$ is the concentration in aqueous phase and $P_i(g)$ is the gaseous partial pressure

in air. The units of K_H are moles liter^{-1} atm^{-1}, also denoted as M atm^{-1}, where M = moles/ liter. A highly water soluble species will have a large dimensional Henry's Law Coefficient. Table 5.1 lists typical K_H values.

Table 5.1: Dimensional Henry's Law Coefficients

Species	K_H @ 298K
HNO_3	3.3×10^{6}
H_2O_2	7.4×10^{4}
HCHO	$(3.0 - 6.3) \times 10^{3}$
CH_3OOH	2.2×10^{2}
HONO	4.9×10^{1}
SO_2	1.2
CO_2	3.4×10^{-2}
O_3	1.3×10^{-2}
NO_2	1.0×10^{-2}
NO	1.9×10^{-3}
CH_4	1.5×10^{-3}
O_2	1.3×10^{-3}
CO	9.6×10^{-4}

An additional point is that the dimensionless Henry's Law Coefficient, H, is related to the dimensional Henry's Law Coefficient, K_H by:

$$H = \frac{273.15K \times P_i}{K_H \times 22.4 \times T \times P_o} \tag{5.4}$$

where T is the local temperature (Kelvin), P_i is the local pressure, and P_o the standard surface pressure. Thus, a large K_H, (or a small H) implies high solubility, and vice versa.

Based on the above values, the following species should be efficiently scavenged: HNO_3, H_2O_2, HCHO, CH_3OOH, HONO, HNO_4, N_2O_5, other aldehydes, and ROOH (non-methane hydrocarbon version only). Conversely, any species with a dimensional Henry's Law Coefficient less than 5×10^{-2} M atm^{-1} would not be easily removed unless it underwent further aqueous chemical reactions or equilibria. The actual values of S_{ij} used in GRANTOUR are shown in Table 5.2 below.

Table 5.2: Precipitation scavenging rate coefficients used in GRANTOUR

Species	S_{ij}, stratiform, cm^{-1}	S_{ij}, convective, cm^{-1}
HNO_3	2.4	4.7
H_2O_2	2.4	4.7
HCHO	2.0	4.0
CH_3OOH	2.0	4.0
HONO	1.5	3.0
HNO_4	1.5	3.0
N_2O_5	1.0	2.0
ROOH*	2.0	4.0

*Present in NMHC version of the model only

5.3 Other methods for determining wet scavenging rates

Other two and three dimensional models have also parameterized wet scavenging. This has been done mainly for aerosol species, sulfate (SO_4^{--}), sulfur dioxide (SO_2), and nitrate (HNO_3 or NO_3^-). These other methods are detailed below. Tables 5.3 and 5.4 list wet scavenging rates used in climatological average precipitation models and episodic precipitation models, respectively.

Note that the following abbreviations are used in Tables 5.3 and 5.4. IR78 = Isaksen and Rodhe, 1978, RI80 = Rodhe and Isaksen, 1980, CZ91 = Crutzen and Zimmermann, 1991, IS85 = Isaksen et al., 1985, IH87 = Isaksen and Hov, 1987, LR91 = Langner and

Rodi. . 1991, GC86 = Giorgi and Chameides 1985, BR91 = Brost et al. 1991, ϕ = latitude, λ = longitude, and z = height. .

Table 5.3: Wet scavenging rates used in climatological average precipitation models

Species	Scavg. Process	Time	Scavenging Rate, s^{-1}	Variation	Theoretical Basis	Reference
Aerosol, soluble gas (e.g. HNO_3)	precip	June to Sept	3.5×10^{-8} to 4.2×10^{-6}	ϕ, z	Energy Balance (Eqn. 5.6)	IR78, Table 4
Aerosol, soluble gas (e.g. SO_4^{--})	cloud + precip	Annual	5.0×10^{-7} to 1.0×10^{-5}	ϕ, z	"	IR78, Table 5
Aerosol, soluble gas	precip	Jan, July	$< 3.5 \times 10^{-6}$	ϕ, z	IR78	RI80, Table 1
SO_2	precip	Jan,July	$< 1.0 \times 10^{-6}$	ϕ, z	IR78	RI80, Table 1
NO, NO_2	precip	Jan,July	$< 1.2 \times 10^{-6}$	ϕ, z	IR78	RI80, p.7402
SO_2	cloud	Jan,July	$< 2.9 \times 10^{-6}$	ϕ, z	IR78	RI80, p.7402
aldehydes	cloud	Jan,July	$< 2.9 \times 10^{-6}$	ϕ, z	IR78	RI80, p.7402
peroxides	cloud	Jan,July	$< 8.7 \times 10^{-6}$	ϕ, z	IR78	RI80, p. 402
HNO_3, H_2O_2	precip	Jan,July	Same as RI80	ϕ, z	IR78	CZ91, p.145
HNO_3	cloud/ precip	Summer	5.0×10^{-6}	hemis. mean	IR78	IS85, IH87
HNO_3	"	Winter	1.25×10^{-6}	"	"	"
SO_4^{--}	"	Summer	5.0×10^{-6}	"	"	"
SO_4^{--}	"	Winter	1.25×10^{-6}	"	"	"
SO_2	"	Summer	9.0×10^{-6}	"	"	"
SO_2	"	Winter	2.25×10^{-6}	"	"	"
SO_4^{--}	incloud precip	Annual	< 7.5 to 12.5×10^{-6}	ϕ, λ, z	Similar to IR78	LR91, Fig.1, p.8
SO_2	incloud precip	Annual	$< 7.0 \times 10^{-6}$	ϕ, λ, z	"	LR91, Table 2

Table 5.4: Wet scavenging rates used in three-dimensional, event precipitation models

Species	Scavenging Process	Precip.Rate, kg/m^3-s	Scavenging Rate, s^{-1}	Theoretical Basis	Ref.
Sol. gases, aerosols	strat. pre	1×10^{-8}	2×10^{-5}	GC86	GC86
"	"	1×10^{-7}	1×10^{-4}		
"	"	1×10^{-6}	2×10^{-4}		
Sol. gases, aerosols	conv. pre	1×10^{-6}	5×10^{-5}	GC86	GC86
"	"	1×10^{-5}	7×10^{-5}		
"	"	1×10^{-4}	7×10^{-5}		
^7Be (aer)	strat. pre	1×10^{-8}	6×10^{-6}	GC86	BR91
"	"	1×10^{-7}	5×10^{-5}		
"	"	1×10^{-6}	3×10^{-4}		
^7Be (aer)	conv. pre	1×10^{-6}	8×10^{-5}	GC86	BR91
"	"	1×10^{-5}	1×10^{-4}		
"	"	1×10^{-4}	1×10^{-4}		
HNO_3	strat pre	0.01 to 0.1 cm/hr	7×10^{-6} to 7×10^{-5}	GRANTOUR	
HNO_3	strat. pre	0.01 cm/hr[b]	7×10^{-6}	GRANTOUR	
HNO_3	conv pre	0.1 to 2.5 cm/hr	4×10^{-5} to 1×10^{-3}	GRANTOUR	
HNO_3	conv. pre	0.03 cm/hr[b]	1×10^{-5}	GRANTOUR	

[a] Typically observed values; [b] Mean GRANTOUR values, taken from average of 60 July GTR files.

5.3.1 Isaksen and Rodhe (1978) Climatological average models

Isaksen and Rodhe (1978), developed a 2D model suitable for 0 - 20 km. They first used the model on a sulfur study. The model uses a climatological average rainfall so precipitation continuously falls. They derive first order removal rates, L, for reversible incloud scavenging and irreversible incloud scavenging.

Reversible incloud scavenging takes place only when cloud droplets form precipitation which falls to the ground. (It's "reversible" because if the cloud evaporates before precipitation occurs, the compound reappears in its initial form.) Irreversible incloud scavenging occurs when a compound is transformed within a cloud drop. Thus, it occurs if a cloud forms (irregardless of whether precipitation occurs). Reversible incloud scavenging can be applied to HNO_3, which will not react further inside a water droplet. Irreversible incloud scavenging can be applied to the sulfur cycle, because SO_2 can be irreversibly oxidized to form SO_4^{2-} once inside a water droplet. Isaksen and Rodhe (1978) assume subcloud scavenging = 0. The change in concentration of species i from wet scavenging is:

$$\frac{dC_i}{dt} = -L_i \times C_i \qquad (5.5)$$

where L_i is equivalent to λ_i in GRANTOUR nomenclature.

5.3.1.1. Reversible incloud scavenging

Scavenging coefficients, L_i, (equivalent to first order removal coefficients) are derived from an energy balance that relates precipitation, latent heat of evaporation, and heating rate. They calculate the removal rate using the equation below.

$$L \equiv \frac{1}{\tau} = \varepsilon \times \frac{C_p \rho}{L_e \rho_w} \times \frac{\partial T}{\partial t} \qquad (5.6)$$

where:

ε = efficiency or fraction of aerosols that are scavenged,

C_p = specific heat at constant pressure,

L_e = latent heat of evaporation,

ρ = air density, and

ρ_w = liquid water content in rain producing cloud, kg/m^3

They assume that:

$$\varepsilon \times \frac{C_p \rho}{L_e \rho_w} = 0.12 K^{-1} \qquad (5.7)$$

The values of $(\frac{\partial T}{\partial t})$ are "...taken from Newell et al. (1972) and based on observed precipitation rates at the surface and educated guesses about the vertical distribution of the precipitation forming process." (Note that Newell et al. (1972) present zonally and seasonally averaged fieldsof $(\frac{\partial T}{\partial t})$.) In Figure 3, Isaksen and Rodhe (1978) show their calculated meridional distribution of precipitation, along with observations.

Table 4 in Isaksen and Rodhe (1978) lists the L_i values as a function of latitude and height for reversible incloud scavenging, in units of $(day)^{-1}$, for a highly soluble species such as SO_4^{--} or HNO_3. The maximum values are 0.36 day^{-1}, or 4.2 x 10^{-6} s^{-1}. Local maxima occur in the lower midlatitudes and at 6 - 9 km near the equator.

5.3.1.2. Irreversible incloud scavenging

The L_i values for irreversible incloud scavenging of other species are given in Isaksen and Rodhe (1978) Table 6 . They derive pertinent equations on p.14-18 and show

parameter choices on p.22. The maximum values are 1.0×10^{-5} s^{-1}, and occur at 2 - 3 km in the midlatitudes.

5.3.1.3. Papers using Isaksen and Rodhe's (1978) formulation

Papers written after Isaksen and Rodhe (1978) either use directly the L_i in Tables 4 and 6 or an average hemispheric value, based on the tabulated values. For example, Rodhe and Isaksen (1980) use the method and values above (involving average rainfall rates and energy balance considerations) for wet scavenging of HNO_3 and sulfate. They also assume that NO and NO_2 are removed at a rate which is 3 times lower than HNO_3. Crutzen and Zimmermann (1991) use in their three dimensional model the scavenging rates of Rodhe and Isaksen (1980).

The papers that use a mean hemispheric value for L_i (based on Tables 4 and 6 in Isaksen and Rodhe (1978)) include Isaksen et al. (1985) and Isaksen and Hov (1987). Both prescribe a hemispheric mean value for L_i of 5×10^{-6} s^{-1} for SO_4^{--} and HNO_3 during the summer, and 9×10^{-6} for SO_2. These values are reduced by a factor of 4 during the winter.

5.3.2 Giorgi and Chameides (1986)

Giorgi and Chameides (1986), studied wet scavenging using both three dimensional event rainfall and climatological average rainfall. They derived equations for both wet scavenging in a GCM (which used locally produced "event" precipitation rates) and a parameterization for models that use climatologically averaged precipitation. A correction factor, incorporated into an effective average species lifetime is required for the climatologically averaged model to address the episodic nature of rainout (that depends on frequency, duration, local flow, etc.).

5.3.2.1 Event Precipitation (Model-calculated or observed)

Giorgi and Chameides (1986) first show that for a three-dimensional, global model, which uses model-calculated event precipitation fields (as opposed to climatological averaged fields):

$$\frac{dC_i}{dt} = -\lambda_i \times C_i \qquad (5.8)$$

Note that this is a repeat of equation (5.1), with λ having units of s^{-1}. It is calculated using the equation below:

$$\lambda = \frac{F}{\Delta t} \times (1 - e^{-\varepsilon\beta T_c}) \qquad (5.9)$$

where:

F = fraction of the grid cell that clouds occupy, dimensionless,

Δt = model time step, s^{-1},

$\varepsilon = 1$ = efficiency of uptake of species by precipitation, dimensionless,

β = frequency of cloud-water conversion to rainwater (and removal), s^{-1}, and

T_c = duration of precipitation event, s^{-1},

are defined separately for stratiform and convective precipitation.

5.3.2.1.1 Stratiform precipitation

Giorgi and Chameides (1986) define F and β as below:

$$F = \frac{F_0}{1 + \beta\tau_s} \qquad (5.10)$$

$$\beta = \frac{\beta_0}{F_0} + \frac{1}{F_0\tau_s} \qquad (5.11)$$

where $\tau_s = L_s/Q$, and:

F_0 = 0.8,

β_0/F_0 = 10^{-4} s^{-1},

Δt = model time step (I used 40 minutes and 6 hours for these calculations),

T_c = stratiform time = model time step,

L_s = liquid water content = 0.5 x 10^{-3} kg/m^3, and

Q = precipitation rate, kg/m^3-s.

Note that T_c is less than or equal to Δt.

5.3.2.1.2 Convective precipitation

Giorgi and Chameides.(1986) assume β has a constant value of 1.5×10^{-3} s^{-1}. F is calculated by:

$$F = \frac{0.3\left(\frac{\Delta t}{T_c}\right)}{\frac{\Delta t}{T_c} + 0.3\beta\tau_c} \qquad (5.12)$$

where:

$\tau_c = L_c/Q$,

T_c = 25 minutes, and

$L_c = 2.0 \times 10^{-3}$ kg/m^3.

5.3.2.1.3 Other models using the 3D, global Giorgi and Chameides (1986) "event" precipitation method

Brost et al.(1991) use the method of Giorgi and Chameides (1986) to parameterize wet removal in a global model of ^7Be. They found, however, excessive scavenging in stratiform clouds (for small to medium amount of precipitation, $Q < 10^{-6}$ kg/m^3-s), and so increased the cloud liquid water content, L_s to 1.5×10^{-3} kg/m^3 . Conversely, they found moderately low scavenging in convective clouds, and so decreased the L_c to 1.5×10^{-3} kg/m^3.

5.3.2.2 Giorgi and Chameides (1986) method for climatological average precipitation fields

Models which parameterize wet scavenging using climatological averaged fields don't explicitly treat phenomenon due to the "episodic" and "asymmetric" nature of real precipitation. Variables which may affect removal include the frequency and duration of

precipitation, and the direction of the species main flow. Giorgi and Chameides (1986) first define a horizontally averaged lifetime, $\tau_{k,t}$, for a given vertical level k and time t, which is summed over all vertical layers, k (their equation (10)). They next define a species "effective average lifetime", $\tau^{e}_{k,t}$, which takes into account the intermittence and assymmetry of precipitation. They compare the effective average lifetime from a parameterized model to lifetimes derived from the GCM to show this "correction" indeed produces reasonable results.

5.3.2.2.1 Other models using the Giorgi and Chameides (1986) correction for climatological average precipitation

Langner and Rodhe (1991) have a three dimensional model of the tropospheric sulfur cycle. They use monthly average surface precipitation values, R_o (g m^{-2} s^{-1}), from Jaeger (1976). The precipitation at any level R, is related to the surface by:

$$R(\phi, \lambda, z, t) = R_0(\phi, \lambda, t) \times g(\lambda, z, t) \qquad (5.13)$$

where ϕ = longitude, λ = latitude, z = height, and g(λ,z,t) is assumed to equal the latent heat release esimated by Newell et al. (1974).

The rate of removal, L_p, is given by:

$$L_p = \frac{\varepsilon R}{L} \qquad (5.14)$$

where ε is the efficiency of uptake of species by precipitation, and L is the liquid water content. For SO_4^{--}, they prescribe a value of $\varepsilon/L = 1.2$, which is a midrange value for both and L. In Figure 1 they plot the zonally and annually average rate of wet removal of sulfate. The maximum rates are (7.5 to 12.5) x 10^{-6} s^{-1}. They then include the effective average lifetime correction of Giorgi and Chameides (1986), but also increase εL to 1.6. This gives them new removal rates, L_p, which are very similar to the original values shown in Figure

1. For SO_2, they assign $\varepsilon/L = 0.5$. They don't show a figure for its wet scavenging rate. In Table 2, they cite wet removal rates of less than or equal to $1.5 \times 10^{-5}\ s^{-1}$ for sulfate incloud scavenging, less than or equal to $7.0 \times 10^{-6}\ s^{-1}$ for SO_2 incloud scavenging, and less than or equal to $1.0 \times 10^{-5}\ s^{-1}$ for SO_2 subcloud scavenging.

Langner and Rodhe discuss the fact that actual precipitation scavenging of SO_4^{--} in the mid and upper troposphere may be as much as 50% higher than in their model. However, since their results are generally in "good agreement" with observations of concentration and deposition, as well as the fact that SO_4^{--} concentrations tend to be low due to inlet losses, they feel fairly confident in their choices of deposition parameters.

5.3.3 Crutzen and Gidel (1983) Method for climatological precipitation

Crutzen and Gidel (1983), parameterize wet removal in a two dimensional ozone model using a mean downward settling velocity. The model uses two- dimensional water vapor distributions from Oort and Rasmussen (1971). The physical basis for doing so is that on an average sense, the net upward flux of water vapor through a horizontal level at z is 0. Thus, they derive:

$$-K_z(M)\frac{\partial \mu_{H_2O}}{\partial z} = w_{H_2O}(H_2O) \qquad (5.15)$$

where K_z is the eddy diffusivity, μ is the mixing ratio, z is height, (H_2O) is concentration (cm^{-3}), and w_{H2O} is an average statistical downward gravitational velocity. Table 1 gives w_{H2O}, and Table 2 gives w for H_2O_2, HCl, and HNO_3 as a function of height and latitude

A typical removal rate for 35N, June - September for HNO_3 was calculated using this method. Assuming Crutzen and Gidel's (1983) value of $w_{HNO3} = -1.2$ cm/s @ z = 0.8 km. and a concentration of HNO_3 of 2 ppbv ($= 4.92 \times 10^{10}\ cm^{-3}$), HNO_3 deposition is 0.5 kg

N/km^2 for a 6 hour timestep. Thus, in 30 days, their model would deposit 60 kg N/km^2. The NO_x version of GRANTOUR calculates a peak of 15 - 20 kg N/km^2 for the peak over the U.S. during July (Penner et al., 1991) and the data suggest a peak of 30 kg N/km^2, inferring that Crutzen and Gidel's (1983) removal rates may be too high.

5.3.3.1 Other models using Crutzen and Gidel's (1983) parameterization

Kanakidou et al. (1991) used a two dimensional ozone model that included ethane and propane. They also prescribed the downward settling velocity method of Crutzen and Gidel (1983) for very soluble gases, which include HNO_3, H_2O_2, CH_3OH, and CH_3COOH. They note in the appendix that the parameterization uses constant wet removal, and needs further investigation.

5.3.4 Stewart et al. (1989) comparison of climatological precip. parameterizations

Stewart et al. (1989) calculated HNO_3 residence times using a box model with wet and dry periods. They compared these results to four other methods which used effective lifetimes and climatological precipitation. The best results came from a paper by Rodhe and Grandell (1972), followed by the instantaneous HNO_3 recovery method of Giorgi and Chameides (1985), the linear HNO_3 recovery method of Giorgi and Chameides (1985), and the quasi-random model of Stewart et al. (1988). Limitations to the Stewart et al. (1989) study, however, include the fact that the model has no horizontal resolution (or tracer spatial assymmetries), the scavenging rate is constant during precipitation (2.0×10^{-4} s^{-1} for HNO_3). A note of interest: Stewart et al. (1989) also showed in their box model that 80 different realizations of a stochastic precipitation model led to differences in a 90-day HNO_3 concentration of a factor of 2.9.

5.4 GRANTOUR precipitation rates

Typically observed ranges of precipitation are 0.1 cm/hr (light stratiform shower) to 2.5 cm/hr (heavy convective activity). However, GRANTOUR precipitation rates are much lower because the rainfall "events" from the CCM1 have been averaged over a 12 hour timestep. Giorgi and Chameides (1986), for example, assumed that the typical time for a convective cloud to precipitate is 25 minutes. In GRANTOUR, this total amount of precipitation is spread over a 12 hour step, giving a much lower precipitation rate than is actually observed.

GRANTOUR precipitation fields for the month of July were analyzed. The 60 CCM1 meteorological files were for the month of July (the meteorology was updated every 12 hours). The total column stratiform rate ranged from 1×10^{-8} to 0.2 cm/hr (mean: 0.01 cm/hr) or 2×10^{-15} to 3×10^{-7} kg/m^3-s (mean: 1×10^{-8} kg/m^3-s). The total column convective rate ranged from 5×10^{-5} to 0.4 cm/hr (mean: 0.03 cm/hr) or 5×10^{-11} to 5×10^{-7} kg/m^3-s (mean: 5×10^{-8} kg/m^3-s). (Note the convective numbers have already been multiplied by a factor of 0.3, the fraction of the grid box they are assumed to occupy).

Assuming typical rainfall rates for stratiform and convective events, rainfall amounts in kg/m^3-s may be calculated. One method is to simply convert cm/hr to kg/m^3-s. For example, a stratiform precipitation rate of 0.1 cm/hr is equivalent to 2.8×10^{-8}, 2.8×10^{-7}, and 2.8×10^{-6} kg/m^3-s for clouds heights of 0.1, 1, and 10 km, respectively. A high convective precipitation rate of 2.5 cm/hr is equivalent to 6.9×10^{-7}, 6.9×10^{-6}, and 6.9×10^{-5} kg/m^3-s, respectively. Thus, a range of precipitation rates might be:

10^{-9} to 10^{-6} kg/m^3-s	Stratiform precipitation
10^{-4} to 10^{-6} kg/m^3-s	Convective precipitation

A second method is to assume the liquid water contents of Langner and Rodhe (1991). The liquid water content may range from Ls = 0.05 - 0.25 g/m^3 for stratiform and Lc = 1 -

2 g/m^3 for convective precipitation. Assuming a cloud time of 40 minutes - 10 hours for a stratiform event, and 25 minutes for a convective cloud event yields precipitation rates of:

10^{-9} to 10^{-7} kg/m^3-s	Stratiform precipitation
10^{-6} to 7 x 10^{-7} kg/m^3-s	Convective precipitation.

Note that Brost et al. (1991) referred to small to medium values of precipitation in stratiform clouds as being < 10^{-6} kg/m^3-s.

5.5 Scavenging Rate calculations: Event precipitation models

Table 5.5 summarizes the HNO_3 scavenging rates calculated for the event precipitation models (Giorgi and Chameides (1986), Brost et al., (1991),), and GRANTOUR. Note total column precipitation rate was used for GRANTOUR. Calculating λ requires a precipitation rate. If typical observed precipitation rates are assumed for all three models, then GRANTOUR's scavenging rates are similar to Giorgi and Chameides (1986) and Brost et al. (1991). This is shown in lines 1-3 and 5-7 of Table 5.5. For Giorgi and Chameides (1986) and Brost et al. (1991), precipitation rates of 10^{-8} to 10^{-6} kg/m^3-s were assumed for stratiform precipitation and rates of 10^{-6} to 10^{-4} kg/m^3-s for convective precipitation. The GRANTOUR calculation assumed rates of 0.01 to 0.1 cm/hr for stratiform precipitation, and 0.1 to 2.5 cm/hr for convective precipitation.

The actual precipitation fields in GRANTOUR, however, are smaller than typical observations. GRANTOUR's precipitation is updated every 12 hours (720 minutes), versus 1 hour for Giorgi and Chameides (1986) and 40 minutes for Brost et al. (1991). GRANTOUR's precipitation is spread evenly over a 12 hour time period, but observed precipitation times are probably shorter. For example, Giorgi and Chameides (1986) cite a typical convective cloud precipitation time of 25 minutes. Thus, GRANTOUR's average convective precipitation rate should be 25/720 (= 0.035) of the observed rate.

Using the actual GRANTOUR precipitation rates derived in Section 5.4 yielded stratiform scavenging rates(lines 4 and 8 in Table 5.5) lower than Giorgi and Chameides

(1986) and on the low end of Brost et al. (1991)'s values for stratiform precipitation. GRANTOUR's convective scavenging rate is lower than both Brost et al. (1991) and Giorgi and Chameides (1986).

Although GRANTOUR's HNO_3 scavenging rate, λ, is lower, because it rains for 12 hours at a stretch in GRANTOUR, the total scavenged amount may be comparable to Brost et al. (1991) and Giorgi and Chameides (1986) (see section 5.7).

Table 5.5: Wet scavenging rates used in three-dimensional, event precipitation models

Species	Precipitation Type	Precipitation Rate, kg/m^3-s	Scavenging Rate, λ, s^{-1}	Reference
Sol. gases, aerosols	stratiform	10^{-8} to 10^{-6}	2×10^{-5} to 2×10^{-4}	GC86
"	stratiform	10^{-8} to 10^{-6}	6×10^{-6} to 3×10^{-4}	BR91
"	stratiform	0.01 to 0.1 cm/hr[a]	7×10^{-6} to 7×10^{-5}	GRANTOUR
"	stratiform	0.01 cm/hr[b]	7×10^{-6}	GRANTOUR
Sol. gases, aerosols	convective	10^{-6} to 10^{-4}	5×10^{-5} to 7×10^{-5}	GC86
"	convective	10^{-6} to 10^{-4}	8×10^{-5} to 10^{-4}	BR91
HNO_3	convective	0.1 to 2.5 cm/hr[a]	4×10^{-5} to 10^{-3}	GRANTOUR
HNO_3	convective	0.03 cm/hr[b]	10^{-5}	GRANTOUR

* Calculations assume [a]typically observed values or [b]actual mean GRANTOUR values for the JULY GTR files.

5.6 Scavenging rates, λ , s-1: Climatological average models

Table 5.6 lists the HNO_3 scavenging rates used in the climatological average precipitation models of Rodhe, Isaksen, and Hov, and GRANTOUR. The GRANTOUR scavenging rates are larger. However, the climatological average models assume that precipitation occurs everywhere, continuously, at an appropriate average rate. In

GRANTOUR's July GTR files, though, stratiform precipitation occurs over 60 - 70% of the grid boxes at any timestep, and convective precipitation over only 13 - 15% of the boxes. Thus, multiplying GRANTOUR's stratiform λ_s by 0.6 - 0.7 yields a "global average" λ_s of 4.2 - 4.9 x 10^{-6} s^{-1}. Multiplying GRANTOUR's convective λ_c by 0.13 - 0.15 yields a "global average" λ_c of roughly 2 x 10^{-6} s^{-1}. These scavenging rates, then, are quite similar to those used by the climatological average models.

A single calculation for HNO_3 using Crutzen and Gidel's (1983) method of assigning a settling velocity for wet deposition leads to wet deposition amounts similar to observations, and higher deposition amounts than GRANTOUR calculates by a factor of 1.5 - 2. (See Section 5.3.3).

Table 5.6: Wet scavenging rates, λ, s^{-1}, used in climatological average precipitation models

Species	Applicable Times	Scavenging Rates, λ, s^{-1}	Reference
Aerosol, sol. gas (e.g. HNO_3)	June-Sept.	3.5 x 10^{-8} to 4.2 x 10^{-6}	IR78 Table 4, 2D model
Aerosol, (HNO_3, SO_4^{--})	Jan July	3.5 x 10^{-6}	RI80 Table 1, 2D model
NO, NO2	Jan July	1.2 x 10^{-6} (1/3 of HNO_3)	RI80 , p7402
HNO_3	Summer	5.0 x 10^{-6}	IS85, IH87, 2D model
HNO_3	Winter	1.25 x 10^{-6}	IS85, IH87, 2D model
HNO_3	Stratiform	7 x 10^{-6}	GRANTOUR
HNO_3	Convective	1 x 10^{-5}	GRANTOUR
HNO_3	Stratiform	(4.2 to 4.9) x 10^{-6}	GRANTOUR "global average"

Table 5.6: Wet scavenging rates, λ, s^{-1}, used in climatological average precipitation models

Species	Applicable Times	Scavenging Rates, λ, s^{-1}	Reference
HNO_3	Convective	2×10^{-6}	GRANTOUR "global average"

5.7 Total Deposited Amount of Material

Because the three event precipitation models have meteorological updates every 40 minutes, 1 hour, and 12 hours, the total amount of HNO_3 deposited over a given amount of time, e.g. 6 or 12 hours, was examined. Two types of scenarios were simulated. In the first (no replenishment), the model has an initial concentration C_0 at time 0 that is steadily depleted over the 6 or 12 hour time period. For the second scenario (replenishment), the concentration is replenished to C_0 at the end of every model time step (40 minute for Brost et al. (1991), 1 hour for Giorgi and Chameides (1986), and 6 hours for GRANTOUR). It is assumed that sources, advection, diffusion, etc. would allow for this.

5.7.1 Stratiform precipitation

The results for stratiform precipitation are shown in Table 5.7. Three different stratiform rain events are shown: (1) Rain for 6 out of 6 hours, (2) Rain for 12 out of 12 hours, and (3) Rain for 4 out of 6 hours. The ranges on Brost et al. (1991) and Giorgi and Chameides (1986) arise because a range of precipitation rates of 10^{-8} to 10^{-6} kg/m^3-s were considered. GRANTOUR results agree with Brost et al. (1991) for lower precipitation rates. It is quite possible that their GCM also calculates precipitation fields that are lower than observations, as does GRANTOUR.

GRANTOUR stratiform removal amounts are lower than Giorgi and Chameides (1986). Brost et al. (1991) adjusted the liquid water content for stratiform precipitation because they found that the Giorgi and Chameides (1986) parameterization removed too

much material with stratiform precipitation.

Table 5.7: Fraction of initial concentration removed by stratiform precipitation event

Model	Rain 6/6 hrs	Rain 12/12 hrs	Rain 4/6 hrs
A. No replenishment			
BR91	0.12 - 0.997	0.23 - 0.99	0.08 - 0.98
Giorgi and Chameides (1986)	0.29 - 0.99	0.50 - 0.99	0.21 - 0.95
GRANTOUR	0.14	0.26	0.14
B. With replenishment			
BR91	0.13 - 4.3	0.25 - 8.6	0.08 - 2.9
GC86	0.34 - 3.2	0.67 - 6.4	0.22 - 2.1
GRANTOUR	0.14	0.28	0.14

5.7.2 Convective precipitation

For convective precipitation,the material removed in one meteorological time step was calculated. The time step is 40 minutes for Brost et al. (1991), 1 hour for Giorgi and Chameides (1986), and either 6 or 12 hours for GRANTOUR. The results are shown in Table 5.8. GRANTOUR in 6 hours removes a similar amount as Brost et al. (1991) and Giorgi and Chameides (1986), but over a 12 hour time-period, GRANTOUR removes more material than the other two models.

Table 5.8: Fraction of initial concentration removed by convective event lasting one meteorological timestep

Model	Meteorological update timestep	Fraction removed
BR91	40 minutes	0.17 - 0.23
GC86	1 hour	0.18 - 0.24
GRANTOUR	12 hour (No replenishment)	0.35
GRANTOUR	12 hour (With replenishment)	0.39
GRANTOUR	6 hour	0.19

CHAPTER 6 INCORPORATING TROPOSPHERIC CHEMISTRY INTO GRANTOUR

6.1 Chemical reaction mechanisms

A chemical reaction mechanism consists of a number of balanced reactions and their associated reaction rate coefficients. Some of the reactions have Arrhenius-type rate coefficients of the form k = A * exp(-B/T), where A is the pre-exponential factor, B is the exponential factor, and T is temperature, in Kelvin. Other reactions have much more complicated rate expressions, which take into account the air density, temperature, and other factors. Finally, the reaction mechanism also contain photolysis reactions, which are reactions that occur when a molecule absorbs a photon. Two different versions of GRANTOUR (predictor-corrector, with the $CO/CH_4/NO_x/OH/O_3$ cycle, and non-methane hydrocarbon, which also included isoprene, alkanes, alkenes, and aromatics) were developed for this work. Each had a different chemical reaction mechanism associated with it. The predictor-corrector $CO/CH_4/NO_x/OH/O_3$ cycle is discussed in Section 6.2. The non-methane hydrocarbon method is discussed in Section 6.3.

The actual atmosphere experiences periods of sunlight and darkness. GRANTOUR, however, models a "gray day" over a 24 hour period. The reaction rate coefficients and photolysis reaction rates must be diurnally averaged so that the correct amounts of species are destroyed and produced over a 24 hour period. This is done via the method of Turco et al. (1978). The photolysis rates are directly incorporated from monthly diurnally averaged values obtained with the LLNL 2D model (Wuebbles et al., 1987). The non-photolysis reaction rate coefficients, however, that describe the reaction of species i with species j must be multiplied by an "alpha factor", α_{ij}, that varies with latitude and altitude, such that this newly derived reaction rate coefficient produces and destroys the correct amount of material over a 24 hour period. If k_{ij} is the reaction rate coefficient for species i reacting with species j, and c_i and c_j are the concentrations of species i and j, respectively, then

$$\alpha_{ij} = \frac{\overline{k_{ij} \times c_i \times c_j}}{\overline{k_{ij} \times c_i \times c_j}}$$

6.2 Chemical reaction mechanism for predictor-corrector version of GRANTOUR

6.2.1 Arrhenius and special function reactions

The predictor-corrector version of GRANTOUR includes the reactions to describe the $CO/CH_4/NO_x/OH/O_3$ cycle. In this model, reaction rate coefficients are calculated at the grid locations using monthly average temperatures. These rate coefficients are then interpolated to the parcels every 12 hours when they are advected. The reaction rate coefficients that are calculated are shown in Table 1. These rates have been updated to those in Demore et al. (1992), and the reaction rate coefficient for $CH_4 + OH$ has been updated to that derived by Vaghjiani and Ravishankara (1991).

Each of the reaction rate coefficients shown in Table 1 is then multiplied by a monthly average diurnal factor, (alpha factor), obtained from the LLNL 2D model. To adequately describe background ozone formation in the stratosphere requires including the Chapman cycle. Note that for work in this thesis, however, the rate coefficient for reaction 32 ($O + O_3 = O + O_2$) and photolysis reaction 17 ($O_2 = O + O$) are set equal to 0, and the O_3 in the stratosphere is fixed based on scaling values from the LLNL 2D model to fit observations at the NOAA CMDL sites. Reaction rates represented by special functions are listed separately below.

Table 6.1: Reactions and rate coefficients in predictor-corrector version of GRANTOUR*

No	Reaction	A	B	k at 298K**
1	$O + O_2 \xrightarrow{M} O_3$	SF1	---	1.56×10^{-14}
2	$O_3 + NO \longrightarrow O_2$	2.0×10^{-12}	1400.	1.82×10^{-14}
3	$O + NO_2 \longrightarrow NO + O_2$	6.5×10^{-12}	-120.	9.72×10^{-12}
4	$O^1D + H_2O \longrightarrow OH + OH$	2.2×10^{-10}	0.	2.20×10^{-10}
5	$O_3 + OH \longrightarrow HO_2 + O_2$	1.6×10^{-12}	940.	6.83×10^{-14}
6	$O_3 + HO_2 \longrightarrow OH + O_2 + O_2$	1.1×10^{-14}	500.	2.05×10^{-15}
7	$HO_2 + HO_2 \longrightarrow H_2O_2 + O_2$	SF3	---	2.97×10^{-12}

Table 6.1: Reactions and rate coefficients in predictor-corrector version of GRANTOUR*

No	Reaction	A	B	k at 298K**
8	$HO_2 + OH \longrightarrow H_2O + O_2$	4.8×10^{-11}	-250.	1.11×10^{-10}
9	$OH + NO_2 \xrightarrow{M} HNO_3$	SF7	---	1.17×10^{-11}
10	$OH + HNO_3 \longrightarrow H_2O + NO + O_2$	SF8a	---	1.62×10^{-14}
11	$H_2O_2 + OH \longrightarrow H_2O + HO_2$	2.9×10^{-12}	160.	1.70×10^{-1}
12	$NO + HO_2 \longrightarrow NO_2 + OH$	3.7×10^{-12}	-250.	8.56×10^{-12}
13	$NO_2 + O_3 \longrightarrow NO_3 + O_2$	1.2×10^{-13}	2450.	3.23×10^{-17}
14	$CO + OH \xrightarrow{O2, M} HO_2$	SF12	---	2.42×10^{-13}
15	$O^1D + XM \longrightarrow O + XM$	2.1×10^{-11}	-95.	2.89×10^{-11}
16	$NO_2 + NO_3 \xrightarrow{M} N_2O_5$	SF5	---	1.27×10^{-12}
17	$N_2O_5 \longrightarrow NO_2 + NO_3$	SF6	---	3.73×10^{-02}
18	$N_2O_5 + H_2O \longrightarrow HNO_3 + HNO_3$	5.0×10^{-22}	0.	5.00×10^{-22}
19	$HO_2 + HO_2 + H_2O \longrightarrow H_2O_2 + O_2 + H_2O$	SF4	---	6.68×10^{-30}
20	$HO_2 + NO_2 \xrightarrow{M} HNO_4$	SF9	---	1.42×10^{-12}
21	$HNO_4 \longrightarrow HO_2 + NO_2$	SF10	---	8.80×10^{-02}
22	$OH + HNO_4 \longrightarrow H_2O + NO_2 + O_2$	1.3×10^{-12}	-380.	4.65×10^{-12}
23	$OH + CH_4 \xrightarrow{O2, M} CH_3O_2 + H_2O$	2.9×10^{-12}	1820.	6.46×10^{-15}
24	$CH3O_2 + NO \xrightarrow{O2} CH2O + NO_2 + HO_2$	4.2×10^{-12}	-180.	7.68×10^{-12}
25	$CH3O_2 + HO_2 \longrightarrow CH_3OOH + O_2$	3.8×10^{-13}	-800.	5.57×10^{-12}
26	$OH + CH_2O \longrightarrow CO + HO_2 + H_2O$	1.0×10^{-11}	0.	1.00×10^{-11}
27	$OH + CH_3OOH \longrightarrow CH_3O_2 + H_2O$	2.7×10^{-12}	-200.	5.28×10^{-12}
28	$OH + CH_3OOH \longrightarrow CH_2O + H_2O + OH$	1.1×10^{-12}	-200.	2.15×10^{-12}
29	$HONO + OH \longrightarrow H_2O + NO_2$	1.8×10^{-11}	390.	4.86×10^{-12}
30	$OH + NO \xrightarrow{M} HONO$	SF11	---	4.96×10^{-12}
31	$OH + HNO_3 \longrightarrow H_2O + NO_2 + O$	SF8b	---	$1.31 \times 10^{-...}$
32	$O + O_3 \longrightarrow O_2 + O_2$	0.***	0.	0.

* Reaction rate coefficients are of the form: $k = A \times \exp(-B/T)$

** Reaction rate coefficients evaluated for T=298K, air density = , and $[H_2O]$ =

*** Currently set equal to 0 in predictor-corrector version

Special function for reactions 1, 7, 9, 10, 14, 16, 17, 19, 20, 21, 30, and 31 are listed below.

Table 6.2: Reactions with special functions for reaction rate coefficients

No	Reaction	Reaction Rate Coefficient
1	$O + O_2 \xrightarrow{M} O_3$	$k = 6.0 \times 10^{-34} \times (300./T)^{2.3} \times xm$
7	$HO_2 + HO_2 \longrightarrow H_2O_2 + O_2$	$k = 2.3 \times 10^{-13} \times \exp(600./T) + 1.7 \times 10^{-33} \times xm \times \exp(1000./T)$
9	$OH + NO_2 \xrightarrow{M} HNO_3$	$k = [xkz \times xm \times fff] / [1.0 + (xkz \times xm / xki)]$, where $fff = 0.6^{[1/\{1 + (\log_{10}(xkz \times xm / xki))^{**}2\}]}$, $xkz = 2.6 \times 10^{-30} \times (300/T)^{3.2}$, and $xki = 2.4 \times 10^{-11} \times (300/T)^{1.3}$
10	$OH + HNO_3 \longrightarrow H_2O + NO + O_2$	$k = 0.11 \times 7.2 \times 10^{-15} \times \exp(785/T) + x1/(1.0 + x1/x2)$, where $x1 = xm \times 1.9 \times 10^{-33} \times \exp(725/T)$, and $x2 = 4.1 \times 10^{-16} \times \exp(1440/T)$
14	$CO + OH \xrightarrow{O2, M} HO_2$	$k = 1.50 \times 10^{-13} \times (1 + (xm \times 2.4 \times 10^{-20}))$
16	$NO_2 + NO_3 \xrightarrow{M} N_2O_5$	$k = [xkz \times xm \times fff] / [1.0 + (xkz \times xm / xki)]$, where $fff = 0.6^{[1/\{1 + (\log_{10}(xkz \times xm / xki))^{**}2\}]}$, $xkz = 2.2 \times 10^{-30} \times (300/T)^{3.9}$, and $xki = 1.5 \times 10^{-12} \times (300/T)^{0.7}$
17	$N_2O_5 \longrightarrow NO_2 + NO_3$	$k = [xkz \times xm \times fff] / [1.0 + (xkz \times xm / xki)]$, where $fff = 0.6^{[1/\{1 + (\log_{10}(xkz \times xm / xki))^{**}2\}]}$, $xkz = 5.5 \times 10^{-4} \times (-10930/T) \times (300/T)^{4.3}$, and $xki = 3.7 \times 10^{14} \times (-10930/T) \times (300/T)^{0.5}$
19	$2\,HO_2 + H_2O \longrightarrow H_2O_2 + O_2 + H_2O$	$k = 3.22 \times 10^{-34} \times \exp(2800/T) + 2.38 \times 10^{-54} \times \exp(3200/T) \times xm$

Table 6.2: Reactions with special functions for reaction rate coefficients

No	Reaction	Reaction Rate Coefficient
20	$HO_2 + NO_2 \xrightarrow{M} HNO_4$	$k = [xkz \times xm \times fff] / [1.0 + (xkz \times xm / xki)]$, where $fff = 0.6^{[1/\{1 + (\log_{10}(xkz \times xm / xki))^{**} 2\}]}$, $xkz = 1.8 \times 10^{-31} \times (300/T)^{3.2}$, and $xki = 4.7 \times 10^{-12} \times (300/T)^{1.4}$
21	$HNO_4 \longrightarrow HO_2 + NO_2$	$k = [xkz \times xm \times fff] / [1.0 + (xkz \times xm / xki)]$, where $fff = 0.6^{[1/\{1 + (\log_{10}(xkz \times xm / xki))^{**} 2\}]}$, $xkz = 8.57 \times 10^{-5} \times (-10900/T)^{3.2}$, and $xki = 2.24 \times 10^{-15} \times (-10900/T)^{1.4}$
30	$OH + NO \xrightarrow{M} HONO$	$k = [xkz \times xm \times fff] / [1.0 + (xkz \times xm / xki)]$, where $fff = 0.6^{[1/\{1 + (\log_{10}(xkz \times xm / xki))^{**} 2\}]}$, $xkz = 7.0 \times 10^{-31} \times (300/T)^{2.6}$, and $xki = 1.5 \times 10^{-11} \times (300/T)^{0.5}$
31	$OH + HNO_3 \longrightarrow H_2O + NO_2 + O$	$k = 0.89 \times 7.2 \times 10^{-15} \times \exp(785/T) + x1 / (1 + x1/x2)$, where $x1 = xm \times 1.9 \times 10^{-33} \times \exp(725/T$ $x2 = 4.1 \times 10^{-16} \times \exp(1440/T)$

* M = third body molecule (e.g. N_2, O_2, etc.); xm = air density, in cm^{-3}

6.2.2 Photolysis reactions

A number of different photolysis reactions are also included. The photolysis rates are taken from monthly, two-dimensional, diurnally averaged photolysis rate fields calculated by the LLNL 2D model (Wuebbles, et al., 1987). As discussed above, the rate for photolysis reaction 17 ($O_2 = O + O$) is set equal to 0 in this version of the model, and

stratospheric O_3 is fixed based on scaled values from the LLNL 2D model.

Table 6.3: Photolysis reactions in predictor-corrector version of GRANTOUR

$O_3 \longrightarrow O + O_2$
$O_3 \longrightarrow O^1D + O_2$
$NO_2 \longrightarrow NO + O$
$HNO_3 \longrightarrow OH + NO_2$
$H_2O_2 \longrightarrow OH + OH$
$HO_2 \longrightarrow OH + O$
$N_2O_5 \longrightarrow NO_2 + NO_2 + O$
$NO_3 \longrightarrow NO + O_2$
$NO_3 \longrightarrow NO_2 + O$
$HNO_4 \longrightarrow OH + NO + O_2$
$CH_3OOH \longrightarrow CH_2O + HO_2 + OH$
$CH_2O \xrightarrow{O2,M} CO + HO_2 + HO_2$
$CH_2O \longrightarrow CO$
$N_2O_5 \longrightarrow NO_2 + NO + O_2$
$HNO_4 \longrightarrow OH + NO_2 + O$
$HONO \longrightarrow OH + NO$
$O_2 \longrightarrow O + O$

6.3 Chemical reaction mechanism used in the non-methane hydrocarbon version of GRANTOUR

The chemical reactions and coefficients used in the non-methane hydrocarbon version of GRANTOUR are given in the long version of the mechanism of Lurmann et al. (1986). The species include CO, CH_4, NO_x, OH, O_3, ethane (C_2H_6), propane (C_3H_8), lumped C4-C5 alkanes, lumped C6-C8 alkanes, ethene (C_2H_4), propene (C_3H_6), trans-2-butene (C_4H_8), PAN, benzene, toluene, and xylene, isoprene (C_5H_{10}), and associated oxidation products.

Several additional reactions were also included. The modifications of Jacob and Wofsy (1988) to allow for low NO_x concentrations were included. These are of the form $RO_2 + HO_2$ forms peroxide, where RO_2 is a peroxy radical. Three other reactions that were included were:

$$OH + HO_2 \text{ -----> } H_2O + O_2 \qquad 6.2$$

$$PAN + OH \text{ -----> } HCHO + NO_2 + CO_2 + H_2O \qquad 6.3$$

$$\text{PAN-analogues} + OH \text{ -----> products} \qquad 6.4$$

Additionally, the original isoprene mechanism of Lloyd et al. (1983) was updated according to Paulson and Seinfeld (1992). Paulson and Seinfeld (1992) not only updated the products and yields for the reactions of isoprene with OH and O_3, but also included the reactions of isoprene with $O(^3P)$, NO_3, and NO_2 (although the last reaction may be negligible). Their work showed that substantial radical formation (of OH and $O(^3P)$) results from the reaction of O_3 with isoprene. They also updated the reactions of OH with two isoprene-daugher products, methyl vinyl ketone, and methacrolein.

In the non-methane hydrocarbon version of GRANTOUR, the regular and special function reaction rate coefficients were multiplied by monthly, diurnally averaging multiplicative factors (alpha factors) from the LLNL 2D model. The photolysis reactions were derived from the LLNL 2D model, and interpolated to the GRANTOUR 3D grid. Reaction rate coefficients were updated to the values suggested by DeMore et al. (1992).

CHAPTER 7 NUMERICAL INTEGRATION TECHNIQUES

For this work, two different numerical integration techniques were incorporated into the chemistry subroutines of GRANTOUR. The first was a predictor-corrector technique and was incorporated into the GRANTOUR version containing $CO/CH_4/NO_x/OH/O_3$ chemistry. The second was based on a solution technique proposed by Sillman (1991), and operated on the basis of an odd-hydrogen balance. It was incorporated into the GRANTOUR version that contained the chemistry above and non methane hydrocarbons and isoprene.

The chemistry integration in GRANTOUR typically takes 99% of the total cpu-time required for simulations. Tropospheric chemistry involves a number of different species and hundreds of reactions. The reaction sets are "stiff" in that they involve concentration and time scales that vary over many orders of magnitude. The species concentrations are also highly coupled and non-linear. While it is relatively straightforward to set up individual differential equations for each species, solving these coupled, stiff equations is a computationally-intensive process. Below are presented the numerical integration techniques used for the chemistry calculations and other methods considered.

7.1 Predictor-Corrector Technique

The predictor-corrector technique was chosen for the GRANTOUR version that contains reactions of the $CO/CH_4/NO_x/OH/O_3$ cycle. If the troposphere is composed of species 1, 2, ... n, then the reaction mechanism may be written down as a series of balanced equations:

$$X_1 + X_2 = X_3 + X_4 \tag{7.1}$$

$$X_3 + X_1 = X_5 + X_6 \tag{7.2}$$

$$X_4 = X_6 + X_7 \tag{7.3}$$

etc., where the subscript refers to the species number. Each species, i, will then have production and loss terms that account for its change in concentration. For example, for species 4 above, the production and loss terms would be:

$$\text{Prod}(X_4) = k_{7.1} \times [X_1] \times [X_2] \tag{7.4}$$

$$\text{Loss}(X_4) = k_{7.3} \tag{7.5}$$

where $k_{7.1}$ and $k_{7.3}$ are the reaction rate coefficients for reaction 7.1 and 7.3, respectively. The differential equation for species 4 would then be:

$$\frac{dX_4}{dt} = P_4(X_2, X_3) - L_4 \times X_4 \tag{7.6}$$

where P stands for production rate, and L stands for loss rate. In general, for a species i in terms of the other species j, the differential equation would be:

$$\frac{dX_i}{dt} = P_i(X_j) - L_i(X_j) X_i \tag{7.7}$$

The predictor-corrector technique assumes that the timesteps taken are small enough that when species i is integrated, all other species j are approximately constant, giving:

$$\frac{dX_i}{dt} = P_i - L_i X_i \tag{7.8}$$

Equation (7.8) can be multiplied by an integrating factor, $e^{L_i t}$ giving:

$$e^{L_i t} \times \left(\frac{dX_i}{dt} + L_i X_i\right) = P_i e^{L_i t} \tag{7.9}$$

which then can be integrated as:

$$\int_{(X_o,\,0)}^{(X_i,\,t)} d\left(X_i e^{L_i t}\right) = \int_0^t P_i e^{L_i t} \tag{7.10}$$

to yield:

$$X_i(t) = \frac{P_i}{L_i} + \left(X_{i,0} - \frac{P_i}{L_i}\right) \times e^{-L_i t} \tag{7.11}$$

where the subscript 0 denotes a quantity at the beginning of the time step.

The predictor-corrector technique first calculates the initial production and loss terms, $P_{i,0}(X_{i,0})$ and $L_{i,0}(X_{i,0})$ in terms of initial concentrations. Next, equation (7.11) is solved to yield a predicted concentration, X_i',using $P_{i,0}$ and $L_{i,0}$. New production and loss terms are then calculated in terms of the predicted concentrations of all species, $P_i'(X_i')$ and $L_i'(X_i')$. The mean production and loss terms, $P_{i,m}$ and $L_{i,m}$ are defined as:

$$P_{i,m} = \frac{P_{i,0} + P'_i}{2} \tag{7.12}$$

$$L_{i,m} = \frac{L_{i,0} + L'_i}{2} \tag{7.13}$$

Using the mean production and loss terms, a new "corrected" concentration, $X_i''(P_{i,m}, L_{i,m})$ is calculated using (7.11). The corrected concentration, X_i'' and the predicted concentration, X_i' are compared. If they are within a certain convergence criteria, then the corrected concentrations, X_i'' are stored in the initial concentrations, and the time step is increased by 10%. If after 10 tries, the predicted and corrected concentrations do not converge, then the timestep is reduced 10%, and the calculation tried again. The timestep

is reduced until convergence is reached.

Recall from the previous section that the predictor-corrector version of GRANTOUR compares the predicted (X'_i) and corrected (X_i'') concentrations to determine if the solution has converged. If a solution converges, the timestep is increasd by 10% for the next calculation. If after 10 tries, however, the solution doesn't converge, the timestep is decreased 10%. The current criteria used by GRANTOUR is:

$$\frac{X''_i - X'_i}{X_i} < 10^{-7} \tag{2.7}$$

This criteria was determined from a number of box model simulations. Box model calculations were performed using two solution techniques. The first technique was the predictor-corrector method currently in GRANTOUR and the second was the GEAR package (Hindmarsh, 1974). The answer from the GEAR package was taken to be the "true" answer. The error after a 6 hour simulation between the predictor-corrector and GEAR techniques was calculated via:

$$E_i = \left| \frac{X_i^{pc} - X_i^{GEAR}}{X_i^{GEAR}} \right| \tag{2.8}$$

where pc denotes predictor-corrector, and GEAR denotes the GEAR package.

T scenarios, A and B, were examined with both box models. The initial concen- ons of the key species are shown in Table 7.4 in this chapter. In Tables 7.1 and 7.2, both initial timestep (dt_i) and error tolerance were varied. The percentage a timestep was increased if the solution converged ($dt_{increase}$) was 1% for scenario A and 5% for scenario B. The percentage the timestep was decreased if a solution didn't converge after 10 tries ($dt_{decrease}$) was 20% for scenario A and 30% for scenario B. Earlier testing showed these to be the optimum choices of $dt_{increase}$ and $dt_{decrease}$ for each scenario.

Table 7.1 and 7.2 present the initial timestep, the species with the largest error (and the associated error), the percentage error in O_3, and the cpu-time required to integrate one parcel for 6 hours

Table 7.1: Error tolerance criteria sensitivity tests for Case A

dt_i, sec	Error tolerance	Species with max error	Max error, %	% error in O_3	cpu-time, sec, for 6 hr simulation
.3.6	10^{-10}	N_2O_5	0.13%	0.07%	9.2
3.6	10^{-9}	N_2O_5	0.26%	0.13%	6.0
3.6	5×10^{-9}	N_2O_5	0.44%	0.22%	4.1
3.6	10^{-8}	N_2O_5	0.57%	0.28%	3.6
3.6	5×10^{-8}	H_2O_2	1.2%	0.58%	2.0
3.6	10^{-7}	H_2O_2	1.9%	0.91%	1.5
3.6	5×10^{-7}	N_2O_5	9.0%	4.1%	0.53
3.6	10^{-6}	N_2O_5	18.4%	7.8%	0.34
3.6	5×10^{-6}	N_2O_5	33.4%	12.7%	0.26
3.6	10^{-5}	N_2O_5	34.8%	13.1%	0.25
3.6	5×10^{-5}	N_2O_5	34.9%	13.2%	0.21
3.6	10^{-4}	N_2O_5	35.1%	13.2%	0.20
3.6	5×10^{-4}	N_2O_5	36.1%	13.6%	0.17
3.6	10^{-3}	N_2O_5	36.9%	14.1%	0.16
3.6	5×10^{-3}	N_2O_5	40.8%	15.5%	0.15
3.6	10^{-2}	N_2O_5	46.1%	17.3%	0.14
3.6	5×10^{-2}	N_2O_5	46.1%	17.3%	0.14
3.6	10^{-1}	N_2O_5	46.1%	17.3%	0.15
36.	10^{-10}	N_2O_5	0.14%	0.07%	9.3
36.	10^{-7}	H_2O_2	1.9%	0.91%	1.5
36.	10^{-6}	N_2O_5	18.8%	8.1%	0.3
36.	5×10^{-6}	N_2O_5	41.8%	18.0%	0.2
36.	10^{-5}	N_2O_5	44.9%	18.5%	0.2
36.	5×10^{-5}	N_2O_5	44.9%	18.5%	0.2
360.	10^{-6}	N_2O_5	18.8%	8.1%	0.33

Table 7.1: Error tolerance criteria sensitivity tests for Case A

dt_i, sec	Error tolerance	Species with max error	Max error, %	% error in O_3	cpu-time, sec, for 6 hr simulation
360.	5×10^{-6}	N_2O_5	54.2%	26.2%	0.15
360.	10^{-5}	N_2O_5	67.2%	35.5%	0.14
360.	5×10^{-5}	N_2O_5	80.0%	42.5%	0.12
360.	10^{-4}	N_2O_5	80.0%	42.5%	0.12
360.	5×10^{-4}	N_2O_5	80.0%	42.6%	0.12
360.	10^{-3}	N_2O_5	80.0%	42.7%	0.12

Table 7.2: Error tolerance criteria sensitivity tests for Case B

dt_i, sec	Error tolerance	Species with max error	Max error, %	% error in O_3	cpu-time, sec, for 6 hr simulation
3.6	10^{-9}	HONO	0.84%	0.009%	0.15
3.6	10^{-8}	HONO	1.3%	0.009%	0.14
3.6	10^{-7}	HNO_4	1.9%	0.009%	0.13
3.6	10^{-6}	HNO_4	1.9%	0.009%	0.13
36.0	10^{-6}	HONO	3.5%	0.09%	0.12
36.0	10^{-5}	HONO	3.5%	0.09%	0.12
36.0	10^{-4}	HNO_4	3.5%	0.09%	0.12
360.	10-4	HONO	6.2%	0.17%	0.11
360.	10-3	HONO	6.2%	0.17%	0.11
720.	10^{-3}	HNO_4	10.9%	0.28%	0.11
1200.	10^{-3}	HNO_4	17.5%	0.42%	0.11

Tables 7.1 and 7.2 show that scenario A is much more difficult to integrate. An error tolerance of 10^{-6} lead to errors of 18-19% in N_2O_5, and 8% in O_3 for the first scenario. A

tolerance of 10^{-7} led to errors of 2% in H_2O^2 and 1% in O_3. Similar studies by other researchers found that an error tolerance of 10^{-7} (and similar timesteps) was required (Sultan Hameed, personal communication) for solutions to converge properly.

7.1.2 Steady state approximations

In atmospheric chemistry, a pseudo-steady state approximation is often applied for very short-lived species. Their differential equations are solved assuming the rate of production is equal to the rate of loss. This simplifies the chemical integration and lessens the cpu-time required.

Using the predictor-corrector version of the box model, an error tolerance of 10^{-7}, initial time step of 0.36s, a $dt_{increase}$ of 1%, and a $dt_{decrease}$ of 20%, 12 hour simulations were conducted. Table 7.3 shows the cpu-time savings for these scenarios, and the number of call to the integration package.

Table 7.3: Results of steady-state approximations with the predictor-corrector technique

Run	CPU-time, sec	Calls to integrator	Steady state species	Percent CPU-time savings	% error in O_3
1	2.78	55,464	NONE	-----	-----
2	2.52	54,308	O^1D	9%	0.01%
3	2.64	55,485	O	5%	0.24%
4	2.12	40,223	OH	24%	0.08%
5	2.13	37,831	HO_2	23%	0.19%
6	2.61	54,326	O^1D, O	6%	0.24%

Table 7.3: Results of steady-state approximations with the predictor-corrector technique

Run	CPU-time, sec	Calls to integrator	Steady state species	Percent CPU-time savings	% error in O_3
7	2.10	39,468	O^1D, OH, O	25%	0.44%
8	1.92	35,801	O^1D, OH, O, CH_3O_2	31%	0.49%
9	1.90	35,729	O^1D, OH, O, CH_3O_2, N_2O_5	32%	0.51%
10	2.94	63,557	O^1D, HNO_4, CH_3O_2, N_2O_5, O	-6%	0.81%

While the time-savings above could be substantial for the single parcel considered, the time savings for a GRANTOUR integration with 25,000 or 50,000 parcels was not as great, and so the steady state approximation was not implemented.

7.1.3 Simplification of chemical reaction mechanism

A considerable time-savings was realized by eliminating 9 reactions involving the species O which, while important in many stratospheric cycles, had a negligible impact on the tropospheric chemistry. The reactions of O with OH, HO_2, O_2, CH_4, CH_2O, CH_3O_2, HNO_4, NO_3, and O_3 were eliminated. For a 6 hour, 50,000 parcel integration of the predictor-corrector version of GRANTOUR, this simplifcation led to a time savings of 31%.

7.1.4 Replacing logic of chemistry production and loss calculations

Although the predictor-corrector version of GRANTOUR does require substantial computational time, it is extensively vectorized to take advantage of the CRAY computer capabilities. As part of the vectorization, generic do loops were implemented to calculate the production and loss terms of each species. In these do-loops, every species had an entire array for every reaction in the mechanism, with array positions either being turned on or off. Based on recommendations of others (Alan Hindmarsh, personal communication), these generic do-loops were replaced with hard-wired versions of the actual production and

loss terms. For a 24 hour, 25,000 parcel integration with GRANTOUR, this led to a time-savings of 33%.

7.2 VODE technique

Because the predictor-corrector chemistry solution technique requires extensive cpu-time, an ordinary differential equation solution package, VODE, (Brown et al., 1989), was used to integrate GRANTOUR's $CO/CH_4/NO_x/OH/O_3$ chemistry. The VODE package is a descendant of the GEAR package. Basically, the GEAR package (Hindmarsh, 1974) uses a fixed-coefficient backward differentiation formula method for stiff systems. Although the GEAR package is able to handle stiff sets of differential equations (and inverts a Jacobian), it has problems with solutions involving intermittent spikes or strong peaks in time (such as might be found in diurnal kinetics).

A follow-up to GEAR was EPISODE (and variants EPISODEB and EPISODEIB), a version of GEAR capable of integrating stiff and non-stiff differential equations using variable coefficients. Because EPISODE was not very user-friendly, scientists then collaborated on a new design for GEAR and related solvers, creating a user-friendly package called LSODE. LSODE performs similarly to GEAR, but is more reliable than GEAR on diurnal problems, although it can be less efficient than GEAR.

The VODE package combines the user-friendliness of LSODE and the variable coefficient method of EPISODE. VODE is appropriate for problems which may or may not require frequent or drastic time step changes. Additionally, it has improvements in methods to (1) change step size and (2) select initial step-size and has capabilities to (3) save the Jacobian and (4) use a linear system relaxation for stiff systems.

The predictor-corrector and VODE solution techniques were first compared in box model simulations. Two scenarios, A and B, were integrated for 6 hours on a CRAY-2 using both techniques. Table 7.4 presents the important initial conditions and integration times for both scenarios. The integration times are actually averages of 5 integration

timings.

Table 7.4: Initial conditions and CPU-times for 6 hour predictor-corrector and VODE box model simulations

	Scenario A	Scenario B
Initial concentration, cm^{-3}		
O_3	1.143×10^{10}	1.470×10^{12}
NO	4.771×10^{10}	1.750×10^{10}
NO_2	3.103×10^{9}	1.750×10^{10}
CO	7.640×10^{12}	9.050×10^{12}
CH_4	4.510×10^{13}	4.510×10^{13}
H_2O	4.630×10^{17}	4.630×10^{17}
O_2	5.320×10^{18}	5.320×10^{18}
XM	2.550×10^{19}	2.550×10^{19}
CPU-time, sec		
Predictor-corrector	2.3	0.436
VODE	0.0127	0.0633

Table 7.4 shows that the VODE technique was at least one to two orders of magnitude faster for identical parcels. However, the VODE technique took 5 times as much time for scenario B as for scenario A. Further work showed that Scenario A was relatively "well-behaved" in that concentrations appeared to be close to steady state initially, and didn't change more than a factor of 4 or so during the first hour. Scenario B, however, had large transients in many key species in the first 5 minutes of integration time, indicating a parcel that was far from steady state (e.g. a parcel with a large source emission). For example, O changed by a factor of 40 and H_2O_2 and CH_3OOH changed by factors of 1000 in the first 5 minutes, which required time steps of less than 1 second for the first minute of integration

Because there was such a difference in timing for two different scenarios, the

predictor-corrector and VODE solution techniques were next compared in a 24 hour, 25,000 parcel simulation in GRANTOUR. The predictor-corrector technique is highly vectorized, which reduces computational time. The VODE package was not vectorized in GRANTOUR. Based on this result, the amount of time needed to integrate a 50,000 parcel simulation for 30 days on the CRAY-2 was 1640 CPU-minutes for the predictor-corrector, and 2048 CPU-minutes for VODE. It was not clear that the VODE technique could be vectorized (Alan Hindmarsh, personal communication). So although the VODE method appeared faster in box model simulations, that savings did not translate to the full GRANTOUR model.

7.3 Odd hydrogen balance of Sillman (1991)

Sillman (1991) has proposed a method for solving the photochemical reactions of the troposphere. It revolves around an analysis of odd-hydrogen sources and sinks. Because most of the reactions in the troposphere involve OH, HO_2, NO, NO_2, or NO_3 as a reactant, the concentration vector, **C**, is broken up into three sub-vectors, **C** = **C**[**X**,**Y**,**Z**] where **Z** is [OH, HO_2], **Y** is [NO_3, N_2O_5, O_3, NO, NO_2], and **X** is [all other species]. All of the sources and sinks of odd-hydrogen are written as functions of OH only. By artfully arranging the solution order, each group is solved for sequentially based on an estimate of OH concentration. (First OH is estimated, then the following are solved for: **X**(t+1), then **Y**(t+1), then **Z**(t+1). Then the procedure repeats with a new estimate of OH). In particular, the subvector **X** is arranged in such a way that $x_i = f\{Y,Z,x_j,\ j \le i\}$ and, for the sub-vector **X**, the Jacobian matrix is close to a lower diagonal form, and no matrix inversion is required. Instead, **X** reduces to an independent scalar equation for each x_i. The solution of the **Z** vector is based on a single equation for sources and sinks of odd-hydrogen, expressed in terms of OH. Once the concentration of OH and HO_2 have been determined, it is fairly simple to solve sequentially for all other species.

This method solves implicit equations for the concentrations using Newton-Raphson

iterations. It can take large time steps (currently 30 minutes), minimizing cpu-time. Besides being computationally fast, this odd-hydrogen technique also includes more species (76 as opposed to the predictor corrector's 21) and more reactions (nearly 300, versus 47). The current version of Sillman (1991) is based on the full Lurmann mechanism (Lurmann, 1986), which includes non-methane hydrocarbons and isoprene, a important and highly reactive biogenic hydrocarbon. Extra reactions appropriate for low NO_x conditions have also been added. Additionally, all reaction rate coefficients were updated to the JPL 1992 values, and the isoprene reaction scheme updated to that of Paulson and Seinfeld (1992).

The Sillman technique was compared to the predictor-corrector technique for two different box model scenarios, A and B presented in Table 7.4. Both scenarios were integrated on a CRAY-2. The timings for six hour simulations of two different scenarios are shown in Table 7.5. The Sillman method was a factor of 20 - 100 faster than the predictor-corrector. Since both methods are vectorizable, these savings are expected to be representative of the CRAY as well.

Table 7.5: Box model timings for predictor-corrector and Sillman techniques

Scenario	Predictor-corrector, sec	Sillman technique, sec
A	2.3	0.027
B	0.44	0.024

CHAPTER 8 GRANTOUR CONCENTRATION AND EMISSION INPUT FILES

GRANTOUR requires that the concentration and/or source emission fields of several trace species be specified. In particular, the concentrations of CH_4 and CO are currently specified on a global scale. Nitrogen oxides, NO_x, enter the model as emissions, and are a prognostic variable. The non-methane hydrocarbon (NMHC) version of the model also requires the emissions of ethane, propane, and isoprene. Chapter 8 discusses current observations of some of these species, and the fields that were developed for use.

8.1 Carbon monoxide, CO

Carbon monoxide, CO, is emitted globally in approximately equal amounts by anthropogenic and natural sources (Logan et al., 1981; WMO, 1985; Penner 1992). The updated total source is estimated to be 2510 Tg CO/year, with a range of 1330-4525 Tg CO/ year (Penner, 1992). The anthropogenic sources include intentional burning of fossil fuel, wood for fuel, and biomass burning of savannas and forests, as well as the oxidation of anthropogenic nonmethane hydrocarbons and anthropogenic CH_4. The natural sources include the oxidation of biogenic CH_4 and other natural hydrocarbons, forest fires, and emissions from plants and the oceans. Table 8.1 lists current estimates of CO sources, which were originally compiled by Logan et al. (1981) and updated by Penner (1992).

The two largest sinks for CO are reaction with OH (which is predominant) and uptake by soils. Total CO consumed by reaction with OH is roughly 10 times larger than uptake by soil (WMO, 1985; Logan et al., 1981). The concentration of CO is increasing globally at estimated rates of 1%/year (Cicerone, 1988) to 5.5%/year (WMO, 1985). For a total source of 2510 Tg CO/year, an accumulation of 1%/year yields a sink of 2240 Tg CO/year due to reaction with OH and a sink of 250 Tg CO/year from uptake by soils.

The concentration of CO is generally lower during the summer season. This is because the main sink for CO is reaction with the hydroxyl radical, OH. The hydroxyl

Table 8.1: Current source estimates of CO (Logan, et al. 1981 and Penner, 1992)

Source	Total, Tg CO/year	Range, Tg CO/year
Anthropogenic:		
Fossil fuel combustion	450	400 - 1000
Oxidation of anthropogenic NMHCs	90	0 - 180
Oxidation of fossil fuel/industrial CH_4	90	45 - 110
Oxidation of man's land-use CH_4 emissions	310	135 - 390
Biomass burning and fuel wood	640	280 - 950
Natural:		
Oxidation of natural NMHCs	560	280 - 1200
Oxidation of natural CH_4 (from land cover)	190	115 - 395
Emissions from plants	130	50 - 200
Emissions from oceans	40	20 - 80
Oxidation of oceanic CH_4	10	5 - 20
Total source	2510	1330 - 4525

radical concentration is higher during the summer, due to stronger photolytic activity. Seiler et al. (1984) measured boundary layer [CO] at Cape Point, South Africa and found average concentrations of 53 ppbv in January and 87 ppbv in September/October. Thus a seasonal variation of 25 - 35 ppbv may occur.

CO has a relatively short atmospheric lifetime with respect to reaction by OH: 0.4 years on a global scale, and as low as 0.1 years in the tropics (WMO, 1985). Consequently, its concentration varies significantly in time and space. Since most CO sources are land-based, the northern hemisphere has higher concentrations than the southern hemisphere. Also, because the CO sources are surface-based, mixing ratio decreases with altitude.

8.1.1 Measurements

8.1.1.1 Boundary layer

In the southern hemisphere, CO is well mixed, both vertically and horizontally. (The

main sources of CO in the southern hemisphere may be biomass burning, oxidation of CH_4, a longer-lived species, and transport from the north (WMO, 1985).) Heidt et al. (1980) measured levels of 50 - 60 ppbv in both the boundary layer and free troposphere during GAMETAG (April/May 1978) over the Pacific Ocean. The flight profiles taken by Seiler and Fishman (1981) for a variety of southern hemisphere locations during July and August, 1974, showed concentrations of roughly 60 - 70 ppbv, with little vertical gradient. Gauntner et al. (1979) measured CO concentrations for 0 - 30 degrees south of 60 - 75 ppbv (average = 65 ppbv) over the Pacific Ocean, and 55 - 90 ppbv (average = 76 ppbv) over the African continent during an airplane trip around the world in October, 1977. Robinson et al. (1984) observed 50 - 65 ppbv of CO south of the ITCZ during November/December 1978, primarily at altitudes of 5.5 - 6.7 km. Additionally, Seiler (1974) summarized many CO observations (boundary layer, free troposphere, all times of the year), which ranged from 30 to 100 ppbv for the southern hemisphere.

The main sources of CO in the northern hemisphere include the oxidation of CH_4 and biogenic and anthropogenic hydrocarbons, as well as the combustion of fossil fuel, wood, and biomass. The concentration of CO is higher for the more northerly latitudes for reasons stated above. As for the southern hemisphere, [CO] varies with season, with lower concentrations measured during the summertime, when [OH] is high, due to increased photolytic activity. Condon et al. (1987) measured CO over the Eastern Pacific Ocean (in the northern hemisphere) during GTE/CITE1 in the fall of 1983 and spring of 1984. They found a seasonal variation of 34 ppbv, which was probably due to a combination of photochemistry and meteorology, similar to the 25-35 ppbv variation found at Cape Point, South Africa (Seiler et al., 1984).

A number of northern hemisphere boundary layer measurements have been made. Heidt et al. (1980) measured concentrations of 150 - 200 ppbv over the Pacific Ocean during the GAMETAG campaign of April and May, 1978. Both Condon et al. (1987) and Fishman et al. (1987) measured CO during GTE/CITE1. Condon et al. (1987) observed

concentrations near California of roughly 100 ppbv during the fall of 1983 and 131 - 149 ppbv during the spring of 1984. Fishman et al. (1987) measured levels of 120 - 140 ppbv near California and 70 - 80 ppbv near Hawaii during the fall of 1983. Seiler and Fishman (1981) measured concentrations of 110 to > 200 ppbv over land during July/August 1974. Seiler (1974) summarized a number of observations, including his own, showing [CO] of 100 to >200 ppbv in the northern hemisphere, mainly from oceanic cruises.

8.1.1.2 Free Troposphere CO measurements

As stated above, CO mixing ratios in the free troposphere are generally lower than in the boundary layer. Gauntner et al. (1979) measured concentrations (for 0 - 30 degrees north) of 55 - 65 ppbv (average = 63 ppbv) over the Pacific Ocean and 95 - 100 ppbv (average = 97 ppbv) over the African continent on a flight around the world. Robinson et al. (1984) observed concentrations of 75 - 90 ppbv over the Pacific Ocean during November/December, mainly at an altitude of 5.5 - 6.7 km. During GTE/CITE1 Condon et al. (1987) observed 75 - 85 ppbv CO during the fall of 1983 near both California and Hawaii. During the spring of 1984, they measured 105 - 116 ppbv CO off the coast of California. Fishman et al. (1987) also measured CO during the fall of 1983 GTE/CITE1 campaign. They observed 70 - 80 ppbv near Hawaii and 80 - 110 ppbv near California. Heidt et al. (1980) observed 130 - 180 ppbv during the April/May 1978 GAMETAG campaign across much of the northern hemisphere. Seiler and Fishman (1981) measured 100 - 130 ppbv at altitudes of 8 - 12 km during July/August 1974.

8.1.1.3 Stratospheric CO measurements

On several aircraft flights, Seiler (1974) measured CO concentrations of less than 50 ppbv at 1 km above the tropopause. These mixing ratios remained constant as high as the aircraft could fly. Gauntner et al. (1979) measured stratospheric concentrations of CO of 49 - 57 ppbv for 50 - 90 degrees north, during a flight around the world (north to south and south to north transects). Warneck (1988) presents in Figure 1-14 a couple of CO vertical profiles taken near western France. The tropopause was located at 8 km. Above 9.5 km,

the concentration was fairly uniform, roughly 60 ppbv. Finlayson-Pitts and Pitts (1986) cite a stratospheric concentration of 40 - 50 ppbv, but don't indicate the source of this number. The LLNL 2D code was run for conditions typical of 1985/86 (July). The model-predicted CO mixing ratios ranged from 14 - 16 ppbv at 25.5 km; from 16 - 40 ppbv at 16.5 km; and from 18 - 55 ppbv at 13.5 km.

8.1.2 Construction of present-day monthly [CO] fields

Three-dimensional, monthly [CO] fields were developed by first constructing January and July CO files, and then sinusoidally interpolating between these two months for all other months.

To create the January and July files, "background" surface CO_b was first prescribed for three latitude bands: (1) 0 - 90° south, (2) 0 - 30° north, and (3) 30 - 90° north. The background surface mixing ratios that were prescribed are shown in Table 8.2 below.

Table 8.2: Prescribed background surface CO_b mixing ratios for January, July

Region	January CO_b, ppbv	July CO_b, ppbv
0 - 90° south	55	80
0 - 30° north	150	120
30 - 90° north	200	170

Next, this background CO_b varied with altitude in a manner appropriate for the latitude band. For the southern hemisphere, which is uniformly mixed, the CO mixing ratio was prescribed to be constant with height from sigma = 1.0 to sigma = 0.245. (Thus it was 55 ppbv in January, and 80 ppbv in July). For sigma < 0.245, the CO mixing ratio was prescribed to be 30 ppbv for all months.

For the northern hemisphere, the CO decreased linearly with altitude from the surface to sigma = 0.664. The CO mixing ratio was then constant from sigma = 0.664 to sigma = 0.245. For sigma < 0.245, the CO mixing ratio was prescribed to be 30 ppbv for all months

Table 8.3 below lists the values of the CO mixing ratios for the northern hemisphere as a function of month.

Table 8.3: Prescribed background CO_b mixing ratios as a function of height in the northern hemisphere

Sigma level	January CO_b, ppbv	July CO_b, ppbv
0 - 30° north		
$\sigma = 1.0^*$	150	120
$\sigma = 0.664$ to 0.245	105	75
$\sigma < 0.245$	30	30
30 - 90° north		
$\sigma = 1.0^*$	200	170
$\sigma = 0.664$ to 0.245	125	95
$\sigma < 0.245$	30	30

* Mixing ratio decreases linearly from $\sigma = 1.0$ to 0.664.

Finally, the anthropogenic influence on CO was added to this background CO_b field The background values derived above were for remote areas, away from anthropogenic influence. However, both biomass burning and fossil fuel combustion emit CO. This anthropogenic effect was incorporated via a normalization factor, N_{ij}. The normalization factor was calculated using emissions of carbon dioxide (CO_2) from biomass burning and fossil fuel combustion. Monthly biomass burning emissions of CO_2 were constructed from the tables of Hao et al. (1990). Annual fossil fuel emissions of CO_2 were constructed by Eddleman (personal communication, 1990). The total biomass burning and fossil fuel combustion CO_2 emission files were then added and normalized to the maximum source per unit area, giving monthly normalization factors, N_{ij}, which were a factor of longitude and latitude, with $0 < N_{ij} < 1$. (Note that the fossil fuel source over Europe and Asia was

reduced by 30%.) The total CO mixing ratios used by GRANTOUR, $CO_t(i,j,k)$, were calculated from the background mixing ratios $CO_b(j,k)$ using the equation:

$$CO_t(i,j,k) = CO_b(j,k) \times [1 + 6 \times \sigma_k \times N_{ij}] \quad (8.8)$$

where σ_k = GRANTOUR sigma level $(0 \le \sigma \le 1)$. In this manner, twelve monthly CO concentration fields were constructed as input files for GRANTOUR.

8.1.3 Preindustrial CO concentrations

Unlike CH_4, which has a historical record in ice cores, preindustrial CO concentrations must be inferred from model simulations. One such model study was by Pinto and Khalil (1991). They examined three different scenarios using a 1D (0-80km) model to resolve if CH_4 increases have been due to decreases in OH concentration, or increases in CH_4 emissions. The scenarios were for present day, pre-industrial (ca. 1850 A.D.), and Last Glacial Maximum (18,000 years BP) conditions. They prescribed surface CH_4 and N_2O concentrations based on ice core data. They also prescribed vertical relative humidity profiles. They emitted CO at a flux appropriate for the era. They calculated surface OH, O_3, and CO concentrations.

Model inputs included surface CH_4 concentrations of 1650, 750, and 350 ppbv for the modern, pre-industrial, and ice age scenarios, respectively. The calculated surface CO concentrations were 110, 57, and 28 ppbv, respectively. Surface OH concentrations were predicted to be 9.2, 9.6 and 11 x 10^5 molecules/cm^3 for the same three scenarios. The model predicted surface O_3 concentrations were 22, 14, and 12 ppbv for the three cases. The present day vertically averaged OH concentration was calculated to be 6 x 10^5 molecules/cm^3.

The results also showed that the OH concentrations varied much less than CH_4, CO, and the calculated O_3. Thus they concluded that the current concentration of CH_4 is due mainly to increased CH_4 emissions, with only a small component due to the decrease in

OH. The concentration of OH tends to decrease due to reactions with CH_4 and CO. The OH concentration tends to increase when concentrations of H_2O, O_3, or NO_x increase, up to a point. Hydroxyl concentrations are also stabilized because variations in its sources and sinks often have square root dependences.

Pinto and Khalil (1991) also note that because they found little variation in the predicted O_3 concentration for a variety of NO_y conditions, the Montsouris measurements taken during the last century (Volz and Kley (1988)) are probably indicative of a global average. This will be important when the GRANTOUR model-predicted preindustrial O_3 fields are compared to observations from the early industrial era.

8.1.4 Construction of preindustrial [CO] field

Based on the information above, an annual average preindustrial CO field was constructed. It was assumed that the CO was relatively well-mixed in the preindustrial atmosphere, as it is now in the southern hemisphere. For all months and latitudes, the CO mixing ratio was specified to be 55 ppbv in the troposphere ($\sigma > 0.245$) and 30 ppbv in the stratosphere ($\sigma < 0.245$).

8.2 Methane, CH_4

Methane is produced mainly by natural processes, although some of these "natural" processes are a result of man's energy and land-use practices. The largest natural sources include anaerobic bacterial fermentation (e.g. in swamps, marshes, etc.) and enteric fermentation in cattle and other species (Khalil and Rasmussen, 1983). Perhaps 8 - 15 % of the atmospheric CH_4 is released in urban locations (Blake et al., 1984). The main CH_4 sources, compiled by Cicerone and Oremland (1988) and updated by Penner (1992) are shown in Table 8.4. The total CH_4 source is estimated to be 525 Tg CH_4/year, with a range of 290-965 (Penner, 1992).

The main sink for CH_4 is reaction with OH. Only a very small amount of CH_4 is taken up by the soils. Global methane concentrations are steadily increasing: from a

global average concentration of 1.52 ppmv in 1978, to 1.625 ppmv in 1983, and up to 1.684 ppmv in 1987 (Blake and Rowland, 1986; Blake and Rowland, 1988). Measurements estimate the global increase in methane concentration to be roughly 1 - 2 %/year (Steele et al., 1987; Blake and Rowland, 1988; Keelhaul et al., 1989). Based on this and an annual source term of 525 Tg CH_4/year, methane sinks should be roughly 500 Tg CH_4/year due to reaction with OH and 10 Tg CH_4/year due to uptake by soils.

The atmospheric lifetime of CH_4 is much longer than CO, and is on the order of 7 - 10 years, depending on assumed OH concentrations. Due to its long lifetime, CH_4 tends to be much more uniformly spread throughout the two hemispheres. The typical concentration gradient between the northern latitude and southern latitudes is 150 ppbv.

Table 8.4: Current source estimates of CH_4 (Penner, 1992), Cicerone and Oremland (1988)

Source	Total, Tg CH_4/year	Range, Tg CH_4/year
Man-influenced:		
Coal mining and gas drilling	80	45 - 100
Landfills	40	20 - 70
Enteric fermentation	80	65 - 100
Rice paddies	110	25 - 170
Biomass burning	40	20 - 80
Natural:		
Natural wetlands	115	100 - 200
CH_4 hydrate destabilization	5	0 - 100
Termites	40	10 - 100
Fresh waters	5	1 - 25
Oceans	10	5 - 20
Total	525	290 - 965

8.2.1 Surface measurements of present day [CH_4] and trends

A number of scientists have measured surface CH_4 concentrations in remote locations. Measurements by Blake and Rowland (1986, 1988) covered from Ketchikan, Alaska to Punta Arenas, Chile. The results showed that the average world tropospheric concentration had increased from 1.52 ppmv in January 1978 to 1.684 ppmv in September, 1987, an 11% increase. Khalil and Rasmussen (1983, 1985, 1989) analyzed both their data and others to find that global annual average CH_4 had increased roughly 13 ± 3 ppbv between 1962 and 1980. In 1980, concentrations were 1.56 ppmv. Steele et al. (1987) sampled CH_4 weekly at 23 different remote NOAA/GMCC sampling sites, ranging from 76 degrees north to 90 degrees south during 1983 - 1985. Although the southern hemisphere sites were fairly uniform, over time the concentrations increased in the northern hemisphere. The results showed an average increase of 12.8 ppbv/year, an approximate 0.8%/year increase. Their Figure 5 is a cubic spline fit to the data for 18 of the sites and covers the globe (north pole to south pole) at time intervals of 0.5 months for May, 1983 to April, 1985.

Although the earlier trend estimates of 1 - 2% increases in CH_4 occurred during the 1960s, 1970s, and 1980s, it appears the trend has slowed recently. By analyzing weekly samples from 37 sites for 1983-1990, Steele et al. (1992) showed that the global CH_4 growth rate has slowed from 13.3 ppbv/year in 1983 to 9.5 ppbv in 1990.

8.2.2 Construction of present-day monthly [CH_4] fields

The monthly, three-dimensional, present day CH_4 fields needed for GRANTOUR were calculated by assuming the surface concentrations of Steele et al. (1987) and the variation with height calculated by the LLNL 2D model. Specifically, Figure 5 of Steele et al. (1987) presents surface CH_4 concentrations that vary smoothly with time and latitude based on measurements at 18 NOAA sites from May 1983 to April 1985. Methane concentrations vary every 2 weeks and at every 10° latitude. A 1983-1985 monthly surface

average for every 10° latitude band was derived from this plot.

Next, the variation of height of CH_4 mixing ratio in the LLNL 2D model was calculated for 18 latitude bands for January and July. This variation was applied directly to the January and July surface concentrations of Steele et al. (1987). For the other 10 months, the variation of CH_4 mixing ratio with height was assumed to vary sinusoidally between the January and July LLNL 2D model results. This variation was applied to the surface CH_4 concentrations. Using this method, twelve different monthly CH_4 concentration input fields were created for GRANTOUR.

8.2.3 Observed preindustrial CH_4 concentrations

Methane is one of the few gases that has a historical record in the polar ice cores. Bubbles of air from past atmospheres are captured in the ice cores. The ice core has layers which correspond to yearly demarcations. Scientists drill the ice core to specific depths (which correspond to specific times) and analyze the ice for CH_4 concentration. In this way, a historical record of CH_4 concentrations may be constructed.

Stauffer et al. (1988) measured CH_4 concentrations in Antarctica (Byrd Station) and Greenland (Dye 3) ice-cores. They showed that the atmospheric CH_4 concentrations were 500 ppbv at 60,000 yr Before Present (BP) and 350 ppbv at 20,000 yr BP. Chappellaz et al. (1990) measured CH_4 concentrations in the Vostok ice core over the past 160,000 years, and saw fluctuations over the 350 - 650 ppbv range.

Measurements have also focused on the past 3,000 years. Craig and Chou (1982) showed that between 1580 A.D. and 27,000 years BP, CH_4 was approximately uniform at 700 ppbv (650 - 760 ppbv). They had only 9 data points, though, and Khalil and Rasmussen (1987) point out that only 5 were for the last 350 years. Khalil and Rasmussen (1982) analyzed polar ice cores to show that CH_4 was approximately 680 ppbv between 1000 and 3000 years ago

Rasmussen and Khalil (1984) sampled ice cores that were 200 years old or older, and

found that the concentration of methane 250 years ago was also roughly 700 ppbv. Roughly 300 years ago, the concentration of methane did begin increasing, however, the most rapid increase of methane started between 140 and 180 years ago. They found a roughly 10% difference in North Pole samples compared to the South Pole samples. This is because CH_4 has land based emissions, and there is more land in the northern hemisphere.

Work by Stauffer et al. (1985) focused on the past 200 years, bridging the time between existing ice core measurements and actual atmospheric measurements. Their Figure 2 shows a concentration of roughly 800 ppbv before 1800 A.D. and roughly 900 ppbv in 1850 A.D.

Khalil and Rasmussen (1987) compiled a number of ice core data sets, and recent GC atmospheric measurements. They increased the south pole ice core measurements by 5% and decreased the north pole ice core measurements by 5%, to account for the interhemispheric gradient. The most significant trends of increase for CH_4 began in the time period of 1900 - 1925 A.D. Their Figure 4 shows that the concentration of CH_4 was roughly 800 - 1000 ppbv in 1865 A.D. and roughly 900 - 1050 ppbv in 1885 A.D.

8.2.4 Construction of preindustrial [CH_4] fields

An annual average, two-dimensional, preindustrial CH_4 field was created on the basis of ice core measurements. The surface concentrations of CH_4 were assumed to be 825 ppbv in the northern hemisphere, and 750 ppbv in the southern hemisphere. Next, the variation with altitude was prescribed for 6 different latitude bands using the variation with height calculated by the LLNL 2D model for CH_4 (1985 atmosphere simulation for January (Kinnison, 1989, personal communication)). The six latitude bands were 30^o each, and stretched from 90^o south to 90^o north.

8.3 NO_x source emissions

Nitrogen oxides, NO_x, enter the GRANTOUR model as emissions, and are a prognostic variable. Three anthropogenic sources (fossil fuel combustion, biomass burning, aircraft) and three natural sources (lightning, soil emissions, and transport from the stratosphere) are used in GRANTOUR. Two NO_x sources, fossil fuel combustion and aircraft emissions, vary annually. The remaining sources all vary monthly. Table 8.5 below lists the annual total source strength of all sources. A brief description of each NO_x source follows.

Table 8.5: Total annual NO_x emissions in GRANTOUR

Source	Annual total strength, Tg N/year*
Fossil fuel combustion	22
Biomass burning	10
Aircraft emissions	0.2
Lightning	10
Soil emissions	5
Transport from stratosphere	1
Total	48.2

* $1\ Tg = 10^{12}\ g$

8.3.1 Fossil fuel (annual)

The fossil fuel combustion NO_x source file used the inventory of Dignon (1992). The original inventory is given in metric tons N emitted per 1^o x 1^ogrid box. This inventory was created using fuel consumption data for individual countries. The total emissions were then distributed according to the country's population. The total annual emissions are 22.4 Tg N/year. The information from the 1^o x 1^o grid was aggregated into the 4.5^o x 7.5^o grid needed for GRANTOUR, and converted to units of kg NO/km^2-hr.

8.3.2 Biomass burning (monthly)

Monthly biomass burning source inventories were created based on the work of Hao et al. (1990). Figures 1a, 1b, and 1c of Hao et al. (1990) give CO_2 emissions (in units of 10^{12} g CO_2-C/month), from biomass burning for 5^o x 5^o grid boxes in Central/South America, Africa, and Asia, respectively. In the figures, Hao et al. (1990) list T, F, S, and M for each 5x 5 degree box for one month of intensive burning, where:

T = total CO_2-C emissions = F + S

F = forest CO_2-C emissions,

S = savanna CO_2-C emissions, and

M = most intensive 3 months of burning.

It is assumed that burning occurs over 5 months (the middle three of which are the most intensive) in relative amounts of 0.125, 0.25, 0.25, 0.25, and 0.125. Thus, to get an annual total emission requires multiplying the numbers in their Figure 1 by 4. Additional information on Australia was supplied by Dignon (personal communication, 1993).

The emissions in units of CO_2-C were first converted to total C burned by multiplying by 1.1. This is because Hao et al. (1990) assume that CO and CO_2 are formed in a molar ratio of $CO/CO_2 = 0.1$. Total kg C burned was converted to kg Dry Mass (DM) burned by:

$$DM = \frac{TotalC}{0.45} \tag{8.9}$$

The total dry mass burned was then converted to kg NO/month using the emission factors of Dignon et al. (1991a). The emission factor for forest was taken to be the average of Dignon's rain forest and forest (3.1 + 2.1)/2 = 2.5 g N/(kg dry matter). The emission factor for savanna was taken to be the average of woodland and scrub and grassland (1.8 + 2 0)/ 2 = 1.9 gN/(kg dry matter). Finally, the total N emissions were converted to kg NO/km^2-hr

Total monthly biomass burning NO_x emissions are given in Table 8.6.

Table 8.6: Biomass burning NO_x emissions by month

Month	Total NO_x emitted, Tg N/month	Percentage of annual total
January	0.94	9.3%
February	0.90	9.0
March	0.68	6.8
April	0.26	2.6
May	0.63	6.3
June	1.23	12.2
July	1.47	14.7
August	1.51	15.1
September	0.98	9.7
October	0.33	3.3
November	0.42	4.2
December	0.71	7.1
Total	10.1	100.0

8.3.3 Aircraft emissions (annual)

The annual aircraft source file for NO_x was developed from a three-dimensional database supplied by the Warren Spring Laboratory (1989). The original database included metric tons NO_2/year for 11 height levels. These were then aggregated into 6 different vertical levels for use by GRANTOUR, and distributed within the correct GRANTOUR grid boxes. The 6 vertical levels, and the total annual source at each are given in Table 8.7 below. Total aircraft emissions are 0.23 Tg N/year.

Table 8.7: Annual Aircraft NO_x emissions

Vertical level	Tg N/year
$1.0 < \sigma < 0.9$	0.092
$0.9 < \sigma < 0.8$	0.025
$0.8 < \sigma < 0.7$	0.025
$0.7 < \sigma < 0.4$	0.0044
$0.4 < \sigma < 0.3$	0.007
$0.3 < \sigma < 0.2$	0.07
Total	0.23

8.3.4 Lightning (monthly)

The lightning source consists of both cloud-cloud and cloud-ground lightning. Monthly source files were constructed using the methodology of Hameed et al. (1981), which is described below. First, mean monthly thunderdays, T_m, were derived from a map of global isobronts (Handbook of Geophysics, 1960) for grid boxes of 10^o x 15^o. The number of cloud-ground flashes in a month m at latitude ϕ, $N_g(\phi,m)$ is given by:

$$N_g(\phi, m) = 0.40 \times T_m \times (0.1 + 0.35 sin\phi) \qquad (8.10)$$

where the units of N_g are #/km^2-month. The number of cloud-cloud flashes per month, $N_c(\phi,m)$, is related to $N_g(\phi,m)$ by:

$$N_c(\phi, m) = N_g(\phi, m) \times \{ (4.16 + 2.16 cos3\phi)\ (0.6 + \frac{0.4T}{(0.72 - 0.98\phi)}) \} \qquad (8.11)$$

for $\phi \leq 60°$ and $T \leq 84$.

For $\phi \leq 60°$ and $T \geq 84$, the following equation holds true:

$$N_c(\phi, m) = 6.3 \times N_g(\phi, m) \qquad (8.12)$$

and for $\phi > 60^o$, equation (8.6) is used:

$$N_c(\phi, m) = \frac{N_g(\phi, m) \times (1 - 0.1\,(1 + (\frac{\phi}{30})^2))}{0.1 \times \left[1 + (\frac{\phi}{30})^2\right]} \qquad (8.13)$$

The relative amounts of NO_x generated by N_c and N_g are calculated by assuming an energy discharge of 2×10^8 joules/ground-flash and that the amount of NO_x generated by this energy is 3.7×10^{16} NO_y molecules/joule. The total annual lightning source term is then constrained to be 10 Tg N/year, and the monthly source files are normalized. Table 8.8 gives the total source terms per month.

Table 8.8: Monthly lightning NO_x source emissions

Month	Cloud-cloud source, Tg N/month	Cloud-ground source, Tg N/month
January	0.41	0.39
February	0.39	0.37
March	0.37	0.37
April	0.41	0.40
May	0.46	0.47
June	0.52	0.54
July	0.45	0.52
August	0.44	0.48
September	0.39	0.40
October	0.41	0.39
November	0.38	0.36
December	0.32	0.40
Total	4.9	5.1

8.3.5 Soil emissions (monthly)

NO_x is emitted by naturally-occurring bacteria in soils. NO is produced by denitrifying bacteria in anaerobic soils and nitrifying bacteria in aerobic soils. The emission rates depend on temperature, soil moisture content, nitrogen content of the soil; and vegetation type. Field measurements have been made for a number of locations (Anderson and Levin, 1987; Slemr and Seiler, 1984; Williams and Fehsenfeld, 1991 (and references therein); Williams et al., 1988; Williams et al., 1987).

The monthly NO_x soil sources used by GRANTOUR was compiled by Dignon (1991b). Soil types were based on those assigned by Matthews (1983). Dignon assumed emissions varied with temperature in the manner suggested by Williams et al. (1987). Completely saturated soils were assumed not to emit NO. Dry soils were specified to emit NO at a rate that was 0.25 times that of wet soils. Wetting of previously dry soils increased the emission rate. The total inventory gives an annual average emission of 5 Tg N/year. Table 8.9 shows the monthly breakdown of soil emissions.

Table 8.9: Monthly soil emissions of NO_x

Month	Soil source, Tg N/month
January	0.39
February	0.33
March	0.40
April	0.46
May	0.46
June	0.45
July	0.46
August	0.51
September	0.34
October	0.37

Table 8.9: Monthly soil emissions of NO_x

Month	Soil source, Tg N/month
November	0.40
December	0.43
Total	5.0

8.3.6 Transport from the stratosphere (monthly)

The final NO_x source term used in GRANTOUR represents the production of reactive nitrogen in the stratosphere due to the reaction of N_2O (which is not reactive in the troposphere) with $O(^1D)$. For the months of January and July files, the reaction rate of N_2O with $O(^1D)$ was calculated as a function of latitude and altitude in the LLNL 2D model (Wuebbles et al., 1987) for the stratosphere. These January and July "source terms" were then sinusoidally interpolated for all remaining months. The total annual stratospheric source term is 1 Tg N/year.

8.4 Isoprene source emissions

Isoprene is an important biogenic hydrocarbon emitted by plants and trees. It is highly reactive, and emitted in large amounts on a global scale. Recently, monthly global inventories of isoprene, monoterpene, and other highly reactive biogenic hydrocarbons (residence times of less than 1 day) were compiled (Alex Guenther, personal communication, 1993). The global inventories are presented on a 0.5 degree by 0.5 degree grid. These monthly global inventories were converted to the grid required by the GRANTOUR model.

Table 8.10 below presents the global monthly total emissions of isoprene, monoterpenes, and other highly reactive biogenic hydrocarbons, although only the isoprene inventories were used in the non-methane hydrocarbon version of GRANTOUR. According to Alex Guenther (NCAR, private communication, 1993), a fourth category of

lesser reactive biogenic hydrocarbons (residence times greater than 1 day) also is emitted, in equal quantities to the reactive biogenic hydrocarbon category. This would add 371 Tg/yr to the total biogenic hydrocarbon emissions.

Most other estimates of naturally emitted NMHCs are similar. Singh and Zimmerman (1992) estimate 350 - 450 Tg isoprene/yr and 480 Tg terpenes/yr, mainly based on work by Zimmerman (1979a). Rasmussen and Khalil (1988) estimated 450 Tg isoprene/yr are emitted globally. Muller (1992) uses an estimate of 250 Tg isoprene/yr, 147 Tg terpenes/yr, and 94 Tg/yr of biogenically emitted paraffins and aromatics. These figures seem low compared to other estimates.

Table 8.10: Monthly global isoprene, monoterpene, and other biogenic hydrocarbon emissions, Tg/year

Month	Isoprene	Terpenes	Other biogenic hydrocarbons
January	347	112	320
February	366	112	317
March	375	120	336
April	369	125	350
May	394	149	406
June	404	165	420
July	451	186	458
August	455	186	471
September	400	153	419
October	370	129	372
November	349	118	345
December	347	116	336
Annual average	386	139	371

8.5 Other Non-methane Hydrocarbons

In addition to isoprene, the non-methane hydrocarbon version of GRANTOUR also includes alkanes, alkenes, and aromatic compounds. All of these species will affect not only the concentrations of O_3 and OH, but also the concentrations of reactive nitrogen and hydrogen compounds and other species in the troposphere. These hydrocarbons are emitted by a number of activities, including industrial processes (e.g. refineries, manufacturing, printing, pulp and paper production, etc.), biomass burning, and biogenic emissions from vegetation, soils, and oceans. GRANTOUR source files for hydrocarbons from industrial processes and biomass burning were constructed as described below in Sections 8.5.1 and 8.5.2, respectively.

8.5.1 Non-methane hydrocarbon emissions from industrial processes

Watson et al. (1991) developed a global inventory of seven groups of hydrocarbons on a 10 degree by 10 degree grid (see also Piccot et al., 1992). The seven hydrocarbon categories included alkanes (paraffins), alkenes (olefins), aromatics (benzene, toluene, and xylene), formaldehyde, other aldehydes, other aromatics, and marginally reactive compounds. The inventory was constructed as described below.

Using earlier NAPAP (National Acid Precipitation and Assessment Program) inventories, over 3000 U.S. source types were first aggregated into 25 different summary source groups. Based on production and emission figures for the U.S., seven emission factors (one for each hydrocarbon category) were derived for each of the 25 source groups. These emission factors were then multiplied by the production amounts in other countries, to give country-specific emissions. Three different biomass burning groups were also considered, giving 28 source types altogether. The emissions were then distributed both by country and on the 10 degree by 10 degree grid based on population and industrial activity information. The inventory of Piccot et al. (1992) gives 110 Tg of NMHCs per year, 23 Tg of which are biomass burning, leaving 87 Tg/year as industrial sources.

Table 6 of Watson et al. (1991) sums the 25 non-biomass burning sources, and presents the total emissions for the seven hydrocarbon categories for each country. These numbers served as the basis of our industrial non-methane hydrocarbon source files.

The seven hydrocarbon groups were further split into the categories required by GRANTOUR (ethane, propane, C4-C5 alkanes, C6-C8 alkanes, ethene, propene, butene, benzene, toluene, and xylene) using ratios obtained from hydrocarbon measurements in 39 U.S. cities (Table 6, Singh and Zimmerman, 1992). The paraffins were assumed to consist of 9% ethane, 9% propane, 46% C4-C5 alkanes, 34% C6-C8 alkanes, and 2% other alkanes not used by GRANTOUR. The olefins were assumed to consist of 46% ethene, 17% propene, 18% butene, and 19% other alkenes not used by GRANTOUR. The aromatics were split into 18% benzene, 47% toluene, and 35% xylene. Finally, the emissions were population distributed in grid boxes the appropriate size for GRANTOUR. The final global annual source terms for each hydrocarbon category in GRANTOUR are shown in Table 8.11 below. Also shown are the industrial emission estimates used by Hough (1991) in a two-dimensional global model and used by Kanakidou and Crutzen (1993) in a three-dimensional model.

Table 8.11: Industrial Non-methane hydrocarbon emissions used by GRANTOUR, Hough (1991), and Kanakidou and Crutzen (1993), Tg species/yr

Species	GRANTOUR source, Tg/yr	Hough (1991) source, Tg/yr	Kanakidou and Crutzen (1993) source, Tg/yr
ethane	4.1	6.0	8.0
propane	4.1	6.0	12.0
C4-C5 alkanes	20.8	20.0	
C6-C8 alkanes	15.4	15.5	
ethene	8.1	10.0	
propene	3.0	10.0	
butene	3.2	---	
benzene	2.5	5.0	

Table 8.11: Industrial Non-methane hydrocarbon emissions used by GRANTOUR, Hough (1991), and Kanakidou and Crutzen (1993), Tg species/yr

Species	GRANTOUR source, Tg/yr	Hough (1991) source, Tg/yr	Kanakidou and Crutzen (1993) source, Tg/yr
toluene	6.6	15.0	
xylene	5.0	---	
Total	73	87.5	

The final source strengths used in GRANTOUR may differ from those actually emitted into the troposphere. First, the urban splits used for the paraffin category (Singh and Zimmerman, 1992) distributed the paraffins among strictly chain and branched alkanes, whereas the Watson et al. (1991) paraffin category actually contained alkanes, alcohols, esters, and ketones. Thus, the GRANTOUR source strengths for ethane, propane, C4-C5 and C6-C8 may be too high.

However, complicating this is the fact that the total industrial source of Watson et al. (1991) (that is, the sum of the 25 non-biomass burning categories) contains fuel-wood burning as its largest source. According to Watson, fuel-wood burning accounts for roughly 24% of the total global emissions (including biomass burning). This gives a fuel-wood contribution of 26 Tg/year, concentrated mainly in the tropics, if we assume a total source of 110 Tg/year total VOCs (Piccot et al., 1992). We have split the paraffin, olefin, and aromatic categories of Watson et al. (1991) based on urban data. However, the fuel-wood burning emissions will have a different split within each category. Table 8.12 below shows the splits among the paraffin, olefin, and aromatic categories for urban areas (Singh and Zimmerman, 1992) and forest burning in Brazil (Greenberg et al., 1984), which is assumed to resemble fuel-wood burning.

Table 8.12: Hydrocarbon emission categories for urban areas and fuel-wood burning (similar to forest burning)

Species	U.S. Cities (urban) (Singh & Zimmerman, 1992)	Brazilian Forest Burning (Greenberg et al., 1984)
PARAFFINS		
ethane	9%	43%
propane	9%	44%
C4-C5 alkane	46%	---
C6-C8 alkane	34%	---
OLEFINS		
ethene	46%	59%
propene	17%	25%
butene	18%	---
AROMATICS		
benzene	11%	58%
toluene	29%	29%
xylene	22%	---

Clearly, the fuel-wood burning splits a higher fraction of alkanes into ethane and propane than does the urban. Also, fuel-wood burning results in slightly higher ethene and propene fractions than the urban. Fuel-wood burning is assumed to create no butene or > C3 alkanes. Finally, the fuel-wood burning gives more benzene, and no xylene, compared to the urban. So, applying the urban split to the fuel-wood category tends to decrease ethane, propane, ethene, propene, and benzene sources, and increase C4-C5 and C6-C8 alkanes, butene, and xylene sources.

For these two reasons, the GRANTOUR C4-C5 and C6-C8 alkanes, ethene, propene, and benzene sources may be higher than those actually experienced. There are compensating factors working on the ethane and propane, though.

The final total industrial NMHC source term used by GRANTOUR is 73 Tg/year (this includes fuel-wood burning). It should be noted, however, this is just the total of the 10 NMHC categories required by the chemical mechanism in GRANTOUR, and our estimate would be higher if we included other NMHC species. For example, Piccot et al. (1992), from which the GRANTOUR estimate was developed, derive 87 Tg/year, but this includes formaldehyde, other aromatics, other aldehydes, and marginally reactive species. As shown in Table 8.11, Hough (1991) derived a total source of 87.5 Tg/year from industrial sources for the same categories as GRANTOUR. Singh and Zimmerman estimate a global NMHC source of 103 Tg NMHCs/year, of which forest fires, open burning, and incineration account for 45 Tg/year. It appears that built into the 45 Tg/year estimate is an estimate of 34 Tg/year emissions from biomass burning. Thus, their non-biomass burning source would be 69 Tg/year. Muller (1992) estimates that technological sources (fossil fuel burning, industrial processes, and waste disposal) account for 98 Tg NMHCs/year, a figure that is higher than used in GRANTOUR. However, again, Muller may be summing more hydrocarbon categories than the 10 used by GRANTOUR. Kanakidou and Crutzen (1993) used higher industrial sources than GRANTOUR for ethane (8 Tg/yr versus 4.1) and propane (12 Tg/yr versus 4.1). Their emissions were distributed relative to CO_2 emissions.

8.5.2 Non-methane hydrocarbon emissions from biomass burning

Biomass burning is also an important source of non-methane hydrocarbons. The biomass burning takes place primarily in South and Central America, Africa, Asia, and Australia. The emission source files for the 10 hydrocarbon categories in GRANTOUR were developed as described below.

Total biomass burning CO_2 emissions for Central/South America, Africa, and Asia were obtained from Figures 1a, 1b, and 1c of Hao et al. (1990) in terms of mass CO_2-C/ month. Additionally, CO_2 emissions for Australia were compiled (Dignon, personal communication, 1992). The emissions were kept as individual forest and savanna

categories. The emission of CO_2-C/month was converted to NMHC-C emissions/month assuming an emission factor of 0.011 for NMHCs relative to CO_2 (Greenberg et al., 1984). The total NMHC-C emitted was distributed among the 10 categories in the GRANTOUR model based on emission fractions derived from Greenberg et al. (1984) for forests and savannas in Brazil. Because they also measured other NMHCs that are not currently used in GRANTOUR (e.g. furan), only 77% of the total NMHCs emitted by the savanna and 94% of the total NMHCs emitted by the forests are input to GRANTOUR. All other forests and savannas were assumed to behave like those in South America.

Table 8.13 below shows the monthly biomass burning emissions for the 10 hydrocarbon categories required.

Table 8.13: Monthly Biomass burning sources of non-methane hydrocarbons, Tg species/yr*

Mo	C_2H_6	C_3H_8	C_4-C_5 alkane	C_2H_4	C_3H_6	C_4H_8	benz	tol.	xyl.	Tg C/yr
1	4.1	2.2	0.78	6.0	3.2	2.8	1.5	0.86	0.39	19
2	4.8	2.6	0.93	7.0	3.8	3.3	1.7	1.0	0.45	22
3	2.9	1.7	0.59	4.3	2.3	2.0	0.99	0.62	0.28	13
4	1.2	0.77	0.26	1.8	0.89	0.72	0.32	0.25	0.11	5
5	2.8	1.3	0.49	4.0	2.3	2.0	1.2	0.58	0.26	13
6	5.9	2.5	0.99	8.2	4.8	4.4	2.6	1.2	0.55	26
7	6.6	2.8	1.1	9.3	5.4	4.9	2.9	1.4	0.62	30
8	6.8	2.9	1.2	9.5	5.5	5.0	2.9	1.4	0.63	30
9	4.7	2.1	0.81	6.6	3.8	3.4	2.0	0.97	0.43	21
10	1.4	0.75	0.27	2.1	1.1	0.98	0.53	0.30	0.13	7
11	2.0	1.1	0.38	2.9	1.6	1.4	0.71	0.41	0.19	9
12	3.1	1.6	0.58	4.5	2.5	2.2	1.2	0.65	0.29	14
Ann. Avg	3.9	1.9	0.70	5.5	3.1	2.8	1.6	0.80	0.36	17

* It is assumed that biomass burning does not emit C_6 - C_8 alkanes

Thus, the annual average biomass burning source of non-methane hydrocarbons used in GRANTOUR is 17 Tg C/year. This is lower than the 34 Tg C/year estimated by Greenberg et al. (1984) for two reasons. First, they assumed a total global biomass burning source of CO_2 to be 3.1×10^{15} g CO_2-C/year, based on Seiler and Crutzen (1980).. A more recent estimate by Hao et al. (1990) gives 2.026×10^{15} g CO_2-C/year, which would lead to a revised global NMHC source of 22 Tg C/year for Greenberg et al. (1984), using their emission factor of 1.1% NMHC/CO_2. Second, because GRANTOUR source files only include 10 hydrocarbon groups, our total biomass burning NMHC source will be slightly lower than the Greenberg estimate, which also includes oxygenates and alkynes. Because most other estimates of global biomass burning include other hydrocarbons, they also are expected to be higher than that used in GRANTOUR. Piccot et al. (1992) estimate 23 Tg C/year from biomass burning. Andreae (1991) estimates 24 Tg C/year of C2-C10 hydrocarbons are emitted by biomass burning. Muller (1992) also uses the estimates of Hao et al. (1990) for biomass burning CO_2 emissions, but assumes an emission factor of 0.014 for NMHCs relative to CO_2, leading to an estimate of 28 Tg C/yr from savanna and forest biomass burning. Laursen et al. (1992) estimated 17 Tg are emitted per year by biomass burning.

8.5.3 Total non-methane hydrocarbon source emissions

The total non-methane hydrocarbon emissions used in GRANTOUR may be calculated by summing the biomass burning and industrial contributions. Table 8.14 shows an annual average total source term for the 10 hydrocarbon categories, as well as global estimates by Singh and Zimmerman (1992) and the values used by Hough (1991) in a global, two-dimensional model. Note that the GRANTOUR and Hough (1991) values include only biomass burning and industrial sources. The Singh and Zimmerman (1992) values also include emissions from oceans, vegetation, terrestrial ecosystems and, therefore, are expected to be higher than the GRANTOUR values.

Table 8.14: Total global NMHC emissions used in GRANTOUR and estimated by Singh and Zimmerman (1992) and Hough (1991), Tg species/yr

Species	GRANTOUR	Singh and Zimmerman (1992)	Hough (1991)
ethane	8.0	10 - 15	13
propane	6.0	15 - 20	10
C4-C5 alkanes	21.5	5 - 9	22
C6-C8 alkanes	15.4	---	15.5
ethene	13.6	20 - 45	20
propene	6.1	7 - 12	15
butene	6.0	2 - 3	---
benzene	4.1	4 - 5	8
toluene	7.4	4 - 5	17
xylene	5.4	2 - 3	---
isoprene	386	350 - 450	450
monoterpenes + other biogenics	510	400 - 500	---

CHAPTER 9 RESULTS OF PERPETUAL JULY PREDICTOR-CORRECTOR GRANTOUR SIMULATIONS

9.1 Introduction

The predictor-corrector version of GRANTOUR, which includes the photochemistry of the $CO/CH_4/NO_x/OH/O_3$ cycle was used to model three scenarios shown in Table 9.1. The scenarios were used to understand the role of anthropogenic sources of NO_x on current

Table 9.1: Three perpetual July $CO/CH_4/NO_x/OH/O_3$ scenarios simulated

Scenario	[CO]	[CH_4]	NO_x emissions
1	Present day	Present day	Natural and Anthropogenic
2	Present day	Present day	Natural
3	Preindustrial	Preindustrial	Natural

O_3 and OH levels, and to understand the total changes in O_3 and OH that have occurred since preindustrial times. The first scenario used the present day concentration fields of CO and CH_4, and both natural (soil activity, lightning, and transport from the stratosphere) and anthropogenic sources (fossil fuel combustion and biomass burning; note that aircraft emissions were NOT included) of NO_x. The present-day [CO] and [CH_4] fields are discussed in sections 8.1.2 and 8.2.2, respectively. The NO_x sources are discussed in section 8.3. The second scenario used present-day [CO] and [CH_4], but only natural sources of NO_x. Thus, comparing scenario 1 and 2 shows the effect of anthropogenic NO_x on present day O_3 and OH levels.

The third scenario contained only preindustrial concentration fields for CO (see section 8.1.4) and CH_4 (see section 8.2.4), and natural NO_x sources only. Comparing scenario 1 and 3 showed the net change introduced in the O_3 and OH fields from man's energy and land use practices since the preindustrial era.

9.2 Description of the three perpetual July scenarios

The three scenarios were conducted using perpetual July meteorology obtained from CCM1. Each scenario was "spun-up" using 25,000 parcels and a 12 hour operator-splitting time step. Meteorological parameters supplied from CCM1 were updated every 12 hours. The chemistry solution technique required small time steps, on the order of less than a second to several hundred seconds.

Once the masses of O_3, NO, and NO_2 reached steady state in the troposphere and stratosphere, the simulation was then continued with 50,000 parcels and a 6 hour operator-splitting time step. (However, meteorology was still updated only every 12 hours.) Daily output files, which contained key chemical and physical information about parcel and grid quantities were created. It typically took several additional months to reach steady state, at which time the daily output was averaged for the month of July and analyzed. For these scenarios, no species concentrations were fixed in the stratosphere.

9.3 Model results of the role of anthropogenic NO_x

Scenario 1 (which contains both anthropogenic and natural NO_x sources) and scenario 2 (which contains only natural NO_x sources) were compared to illustrate the role of anthropogenic NO_x.

9.3.1 Comparison of model predicted O_3 with observations

Scenario 1 contains both anthropogenic and natural NO_x sources. Although this scenario does not include the non-methane hydrocarbons, the predicted O_3 concentration may be compared to O_3 observations at remote NOAA Climate Monitoring and Diagnostics Laboratory (CMDL) sites (Oltmans, personal communication, 1993; Oltmans and Levy, 1993). The CMDL sites are located away from local sources of pollution, and provide a reasonable estimate of "background" O_3 concentrations. The CMDL observations are made every 20 seconds, and hourly and monthly averages calculated. Thus, they represent a monthly, diurnal average. It would be expected that the model-

predicted concentrations are lower than actual observations because the model does not contain non-methane hydrocarbons, an important ozone precursor. Table 9.2 shows both the model and observed O_3 levels.

Table 9.2: Model predicted present day (Scenario 1) and CMDL observed surface O_3, ppbv, for July

Site	Site elevation, m	CMDL record	CMDL, ppbv	Scenario 1, ppbv
Barrow (71N, 157W)	11	1/81 - 12/91	22.0	14.8
Reykjavik (64N, 22E)	60	9/91 - 9/92	20.7	15.7
Mace Head (53N, 10W)	30	7/89 - 12/92	32.2	22.0
Niwot Ridge (40N, 106W)	3000	7/90 - 12/92	46.0	25.5
Bermuda (32N, 65W)	40	10/88 - 11/92	21.8	28.1
Izania (28N, 17W)	2360	4/87 - 10/89	47.2	24.0
Mauna Loa (20N, 156W)	3397	1/81 - 12/91	37.8	19.2
Barbados (13N, 60W)	45	4/89 - 9/92	17.3	21.7
Samoa (14S, 171W)	82	1/81 - 12/91	20.1	21.1
South Pole (90S, 102E)	2835	1/81 - 12/91	34.6	9.1

In Table 9.2, the model predicted values are lower than observations for the majority of sites: Barrow, Reykjavik, Mace Head, Niwot Ridge, Izania, Mauna Loa, and the South Pole, as expected. The largest discrepancies between the model and observations occur at sites which have appreciable elevations: Niwot Ridge, Izania, Mauna Loa, and the South Pole. Some of the site elevations are so high they may actually be sampling free tropospheric air, which would have a higher O_3 concentration thatn at the surface. For all but the South Pole though, the model is calculating a surface average for a large grid square (roughly 450 km by 750 km). Thus, GRANTOUR cannot resolve locally highly elevated locations, and the model average grid elevation may be much lower than the actual site elevation. On the other hand, the model predicted values at Samoa are very similar to the observations and, at Bermuda and Barbados, the model predicts higher O_3 levels than

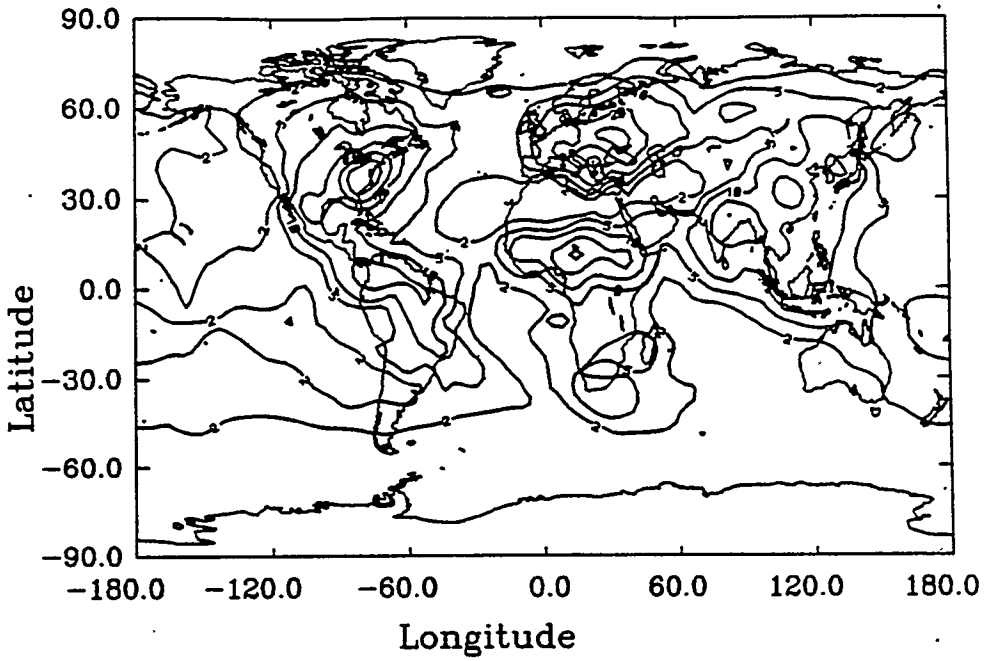

Figure 9.1 Predicted wet nitrate deposition for the all NO_x scenario. Contours are 2, 5, 10, 20, 30, 40, 50, and 60 kg N/km^2.

observed.

9.3.2 Comparison of model predicted HNO_3 deposition with observations

Penner et al. (1991) presented HNO_3 wet deposition data for July over North America in Figure 22.c. The all NO_x source scenario nitrate deposition is shown in Figure 9.1. For comparison, only North America is considered. The model results are similar to observations, although model peak values are higher than observed. However, the model contours show more of a northeasterly tilt than the observations (perhaps due too strong CCM1 winds). In Figure 9.1, the model 10 kg N/km^2 contour covers much of the U.S., as do the measurements. The model 20 kg N/km^2 covers an area of northern Mexico not seen in the observations. Finally, model nitrate deposition peaks are 40 kg N/km^2, while the data peak at 30 kg N/km^2.

9.3.2 The role of anthropogenic NO_x on present day O_3

For simplicity, the two present day scenarios (scenario 1 and scenario 2), which both contain present day concentrations of CO and CH_4, will be referred to by the NO_x sources they incorporate. Thus, scenario 1 will be referred to as the all NO_x scenario, and scenario 2 will be called the natural NO_x scenario. Figure 9.2 shows the surface ozone concentrations predicted for the all NO_x and natural NO_x scenarios. The anthropogenic NO_x (from fossil fuel combustion and biomass burning) leads to higher O_3 levels in both the northern and southern hemisphere. In the northern hemisphere, the main contribution is from fossil fuel combustion. When anthropogenic NO_x is included, O_3 levels over Northern America increase from 10 - 20 ppbv to 15 - 35 ppbv. Over Europe and Asia, including anthropogenic NO_x increases O_3 levels from 15 - 20 ppbv to 20 - 25 ppbv. Anthropogenic NO_x from biomass burning increases O_3 levels over the tropical and southern hemisphere regions. For example, O_3 levels increase from 10 - 20 ppbv over both South America and Africa to 15 - 30 ppbv when anthropogenic NO_x is included. Additionally, the oceanic peaks of 20 - 25 ppbv increase to 25 - 30 ppbv in the southern hemisphere. Note that there exists peaks just west of South America, Africa, and Asia/ Australia. The O_3 peak west of Africa has been documented by satellite observations, and is hypothesized to result from extensive biomass burning (Fishman et al., 1991).

A calculation of average tropospheric O_3 levels (similar to average tropospheric OH calculations) shows that using only natural NO_x sources gives a global average tropospheric O_3 concentration of 5.4×10^{11} cm^{-3}. However, including anthropogenic NO_x increases the global average tropospheric O_3 concentration to 6.1×10^{11} cm^{-3}, roughly 10% higher. Thus, anthropogenic NO_x sources results in higher O_3 levels on a global scale.

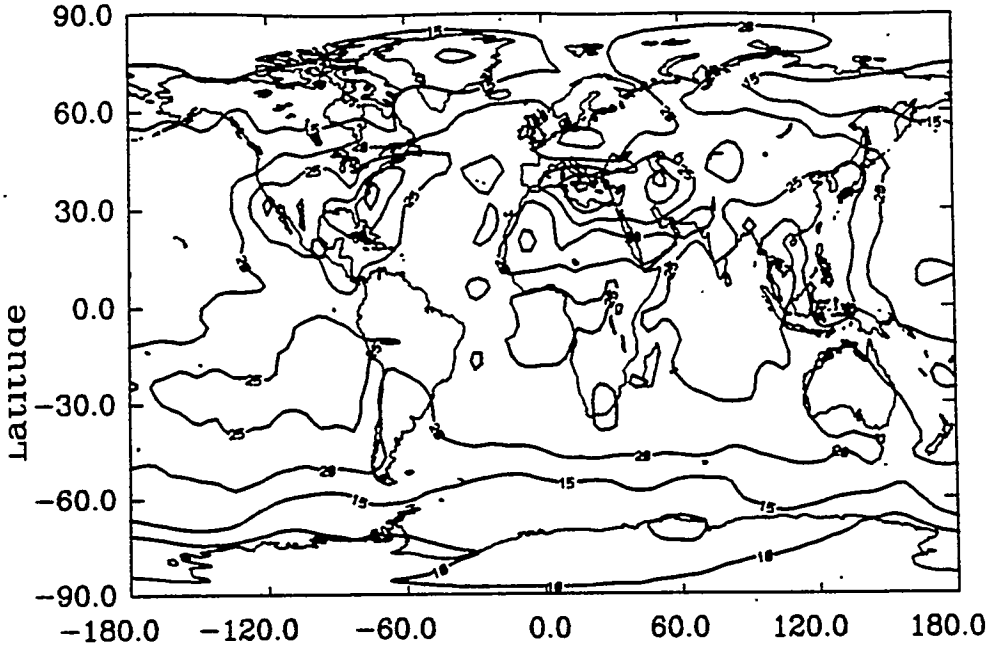

(a) All NO_x scenario

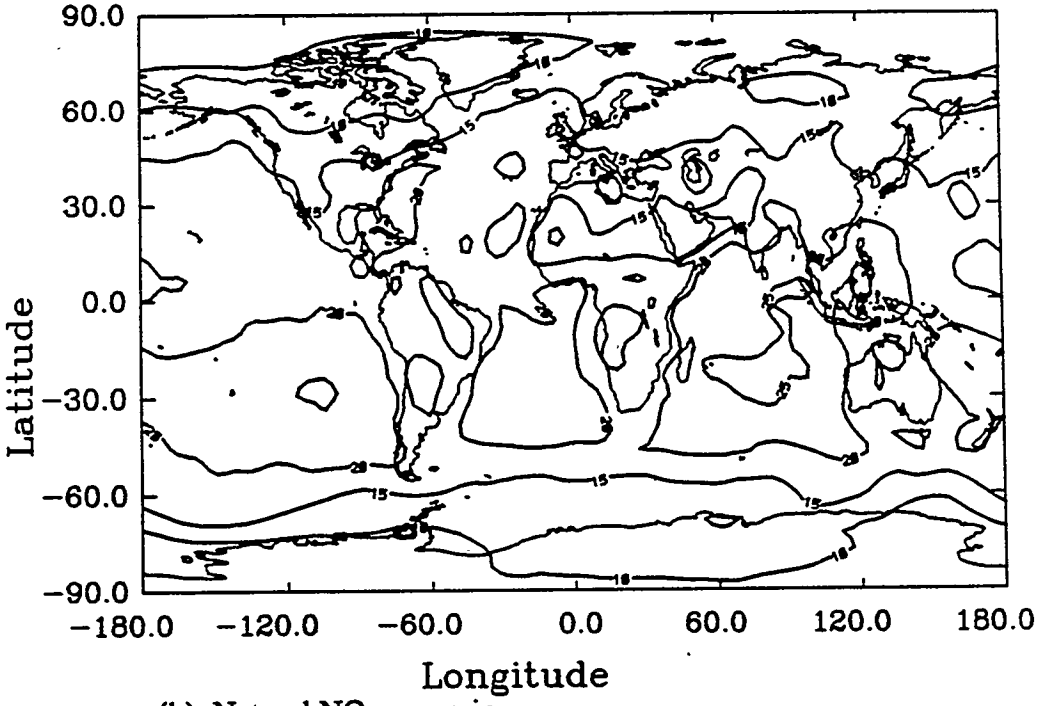

(b) Natural NO_x scenario

Figure 9.2 Surface ozone concentrations for the (a) All NO_x and (b) Natural NO_x scenarios. Contours are 5, 10, 15, 20, 25, 30, 35, 40, 45, and 50 ppbv.

9.3.3 The role of anthropogenic NO_x on present day OH

Figure 9.3 shows the surface OH concentrations for the all NO_x and natural NO_x scenarios. Including anthropogenic NO_x tends to increase surface OH concentrations north of 30 degrees south. For example, over the U.S., including anthropogenic NO_x increases the OH level from 1 x 10^6 cm^{-3} to 2 - 2.5 x 10^6 cm^{-3}. Over northern Europe, levels increase from 1- 5 x 10^5 cm^{-3} to 5 x 10^5 to 1 x 10^6 cm^{-3}. Increases in OH levels can also be seen over northern South America, central Africa, and Eastern Asia and India. This increase is also seen over the Pacific Ocean (west of North and South America), where levels increase from 5 x 10^5 cm^{-3} to 1 x 10^6 cm^{-3}.

Zonal average OH concentrations are shown in Figure 9.4. As with the surface fields, the OH concentrations tend to increase north of 30 degrees south when anthropogenic NO_x is added. This effect is evident near 30 degrees north, where peak OH levels increase from 1.5 x 10^6 to greater than 2.0 x 10^6 cm^{-3}. A calculation of global average tropospheric [OH] shows that it increases from 9.2 x 10^5 to 1.0 x 10^6 cm^{-3} when anthropogenic NO_x is added. Thus; adding anthropogenic NO_x increases present day O_3. Concentrations of OH, whose formation is initiated by the photolysis of tropospheric O_3, also increase.

9.4 Model results of the changes in O_3 and OH since preindustrial times

Scenario 1 and 3 are the present day and preindustrial scenarios. Comparing the two shows how the chemistry of the troposphere has changed since preindustrial times. Figure 9.5 shows the surface O_3 concentrations predicted for the preindustrial scenario. Historical data from three regions (Montsouris, France; Moncalieri, Italy; and South America) have recently been re-examined (Volz and Kley, 1988; Anfossi et al., 1991; Sandroni et al. 1992). July O_3 values in these three areas are 6 - 7 ppbv at Montsouris (1876 - 1886), 10 - 11 ppbv at Moncalieri (1868-1893) and 10 - 12 ppbv for two South American locations

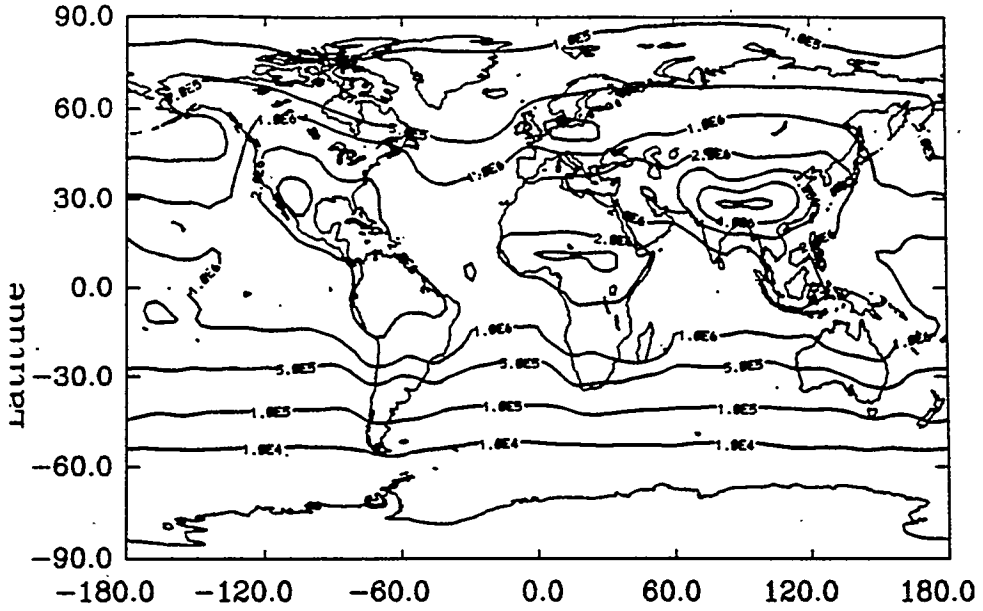

(a) All NO_x scenario

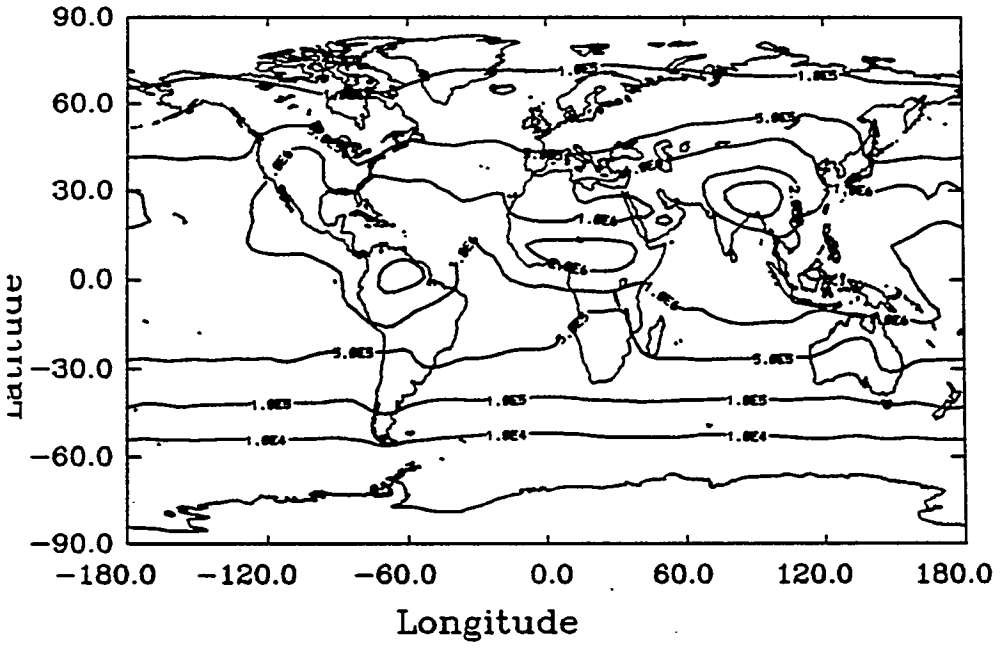

(b) Natural NO_x scenario

Figure 9.3 Surface OH concentrations for the (a) All NO_x and (b) Natural NO_x scenarios. Contours are 1.e4, 1.e5, 5.e5, 1.e6, 2.e6, 3.e6, 4.e6, 5.e6, and 6.e6 cm-3.

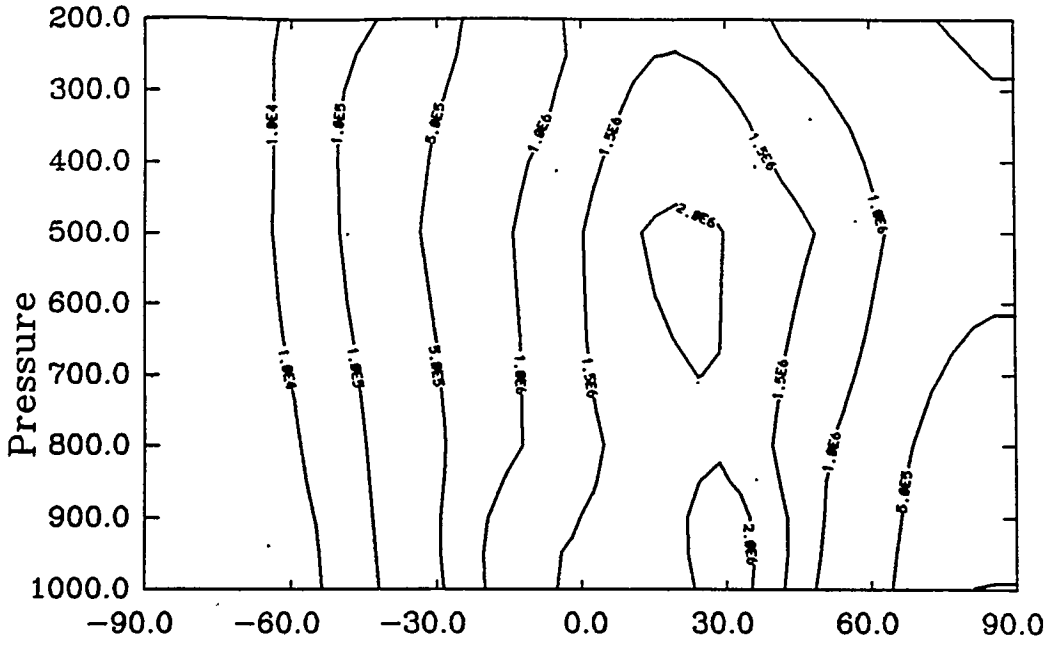

(a) All NO_x scenario

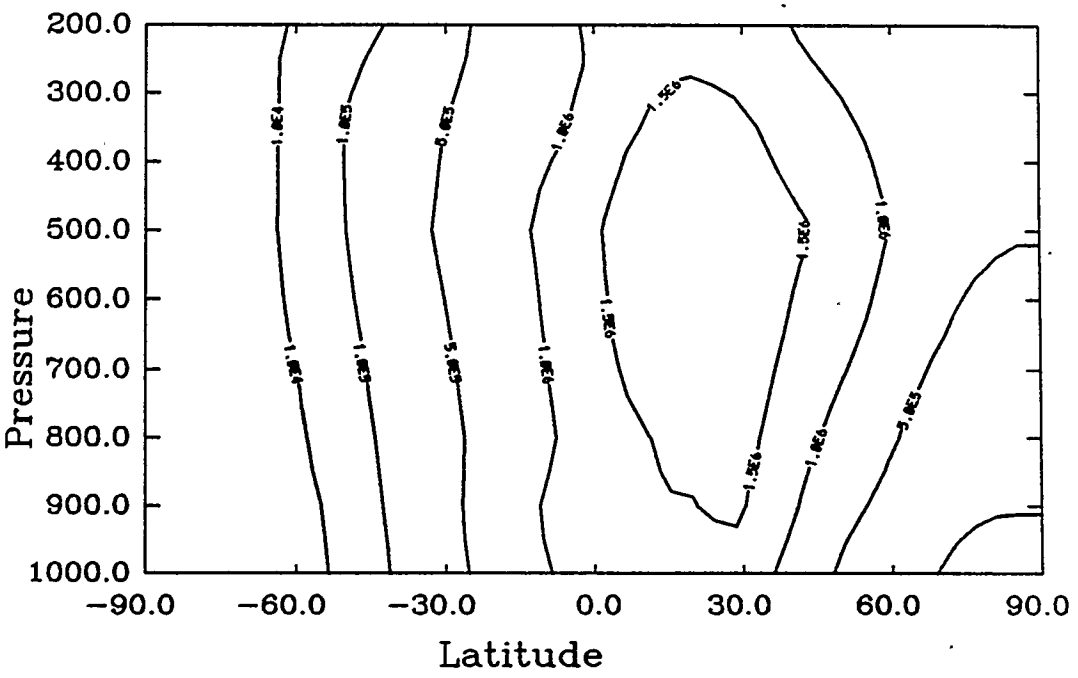

(b) Natural NO_x scenario

9.4 Zonal average OH concentrations for the (a) All NO_x and (b) Natural NO_x scenarios. Contours are 1.e4, 1.e5, 5.e5, 1.e6, 1.5e6, 2.e6, 2.5e6, and 3.e6 cm^{-3}.

(Montevideo, 1883-1885 and Cordoba, 1886-1892). In Figure 9.5, the model predicted surface levels are 10 - 15 ppbv at these locations, indicating the model predicted O_3 values are reasonable, although they may be slightly high for the French location.

Figure 9.6 shows the net O_3 increase predicted from preindustrial times. Over the oceans, the increase is roughly 5 ppbv. Over continents, the increase is from 5 - 15 ppbv. Since the preindustrial values are on the order of 10 - 20 ppbv, this indicates regional relative increases of 50 - 100%. Also, because the preindustrial model O_3 levels may be too high, and the present-day model O_3 levels too low, the actual total O_3 increases experienced will probably be higher if non-methane hydrocarbons are included in the calculations. The global average tropospheric O_3 has increased from 4.3×10^{11} cm^{-3} to 6.1×10^{11} cm^{-3}, an increase of nearly 50%. Thus, due to the increase in the ozone precursors (CO, CH_4, and NO_x), ozone levels have increased since the preindustrial times.

The zonal average OH field calculated for preindustrial times is shown in Figure 9.7. Comparing this to Figure 9.4a (zonal OH for the present day) shows OH has decreased since preindustrial times, mainly from 0 to 30N. In fact, the global average tropospheric [OH] has decreased roughly 10% from 1.1×10^6 cm^{-3} in preindustrial times to 1.0×10^6 cm^{-3} for the present day.

The model predicted OH fields may also be used to examine the total sink of CH_4 and CO due to reaction with OH. Since this is the overwhelmingly predominant loss mechanism for both species, the sink may then be compared with current source estimates. Thus, using the prescribed model input fields for CH_4 and CO, and the model calculated OH fields, the total tropospheric sinks due to CH_4 + OH and CO + OH are give in Table 9.3 below. Both the CH_4 and CO sinks have increased dramatically from preindustrial times. For reference, the current estimates of CH_4 and CO sources (discussed in sections 8.1 and 8.2) are also given. The model results compare well with current estimates

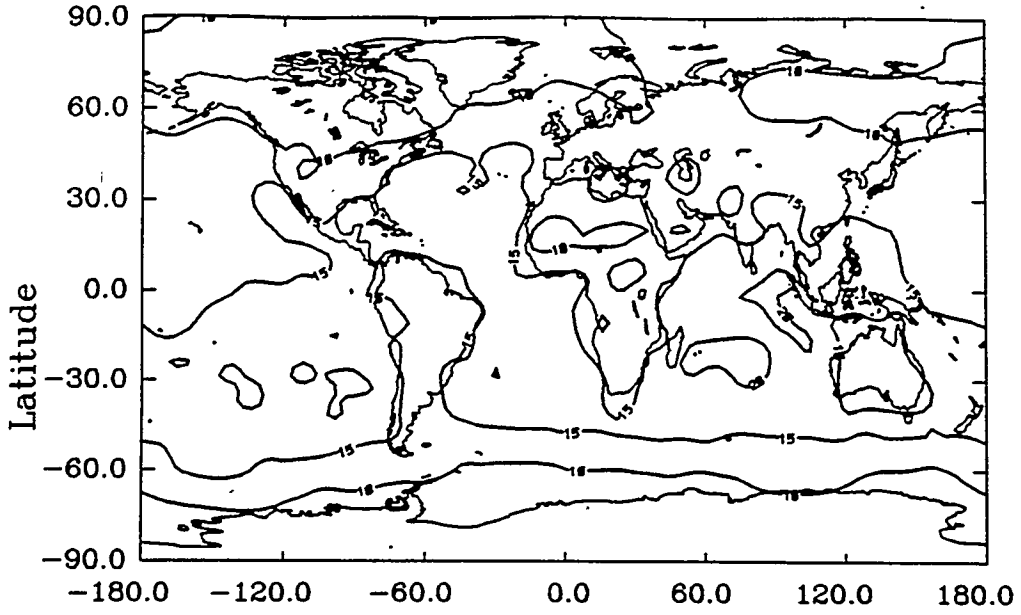

Figure 9.5 Surface O_3 concentrations predicted for the preindustrial scenario. Contours are 5, 10, 15, 20, and 25 ppbv.

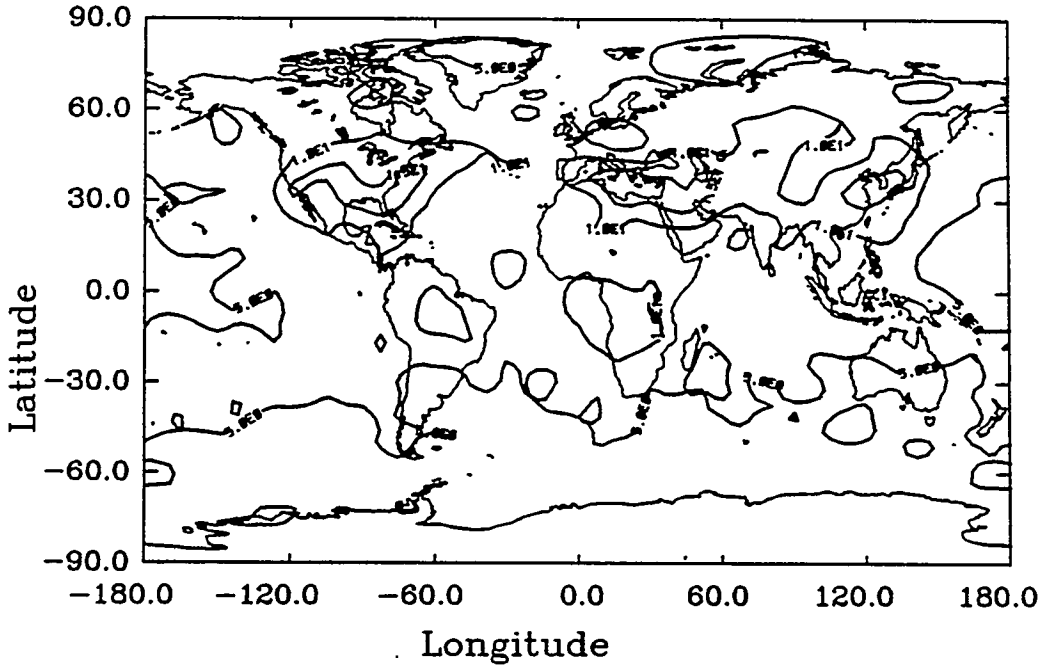

Figure 9.6 The increase in surface O_3 concentrations in ppbv since preindustrial times. Contours are 5, 10, 15, 20, and 25 ppbv.

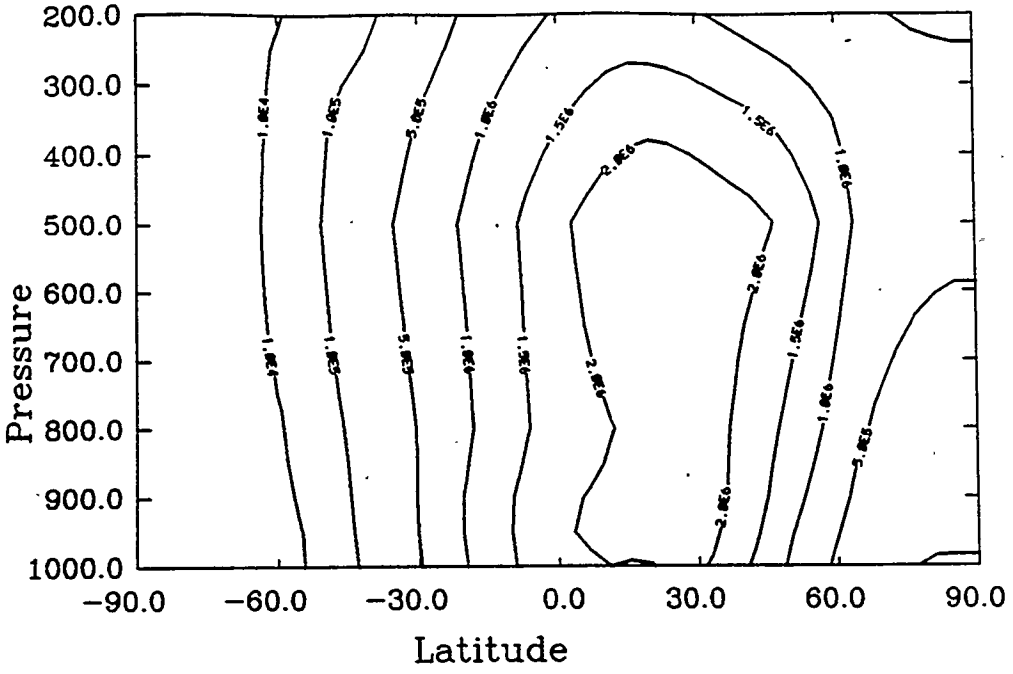

Figure 9.7 Zonal average OH concentrations for the preindustrial scenario. Contours are 1.e4, 1.e5, 5.e5, 1.e6, 1.5e6, 2.e6,and 2.5e6 cm^{-3} .

Table 9.3: Model predicted tropospheric CH_4 and CO sinks compared to current source estimates

Scenario	CH_4 + OH	CO + OH
Preindustrial	270 Tg CH_4/yr	1640 Tg CO/yr
Present day	510 Tg CH_4/yr	2870 Tg CO/yr
Present day source estimates	290 - 965 Tg CH_4/yr	1330 - 4525 Tg CO/yr

Thus, although O_3 has increased roughly 50% since preindustrial times, OH has decreased by roughly 10%. The O_3 increase is because the concentrations of the precursors (CO,CH_4, NO_x) have all increased. Two competing processes affect the OH field. The increase in O_3 tends to increase OH, because OH formation in the troposphere is initiated

by O_3 photolysis. However, because the primary sink for both CO and CH_4 is reaction with OH; increasing the concentration of CO and CH_4 decreases the concentration of OH. This second process is more significant, leading to an overall decrease in OH of 10%.

CHAPTER 10 RESULTS OF SEASONAL PREDICTOR-CORRECTOR GRANTOUR SIMULATIONS

10.1 Introduction

The predictor-corrector version of GRANTOUR, which includes the photochemistry of the $CO/CH_4/NO_x/OH/O_3$ cycle was used to model two present-day condition scenarios for an entire annual cycle (also called a seasonal cycle). For the seasonal simulations, many of the input files were updated on a monthly basis. Because many factors (including input concentrations, emissions, and meteorology) change on a monthly basis, it is expected that the seasonal cycle will be more realistic than a perpetual July or January calculation. Both seasonal scenarios used the present day concentration fields of CO and CH_4 discussed in sections 8.1.2 and 8.2.2. One scenario used both natural (soil activity, lightning, and transport from the stratosphere) and anthropogenic sources (fossil fuel combustion, biomass burning, and aircraft emissions) of NO_x while the second scenario used only natural sources of NO_x. The NO_x emissions are discussed in section 8.3.

Table 10.1: Required input files for seasonal run

Quantity	Variation
Meteorology (Transport, precipitation)	Monthly (but updated every 12 hours)
Reaction rate coefficients, Photolysis rate coefficients, Diurnally averaging factors	Monthly
[CO], [CH_4], [H_2O] (trop & strat) [O_3] (strat only)	Monthly
Temperature	Monthly
NO_x emissions: Fossil fuel combustion Aircraft	Annually

Table 10.1: Required input files for seasonal run

Quantity	Variation
NO_x emissions: Biomass burning Soil activity Lightning Transport from stratosphere	Monthly

10.2 Description of the two seasonal cycles

Two seasonal scenarios were simulated. The initial concentrations for each scenario were based on the final results of the appropriate perpetual July scenario, discussed in chapter 9. Each scenario was "spun-up" for a seasonal July using 25,000 parcels and a 12 hour operator-splitting time step. The meteorological files for July were seasonal files obtained from the CCM1 and updated every 12 hours. Spin-up was continued until the masses of O_3, NO, and NO_2 reached steady state in the troposphere and stratosphere for the month of July. Then, the simulation was started using 50,000 parcels and a 6 hour operator-splitting time step. First July was simulated, then the remaining 11 months of the year. A second July was then simulated at the end. This second July containing 50,000 parcels was used for analysis, rather than the first.

For the seasonal simulations, the O_3 concentrations above sigma = 0.2 were specified using concentrations obtained by the LLNL 2D model (Wuebbles et al., 1987). However, two dimensional models spread NO_x concentrations over entire latitude bands, which tends to dilute the NO_x. Because O_3 production per unit NO_x consumed is much more efficient at lower NO_x values (Liu et al., 1987; Lin et al., 1988), two dimensional models may predict higher O_3 concentrations than observed or predicted by three dimensional models (Kanakidou and Crutzen, 1993). Thus, when the LLNL 2D model O_3 concentrations greatly exceeded actual ozonesonde observations made at nine CMDL O_3 monitoring sites (Komhyr et al, 1989), the 2D model fields were scaled to the observations.

10.3 Predicted O_3 fields

Two present day scenarios, one with all NO_x sources, and one with natural NO_x sources only were simulated. In this section, model predictions from the all NO_x scenario are first compared with observations of O_3. Then, the results from the two scenarios are compared to understand the impact of anthropogenic NO_x on tropospheric chemistry.

10.3.1 Comparison of model predicted and observed surface O_3

The model results for the all NO_x scenario may be compared directly to surface O_3 observations made by the NOAA Climate Monitoring and Diagnostics Laboratory (Oltmans, personal communication, 1993; Oltmans and Levy, 1993). The CMDL sites are located away from local sources of pollution, and provide a reasonable data base for comparison to GRANTOUR. The CMDL observations are made every 20 seconds, and hourly and monthly averages calculated. Thus, they represent a monthly, diurnal average.

Figure 10.1 shows the monthly mean surface O_3 concentrations observed at the CMDL sites and the 25% and 75% values (solid lines) and surface O_3 calculated by GRANTOUR (dashed line). The site locations and elevations are: Barrow (71N, 157W, 11m), Reykjavik (64N, 22W, 60m), Mace Head (53N, 10W, 30m), Niwot Ridge (40N, 106W, 3000m), Bermuda (32N, 65W, 40m), Izania (28N, 17W, 2360m), Mauna Loa (20N, 156W, 3397m), Barbados (13N, 60W, 45m), Samoa (14S, 171W, 82m), and the South Pole (90S, 25W, 2835m). Figure 10.1 also lists the total length of the observational record at each CMDL site.

At four of the sites (Mace Head, Bermuda, Barbados, and Samoa), the model predictions compare well with observations both for total abundance and seasonality. At two sites, Izania and Mauna Loa, predicted O_3 levels are lower than observations, both show similar seasonality. These two sites may be affected either by elevation or by non-methane hydrocarbon chemistry. The actual site elvations are 2360m and 3397m, respectively. At these heights, the O_3 measurements may be more representative of the free

troposphere and, therefore, higher than the surface concentrations predicted for a large grid box by GRANTOUR. Including more NMHCs which would tend to increase O_3 concentrations predicted by GRANTOUR. Specifically, these two oceanic sites may experience appreciable oceanic emissions of ethane and propane, which would increase O_3 concentrations. At Niwot Ridge, the model predictions are also lower than observations. Again, this may be due to the high elevation of the site or the fact that Niwot Ridge experiences appreciable vegetative emissions of non-methane hydrocarbons (including alkanes and monoterpenes), which are not included in this version of GRANTOUR. These non-methane hydrocarbons would lead to higher O_3 observed concentrations. Additionally, peroxyacetyl nitrate (PAN) is an important reservoir species of NO_x which is not included in this model version (since non-methane hydrocarbons, a PAN-precursor) are not included. Including this chemistry may also increase O_3 in these more remote regions.

The three other sites, Barrow, Reykjavik, and the South Pole are relatively high latitude sites. The model and data may disagree because CCM1 dynamics may not be represented well at higher latitudes. Second, PAN formation may also affect O_3 at these sites in some months.

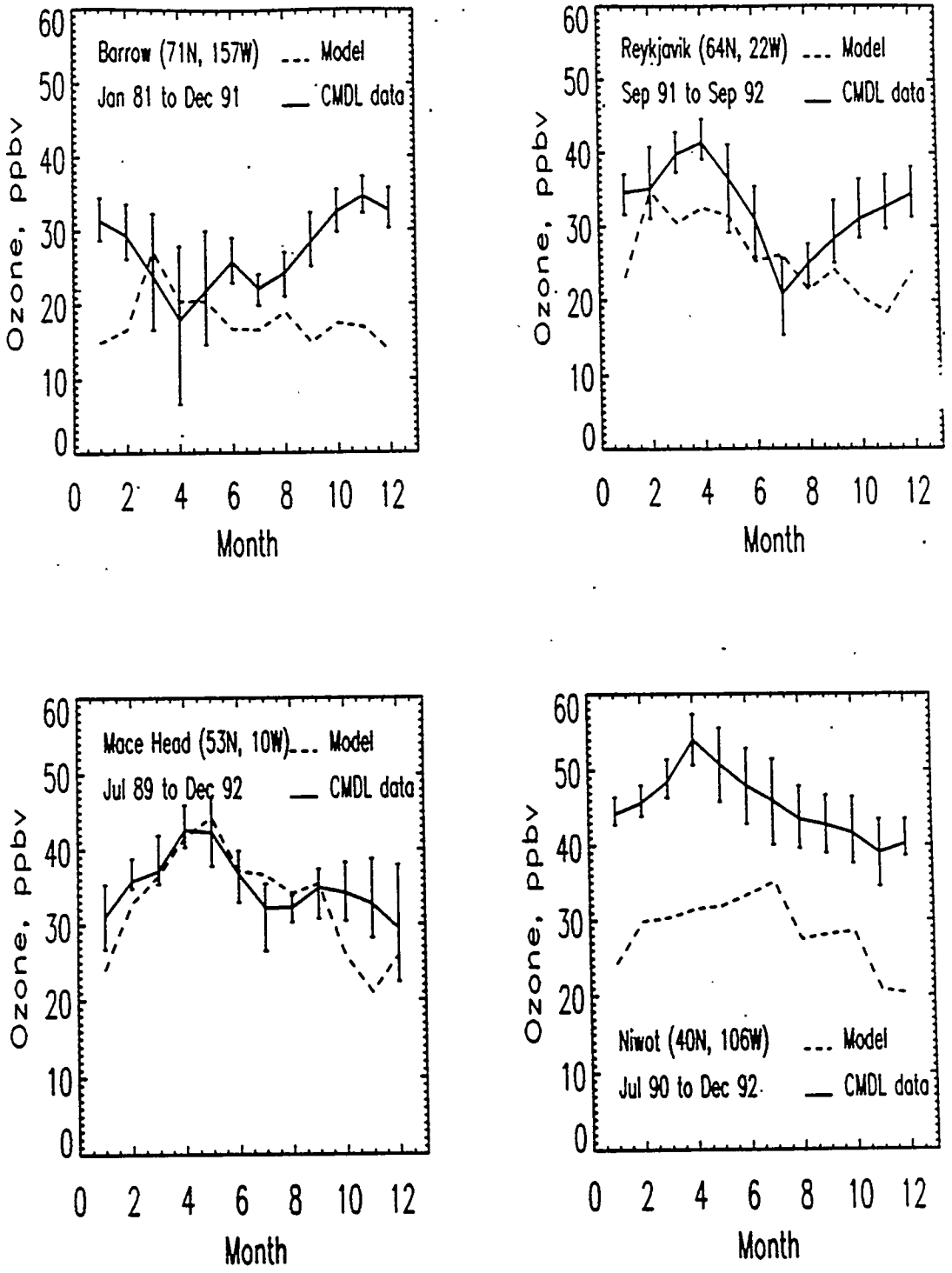

Figure 10.1 Observed mean and 25-75% O_3 and predicted O_3 concentrations (surface) at (a) Barrow, (b) Reykjavik, (c) Mace Head, and (d) Niwot Ridge. Observations from the NOAA Climate Monitoring and Diagnostics Laboratory (S. Oltmans, personal communication 1993 and Oltmans and Levy, 1993).

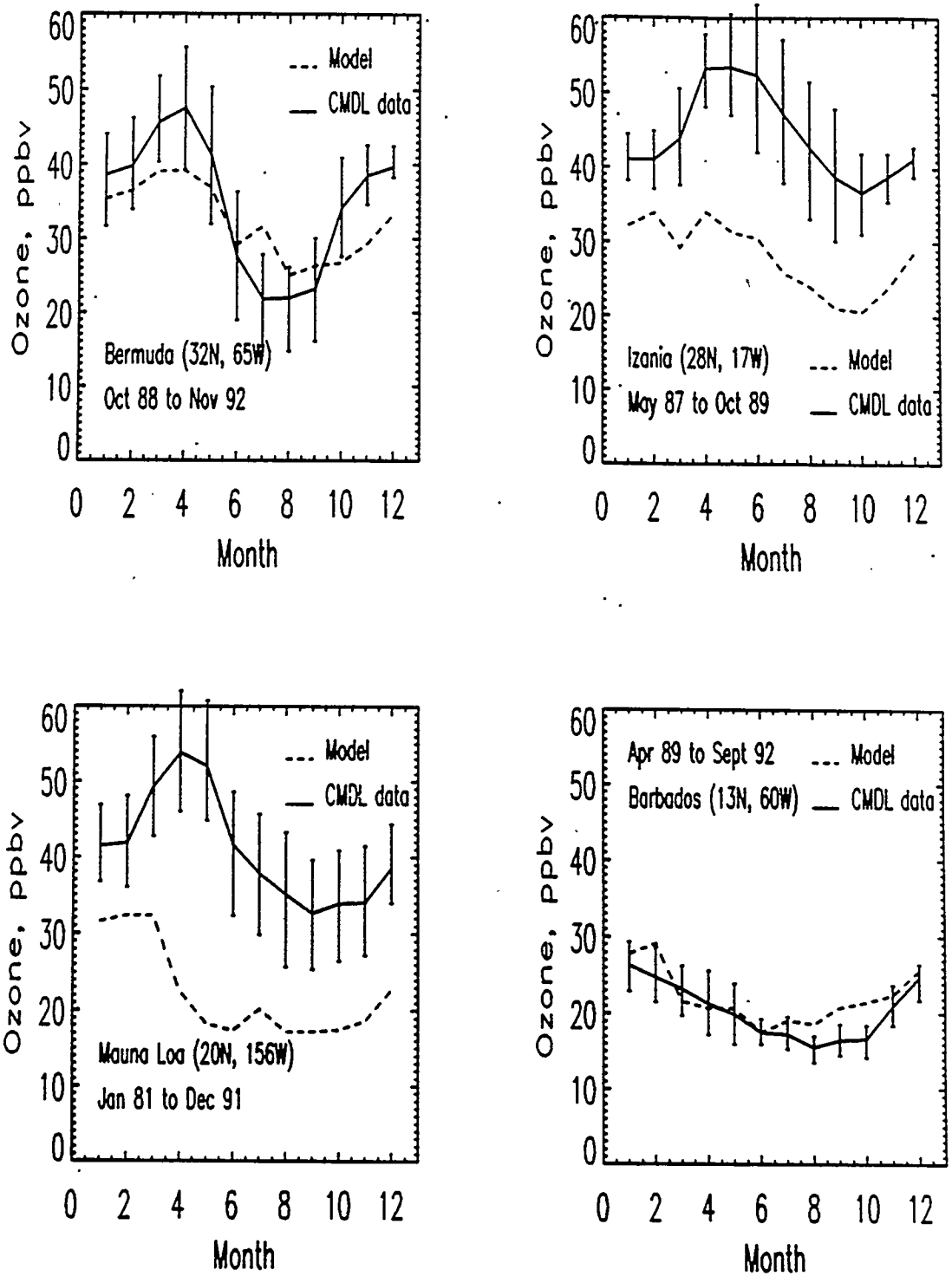

Figure 10.1 Observed mean and 25-75% O_3 and predicted O_3 concentrations (surface) at (e) Bermuda, (f) Izania, (g) Mauna Loa, and (h) Barbados. Observations are from the NOAA Climate Monitoring and Diagnostics Laboratory (S. Oltmans, private communication, 1993 and Oltmans and Levy, 1993).

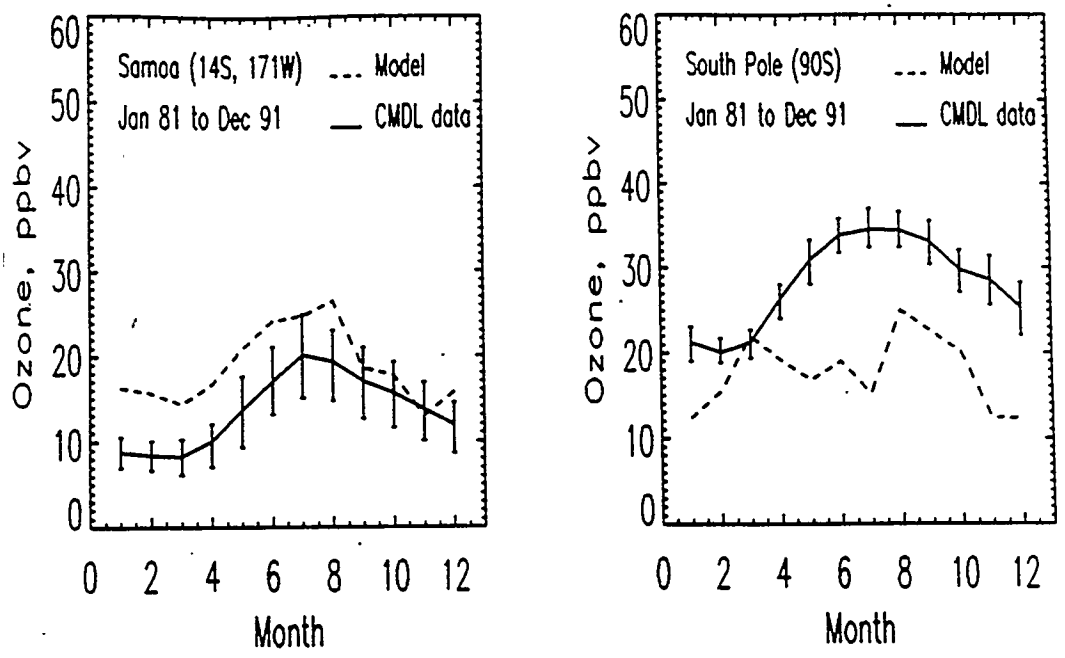

Figure 10.1 Observed mean and 25-75% O_3 and predicted O_3 concentrations (surface) at (i) Samoa and (j) South Pole. Observations are from the NOAA Climate Monitoring and Diagnostics Laboratory (S. Oltmans, personal communication, 1993 and Oltmans and Levy, 1993).

10.3.2 Comparison of model predicted and observed O_3 vertical profiles

Annual average vertical O_3 profiles predicted by the all NO_x scenario are compared to measurements at nine different sites in Figure 10.2. Ozone partial pressures as a function of altitude were collected using ozonesondes at Resolute (74N, 95W), Barrow (71N, 157W), Edmonton (53N, 114W), Boulder (40N, 105W), Hilo (19N, 155W), Samoa (14S, 170W), Lauder (45S, 170E), Syowa (69S, 39E), and the South Pole (90S, 25W) during 1985 - 1987 (Komhyr et al., 1989). Both seasonal and annual average profiles are presented in Komhyr et al. (1989), however, only the annual averages are discussed here. Recall that above sigma = 0.2, the model O_3 levels are specified based on 2D model results (see section 10.2).

For every site but Edmonton, the model predicted O_3 is too large in the free troposphere. However, the change in O_3 with altitude is simulated well at most locations. Although the O_3 levels specified in the model's stratosphere are adjusted to match actual ozonesonde measurements, at many sites the model still sets slightly higher ozone concentrations in the stratosphere than observed. Elevated transport from the stratosphere to the troposphere may produce the high model free troposphere values.

At Edmonton the model and observed values actually cross in the troposphere. At this site, the stratospheric specified O_3 levels much more closely approximate actual ozonesonde measurements than the other sites mentioned above.

It should be noted that after the model simulations were completed, an error in the published CMDL observations was noted for Lauder, Syowa, and the South Pole (Komhyr et al., 1992). This resulted in GRANTOUR using too high values in the stratosphere at these sites. However, the actual corrected data is plotted in Figure 10.2. Thus, it is expected that GRANTOUR values will be lower that the corrected observations of Komhyr et al. (1992).

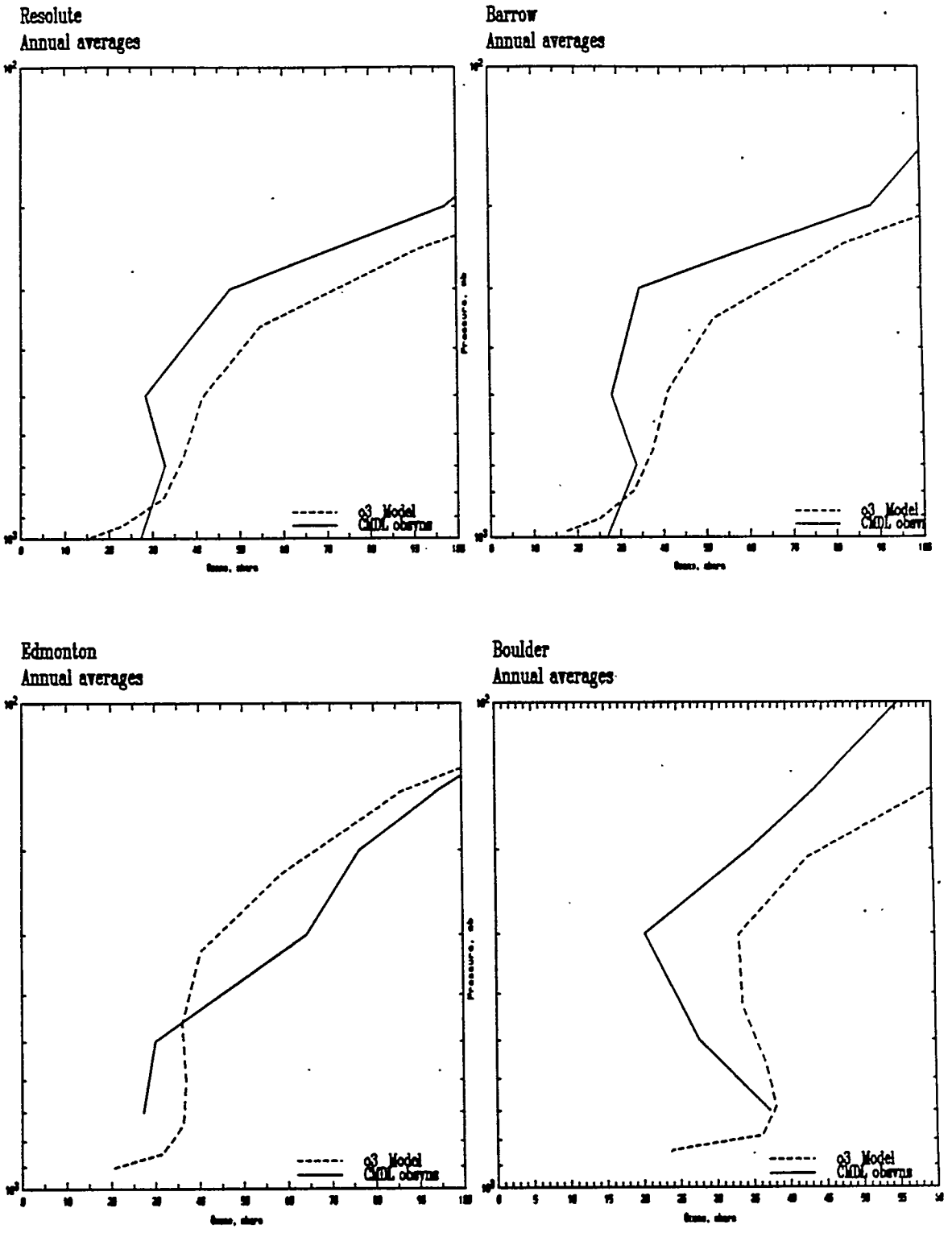

Figure 10.2 Observed and calculated annual average tropospheric ozone partial pressures in nbars as a function of altitude at (a) Resolute (74N, 95W), (b) Barrow (71N, 157W), (c) Edmonton (53N, 114W), and (d) Boulder (40N, 105W) (Komhyr et al., 1992).

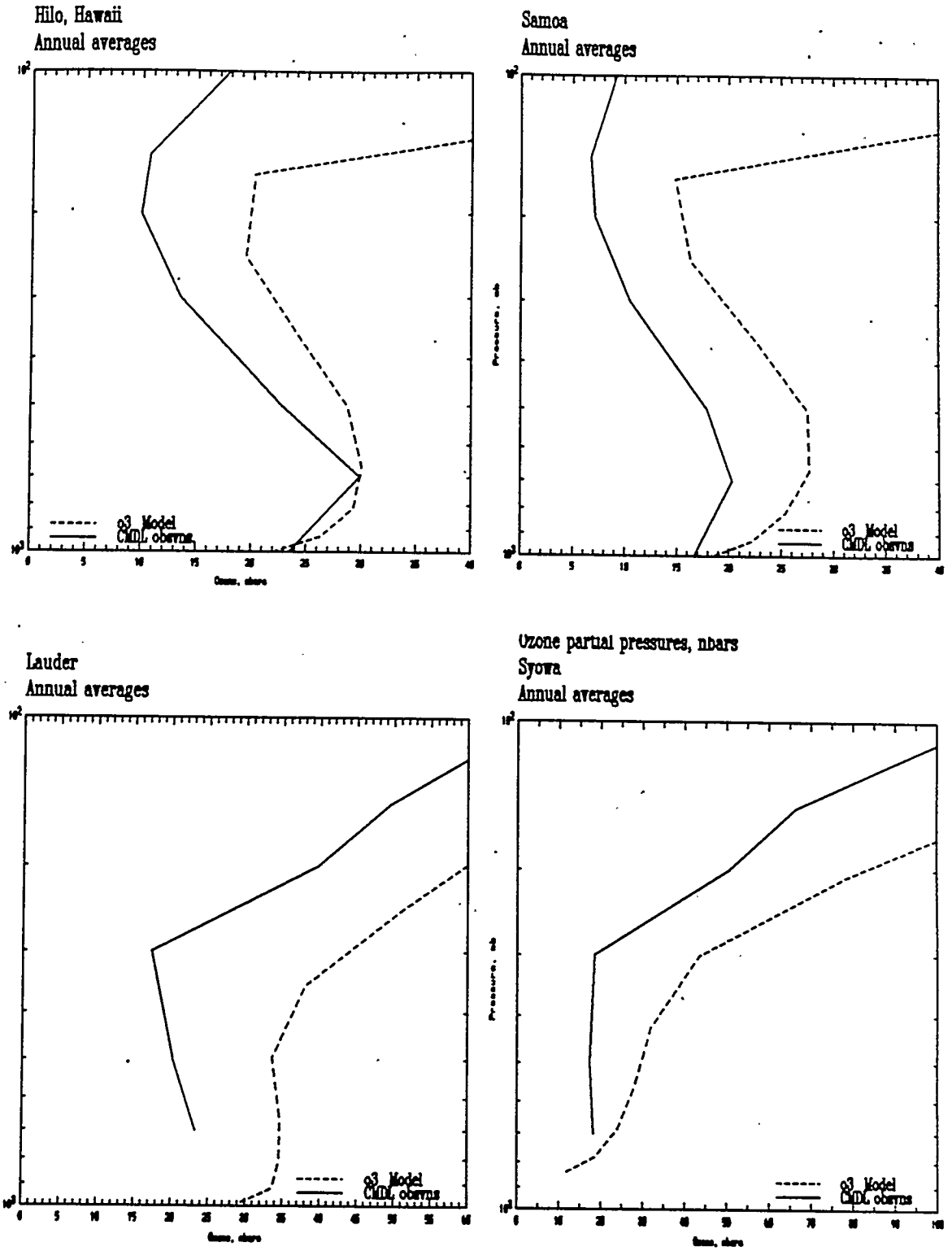

Figure 10.2 Observed and calculated annual average tropospheric ozone partial pressures in nbars as a function of altitude at
(e) Hilo (19N, 155W), (f) Samoa (14S, 170W), (g) Lauder (45S, 170E), and
(h) Syowa (69S, 39E) (Komhyr et al., 1992)

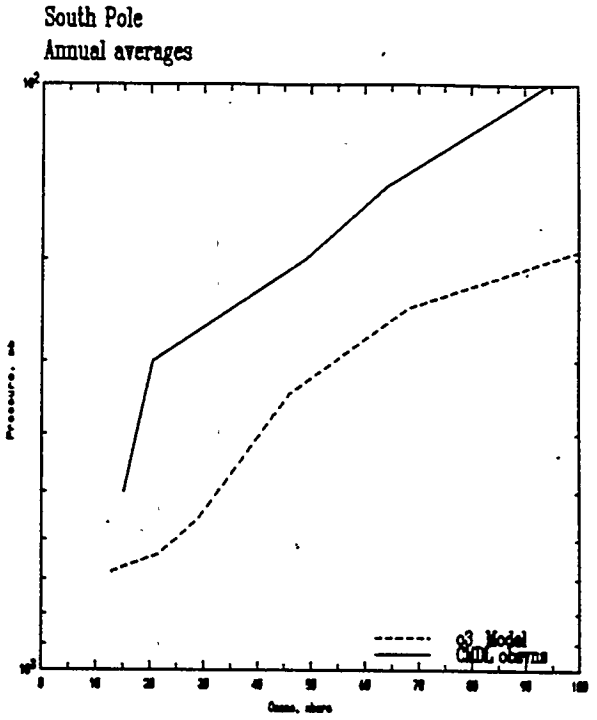

Figure 10.2 Observed and calculated annual average tropospheric ozone partial pressures in nbars as a function of altitude at (i) South Pole (90S) (Komhyr et al., 1992)

10.3.3 The role of anthropogenic NO_x on predicted present day O_3

Comparing the all NO_x and natural NO_x seasonal scenarios illustrates the effect of anthropogenic NO_x on present day tropospheric species. Figure 10.3a shows surface O_3 concentrations for the all NO_x scenario, and Figure 10.3b shows the difference in surface O_3 between the all NO_x and natural NO_x scenarios (All NO_x - Natural NO_x scenarios). Increases in O_3 can be seen over most continental areas in January. For example, the O_3 concentrations increase between 2 - 10 ppbv over North America and 2 - 5 ppbv over Europe and Asia, mainly due to fossil fuel combustion. Increases in O_3 in the southern hemisphere are mainly due to biomass burning. Over Africa, O_3 increases from 2 - 30 ppbv, with a substantial portion of the continent seeing at least a 10 ppbv increase. Over South

America, an increase of 2 - 5 ppbv is seen. Ozone concentrations also increase over the oceans by roughly 2 - 5 ppbv. Thus, in January, surface O_3 increases globally by at least 2 ppbv almost everywhere, and up to 10 - 30 ppbv over heavy NO_x source regions.

Figure 10.4a shows surface O_3 for the all NO_x scenario, and 10.4b shows again the net increase in O_3 when anthropogenic NO_x is added. Substantial increases are seen over much of the globe, with the net increase generally being higher in July than in January for continental northern hemisphere locations and South America. Over the U.S., increases of at least 10 ppbv are seen everywhere, with some locations experiencing increases of 20 ppbv. Similarly, Europe shows increases of at least 10 ppbv, and as much as 30 ppbv. Eastern Asia also sees O_3 increases of 10 ppbv. In the southern hemisphere, O_3 increases are generally 2 - 10 ppbv. Over the oceans in July, the O_3 increases by less than 2 ppbv, which is lower than in January.

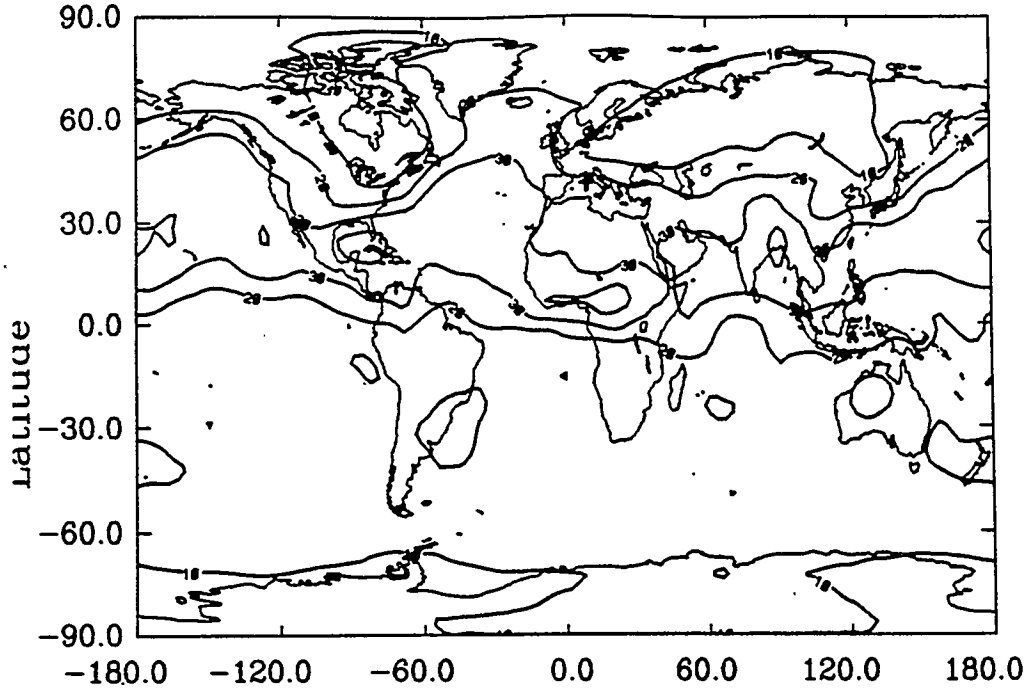

Figure 10.3(a) Calculated ozone surface concentrations in January for the All NO_x source scenario. Contour units are 10, 20, 30, 40, and 50 ppbv.

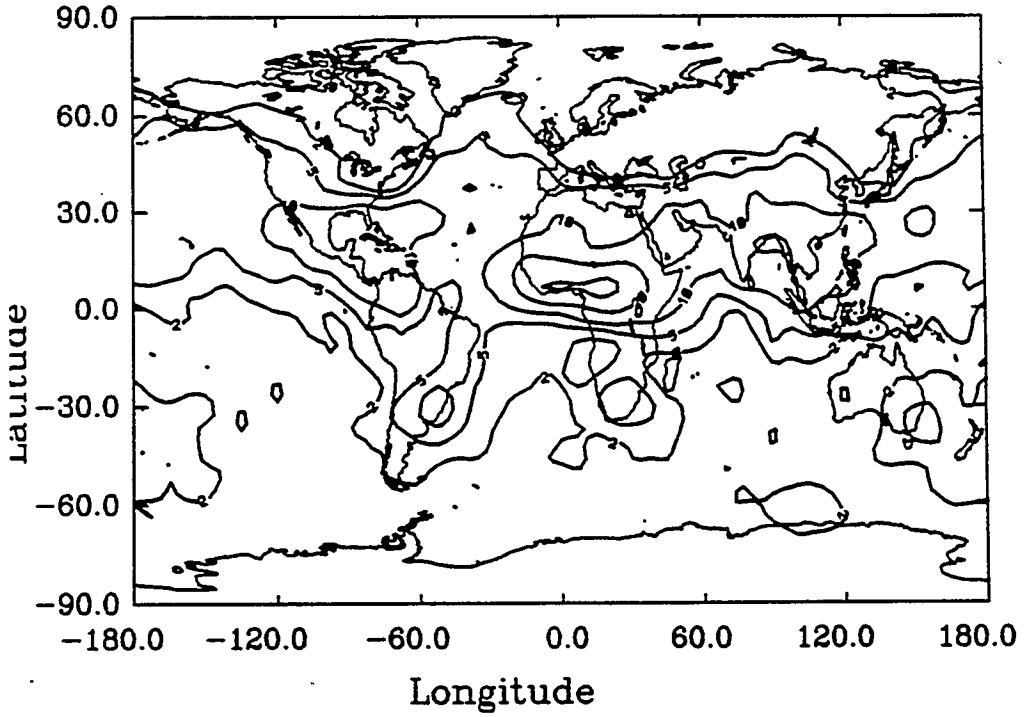

Figure 10.3(b) The increase in surface ozone predicted for January when anthropogenic NO_x sources are included (All NO_x scenario - Natural NO_x scenario). Contours are 2, 5, 10, 20, 30, and 40 ppbv.

10.4 Predicted OH fields

Predicted surface OH concentration fields are shown in Figure 10.5 for January for both the all NO_x and natural NO_x scenarios. For both months, anthropogenic NO_x tends to increase the surface OH concentrations. The effect is seen most strongly near the source regions. For example, in January, large increases are seen over South America, and equatorial and southern Africa. In these locations, the OH concentration increases from 2 x 10^6 cm^{-3} to 4 - 7 x 10^6 cm^{-3}. Smaller increases are also seen over North America and southern Europe.

July OH concentrations for the all NO_x and natural NO_x scenarios are shown in Figure 10.6. In July, substantial increases in the OH fields are seen in most continental regions, as well as over much of the oceans, too. In July, the global average tropospheric OH concentration increases from 1.7 x 10^6 to 1.9 x 10^6 cm^{-3} in the northern hemisphere and from 8.0 x 10^5 to 8.7 x 10^5 cm^{-3} in the southern hemisphere when anthropogenic NO_x is included.

The results of the seasonal predictor-corrector simulations are that anthropogenic NO_x increases both surface O_3 and OH levels, often significantly.

10.5 Predicted HNO_3 wet deposition

Penner et al. (1991) presented (Figure 22.c) HNO_3 wet deposition data for both January and July over North America. Figure 10.7 presents the seasonal all NO_x model results for January and July. Here, the North American results only are discussed. The all NO_x source scenario predicts January wet deposition of nitrate to be 5 - 20 kg N/km^2, whereas the data show levels of 5 - 25 kg N/km^2, indicating the model levels may be slightly low over the northeastern U.S. In July, the location of the 10 and 20 kg N/km^2 model contours are very similar to that of the data. However, the model predicts a very small peak of 50 kg N/km^2, which is not seen in the data (broad peak of 30 kg N/km^2).

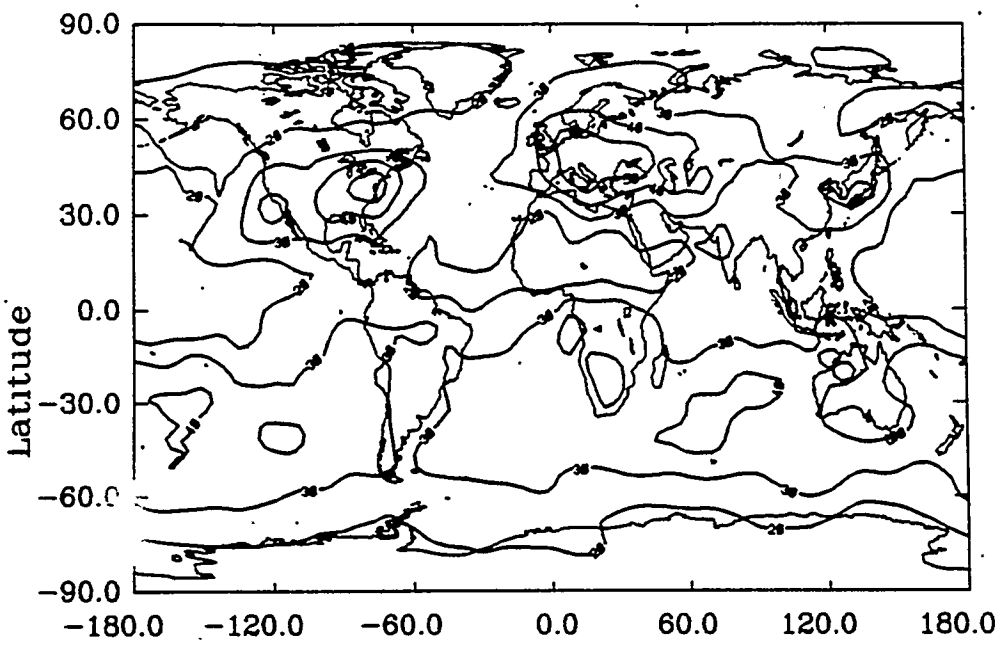

Figure 10.4(a) Calculated ozone surface concentrations in July for the All NO_x source scenario. Contour units are 10, 20, 30, 40, 50, and 60 ppbv.

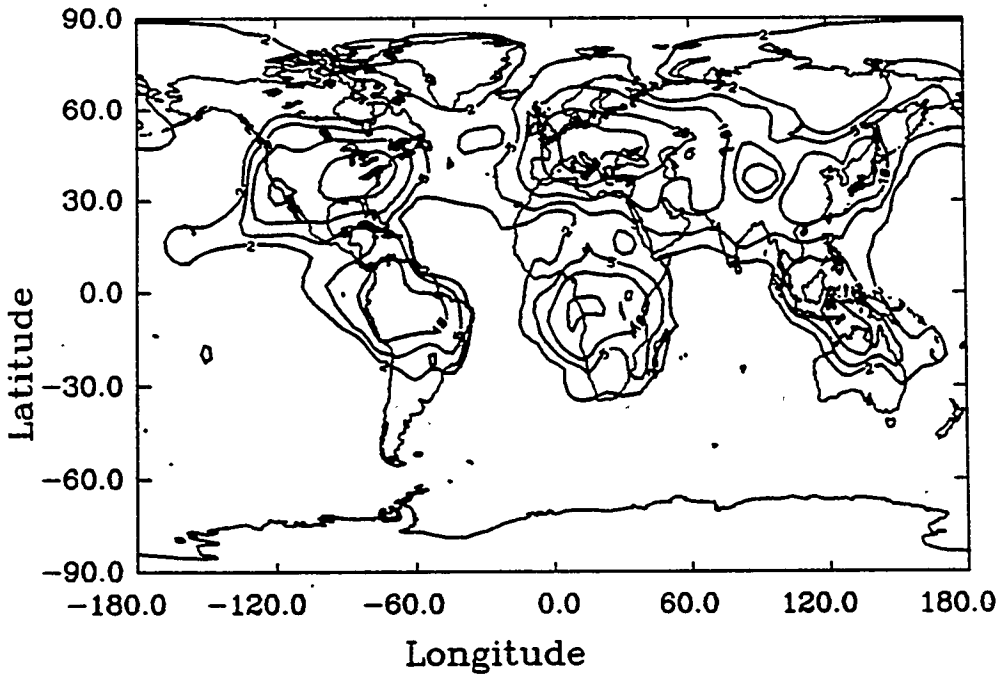

Figure 10.4(b) The increase in surface ozone predicted for July when anthropogenic NO_x sources are included (All NO_x scenario - Natural NO_x scenario). Contours are 2, 5, 10, 20, 30, and 40 ppbv.

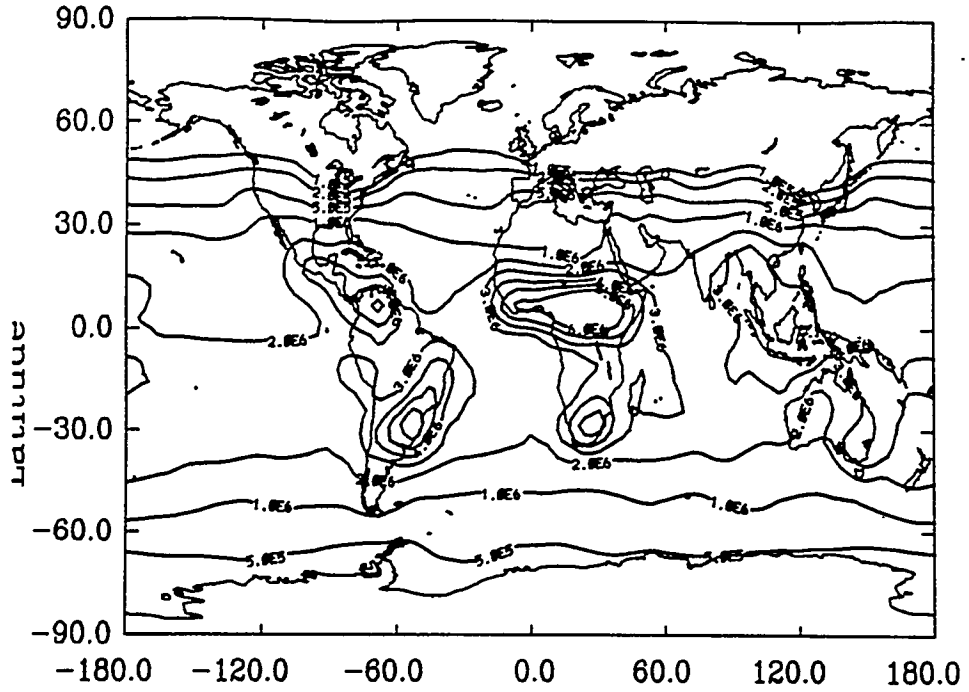

(a) All NO_x scenario

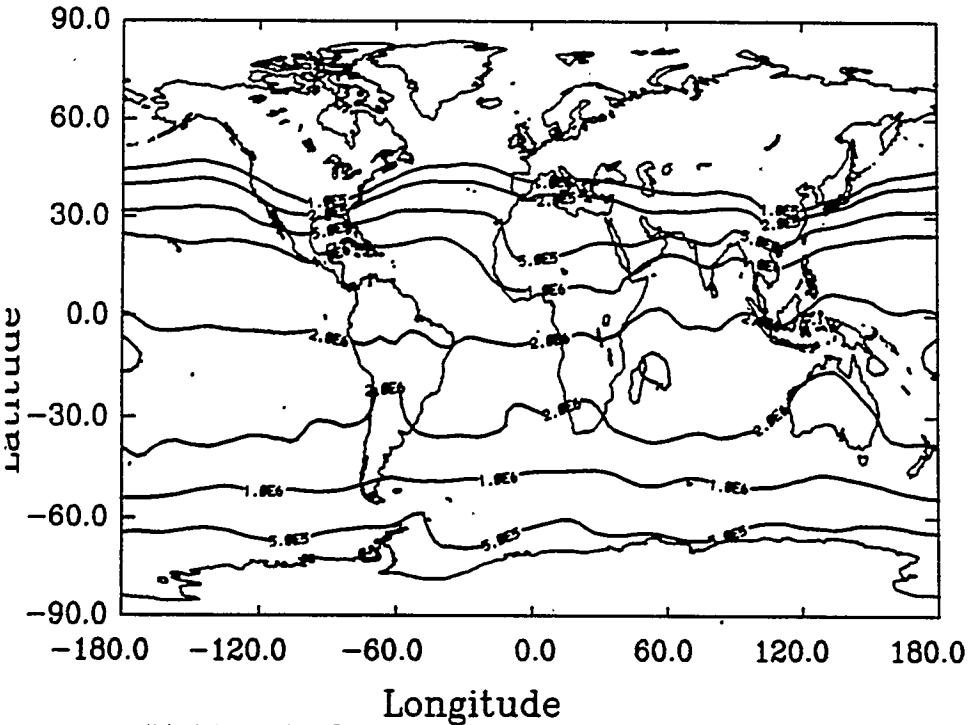

(b) Natural NO_x scenario

Figure 10.5 Calculated hydroxyl radical surface concentrations in January for the (a) All NO_x scenario and (b) Natural NO_x scenario. Contours are 1.e5, 2.e5, 5.e5, 1.e6, 2.e6, 3.e6, 4.e6, 5.e6, and 6.e6 cm^{-3}.

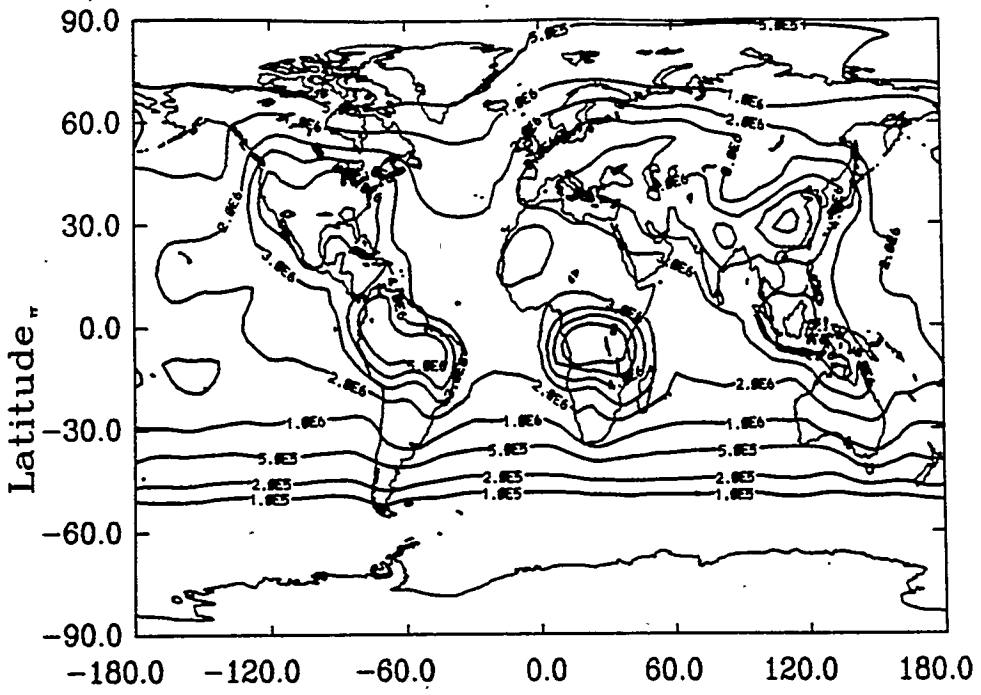

(a) All NO_x scenario

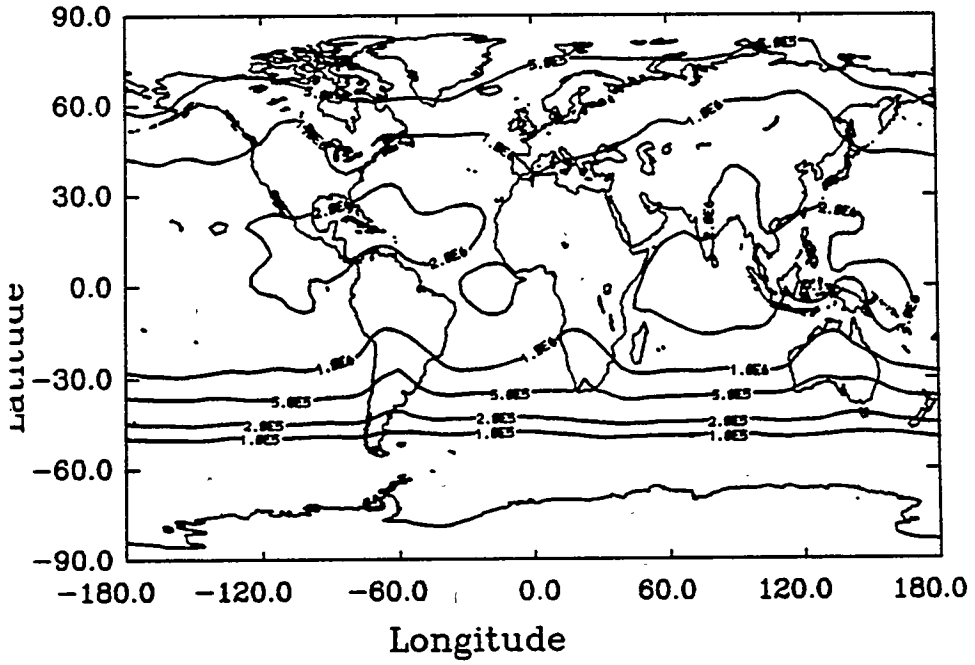

(b) Natural NO_x scenario

Figure 10.6 Calculated hydroxyl radical surface concentrations in July for the (a) All NO_x scenario and (b) Natural NO_x scenario. Contours are 1.e5, 2.e5, 5.e5, 1.e6, 2.e6, 3.e6, 4.e6, 5.e6, and 6.e6 cm^{-3}.

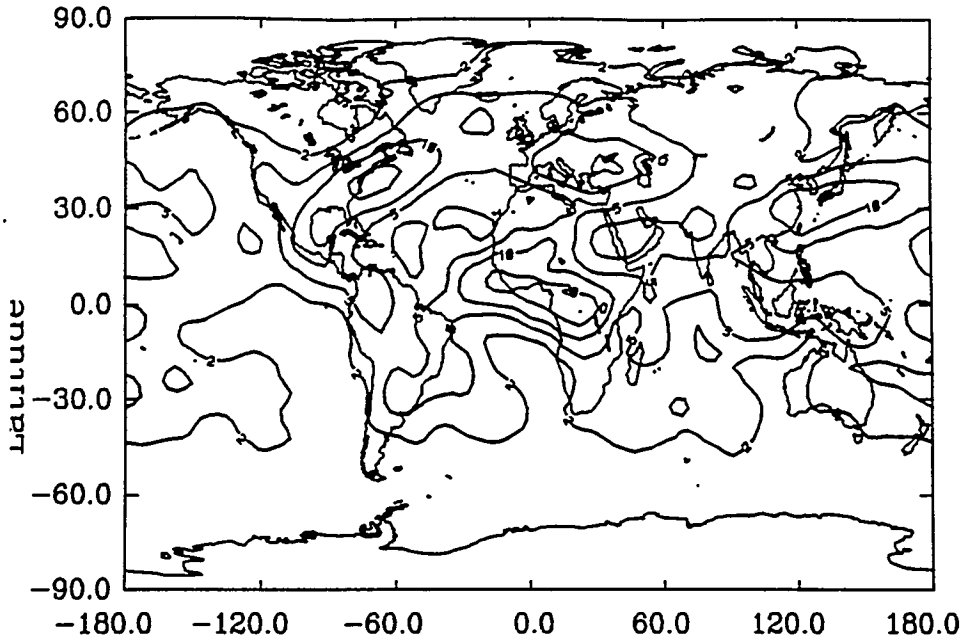

(a) January

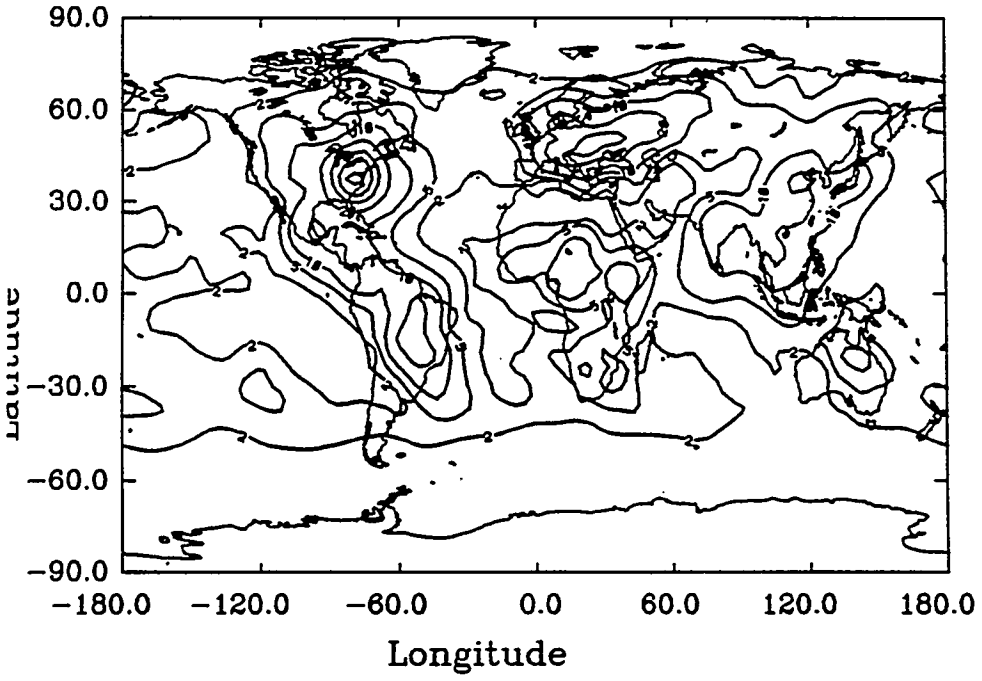

(b) July

Figure 10.7 Predicted wet nitrate deposition for the All NO_x source scenario for (a) January and (b) July. Contours are 2, 5, 10, 20, 30, 40, 50, and 60 kg N/km^2.

CHAPTER 11 RESULTS OF PERPETUAL JULY NON-METHANE HYDROCARBON (NMHC) GRANTOUR SIMULATIONS

11.1 Introduction

Three different perpetual July scenarios (see Table 11.1) were modeled using the non-methane hydrocarbon version of GRANTOUR. The first scenario considered only the "background" photochemistry of $CO/CH_4/NO_x/OH/O_3$. This was the same cycle that had been modeled using the predictor-corrector version of GRANTOUR. The second scenario also included the oxidation chemistry of two of the longer-lived alkanes, ethane and propane. These two alkanes are not highly reactive and, hence, would be expected to be transported in the global model and affect non-source regions. Ethane and propane both have anthropogenic and natural sources. However, for this scenario, only the sources due to industrial activity and biomass burning (the two largest sources) were considered. The third scenario included the $CO/CH_4/NO_x/OH/O_3$ chemistry, as well as the oxidation of isoprene, a highly reactive, naturally emitted hydrocarbon. Isoprene is very short-lived and may not be transported long distances, but is emitted in very large amounts globally, and is expected to significantly alter the oxidation capacity of the atmosphere.

Table 11.1: Non-methane hydrocarbon simulations

Scenario	"Hydrocarbons"
Background	CO, CH_4
Alkane	CO, CH_4, ethane, propane
Isoprene	CO, CH_4, isoprene

Table 11.2 lists the three different non-methane hydrocarbons considered, their reaction rate coefficients with OH and O_3 (isoprene only), the characteristic lifetimes of each with respect to OH and O_3 (for isoprene only), and their total global source strengths. The charcteristic lifetime for a species with respect to OH is defined as $\tau_{OH} = 1/\{k_{OH} \times$

[OH]}. The calculations are performed for conditions representative of the tropics (T=298K, [OH] = 2 x 10^6 cm^{-3}, [O_3] = 7.4 x 10^{11} cm^{-3} (= 30 ppbv)) and of the globe in general (T=275K, [OH] = 6 x 10^5 cm^{-3}, [O_3] = 7.4 x 10^{11} cm^{-3}). Table 11.2 shows that the alkane lifetimes are on the order of days to months, although their total source strengths are low compared to isoprene. Isoprene has an extremely short lifetime of minutes to hours, and although it may not be transported long distances, it will greatly affect tropospheric chemistry in the source region because it is emitted in such large quantities.

Table 11.2: Reaction rate coefficients, characteristic lifetimes, and annual source strengths of non-methane hydrocarbons in GRANTOUR

Species	k_{OH}, cm^3 $molecule^{-1}s^{-1}$	k_{O3}, cm^3 $molecule^{-1}s^{-1}$	τ_{OH}, tropics	τ_{O3}, tropics	τ_{OH}, global	τ_{O3}, global	Source, Tg/yr
ethane[a]	$8.7 \times 10^{-12} \times \exp(-1070/T)$	-----	24 days	---	107 days	---	8.0
propane[a]	$1.1 \times 10^{-11} \times \exp(-700/T)$	-----	5.3 days	---	22 days	---	6.0
isoprene[b]	$2.55 \times 10^{-11} \times \exp(410/T)$	$1.23 \times 10^{-14} \times \exp(-2013/T)$	80 mins	26 hours	4.2 hours	1.9 days	386

[a]From JPL, 1992; [b]From Paulson and Seinfeld (1992)

The non-methane hydrocarbons can react with O_3 and OH. However, the non-methane hydrocarbons also affect O_3 and OH indirectly through the formation of peroxyacetyl nitrate (PAN), an important reservoir species for NO_x. PAN is formed when the peroxy acetyl nitrate ($CH_3C(O)O_2$) reacts with NO_2:

$$CH_3C(O)O_2 + NO_2 \text{ -----> } CH_3C(O)O_2NO_2 \text{ (PAN).} \qquad (2.14)$$

The peroxyacetyl radical is formed when the acetyl radical $CH_3C(O)$ reacts with O_2. Since the acetyl radical contains two carbon atoms, it is formed by non-methane hydrocarbon oxidation (methane contains only one carbon atom).

The destruction of PAN occurs mainly through its thermal decomposition:

$$CH_3C(O)O_2NO_2 \text{ -----> } CH_3C(O)O_2 + NO_2. \quad (2.15)$$

The thermal decomposition is highly temperature dependent. The rate for PAN decomposition is (JPL, 1992):

$$k_{PAN} = 1.95 \times 10^{16} \times \exp(-13543/T). \quad (2.16)$$

Table 11.3 shows the characteristic lifetime for PAN for a range of tropospheric temperatures. PAN that is formed in or transported to the higher levels of the troposphere may exist for days to weeks and be transported to remote locations. Once in remote regions, if the temperature increases, PAN can decompose and release NO_2. Thus, PAN serves as a potentially large NO_x reservoir, and may significantly affect the chemistry of remote regions.

Table 11.3: Characteristic lifetimes of PAN as a function of temperature

Temperature, K	τ_{PAN}
298	47 mins.
290	2.7 hours
280	14 hours
270	3.6 days
260	25 days
250	200 days

11.2 Description of the three non-methane hydrocarbon scenarios

Three perpetual July scenarios were conducted. Each scenario was "spun-up" using 25,000 parcels and a 6 hour operator-splitting time step. Meteorological parameters were supplied from the CCM1, and were updated every 12 hours. The chemistry solution technique (Sillman, 1991) required a 30 minute time step, meaning it was called 12 times consecutively during the 6 hour model time step. Once the masses of O_3, NO, and NO_2 reached steady state in the troposphere and stratosphere, the simulation was then conducted

with 50,000 parcels. It typically took 4 - 6 months to reach steady state with 25,000 parcels. However, it should be noted that these simulations were initialized with a "settled" monthly average file from the predictor-corrector present day scenario. The simulation continued with 50,000 parcels (and still a 6 hour model time step and 12 hour meteorological update) until the masses of O_3, NO, and NO_2 reached steady state, typically 2 - 3 months. The model output for the month of July was then averaged and analyzed.

Although the numerical technique used in the non-methane hydrocarbon simulation is computationally fast, it does not include all of the chemical species and reactions which are important for the stratosphere. For this reason, the concentrations of important species were specified in the stratosphere. Once a parcel was transported above 200 mbar, its chemistry calculation was turned off, and the concentrations of important species were specified based on results from the LLNL 2D model (Wuebbles et al., 1987) for O_3 and PAN and 3D predictor-corrector model for other species.

PAN was specified above sigma = 0.2 based on concentrations from the LLNL 2D model. The O_3 concentrations were also specified by levels from the 2D model. However, two dimensional models spread NO_x concentrations over entire latitude bands, which tends to dilute the NO_x. Because O_3 production per unit NO_x consumed is much more efficient at lower NO_x values (Liu et al., 1987; Lin et al., 1988), two dimensional models may predict higher O_3 concentrations than observed or predicted by three dimensional models (Kanakidou and Crutzen, 1993). Thus, when the LLNL 2D model O_3 concentrations greatly exceeded actual ozonesonde observations made at nine CMDL O_3 monitoring sites (Komhyr et al., 1989), the 2D model fields were scaled to the observations.

Similarly, the concentrations of 13 other species, which were simulated in the predictor-corrector version of GRANTOUR were also specified above sigma = 0.2. These species included NO, NO_2, OH, HO_2 , H_2O_2, HNO_3, NO_3, N_2O_5, HNO_4, CH_3O_2, HCHO, CH_3OOH, and HONO.

11.3 Predicted ozone (O_3) fields

One prognostic species of particular importance in the model is O_3, a greenhouse gas and tropospheric pollutant. This section compares the model predictions with observations to understand how well this species is simulated. Then, the three scenarios (background, alkane, and isoprene) are compared with each other to understand how the role of these chemicals on global O_3.

11.3.1.1 Comparison of model predicted and observed surface O_3

Figure 11.1 shows the predicted O_3 concentrations at the surface for the three scenarios. There are only very subtle differences in O_3 predicted for the background and alkane scenarios. However, the isoprene scenario results in O_3 increases of 5 - 20 ppbv O_3 over continental areas. The isoprene does not appear to dramatically increase O_3 away from isoprene source regions (e.g. remote marine concentrations increase on the order of 2 ppbv). These will be discussed in more detail later.

Typical **summertime daily maximum** O_3 observations are 20 - 40 ppbv in remote marine and tropical forest environments, 50 - 120 ppbv in rural environments, and 100 - 400 ppbv in urban-suburban environments (National Research Council, Washington, D.C., 1991). The GRANTOUR predicted values are expected to be, in general, lower than these observations. The observations are daily maximum, and GRANTOUR predicts diurnally averaged concentrations (concentrations averaged over an entire day). Because O_3 concentrations peak during sunlight hours, and then decrease after sundown, the GRANTOUR values can be expected to be between 50 - 100% of the daily maximums. Also, the GRANTOUR scenarios include only alkanes or isoprene as the non-methane hydrocarbons. Future scenarios, which will include more NMHCs should produce higher O_3 levels.

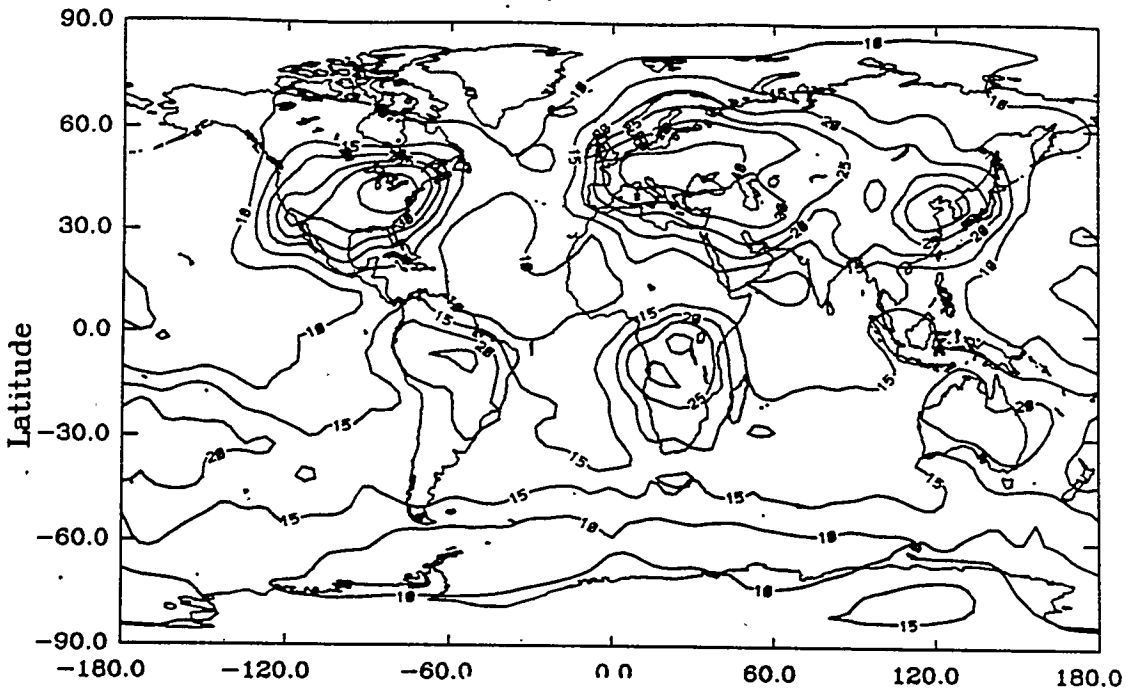

(a) Background scenario

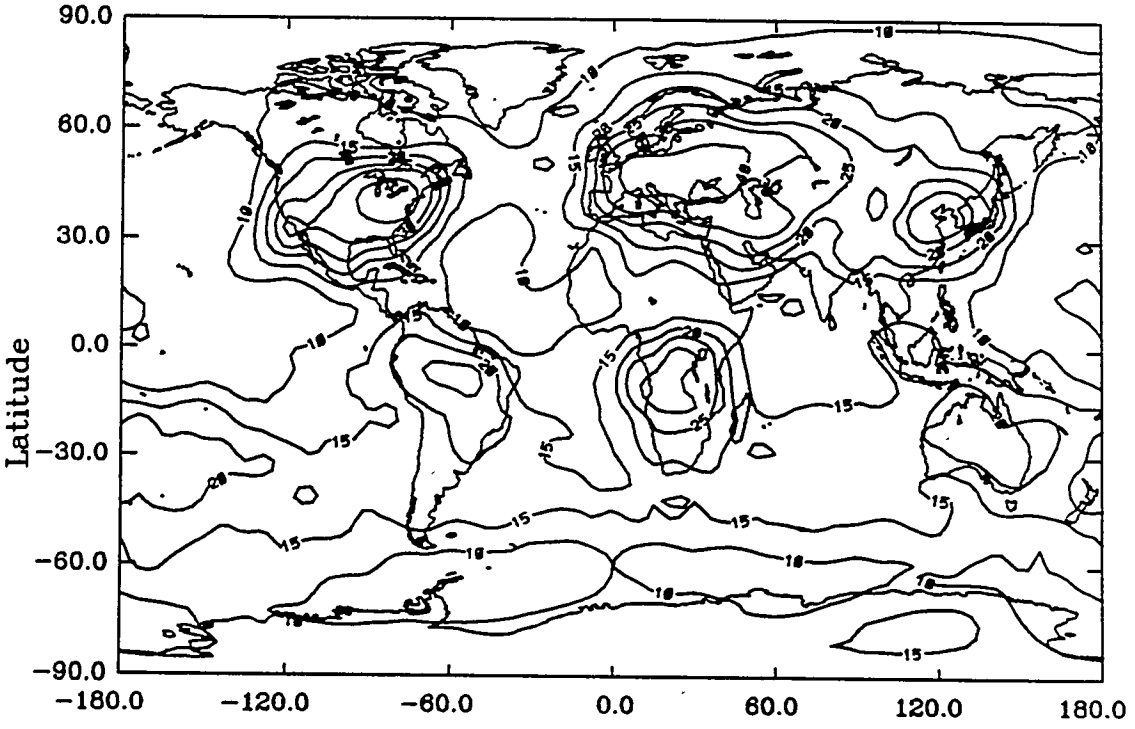

(b) Alkane scenario

Figure 11.1 Surface ozone concentrations for the (a) background, (b) alkane, and (c) isoprene scenarios. Contours are 5, 10, 15, 20, 25, 30, 40, 50, 60, and 70 ppbv.

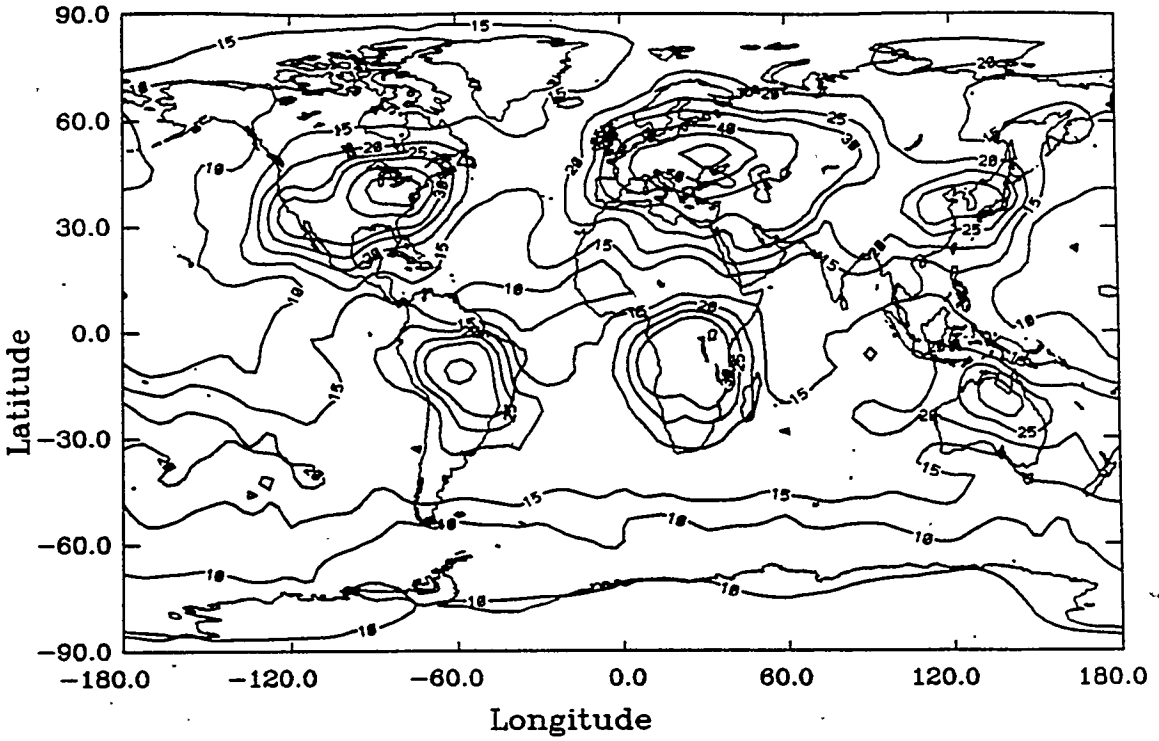

Figure 11.1 (c) Surface ozone for the isoprene scenario. Contours are 5, 10, 15, 20, 25, 30, 40, 50, 60, and 70 ppbv.

The highest O_3 levels are predicted for the isoprene scenario (Figure 11.1c). In this simulation, remote marine O_3 levels are 10 - 20 ppbv, which are about half of the observed range of 20 - 40 ppbv daily maximum. The continental regions are predicted to have O_3 concentrations greater than 15 ppbv. Over the southern hemisphere continents, concentrations range from 15 ppbv to 30 - 40 ppbv, which is similar to diurnally averaged levels expected in rural environments (which have daytime peaks of 50 - 140 ppbv). The more highly industrialized nothern hemisphere continents see peaks of 50 ppbv (North America), 60 ppbv (Europe), and 30 ppbv (Eastern Asia). Again, given that GRANTOUR results are diurnal averages, they are within 50 - 100% of the range expected for rural to urban areas (50 - 400 ppbv) .

Model results may be compared directly to surface O_3 observations made by the

NOAA Climate Monitoring and Diagnostics Laboratory (Oltmans, personal communication, 1993; Oltmans and Levy, 1993). The CMDL sites are located away from local sources of pollution, and provide a reasonable data base for comparison to GRANTOUR. The CMDL observations are made every 20 seconds, and hourly and monthly averages calculated. Thus, they represent a monthly, diurnal average. Table 11.4 shows the observed and predicted surface O_3 concentrations for the ten CMDL sites.

Table 11.4: Model predicted and CMDL[a] observed surface O_3, ppbv, for July

Site	CMDL record	Ele-vation, m	CMDL, ppbv[a]	Back-ground Scenario, ppbv	Alkane Scenario, ppbv	Isoprene Scenario, ppbv
Barrow (71N, 157W)	1/81 - 12/91	11	22.0	8.0	8.3	9.6
Reykjavik (64N, 22E)	9/91 - 9/92	60	20.7	28.3	28.6	28.5
Mace Head (53N, 10W)	7/89 - 12/92	30	32.2	19.8	20.3	24.2
Niwot Ridge (40N, 106W)	7/90 - 12/92	3000	46.0	28.7	28.9	28.5
Bermuda (32N, 65W)	10/88 - 11/92	40	21.8	15.9	16.2	21.5
Izania (28N, 17W)	5/87 - 10/89	2360	47.2	12.2	12.6	18.9
Mauna Loa (20N, 156W)	1/81 - 12/91	3397	37.8	8.4	8.6	9.8
Barbados (13N, 60W)	4/89 - 9/92	45	17.3	9.3	9.5	10.5
Samoa (14S, 171W)	1/81 - 12/91	82	20.1	11.6	11.8	11.5
South Pole (90S, 102E)	1/81 - 12/91	2835	34.6	10.0	10.0	11.4

[a] Oltmans, personal communication, 1993.

For all sites, the ozone concentrations are either approximately equal for all three model scenarios, or the isoprene scenario results in the highest ozone concentration. For this reason, the focus will be on comparing the isoprene scenario with measurements. Except for the Reykjavik site, the model-predicted concentrations are less than observed: It is expected that when more non-methane hydrocarbons (e.g. alkenes, other alkanes) are included in GRANTOUR, the ozone concentrations will increase. Thus, the model predicted ozone concentrations should be lower than the observations.

Additionally, however, the O_3 dry deposition velocity was inadvertently set equal to 0.3 cm/s over both the land and the ocean. A more appropriate value for the oceanic deposition is 0.03 cm/s. This led to too much deposition and, therefore, depleted surface O_3 predictions over the oceans. Since many of the CMDL sites are remote marine sites, the GRANTOUR values are expected to be lower than the measurements there.

In several locations such as Mace Head, Bermuda, Barbados, and perhaps Samoa, the model predictions are less than the observations by less than 10 ppbv. Several other sites, however, show much larger discrepancies. The largest differences between the model and observations occurs at the Barrow, Niwot Ridge, Izania, Mauna Loa, and South Pole sites. The differences are between 12 - 27 ppbv. Except for Izania, these sites show little difference between the background, alkane, and isoprene scenario.

The general circulation model's performance is poorer at high latitudes, which may explain the discrepancies between the model and measurements at Barrow and the South Pole .Also, the fact that there is little difference between the three scenarios at the two high latitude sites (Barrow, South Pole) indicate that PAN is probably not contributing much to the regional NO_x budget. In fact, at the high latitude sites, model NO_x concentrations are on the order of 10 pptv or less (see Figure 11.12), indicating these regions may be ozone-destruction regions in the model. The model may require further hydrocarbons to produce enough PAN to act as a reservoir for NO_x at these latitudes. The model may either be inadequately transporting PAN and/or NO_x to these polar regions, as well.

Model predictions are lower than observations at Izania, Mauna Loa, and Niwot Ridge. It is possible that these regions experience local emissions (e.g. oceanic alkane emissions for Mauna Loa and Izania and terpenes for Niwot Ridge) that are not captured by the model. All three sites also have very high elevatrions (3000 m, 2360 m, and 3397 m for Niwot Ridge, Izania, and Mauna Loa, respectively). Measurements at these sites may be influenced by free tropospheric air, which would tend to have higher O_3 levels. However, due to its large grid size, GRANTOUR cannot resolve locally high topography and the model values shown are for much lower average elevation surfaces.

In summary, the model predicted surface O_3 concentrations are lower than observations. Once more alkanes, alkenes, and possibly other terpenes are included in the calculation, the model predicted O_3 concentrations are expected to increase at the surface. A bug in the dry deposition subroutine led to excessive O_3 deposition (and, therefore, lower surface O_3 measurements) over the ocean. Additionally, several observations sites have very high elevations, which should be affected by free tropospheric air (which has higher O_3 levels). Because GRANTOUR cannot resolve these locally high elevations, its predicted values will tend to be lower than observations.

11.3.1.2 Comparison of model predicted and observed O_3 profiles

In Figure 11.2, model predicted vertical O_3 profiles are compared with ozonesonde observations made during 1982 - 1987 at nine different stations (Komhyr et al., 1989). The ozonesonde measurements are actually an average for June, July, and August, while the GRANTOUR results are strictly for a perpetual July.

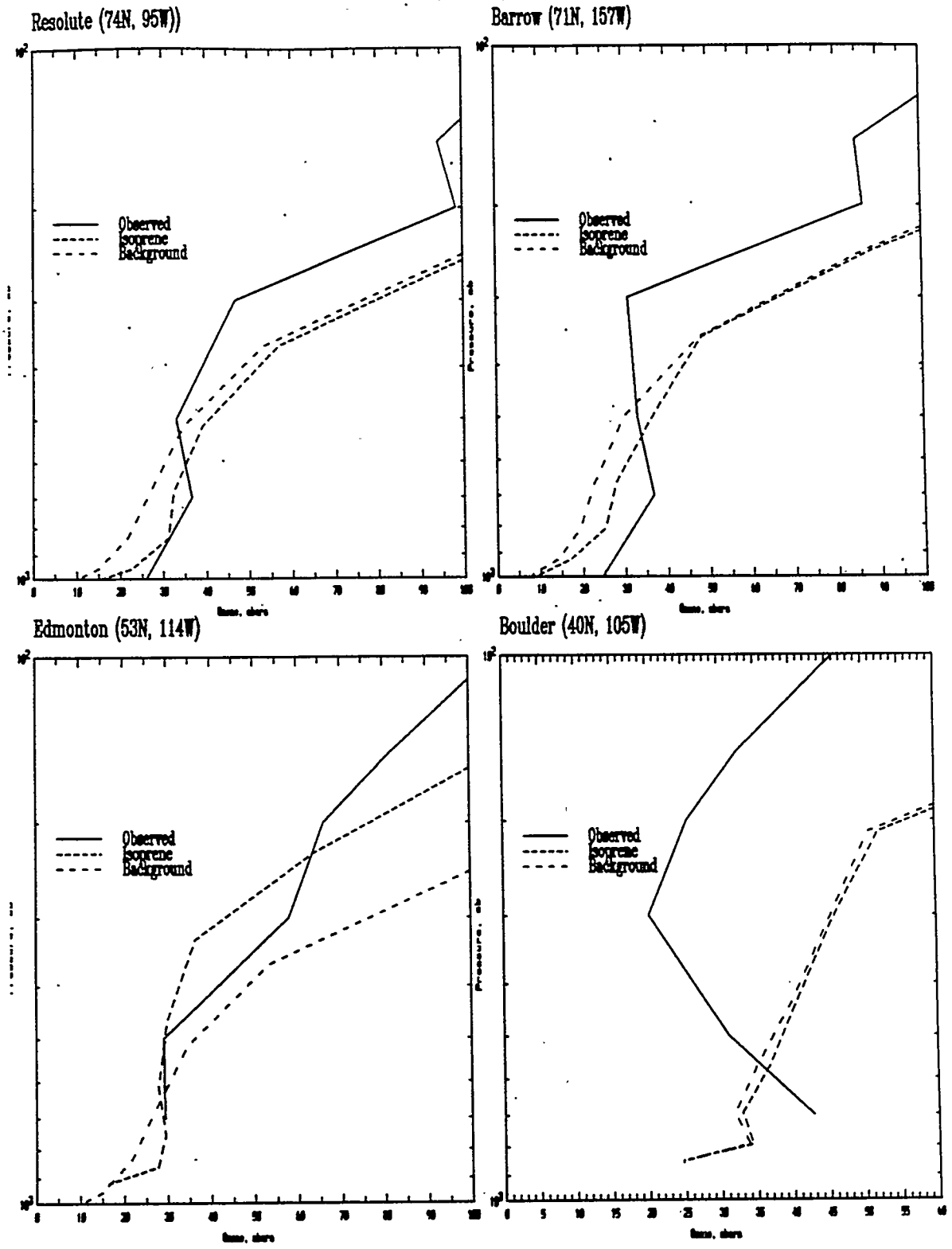

Figure 11.2 Observed and calculated tropospheric O_3 partial pressures (nanobars) as a function of altitude at (a) Resolute; (b) Barrow; (c) Edmonton; and (d) Boulder. Observations are from Komhyr et al. (1989).

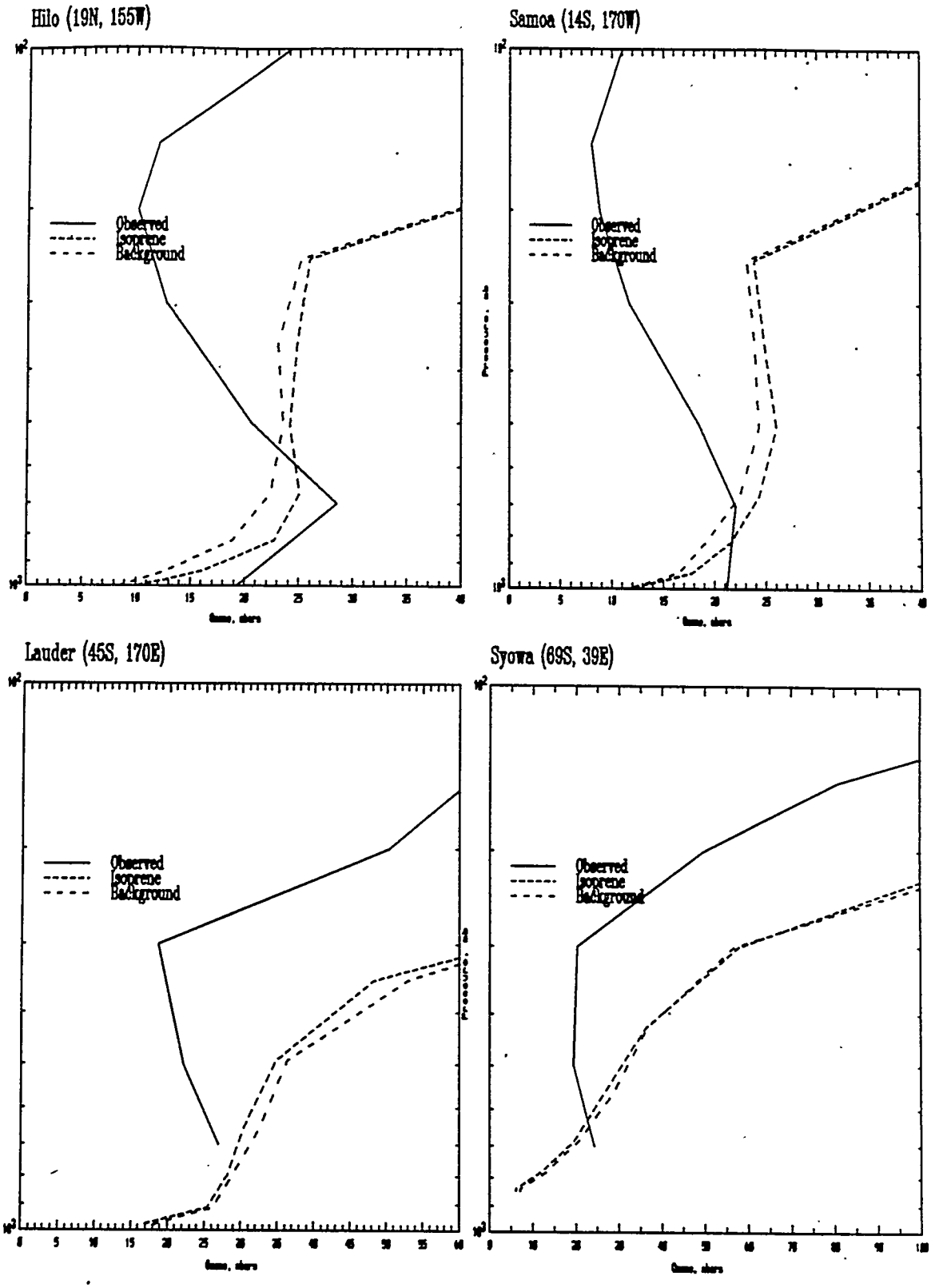

Figure 11.2 Observed and calculated tropospheric ozone partial pressures (nbars) as a function of altitude at (e) Hilo; (f) Samoa; (g) Lauder, and (h) Syowa.

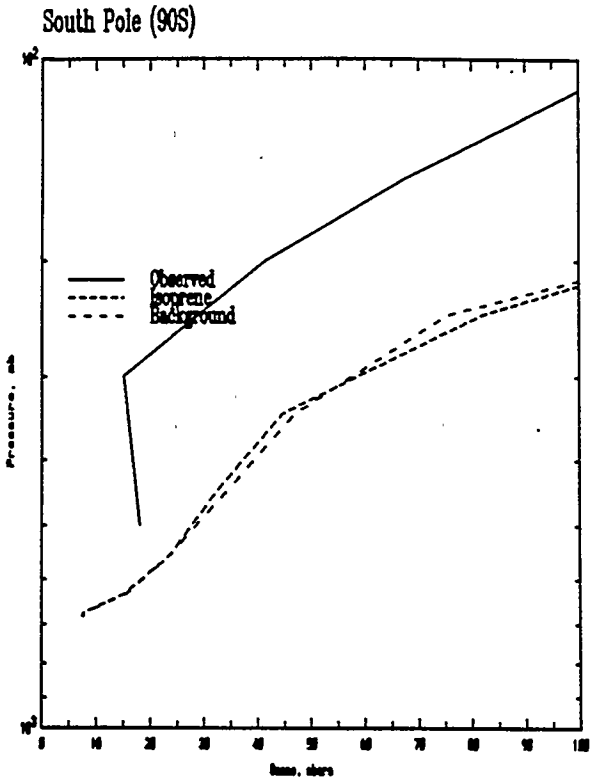

Figure 11.2 Observed and calculated tropospheric ozone partial pressures (nbars) as a function of altitude at the South Pole.

As can be seen in Figure 11.2, good agreement of the increase in O_3 with latitude and altitude is seen at the sites of Resolute, Barrow, Edmonton, Syowa, and the South Pole. At a number of sites, however, the model under-predicts surface concentrations, while it over-predicts concentrations in the free-troposphere.

The surface concentrations may be strongly affected by the choice of model deposition velocity, and also local meteorology. The dry deposition velocity for O_3 over the oceans was roughly a factor of 10 too high (0.3 cm/s instead of 0.03 cm/s) and resulted in excessive removal of surface layer O_3 over oceans. Because most of the CMDL sites are in remote marine locations, they were affected.

An error reported in the CMDL measurements (Komhyr et al., 1992) will affect the concentrations at Lauder, Syowa, and the South Pole. The error caused the stratospheric

concentrations at these locations to be specified at much higher levels than the actual data. Figure 11.2, however, plots the corrected CMDL profiles. The model is, therefore, expected to over-predict O_3 at these sites.

The model predicts especially high free tropospheric O_3 concentrations at the remote marine sites of Hilo and Samoa. As discussed in Section 10.3.2, the O_3 levels specified by the model in the stratosphere are higher than observations for Resolute, Barrow, Boulder, Hilo, Samoa, and Lauder. Elevated transport from the stratosphere to the troposphere may also produce the high model free troposphere values.

11.3.2 Comparison of O_3 from the three scenarios

The three model scenarios are now compared with each other to understand the role that alkanes and isoprene play in the predicted concentrations of O_3.

11.3.2.1 Model predicted zonal average O_3

Figure 11.3 presents the model predicted zonal average O_3 for the background, alkane, and isoprene scenarios, respectively. Comparing panels (a) and (b) show that introducing the alkanes into the model didn't appreciably affect the zonal average O_3 concentrations. This is because the alkanes only increased surface O_3 concentrations by 1 - 2 ppbv, an effect that is further diluted by averaging over a 360 degree latitude band. The zonal averages in Figure 11.3 (a) and (b) do show though, that the northern hemisphere tends to experience higher levels of O_3 at mid-latitudes from the surface up through 600 mbars than the southern hemisphere.

Comparing Figures 11.3(a) and 11.3(c) (background versus isoprene scenarios) shows that isoprene results in higher O_3 concentrations from the surface up through roughly 400 - 500 mbars. Physically overlaying the two figures shows that this effect is more prominent in the northern hemisphere. This is probably due to the fact that the land coverage is greater in the northern hemisphere and, since isoprene is a land-based source, the zonal average O_3 will be affected more in the northern hemisphere than the southern.

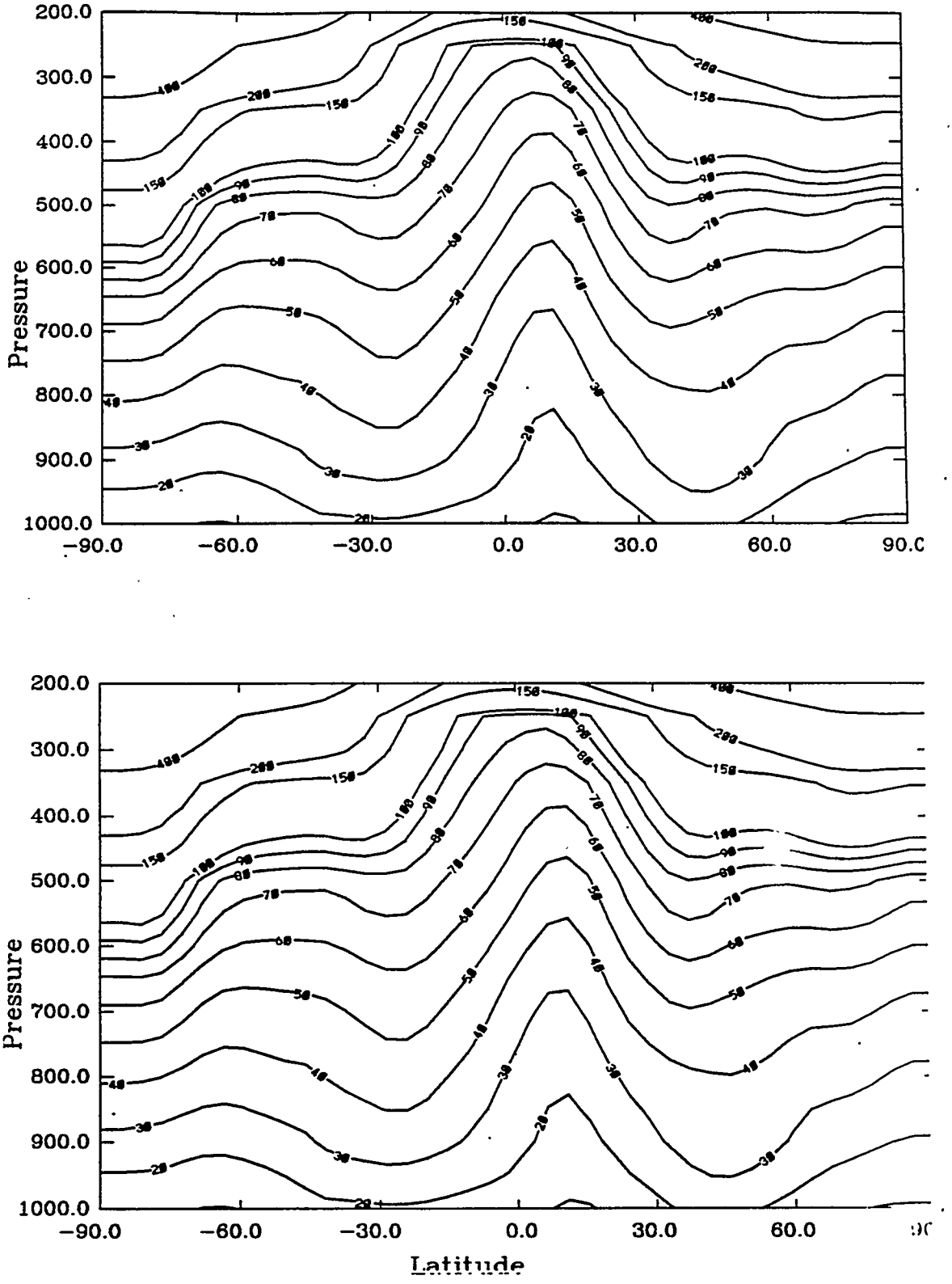

Figure 11.3 Zonal average concentrations of O_3 in ppbv for the (a) background. (b) alkane, and (c) isoprene scenarios.

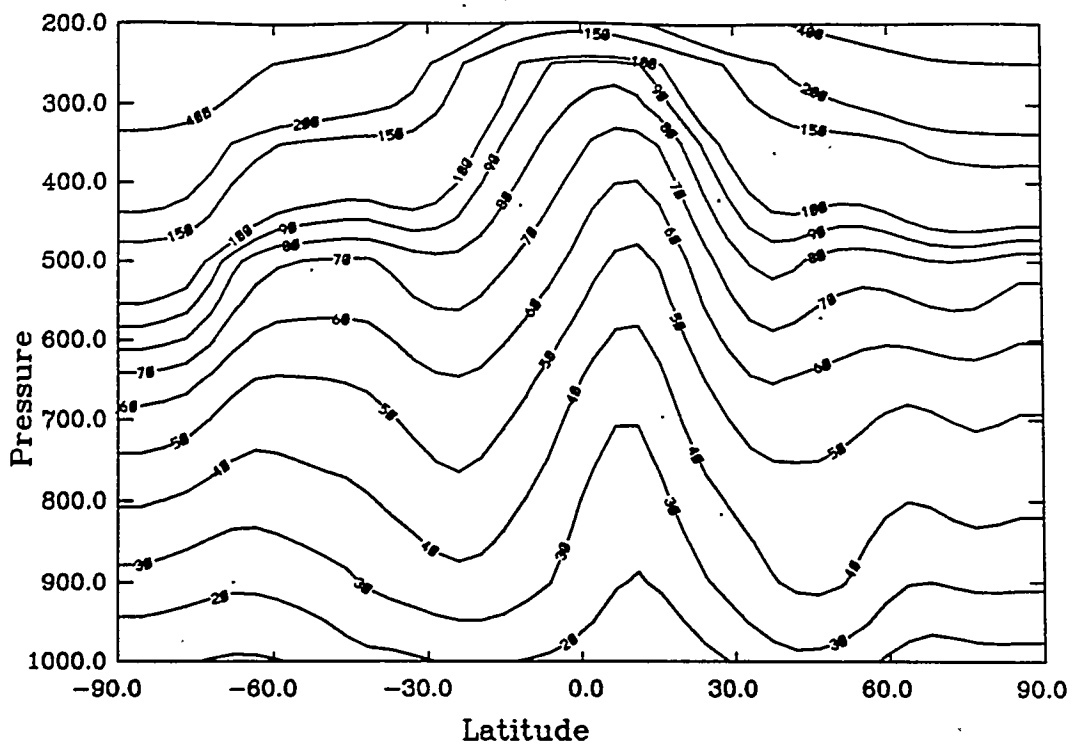

Figure 11.3(c) Zonal average concentrations of O_3 in ppbv for the isoprene scenario.

11.3.2.2 Model predicted latitudinal O_3 transects

Because the non-methane hydrocarbons are land-based sources, examining latitudinal transects that both pass over the continents and over remote marine environments illustrate how localized the effect of the hydrocarbons is. Figures 11.4, 11.5, and 11.6 present latitudinal transects for the three scenarios at 22E and 165W, for the surface, sigma = 0.811, and sigma = 0.500, respectively. The north-south transect through 22E passes through Africa and Europe, both of which have large alkane and isoprene sources. The north-south transect through 165W passes over the remote North and South Pacific Oceans, an area which does not have any alkane or isoprene sources in the model.

Figure 11.4(a) shows that at the surface and 22E, the alkane and background scenario predicted O_3 never differ by more than 1 - 3 ppbv, indicating that over this alkane source region, the O_3 is only slightly affected by the presence of alkanes. The addition of isoprene,

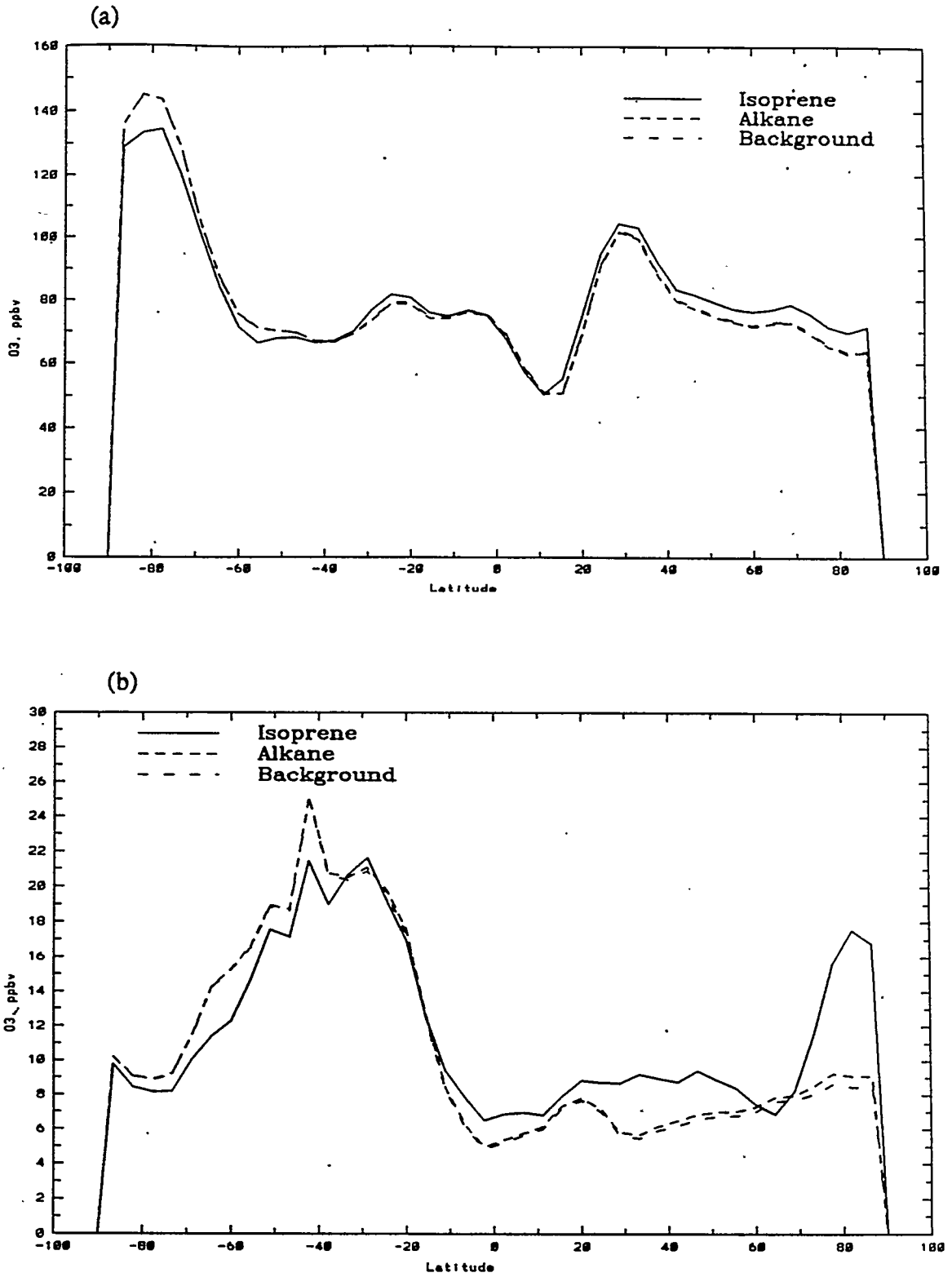

Figure 11.4 Latitudinal surface transects of O_3 in ppbv for (a) 22E and (b) 165W.

however, increases surface O_3 by roughly 8 ppbv over Africa, and up to 15 ppbv over Europe. This shows that the alkanes do not have a large localized effect, but the isoprene does.

Figure 11.4(b), however, shows that even over remote locations (165W), the alkanes still do not dramatically alter the predicted surface O_3 concentrations. The difference between the background and alkane scenarios is never more than 1 ppbv. The model may not contain a strong enough alkane source to appreciably affect O_3 concentrations. The isoprene scenario, however, results in O_3 increases of nearly 10 ppbv in the high northern latitudes. This effect can also be seen in the surface contours (Figure 11.1), which show the O_3 increasing from 10 to 20 ppbv near the northern coast of Europe in the isoprene scenario. Surface O_3 also increases over the nothern mid-latitudes by up to 5 ppbv for the isoprene scenario.

Interestingly enough, Figure 11.4(b) shows that the introduction of isoprene in the southern hemisphere can actually lead to lower O_3 concentrations at the surface (roughly 2 - 3 ppbv). This could possibly be due to the reaction of O_3 with isoprene itself. Or, the formation of PAN from the isoprene oxidation may lower the NO_x concentrations, resulting in lower O_3.

Figure 11.5 shows the latitudinal tracks at 22E and 165W for sigma = 0.811. As in the surface case, isoprene tends to result in higher O_3 concentrations in the northern hemisphere, and slightly lower O_3 concentrations in the southern hemisphere. The increases occur for both the remote transect at 165W and the "locally polluted" transect at 22E in the northern hemisphere. The O_3 increase over the isoprene source regions at 22E may be due directly to the oxidation of isoprene to form O_3. The O_3 increase over remote regions, however, may be due to the formation of PAN, which is transported to these regions, and then decomposes to form NOx, increasing O_3. Likewise, similar results can be seen at sigma = 0.5 (Figure 11.6).

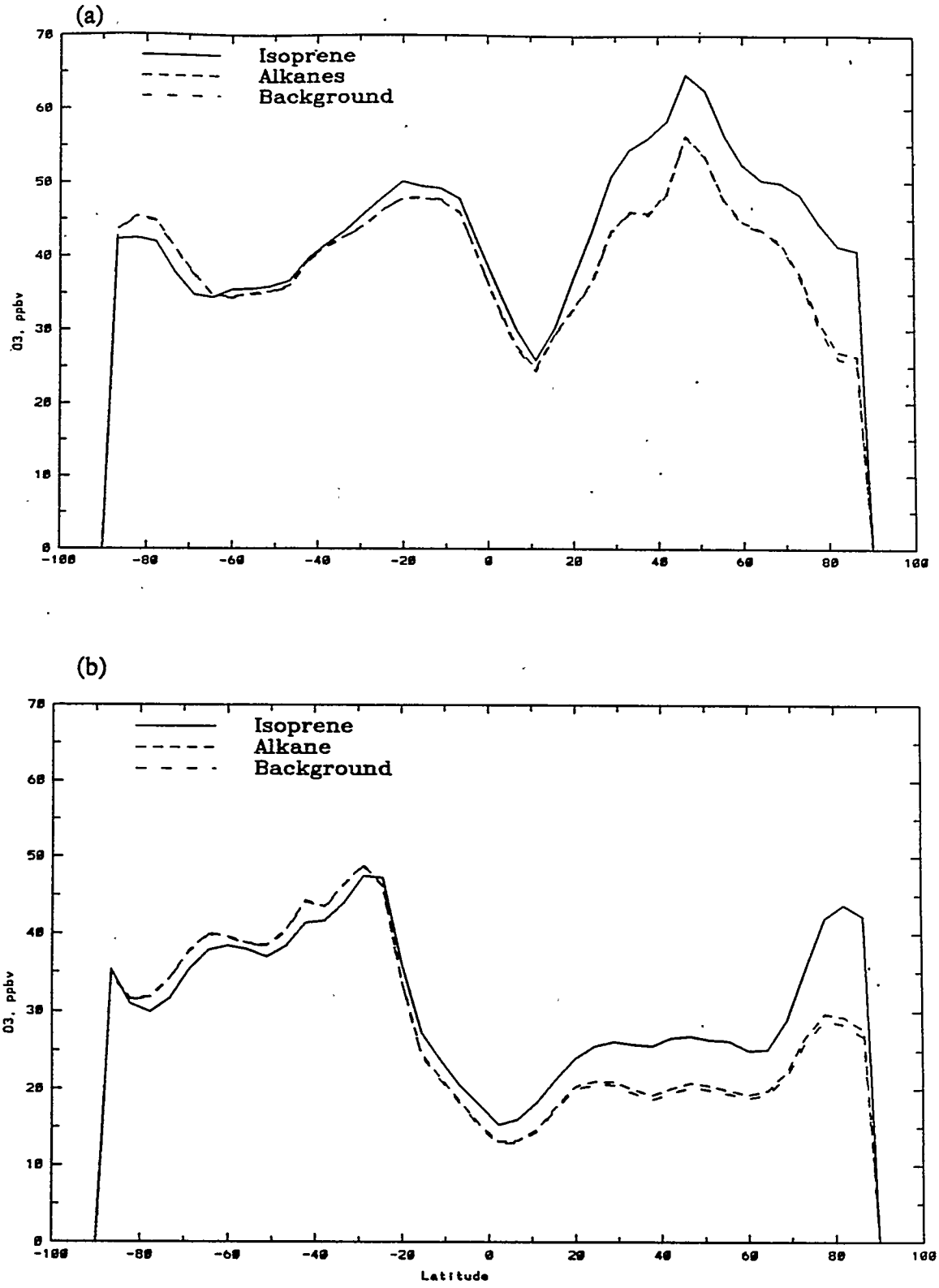

Figure 11.5 Latitudinal transects of O_3 in ppbv for sigma = 0.811 at (a) 22E and (b) 165W.

(a)

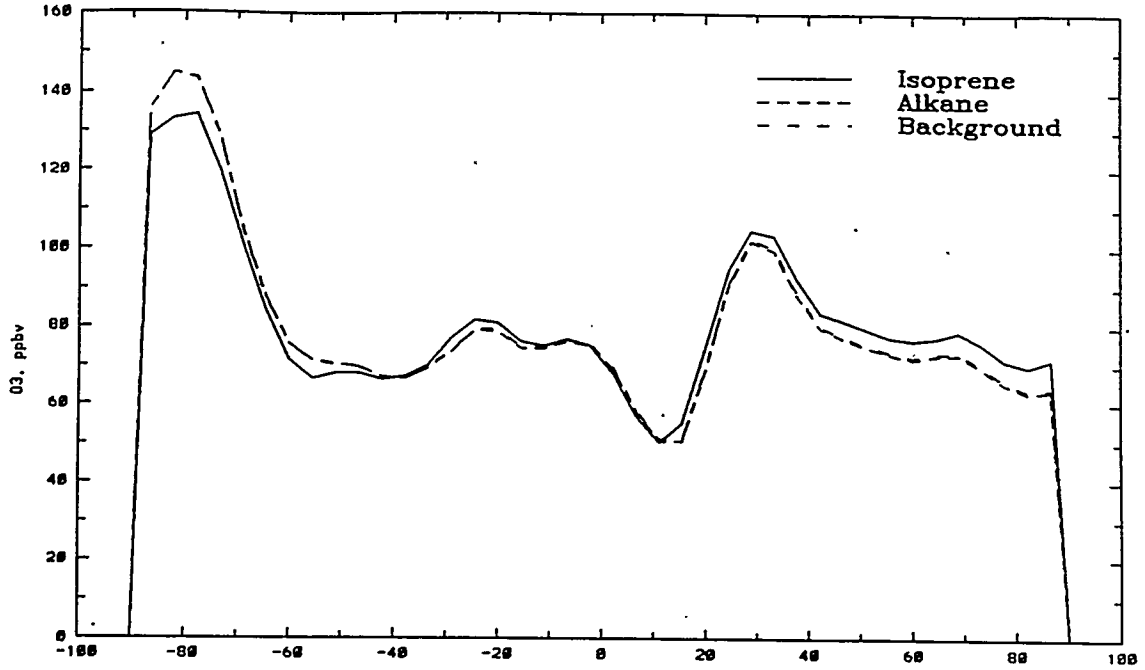

(b)

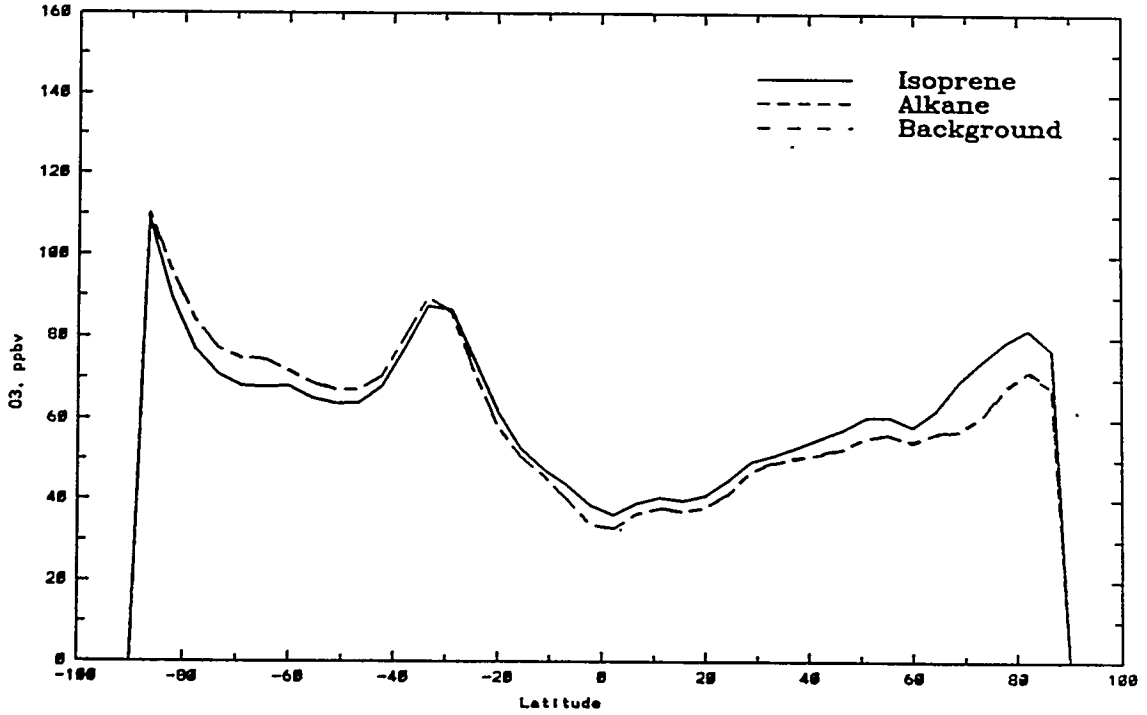

Figure 11.6 Latitudinal transects of O_3 in ppbv for sigma = 0.5 at (a) 22E and (b) 165W.

11.3.2.3 Differences in model predicted O_3 at the surface and sigma = 0.5

The addition of alkanes and isoprene are expected to affect the O_3 concentrations. Figure 11.7 shows the difference in surface O_3 predicted for the background and alkane scenario. Including ethane and propane in the scenario only resulted in increases in surface O_3 concentrations or no change in O_3 concentrations. In no grid box did the O_3 surface concentrations decrease when alkanes were added. As can be seen in Figure 11.7, only small increases in O_3 were seen when ethane and propane oxidation was added, typically less than 2 ppbv.

Figure 11.8 shows the changes in surface O_3 predicted when isoprene oxidation is added. Figure 11.8(a) shows the regions in which the surface O_3 concentrations **increased** upon adding isoprene chemistry, and Figure 11.8(b) shows the regions in which the surface O_3 **decreased** upon adding isoprene chemistry. In Figure 11.8(b) the O_3 decrease is basically small and contained to part to several regions. Over eastern Asia, O_3 decreases by roughly 4 ppbv. Over the northern part of South America, the O_3 decreases by only 2 ppbv. From 60S to 90S, O_3 decreases of 1 ppbv, with a peak decrease of 4 ppbv over the Antarctican continent are seen.

The areas of surface O_3 increase include the continental regions (where isoprene is a source) and much of the world's oceans north of 30S - 60S. The increases are largest over the continents, showing that isoprene has a heavy localized effect. For example, O_3 is predicted to increase 5 ppbv over most of South America, and up to 20 ppbv in some locations (somewhat over the Amazon). Likewise, the African continent experiences increases of 2 - 5 ppbv everywhere. Northern Australia is predicted to have O_3 increase by 10 ppbv. Eastern Asia generally sees no increase, or a small decrease in surface O_3 when

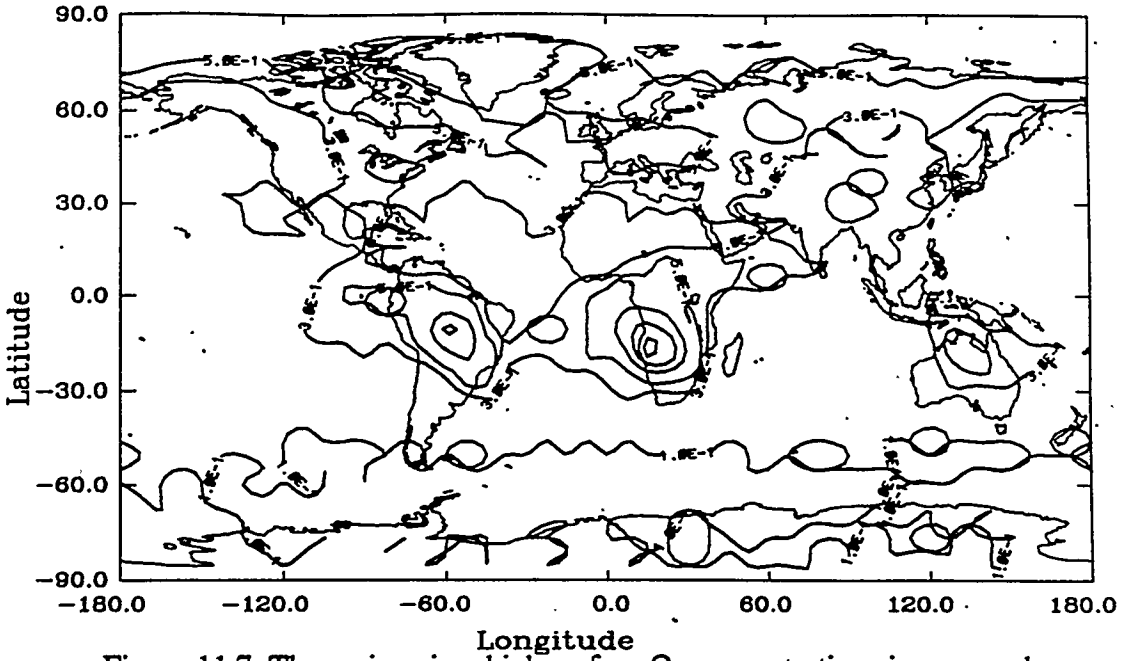

Figure 11.7 The regions in which surface O_3 concentrations increase when ethane and propane are added. Contours: 0.1, 0.3, 0.5, 1, 1.4, 1.8, and 2 ppbv.

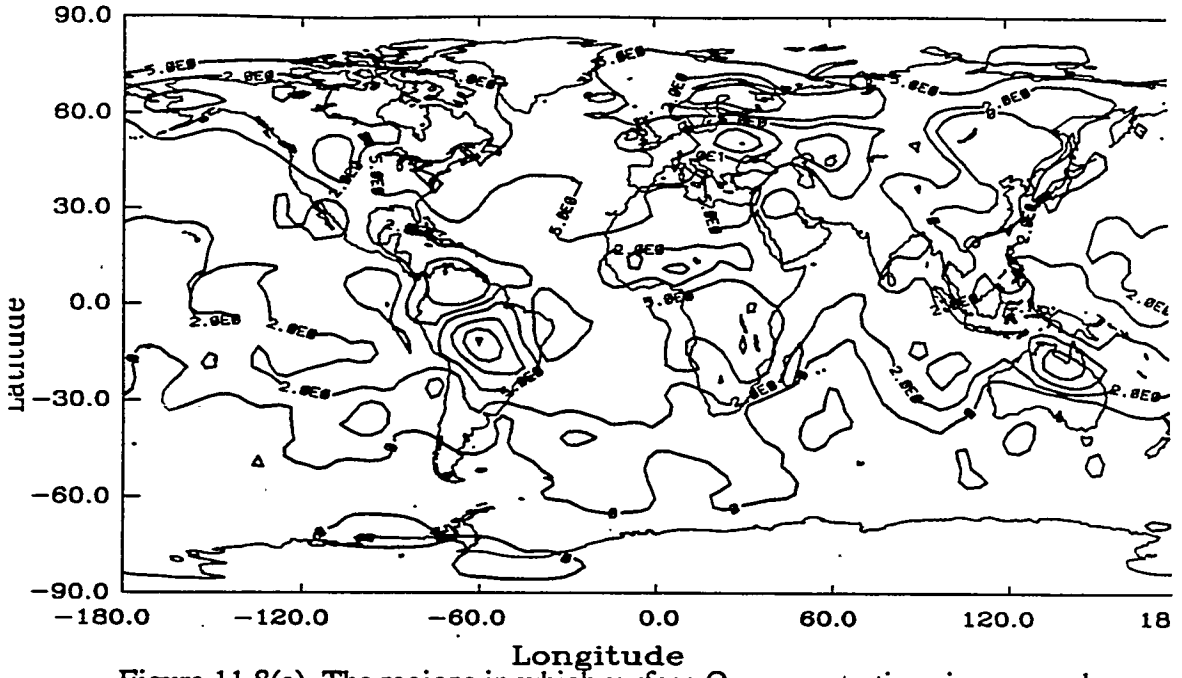

Figure 11.8(a) The regions in which surface O_3 concentrations increase when isoprene is added. Contours are 0, 2, 5, 10, 15, and 20 ppbv O_3.

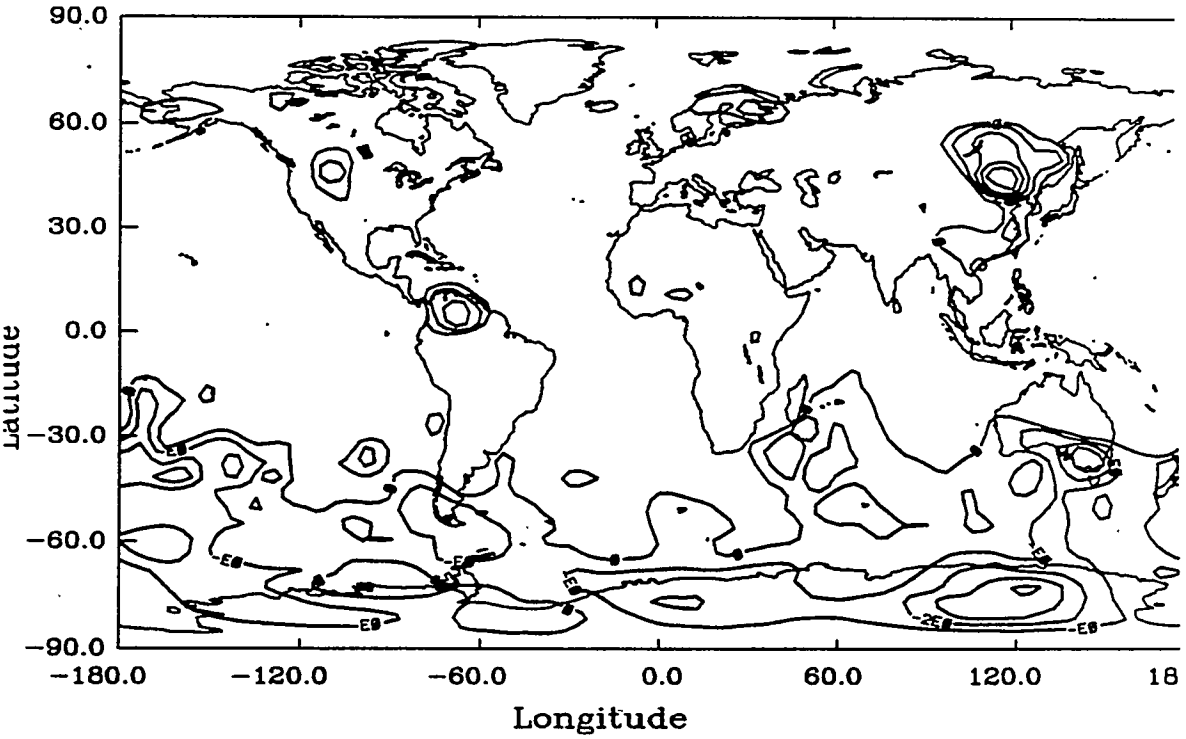

Figure 11.8(b) The regions in which surface O_3 concentrations decrease when isoprene is added. Contours are -5, -4, -3, -2, -1, and 0 ppbv O_3.

isoprene is added. North America sees O_3 increases of 2 to 5 ppbv, and Europe experiences 5 ppbv increases over the bulk of the continent, with some regions experiencing 15 ppbv increases.

Although the the increases are largest over the continents, O_3 also increases over much of the world's oceans and remote areas by approximately 2 ppbv. Although isoprene is short-lived, and greatly affects O_3 in source regions, it also appears have an effect in remote regions. This may be due either to the increased transport of O_3 over the oceans, or the formation of PAN, which then serves as a reservoir of NO_x in remote regions and also increases O_3.

Figure 11.9 shows the change in O_3 concentrations at sigma = 0.500 for the isoprene versus the background scenario. For most locations north of 30S, O_3 increases of 2 ppbv are still evident, similar to the surface predictions. The higher northern latitudes experience O_3 increases of 5 - 10 ppbv, even at this altitude. Not shown in the figure is a decrease of O_3 that occurs over Antarctica, from 75S to 90S and 0 to 120E. The reason for this is unknown.

11.3.3 Summary of O_3 results in the non-methane hydrocarbon model

Three model scenarios, background, background + alkane, and background +. isoprene were simulated. Comparing the model results with data shows that the model tends to underpredict surface O_3 concentrations, perhaps because the model does not include all reactive non-methane hydrocarbons in the atmosphere, dry deposition was excessive over the oceans, and some observations are at elevated locations. The free troposphere O_3 concentrations tend to be overpredicted in both the background and isoprene scenarios, however, this may be due to how O_3 concentrations are specified in the stratosphere.

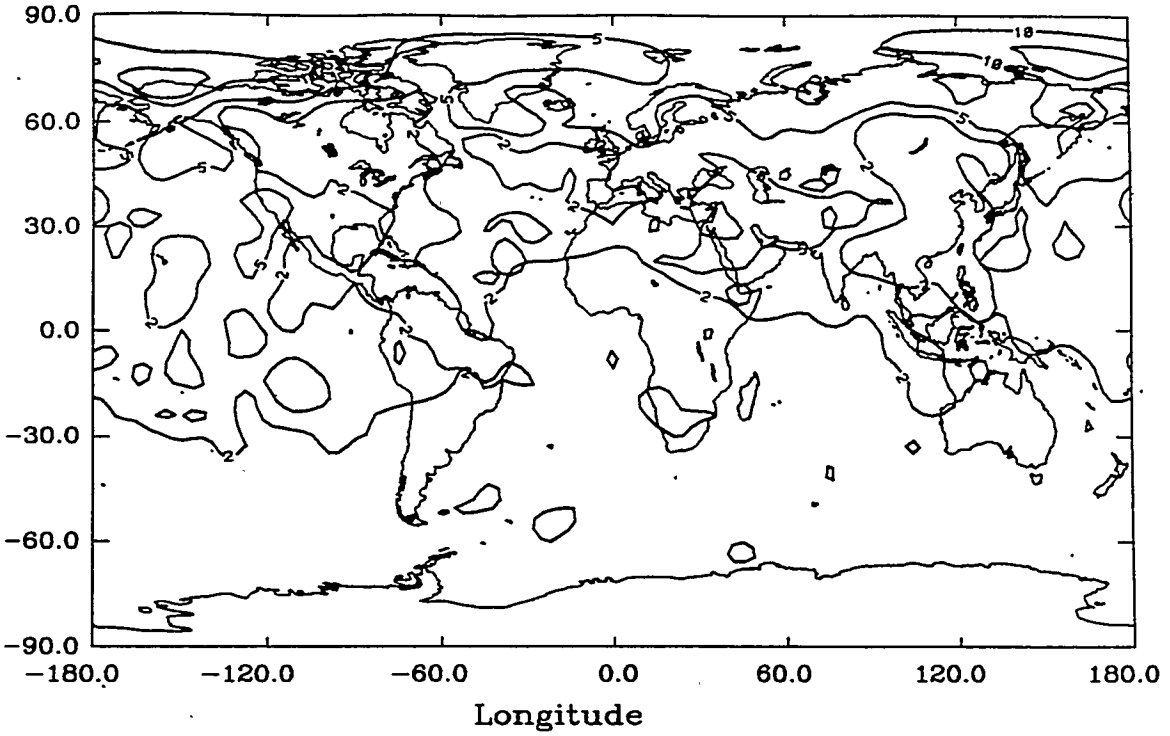

Figure 11.9 The increase in O_3 in ppbv at sigma = 0.5 when isoprene chemistry is included. Contours are 2, 5, 10, 12, and 15 ppbv.

Comparing the background and alkane scenarios shows that with a total ethane source of 8 Tg/yr and propane source of 6 Tg/yr, O_3 is not appreciably affected on a global scale at the surface, or sigma = 0.811 and 0.500. At most, ozone concentrations increase 1 - 2 ppbv. Isoprene, however, does appreciably affect O_3 concentrations at the surface and in the free troposphere. The increases in surface O_3 are highest over the source regions (continents), where O_3 rises 5 - 20 ppbv. Over remote and marine locations the O_3 also increases by roughly 2 ppbv. The increase over remote regions may either be due to increased transport of O_3 to these areas, or the formation of PAN, which is then transported and acts as a reservoir of NO_x in remote locations.

11.4 Predicted hydroxyl radical (OH) fields

Another key component of the oxidative capacity of the atmosphere is the hydroxyl radical. Reaction with the hydroxyl radical is the primary chemical loss for many

tropospheric species. As more species are added to the atmosphere and react with OH, its concentration should be depleted. However, increased emissions of non-methane hydrocarbons can also increase O_3 concentrations. Since the formation of OH in the troposphere is initiated by the photolysis of O_3, increasing non-methane hydrocarbon concentrations and O_3, which would tend to increase OH concentrations. It is precisely due to this non-linear chemistry of the atmosphere that models are necessary.

11.4.1 Surface OH fields

Similar to the ozone results, the background and alkane scenarios predict almost identical OH fields. For this analysis, then, the background and isoprene scenarios will be examined. Figure 11.10 shows the surface OH concentration fields, in molecules/cm^3 for the background and isoprene scenarios. For most continental areas, isoprene causes the OH concentrations to decrease. For South America, including isoprene decreased the OH concentrations from peaks of 5×10^6 cm^{-3} to peaks of 3×10^6 cm^{-3}. Over Africa, while there are still peaks of 6×10^6 cm^{-3}, they are not as large. Additionally, the concentration of OH over central Africa (0 to 20N) is now 1×10^6 cm^{-3}, where it previously had been 2 $\times 10^6$ cm^{-3}. Over the U.S., the background scenario predicted OH of 4 - 5×10^6 cm^{-3}. This decreased to 2 - 3×10^6 cm^{-3} when isoprene was added. Over Europe, the 3×10^6 cm^{-3} contour that enveloped the contour has greatly reduced in size, and the peak of 4×10^6 cm^{-3} has almost shrunk. The OH concentrations have also decreased over Eastern Asia.

Over the remote Pacific and Atlantic Oceans, however, OH concentrations appear to have increased slightly when isoprene was included. While the concentration in the background case is 1×10^6 cm^{-3}, this increases slightly to 2×10^6 cm^{-3}. The concentration of OH may have increased slightly over the Northern Indian Ocean, as well.

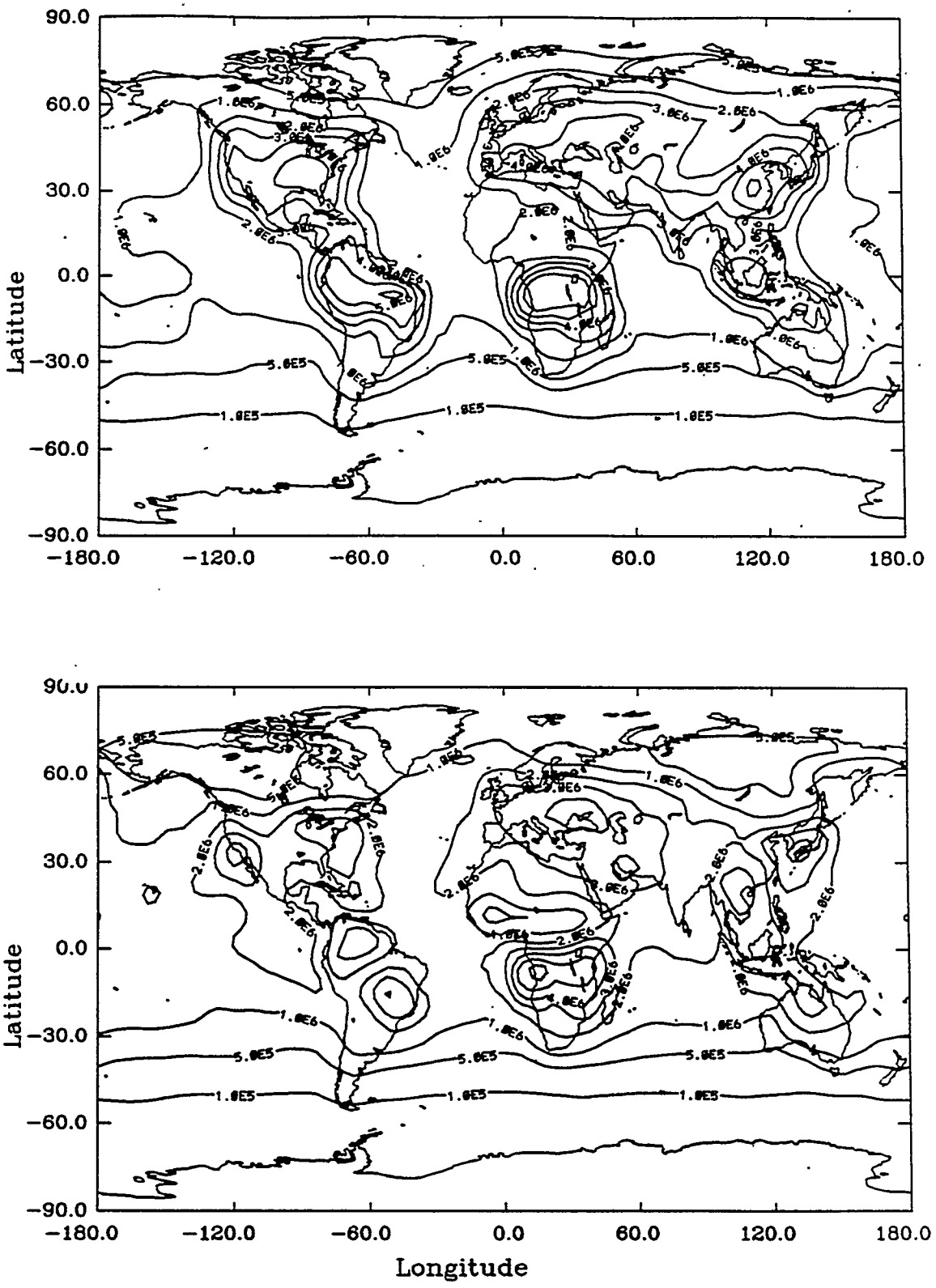

Figure 11.10 Surface OH concentrations, cm^{-3}, for the (a) background and (b) isoprene scenarios. Contours are 1.e5, 5.e5, 1.e6, 2.e6, 3.e6, 4.e6, 5.e6, 6.e6, and 7.e6 cm^{-3}.

11.4.2 Zonal average OH fields

Zonal average OH concentrations are plotted in Figure 11.11 for the background and isoprene scenarios. In the tropics, the most significant decreases in OH occur in the lowest 200 mb of the troposphere, due to the high isoprene concentrations and reactivity there. From 0 to 20S, peak OH has decreased from 2.5×10^6 cm^{-3} to 2.0×10^6 cm^{-3} in the lowest 100 mb. The peak of 2.5×10^6 cm^{-3} from 20 to 45N has also greatly shrunk, particularly at the surface. The other area of interest is near the North Pole, at the surface. In the background scenario, the zonal average OH concentration was 5×10^5 cm^{-3}, but with the isoprene scenario, it increases to 1×10^6 cm^{-3}. This may be due to the increase in O_3 also seen here, whose photolysis could lead to higher OH levels.

11.4.3 Summary of OH changes

Adding isoprene tends to decrease OH concentrations over the isoprene source regions (continents) significantly. This phenomenon is constrained to the lowest 200 mb of the atmosphere, because isoprene is so reactive. Over remote marine locations, and possibly in the high northern latitudes, the addition of isoprene actually slightly increased the OH concentrations, perhaps due to increased O_3 levels photolyzing to create OH.

11.5 Predicted NO_x and PAN fields

Along with non-methane hydrocarbons, nitrogen oxides ($NO_x = NO + NO_2$) are the other chemical precursor of O_3. The GRANTOUR model has a number of explicit sources of NO_x that are well characterized. The non-methane hydrocarbon chemistry, however, also leads to peroxyacetyl nitrate (PAN) an inherent source of NO_x. As mentioned earlier, PAN is thermally stable, and may be transported long distances away from NO_x source regions, where it can thermally decompose and serve as a source of NO_x in remote locations. Because of this intertwining of the two reactive nitrogen species, they will be examined together in this section.

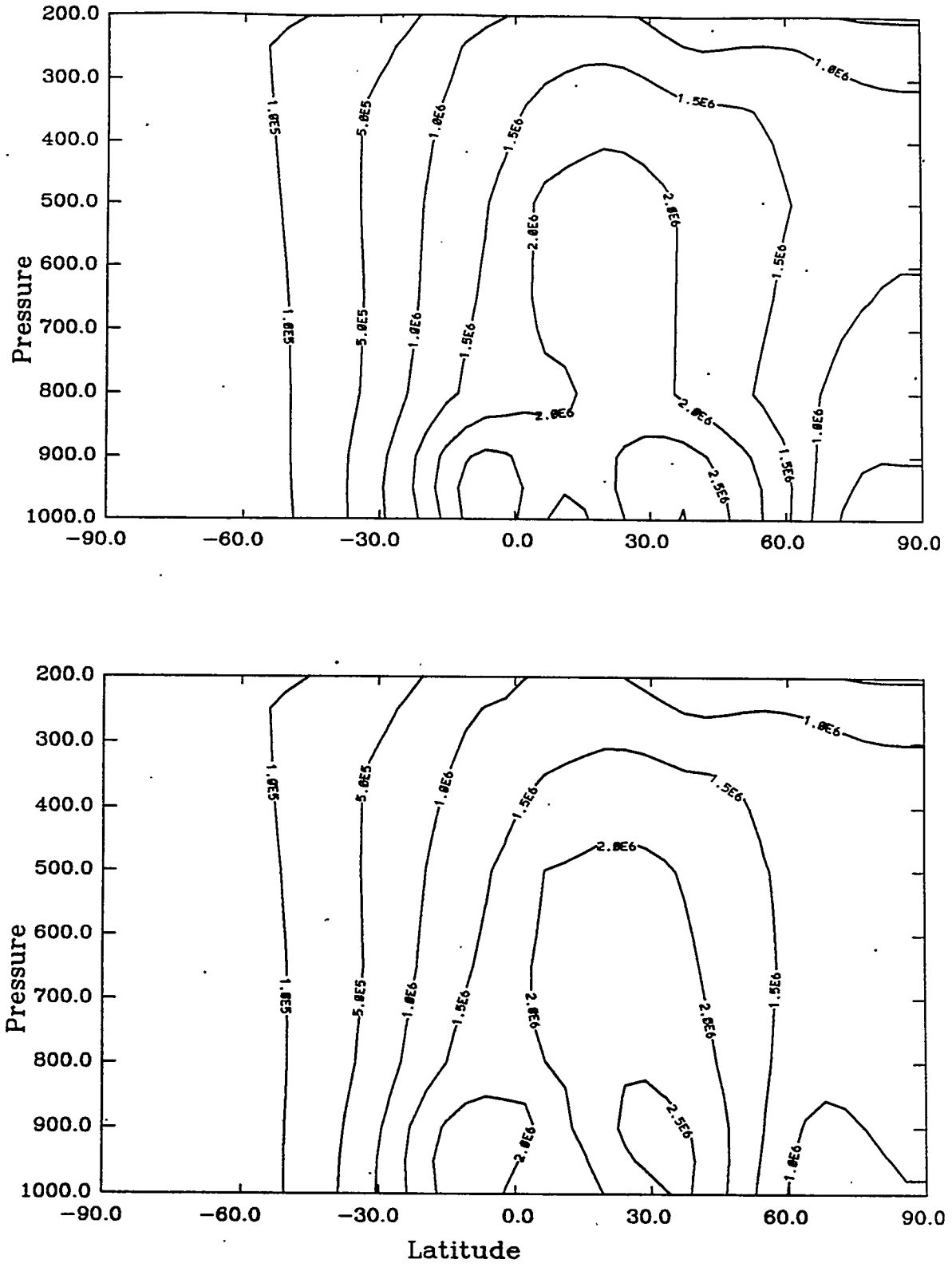

Figure 11.11 Zonal average OH concentrations for the (a) background and (b) isoprene scenarios. Contours are 1.e5, 5.e5, 1.e6, 2.e6, 2.5e6, and 3.e6 cm^{-3}.

11.5.1 Surface NO_x fields

PAN formation requires molecules with at least two carbon atoms. The background scenario, whose only hydrocarbon is methane, does not produce any PAN. The other two scenarios, alkane and isoprene, do produce PAN. Figure 11.12 shows the surface NO_x concentrations predicted for the background scenario. Most of the remote marine locations are predicted to have concentrations of 10 pptv NO_x. Over the Atlantic Ocean, which is affected by transport from North America, model NO_x levels reach 20 pptv. Over most continental areas, model NOx concentrations peak at 1 - 2 ppbv. Typical NO_x observations are less than 50 pptv in remote areas, 50 pptv - 20 ppbv in rural areas, and 20 ppbv - 1 ppm in moderately polluted areas (Finlayson-Pitts and Pitts, 1986). The remote marine GRANTOUR regions certainly fall within the observed range. The GRANTOUR continental areas have NO_x values typical of rural areas. In a global model such as GRANTOUR, where by necessity point sources do not exist, per se, levels above 3 or 4 ppbv NO_x will not be seen. However, the model predicted NO_x levels are reasonable.

Figure 11.13 shows the change in surface NO_x predicted when the alkanes, ethane and propane, are added to the model. This figure shows only the decreases in NO_x that occured when the alkanes were added. The only NO_x increases that occurred were so small (< 1 pptv) that they were not plotted. Adding the alkanes decreased NO_x levels over Australia and South America (by 10 - 100 pptv), Africa (10 - 300 pptv), and Europe (10 - 50 pptv). A small decrease over the northeastern U.S. of 10 pptv was also noted. The NO_x has decreased because the nitrogen is now tied up as PAN.

Figures 11.14 (a) and (b) show the regions in which the isoprene resulted in a net NO_x decrease and NO_x increase, respectively. NO_x tended to decrease over the isoprene source regions, which include South America (250 - 1500 pptv), Africa (10 - 500 pptv), Australia (10 - 1000 pptv), North America (10 - 250 pptv), Europe/Asia (10 - 1000 pptv). Thus, the

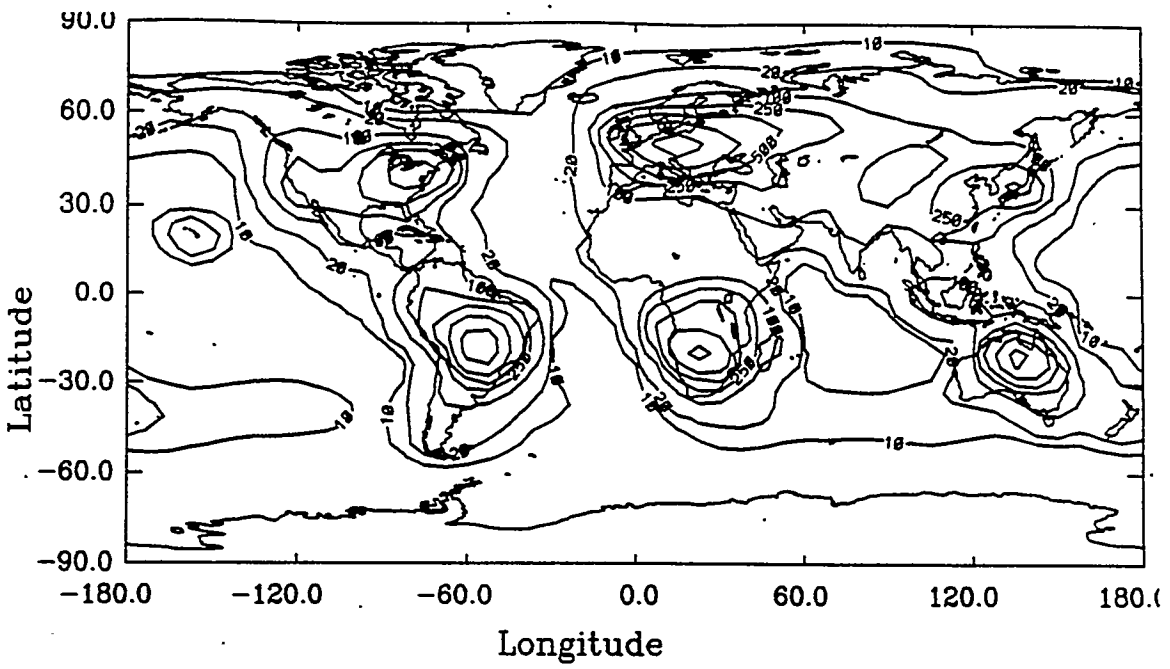

Figure 11.12 Surface NO_x concentrations for the background scenario. Contours are 10, 20, 100, 250, 500, 1000, and 2000 pptv.

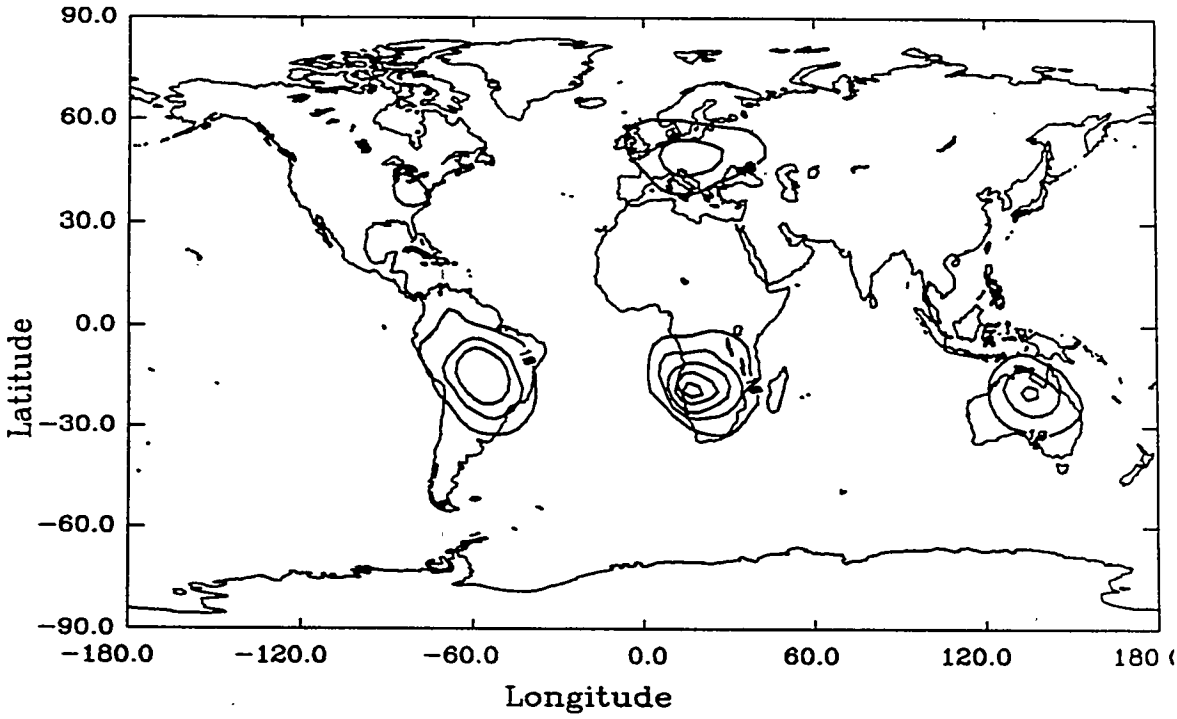

Figure 11.13 The decrease in surface NO_x, pptv, when alkane chemistry is added. Contours are 10, 50, 100, 200, 300, and 400 pptv.

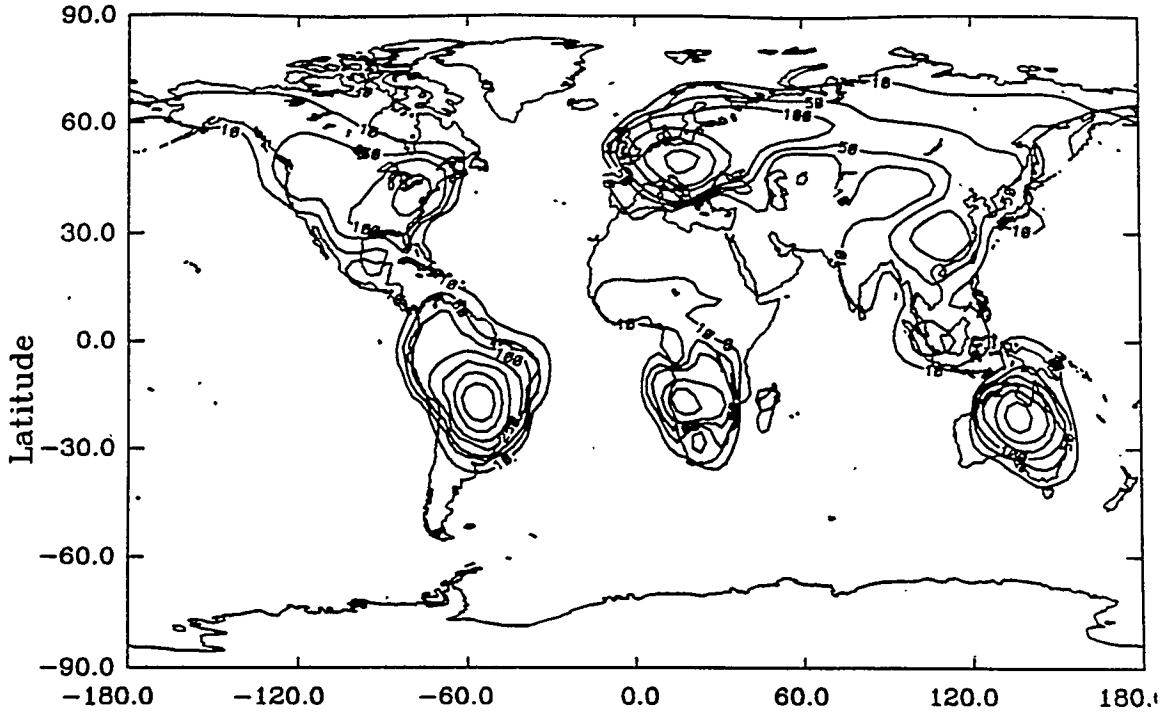

Figure 11.14(a) Regions in which the surface NO_x concentrations decreased when isoprene was added. Contours are 10, 50, 100, 250, 500, 100, 1500 pptv.

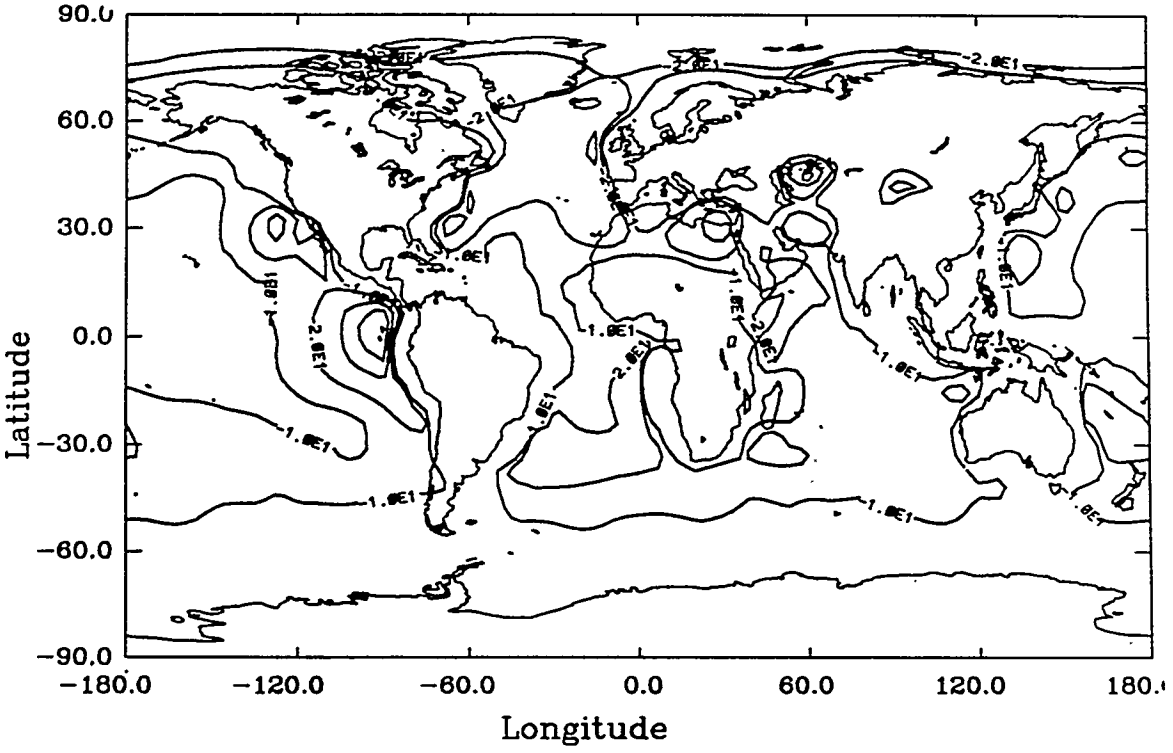

Figure 11.14 (b) Regions in which the surface NO_x concentrations increased when isoprene was added. Contours are 10, 20, 40, 60, 80, and 100 pptv NO_x.

addition of isoprene reduced NO_x peak concentrations by 1 - 2 ppbv over the continental regions due to the formation of PAN.

The net NO_x increases seen when isoprene chemistry was added are expected to be in the more remote regions. If PAN is formed and temperatures are low enough, it is thermally stable enough to be transported long distances and serve as a reservoir of NO_x, thereby increasing NO_x in remote areas. Figure 11.14(b) shows that the NO_x increases are generally seen just off shore of most of the continents, and extending over the oceans. Much of the world's oceans see increases in NO_x of 10 - 20 pptv. While these increases are small, recall that the baseline NO_x concentrations were on the order of 10 - 20 pptv over the oceans in the background case. Below this NO_x levels, O_3 is generally destroyed rather than produced. So, introducing isoprene creates PAN, which can supply enough NO_x to the remote regions that they are no longer ozone destruction regions but, rather, ozone production regions. Figure 11.8(a) shows that adding isoprene chemistry did result in O_3 increases over remote marine regions by 2 ppbv or more.

11.5.2 Zonal average NO_x fields

Finally, to illustrate how NO_x concentrations change at different altitudes when isoprene is added, the zonal average NO_x is plotted for the background and isoprene cases in Figure 11.5. There are notable regions. One is from 600 to 800 mb over 0 to 30S, where NO_x increases from 25 to 50 pptv when isoprene is added. Later zonal plots of PAN will show high levels of PAN in this region. NO_x decreases when isoprene is added in the lowest 100 mb of the atmosphere for the southern hemisphere tropics and northern hemisphere mid-latitudes, as was shown in the surface contours.

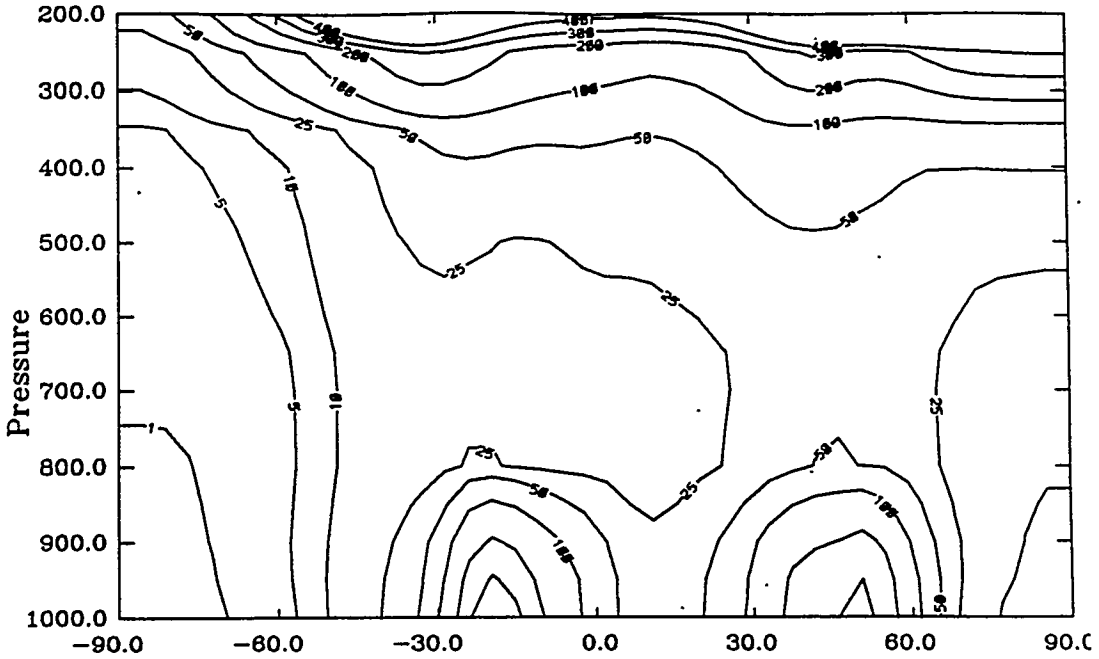

(a) Background scenario

(b) Isoprene scenario

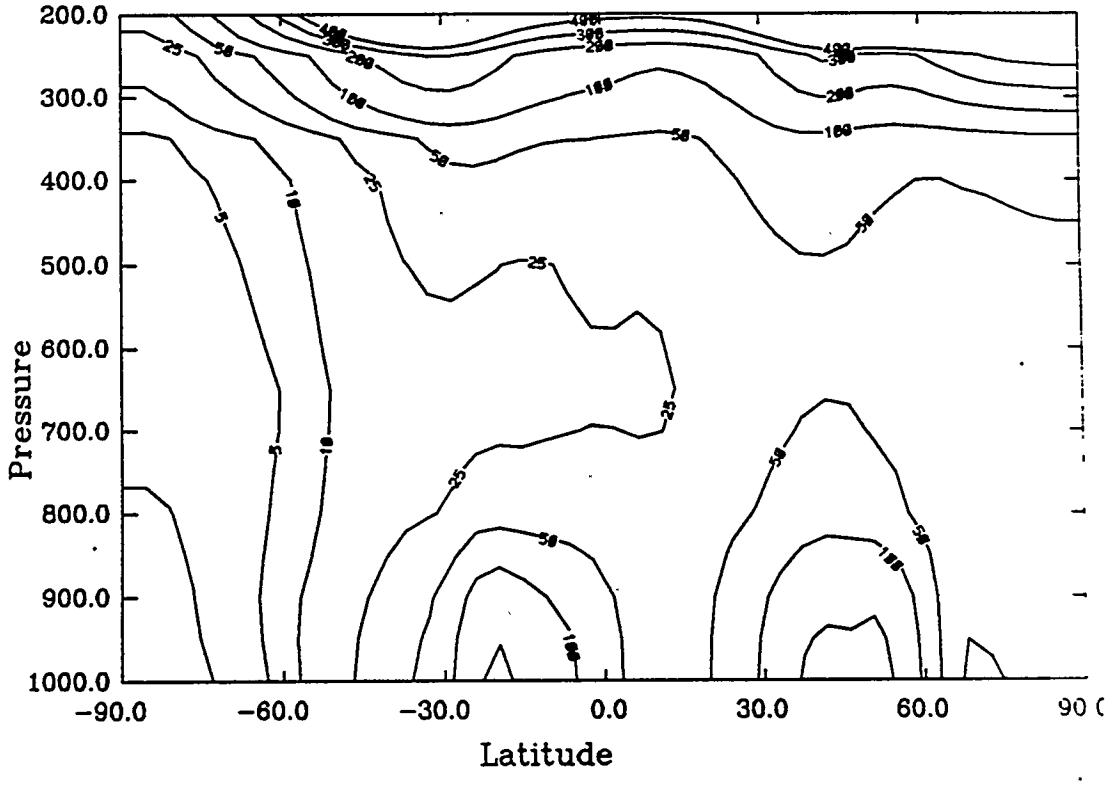

Figure 11.15 Zonal average NO_x concentrations, pptv, for the (a) background and (b) isoprene scenarios. Contours are 1, 5, 10, 25, 50, 100, 200, 300, and 400 pptv.

11.5.3 Surface PAN fields

Before drawing any futher conclusions about the NO_x fields, the PAN fields will now be compared with observations. Figure 11.16 shows the predicted surface PAN concentrations for the alkane and isoprene scenarios, respectively. Recall that the background scenario yields no PAN.

Surface PAN measurements have been made at a number of sites. Observations for marine regions follow. Singh and Salas (1983a, b) measured surface PAN during August, 1982 off the coast of California (Pt. Arena) in air that represented clean marine air. They found a mean surface concentration of 32 pptv, with a diurnal range of 15 - 120 pptv. At Point Arena in a different season (January), the mean surface concentration was 123 pptv, perhaps due to cooler surface temperatures (Singh and Salas, 1989). Singh et al. (1990b) measured PAN during GTE-CITE2 (August, 1986) and found that for marine boundary layer air, PAN concentrations were 5 - 20 pptv. During the MLOPEX study at Mauna Loa (May - June, 1988) mean surface concentrations of PAN were 27.5 pptv (in upslope air that represented boundary layer air, so these measurements may contain local influences) (Walega et al., 1992).

For remote marine environments, the isoprene scenario predicts PAN levels of roughly 20 pptv. In some areas, the concentrations are 20 - 50 pptv. These measurements are comparable to the observations mentioned above. However, note that this simulation did not include oceanic sources of non-methane hydrocarbons. If these NMHCs are included, it is likely that PAN levels in oceanic regions may rise.

Measurements have also been made for a variety of continental locations. Surface measurements at Niwot Ridge, Colorado (Singh and Salas, 1989) showed July mean PAN concentrations of 275 pptv. Those authors also cite unpublished work in which they measured PAN levels of 253 pptv at a remote Kansas site in May. Bottenheim et al. (1986) measured PAN concentrations of 189 - 235 pptv during March, 1985 at Alert, Canada (82N). These measurements will be higher than those found during July because the cooler

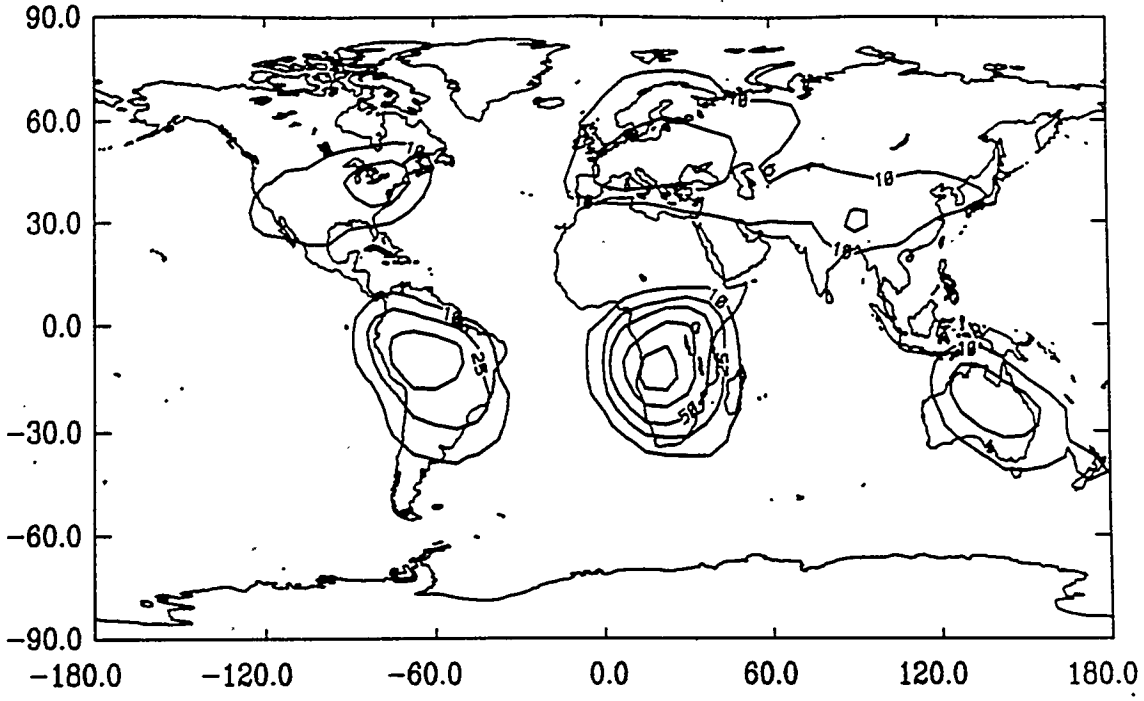

Figure 11.16(a) Surface PAN concentrations for the alkane scenario. Contours are 10, 25, 50, 100, 150, 200, and 250 pptv.

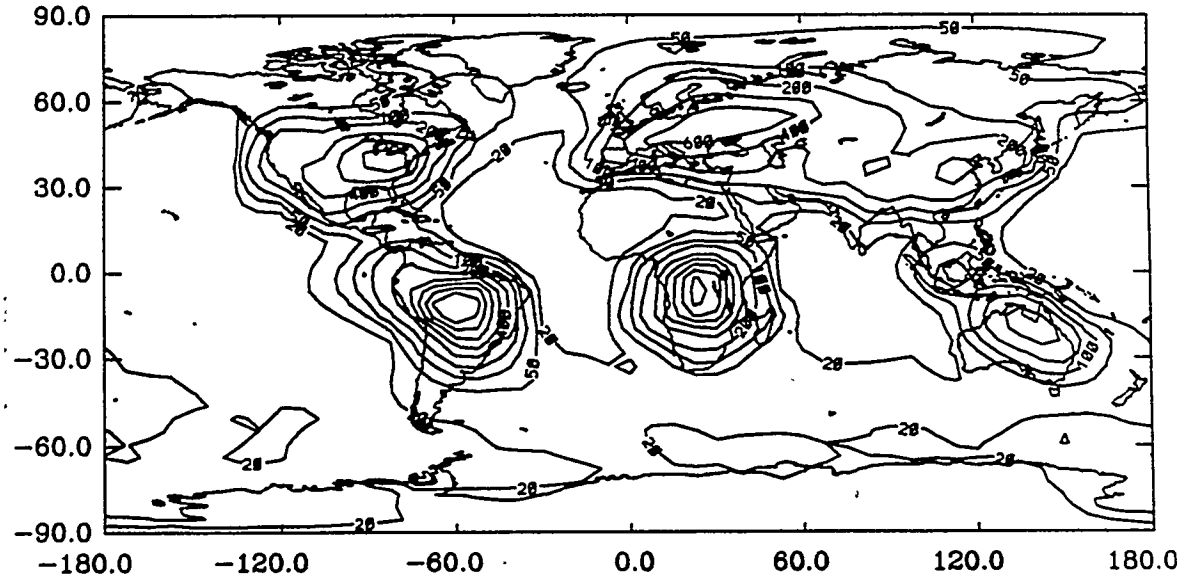

Figure 11.16(b) Surface PAN concentrations for the isoprene scenario. Contours are 20, 50, 100, 200, 400, 600, 800, 100, and 1200 pptv.

March temperatures will keep PAN from thermally decomposing. Singh et al. (1990b) measured PAN during the GTE-CITE2 (August, 1986) expeditions across the U.S. in August - September, 1986. They found that for continental air, at altitudes less than 4 km, PAN was roughly 120 pptv. During ABLE3A over North America and Greenland (July - August, 1988), Singh et al. (1992) measured 0 - 50 pptv PAN in the boundary layer. They inferred PAN concentrations were low there due to warm surface temperatures. Singh et al. (1990a) also measured PAN over the Amazon during ABLE 2B (April - May, 1987). They found median PAN concentrations of 12 pptv in air 0 - 2 km in height. For reference, typical urban levels of PAN were measured for 5 different sites in 1983-1985 (Singh and Salas, 1989). The mean concentrations were 644, 751, 1068, 1231, and 1578 pptv.

The model-predicted PAN levels shown in Figure 11.16 for isoprene are generally higher than those observed for remote and rural regions. PAN levels reach 800, 600, 1200, 1200, and 400 pptv, respectively over North America, Europe, South America, Africa, and Australia. This phenomenon has been observed in other global models (Jacob et al., 1993). It may be due to the fact that NO_x and non-methane hydrocarbon concentrations are diluted in the model over a large grid box, rather than concentrated in small point source regions, allowing PAN-formation reactions over a much larger grid domain. The smearing would tend to increase PAN levels within the model grid boxes.

11.5.4 Zonal average PAN fields

Zonal average PAN concentrations are presented in Figure 11.17 for the alkane and isoprene scenario. The isoprene scenarios show localized peaks over 0 - 20S and 0 - 30N which extend upward to 750 mb. These peaks are located near the strong source regions. PAN levels reach a maximum over the northern mid-latitudes, between 300 and 650 mb, probably because PAN is thermally stable there.

11.5.5 PAN fields at sigma = 0.811 and 0.5

PAN concentrations for the isoprene scenario (which has the highest PAN

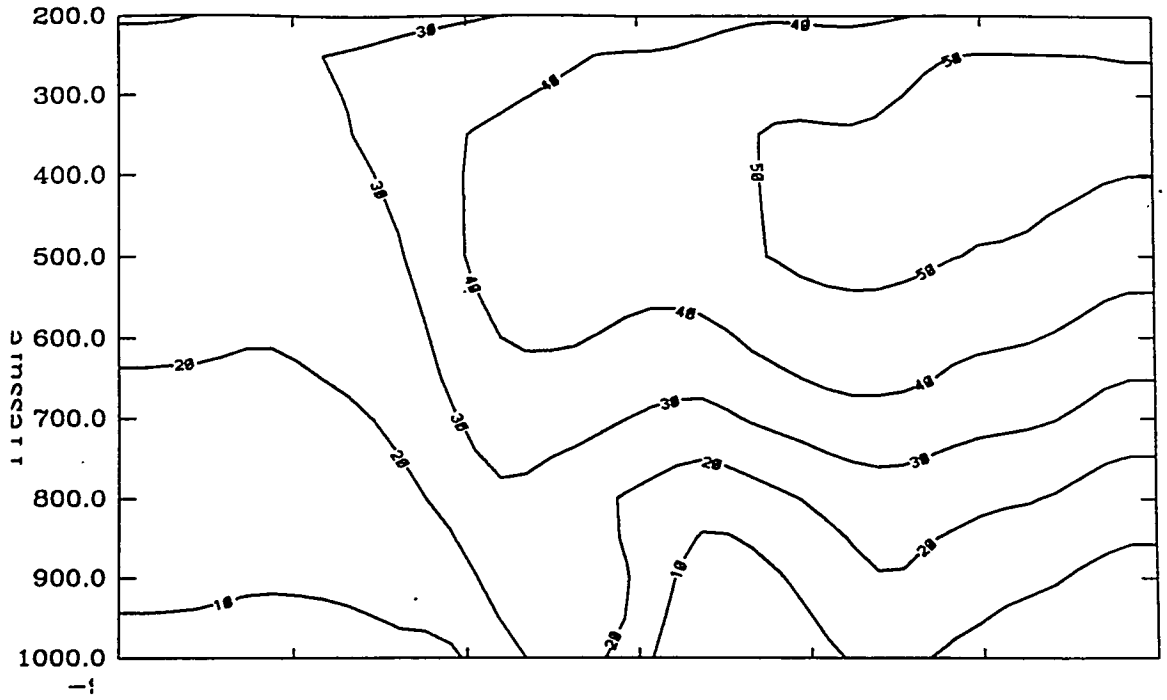

(a) alkane scenario

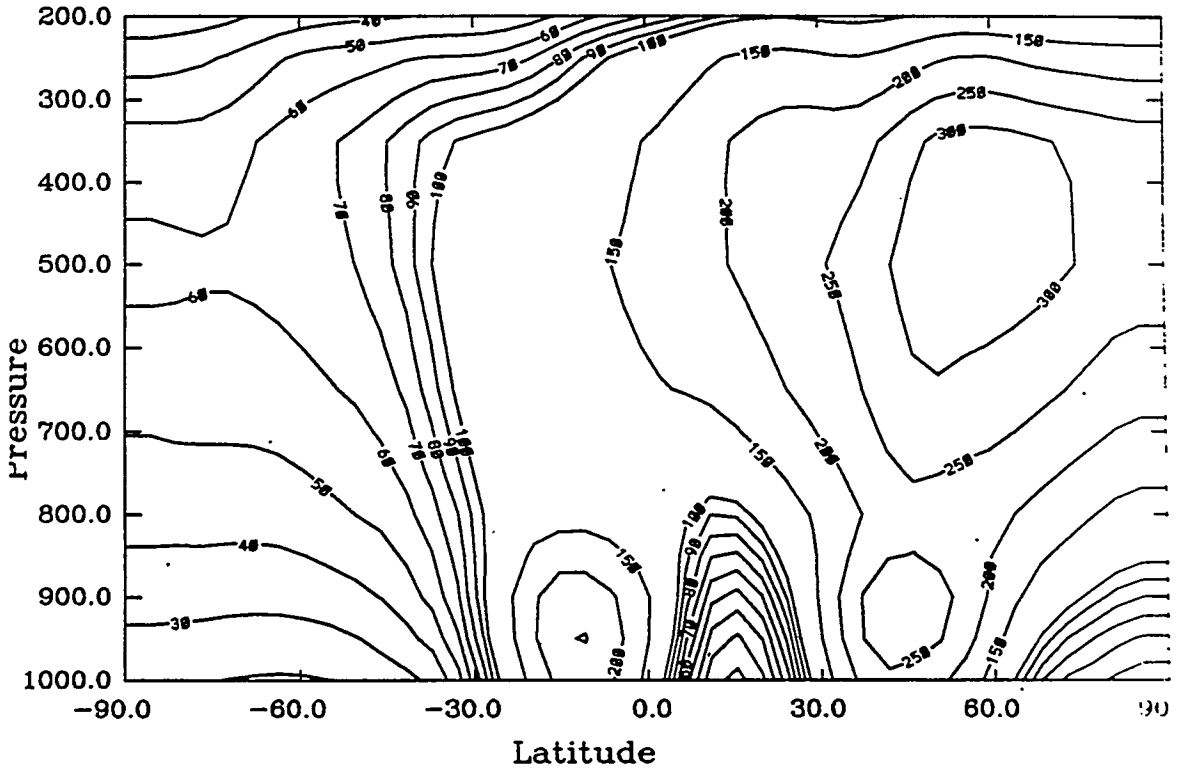

Figure 11.17 Zonal average concentrations of PAN for the (a) alkane and (b) isoprene scenarios. Contours are (a) 10, 20, 30, 40, 50, and 60 pptv; (b) 10, 20, 30, 40, 50, 60, 70, 80, 90, 100, 150, 200, 250, and 300 pptv.

concentrations) are shown for sigma = 0.811 and 0.5 in Figure 11.18. In general, the model PAN levels either compare favorably or are slightly higher than observed, although the discrepancy is not as large as at the surface.

In flights over Colorado during July, Singh et al. (1986) measured 80 - 200 pptv PAN in the free troposphere (the model gives 250 - 300 pptv there). For remote marine flights off of the Pacific coast, they measured concentrations of 15 - 60 pptv for altitudes of 2 - 10 km (model results are 20 - 50 pptv for sigma = 0.811). For flights over the continental U.S. during August-September, 1986, Singh et al. (1990) measured 100 - 300 pptv for altitudes of 4 -6 km, which was were the PAN concentrations peaked. The median value for 4 - 6 km was 140 pptv. The isoprene scenario yields 300 - 350 pptv PAN for the same location. For marine air, at 4 - 6 km, the median value was roughly 120 pptv (the model gives 100 pptv at sigma = 0.500). During MLOPEX, Walega et al. (1992) measured free tropospheric PAN values of 16.9 pptv for marine air. Singh et al. (1990) measured 20 pptv for 2 -4 km altitudes and 48 pptv for 4 - 6 km altitudes over the Amazon during ABLE 2B (April - May, 1987). The model predictions are much higher there. During ABLE3A, over North America and Greenland, Singh et al. (1992) measured PAN values of 100 - 700 pptv from 0 - 6 km. Over 90% of the measurements fell between 0 - 350 pptv, with the mean PAN during all flights roughly 100 - 200 pptv. Model values are 100 - 400 pptv at sigma = 0.811, and 250 - 400 pptv at sigma = 0.5.

11.6 Predicted HNO_3 wet deposition

Figure 11.19 shows the predicted wet nitrate deposition for the background and isoprene scenarios. The deposition values may be compared to Figure 22.c in Penner et al. (1991), which plots wet nitrate deposition for North America. The background scenario (Figure 11.19a predicts a 10 kg N/km^2 contour that covers much of the U.S., just as the observations do. The model peak deposition is located in the same region as the data, but model values reach 50 kg N/km^2 and the measurements only 30 kg N/km^2.

Figure 11.19b shows predicted nitrate deposition for the isoprene scenario. The

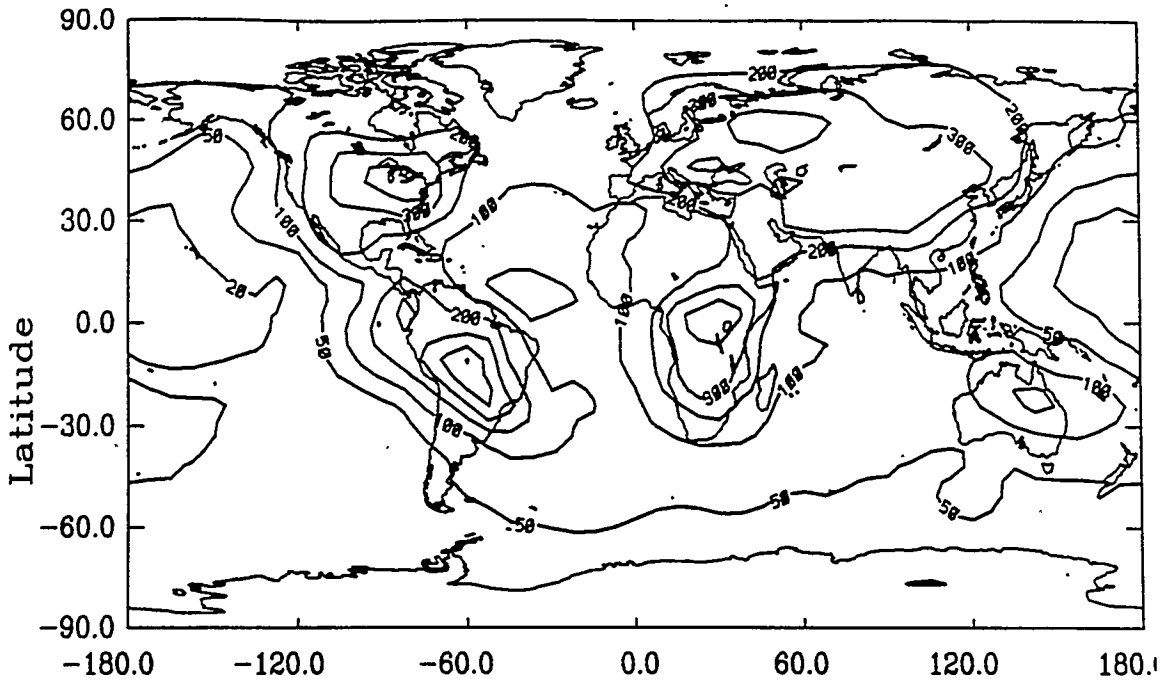

Figure 11.18(a) PAN concentrations at sigma = 0.811 for the isoprene scenario Contours are 20, 50, 100, 200, 300, 400, and 500 pptv.

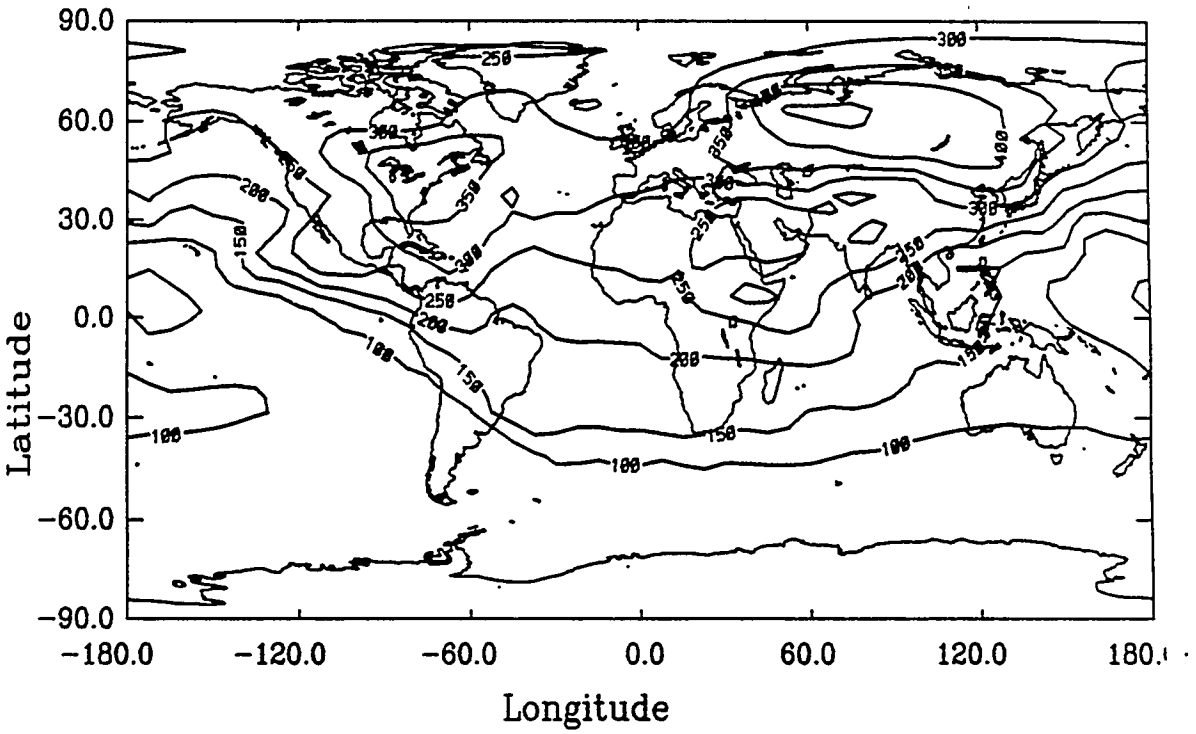

Figure 11.18(b) PAN concentrations at sigma = 0.500 for the isoprene scenario. Contours are 50, 100, 150, 200, 250, 300, 350, 400, 450, and 500 pptv

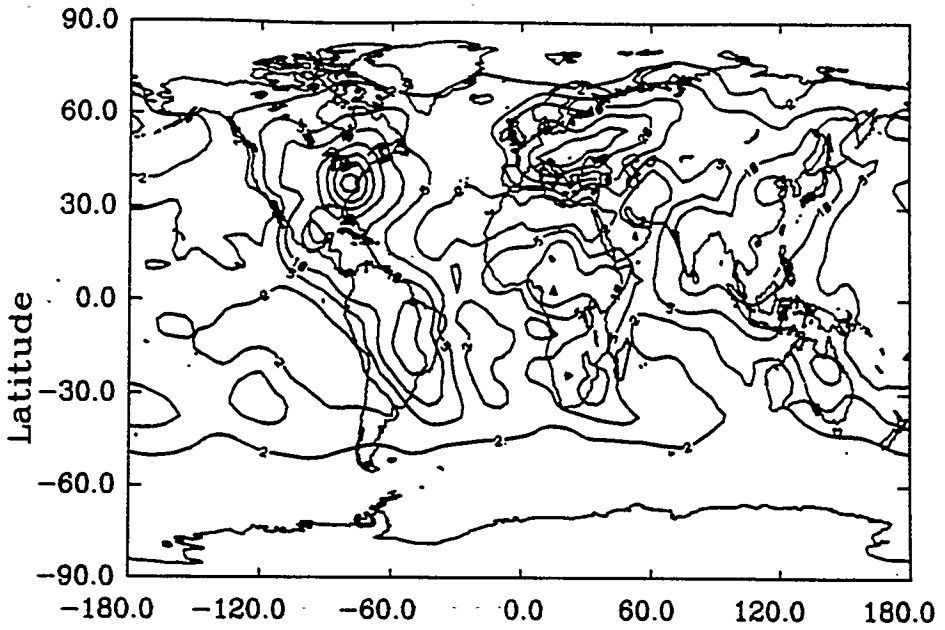

(a) Background scenario

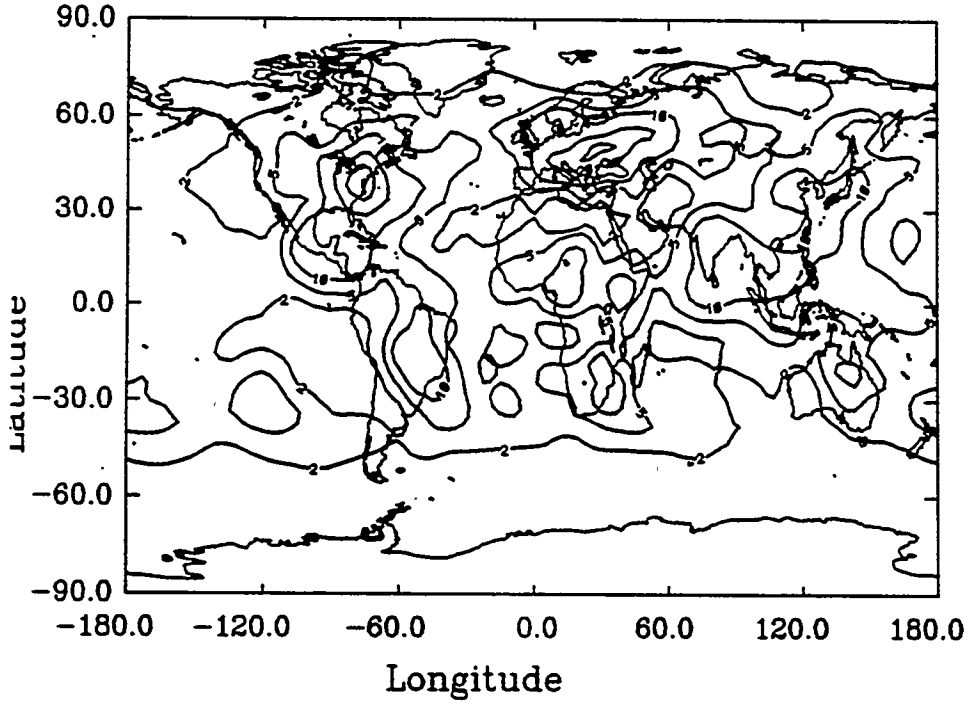

(b) Isoprene scenario

Figure 11.19 Predicted wet nitrate deposition in July in kg N/km^2 for the (a) Background scenario and (b) Isoprene scenario. Contours are 2, 5, 10, 20, 30, 40, 50, and 60 kg N/km^2.

model deposition is 5 kg N/km^2 over the greater U.S., while observations reach 10 kg N/km^2. However, the model peaks at 30 kg N/km^2, as do observations. The model peak does not cover as large of an area, however. These results indicate that the background CO/CH_4/NO_x/OH/O_3 creates too much HNO_3 because NO_x is allowed to form HNO_3, but not PAN. The isoprene scenario allows more NO_x to be tied up as PAN and, therefore, has less NO_x converted to HNO_3. It appears that the actual observed values lie somewhere between those predicted by the background and isoprene scenarios.

.11.7 Predicted concentrations of non-methane hydrocarbons

Chapter 8 discusses the ethane, propane, and isoprene source inventories used in the non-methane hydrocarbon version of GRANTOUR. As stated previously, only the industrial and biomass burning sources of ethane and propane are used, although these species can also be emitted by vegetation and oceans. Isoprene is emitted by plants and trees. The sources are land-based, and their concentrations are expected to be highest there.

11.3.1 Ethane concentrations

Figure 11.20 shows the global surface contours for ethane concentrations present in the alkane scenario. The highest values occur over regions of biomass burning, which include Africa (500 - 3000 pptv), South America (500 - 2500 pptv), and Australia (500 - 2000 pptv). The ethane concentrations are 300 - 1000 pptv over North America and 400 - 1000 pptv over Europe. Over the more remote regions of the globe (e.g. over oceans) concentrations are 200 pptv in the Northern Hemisphere, and 300 pptv in the Southern Hemisphere.

Ethane concentrations have been measured in both urban and remote locations and summarized by various authors (See, e.g. Singh and Zimmerman, 1992; Donahue and Prinn, 1990). The observed concentrations are expected to be higher than those predicted by GRANTOUR for two reasons. First, the measurements are made in regions with

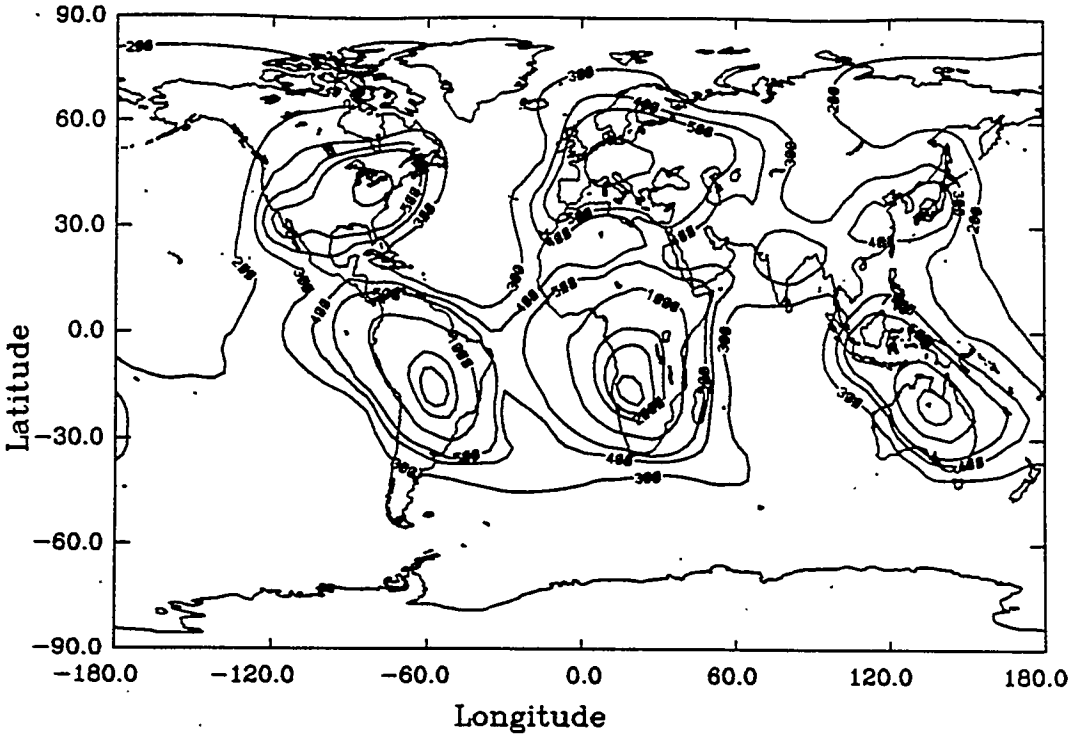

Figure 11.20 Surface ethane concentrations in the alkane scenario. Contours are 100, 200, 300, 400, 500, 1000, 2000, 2500, and 3000 pptv.

potential local sources (vegetation or oceanic fluxes). Second, the emissions in GRANTOUR are distributed over a 4.5 x 7.5 degree horizontal grid, which can lower the concentration. Singh and Zimmerman estimate global oceanic sources to be 0.89 Tg/yr for ethane and 0.42 Tg/yr for propane. Estimates were not given for vegetation, however, they are expected to be higher than the oceanic source.

Urban measurements of ethane in 39 U.S. cities (Singh and Zimmerman, 1992) yielded a median ethane concentration of 23.3 ppbv. In more rural and remote locations (e.g. Southern Appalachian Mountains), Seila et al. (1984) measured concentrations of 2.6, 9.1, and 6.7 ppbv ethane. These regions are expected to have high vegetation emissions of ethane. The levels in GRANTOUR are certainly lower than the urban values, as would be expected in a global model in which alkane concentrations are spread over large areas. In non-biomass burning regions (e.g. much of the Northern Hemisphere continents), ethane concentrations are lower than measured by Seila et al. (1984). Again, however,

GRANTOUR does not include biogenic emissions of ethane.

Also interesting are the measurements of Greenberg et al. (1992) at Mauna Loa. During periods of downslope flow, free tropospheric air had a median concentration of 742 pptv ethane, and surface air had a median concentration of 820 pptv ethane. The GRANTOUR concentrations are on the order of 200 pptv there, however, they reflect transport from large continental areas, and do not include local sources, such as oceanic emissions, which would tend to increase concentrations. Greenberg et al. (1991) found for three aircraft profiles measured off the coast of Washington and Alaska that consisted of marine air not recently influenced by surface sources, ethane concentrations at 0.1 km were 508, 2213, and 610 pptv. These values are still slightly higher than those seen by GRANTOUR, roughly 200 - 300 pptv.

Bonsang et al. (1990) sampled air at Amsterdam Island (38S, 78E), in the Indian Ocean. Under periods of marine influence during May - August, they found the average mixing ratio of ethane to be 442 pptv, which is slightly higher than the nearly 300 pptv GRANTOUR predicts. Bonsang et al. (1988) sampled air along the east coast of Africa during a cruise from 25S to 13N during April, 1985. The ethane concentrations ranged from 390 to 2200 pptv. GRANTOUR values are 500 - 1000 pptv in this same region. So, it appears that GRANTOUR ethane surface concentrations are in general lower than measurements, as expected.

Penkett et al. (1993) used aircraft to sample a number of hydrocarbons over the North Atlantic Ocean in the free troposphere and at low altitudes. They found that at low altitudes (less than 500 m), in July the ethane concentrations were roughly 1000 pptv. This is higher than the 300 - 500 pptv that the model predicts for the same region.

11.3.2 Propane concentrations

Figure 11.21 shows the global surface concentrations of propane present during the alkane scenario. The propane concentrations are lower than ethane concentrations. Again, the largest concentrations occur over the continental source regions. The areas with

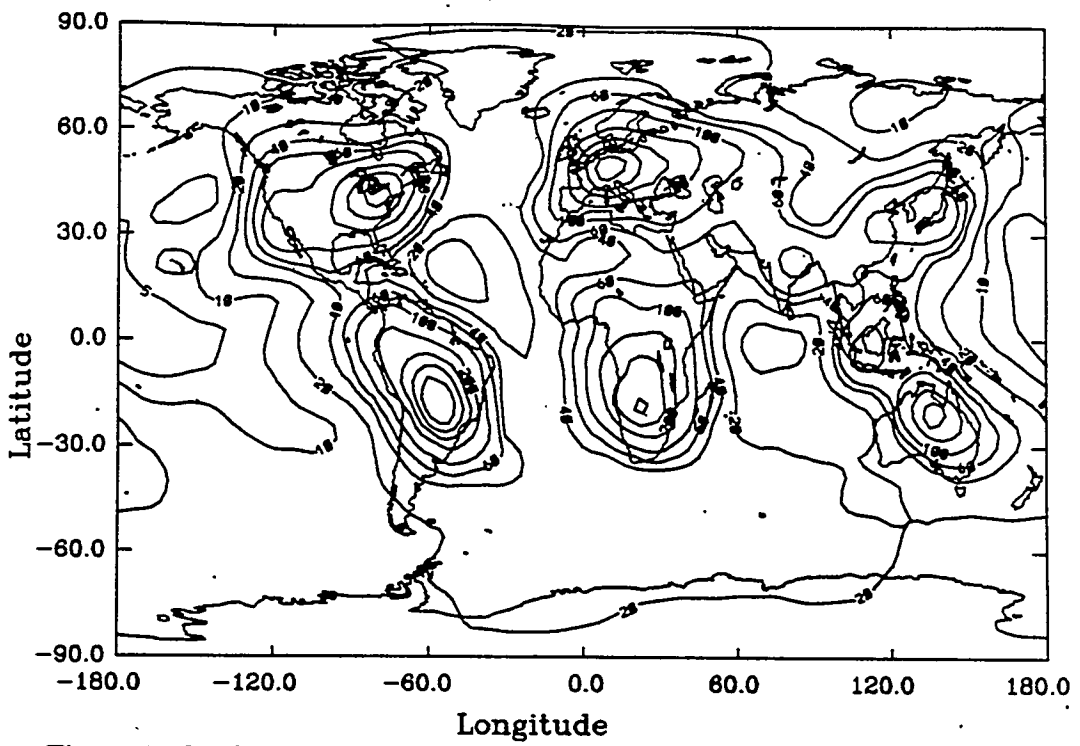

Figure 11.21 Surface propane concentrations in the alkane scenario. Contours are 5, 10, 20, 40, 60, 100, 200, 300, 400, and 500 pptv.

substantial biomass burning experience the highest propane concentrations. For example, over South America, concentrations range from 50 to 500 pptv. Likewise, over Africa, the range is 50 to 400 pptv, and 50 to 300 pptv over Australia. Over North America, concentrations range from 100 to 400 pptv, and over Europe, from 100 - 500 pptv. Over the southern hemisphere oceans, concentrations are generally 10 - 40 pptv. Over the northern hemispher oceans, concentrations are 5 - 20 pptv.

Similar to ethane, propane observations are, in general, higher than the values predicted in GRANTOUR because the model doesn't include biogenic emissions and distributes the sources over a 4.5 x 7.5 degree horizontal grid. The median urban propane concentration for 39 cities was 23.5 ppbv, which is far higher than GRANTOUR's predictions. Over the Appalachian Mountains, concentrations of 3400, 6000, and 5600 pptv were measured in rural/remote locations, which are expected to have high vegetation emissions.

Greenberg et al. (1992) measured propane concentrations of 29 pptv in free

tropospheric air, and 42 pptv in surface air at Mauna Loa. These levels are higher than the 10 pptv estimated by the model . Greenberg et al. (1990) found in marine air at a height of 0.1km off of the coasts of Alaska and Washington, the propane concentrations were 194, 583, and 726 pptv, which are higher than the 40 - 100 pptv predicted by GRANTOUR.

At Amsterdam Island in the Indian Ocean, Bonsang et al. (1990) found the average mixing ratio of propane to be 193 pptv during periods of marine influence from May - August. The values in GRANTOUR are much lower, roughly 20 - 50 pptv there. Off the west coast of Africa, Bonsang et al. (1988) measured 100 - 760 pptv of propane, where GRANTOUR shows 40 - 200 pptv.

Penkett et al. (1993) used aircraft to sample a number of hydrocarbons over the North Atlantic Ocean. They found low altitude (< 500m) levels of propane to be on the order of 80 - 100 pptv in July (their Figure 3). The GRANTOUR model predicts concentrations of 60 - 100 pptv there.

So, for both ethane and propane, the levels in GRANTOUR are usually lower than atmospheric measurements, sometimes substantially so. However, the measurements are often made in areas expected to have significant vegetation emissions or local oceanic emissions, and are expected to be higher than those in GRANTOUR. Additionally, GRANTOUR spreads the emissions over an entire grid box of 4.5 x 7.5 degrees, and is not expected to experience the regionally high values certain regions might.

11.7.3 Isoprene concentrations

During the month of July, isoprene is emitted in GRANTOUR at an annual rate of 451 Tg/yr. Otherwise, the isoprene emission rate averaged over all 12 months is 386 Tg/yr. The July surface isoprene concentrations are shown in Figure 11.22, from the isoprene scenario. By far, the largest concentrations are over South America (50 - 3000 pptv isoprene) and Africa (50 - 2000 pptv). This is because these areas have dense, lush, tropical vegetation, which emits large amounts of isoprene. The contours over North America and Europe range from 50 to 1000 pptv. Much of North America sees 250 - 500 pptv, and much

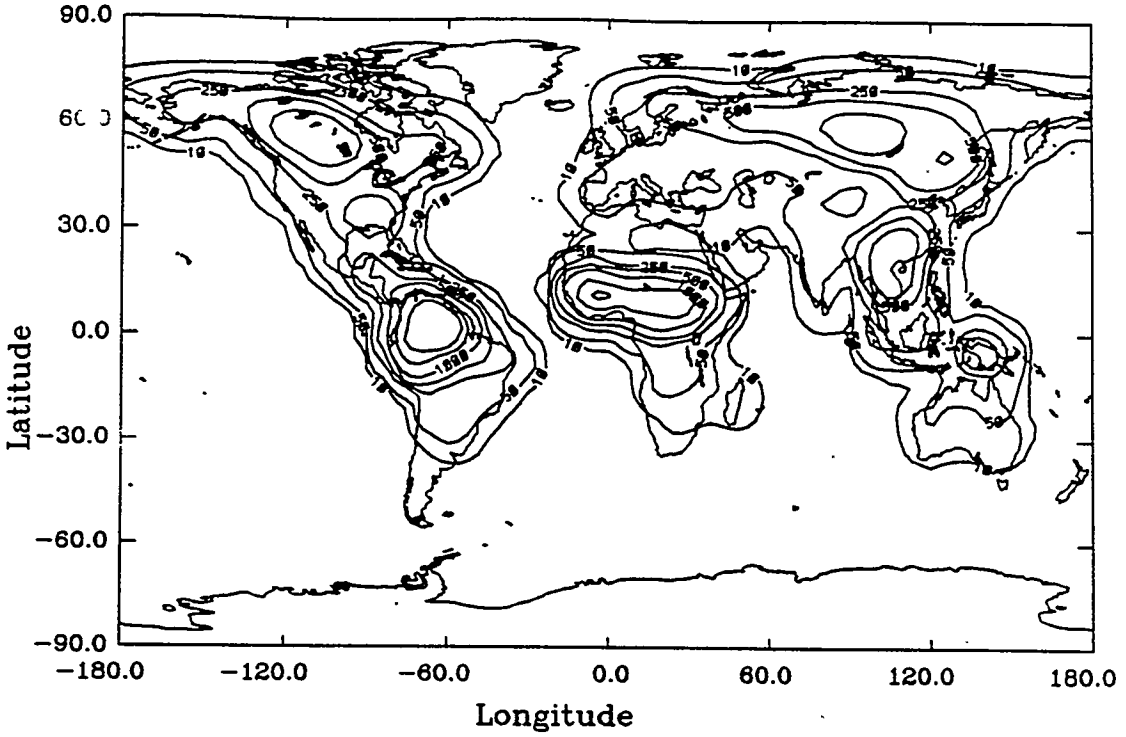

Figure 11.22 Surface isoprene concentrations in the isoprene scenario. Contours are 10, 50, 250, 500, 1000, 2000, and 3000 pptv isoprene.

of Europe experiences 50 - 250 pptv isoprene.

In general, the surface GRANTOUR concentrations compare favorably with measurements. Zimmerman et al. (1988) measured isoprene concentrations of 1730, 1780, 2040, 2650, and 2040 pptv over Brazil in July and August, 1985. Sampling was conducted at heights of 15 - 81 m. They also cited unpublished measurements they had made earlier in Brazil (2040, 2400, and 5450 pptv), Nigeria (1210 pptv), and Kenya (40 pptv and lower). Rasmussen and Khalil (1988) found isoprene concentrations over Brazil generally peaked at 2 - 4 ppbv during midday, with lower concentrations during other parts of the day. The diurnal variation was typically 1 - 3.5 ppbv during the day. Greenberg and Zimmerman (1984) measured summertime isoprene concentrations of 630 pptv (range of 220 - 1760 pptv) at Niwot Ridge (in the Rocky Mountains) and 110 pptv (range of 30 - 160 pptv) at the Pawnee Grasslands in Colorado.

CHAPTER 12 BERYLLIUM CASE STUDY: PERPETUAL AND SEASONAL JULY SIMULATIONS

12.1 Introduction

The model simulations discussed in Chapters 9, 10, and 11 were conducted for both perpetual and seasonal CCM1 meteorology. It is expected that concentrations predicted from a perpetual July, for example, will differ from a seasonal July, due to differences in the meteorology. The CCM1 meteorological files for the perpetual July simulations were obtained by specifying the solar insolation and sea surface temperature, and then running CCM1 for 90 days of July conditions. Additionally, soil moisture was fixed at a July value so that it wouldn't be totally depleted by the end of the simulation. The meteorology for the seasonal July simulation was obtained from a CCM1 run in which the solar insolation and sea surface temperatures were also prescribed to be their seasonally varying values. However, the CCM1 was run in a seasonal mode, meaning that all twelve months of the year were run sucessively. Thus, the seasonal July meteorology should be affected by the earlier months' meteorology, while the perpetual July should not.

The two types of meterological files may vary for several reasons. First, the perpetual July is an average of 90 days, while the seasonal only averages over 30 days. Second, as stated above, the seasonal meteorology should be influenced by earlier months, while the perpetual will not. The differences between the two meteorologies may include slight shifts in the location of general circulation features. This, in turn, could affect the transport from the stratosphere to the troposphere. Since 90% of the atmosphere's O_3 is located in the stratosphere, the difference in stratosphere-troposphere exchange could affect the model results.

Transport from the stratsophere is thought to occur via several mechanisms: large scale circulation (the Hadley Cell), large scale eddies (and associated tropopause folding events), differences in the tropopause height which leads to stratospheric mass exchange

between the two hemispheres, and diffusion. Different estimates of the importance of each process exist. Danielsen (1968) assumes all stratosphere-troposphere exchange takes place via tropopause folding. Reiter (1975) estimates that stratosphere-troposphere exchange may be split into general circulation (52%), change in tropopause height (21%) and tropopause folding (27%). Diffusion was found to be minimal (less than 2%). Singh et al. (1980) estimate that 60 - 80% of the exchange is due to tropopause folding events and 20 - 40% is due to mean meridional circulation.

Because the CCM1 meteorology is updated every 12 hours for a 4.5 by 7.5 degree grid, only processes that have temporal and spatial scales larger than this will be resolved. Thus, features of the Hadley Cell are present, but tropopause folding events are not. The GRANTOUR model calculates its own vertical diffusive flux of species. The differences in general circulation between the perpetual and seasonal GRANTOUR model simulations may yield different results for identical input conditions. To study this variability, a perpetual July and a seasonal simulation with ^{7}Be, a radiative "tracer" were performed. The July results were compared.

Beryllium-7 is a radioactive tracer produced by cosmic rays. Its production is primarily in the stratosphere (over 9 ·), but some is produced in the troposphere. Because it is cosmogenically produced, it is affected by variations in the solar cycle. Stronger sunspot activity leads to solar winds, which tend to deflect the ^{7}Be from the earth, and lower its concentration. Once in the earth's atmosphere, ^{7}Be attaches to submicron aerosols, which are removed by precipitation and dry deposition.

A ^{7}Be source function was constructed based on Lal and Peters (1967). The deposition velocity for ^{7}Be was taken to be 0.1 cm/sec, and its precipitation scavenging coefficients were 1.0 cm^{-1} (stratiform) and 0.33 cm^{-1} (convective precipitation). The seasonal simulation consisted of three annual cycles, and the third seasonal July (50,000 parcels; 6 hour timestep) was analyzed. The perpetual simulation was "spun-up" from the

results of the seasonal simulation for 10 months with 50,000 parcels and a 6 hour timestep. Then, a final month was simulated and analyzed.

12.2 Results of the perpetual and seasonal ^{7}Be simulations

Figure 12.1 presents the surface ^{7}Be concentrations predicted for the perpetual and seasonal July simulations. Figure 12.2a shows the regions in which the perpetual values are higher than the seasonal, while Figure 12.2b shows the regions in which the seasonal values are higher. Likewise, Figure 12.3 presents concentrations for both scenarios at 800 mb, and figure 12.4 the differences between the perpetual and seasonal July, and Figure 12.5 presents concentrations for 500 mb, and Figure 12.6 the differences between the two.

The positive differences between the perpetual and seasonal July concentrations occur in similar locations at the surface, 800 mb, and 500 mb in Figures 12.2a, 12.4a, and 12.6a. As shown by Reiter (1975), during June-August, large-scale downward transport has a maximum for 0 - 20S, but extends below 30S. Differences in the perpetual and seasonal simulations in this region may be due to differing strengths of the subsidence here. The differences may also be due to differences in local meteorology. The negative differences also occur in similar regions for the surface, 800 mb, and 500 mb.They tend to be located in the northern hemisphere tropics and subtropics, again possibly due to differences in the general circulation. The surface ^{7}Be concentrations are on the order of 100 - 150 femto-Curies/standard m^3, with the differences between the perpetual and seasonal 20 - 60 fCi/sm^3. The 800 mb concentrations are on the order of 300 - 500 fCi/sm^3, with differences of 100 - 200 fCi/sm^3 seen in some locations.

The differences between the perpetual and seasonal simulations may be due in part to differences in the parcel locations, since each simulation was started with a separate initial random parcel distribution. An additional perpetual July simulation was conducted to ascertain the variability in concentrations due to different initial parcel locations. Figure 12.7 shows where the two perpetual July simulations differed in surface concentrations.

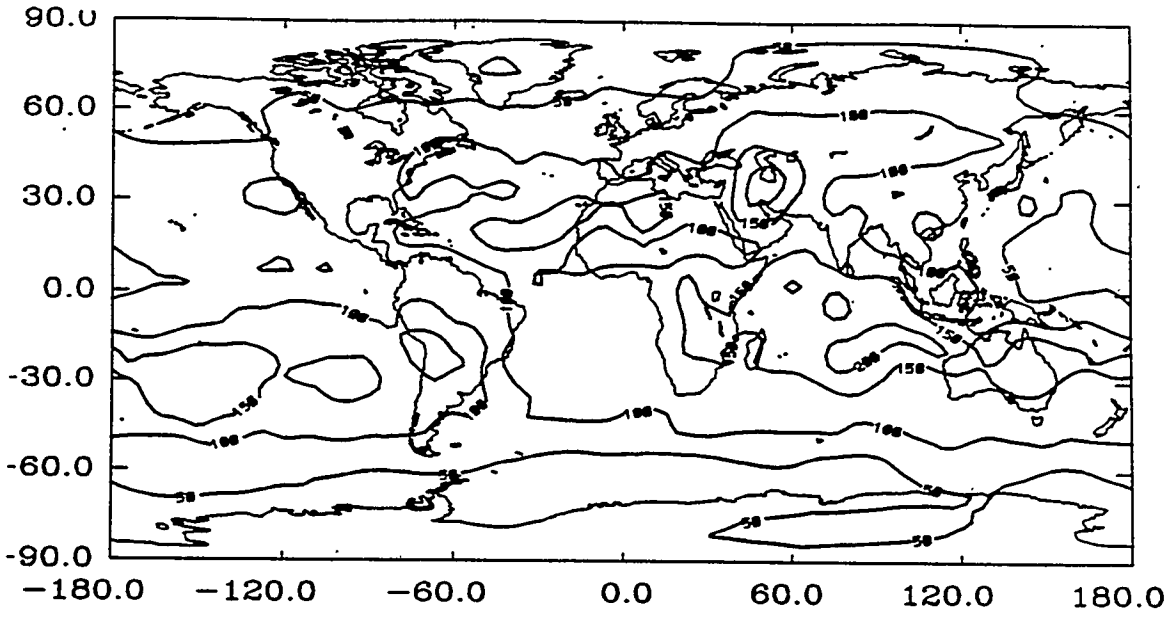

(a) Perpetual July

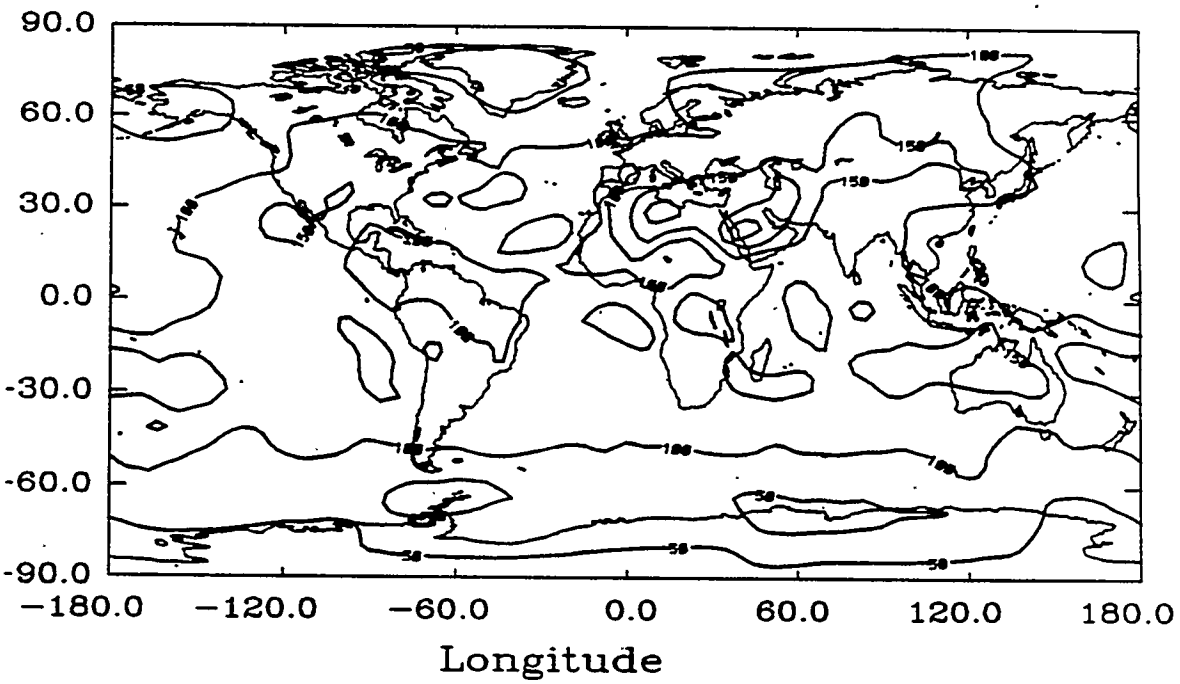

(b) Seasonal July

Figure 12.1 Predicted surface concentrations of ^{7}Be for the (a) Perpetual and (b) Seasonal July scenarios. Contours 25, 50, 100, 150, 200, 250 fCi/sm^3.

The differences are located in some of the same regions, but are on the order of 10 - 30 fCi/sm^3, instead of the 20 - 60 fCi/sm3 difference between the perpetual and seasonal July. Thus, the difference between the perpetual and seasonal simulations appears to be real.

Additionally, surface ^{7}Be concentrations were examined for the CMDL surface sites that have O_3 data (Oltmans, personal communication, 1993). The results are shown in Table 12.1.

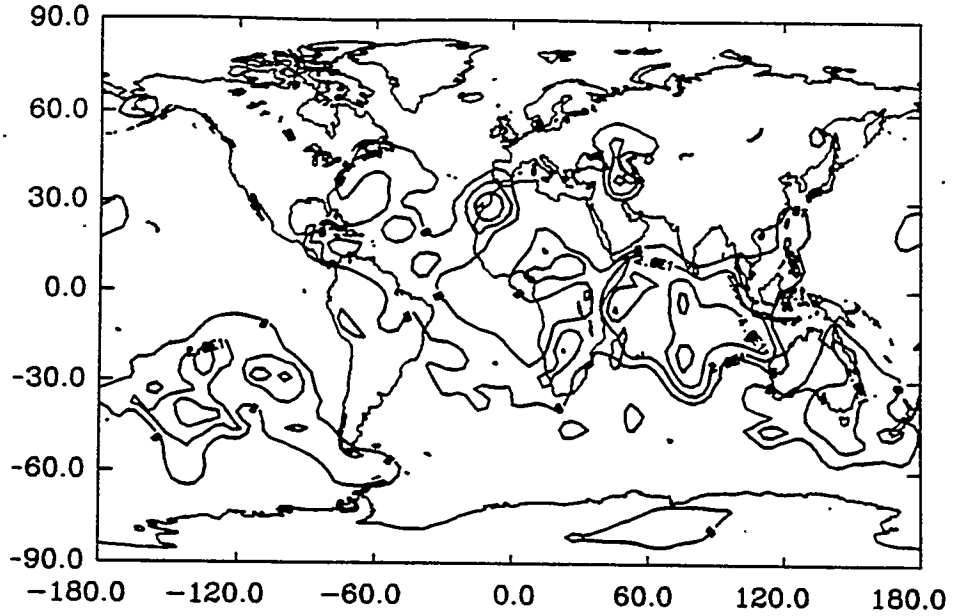

Figure 12.2a The difference between surface ^{7}Be concentrations predicted for perpetual and seasonal July, when the perpetual concentrations are greater. Contours are 0, 20, 40, 60, 80, and 100 fCi/sm^3.

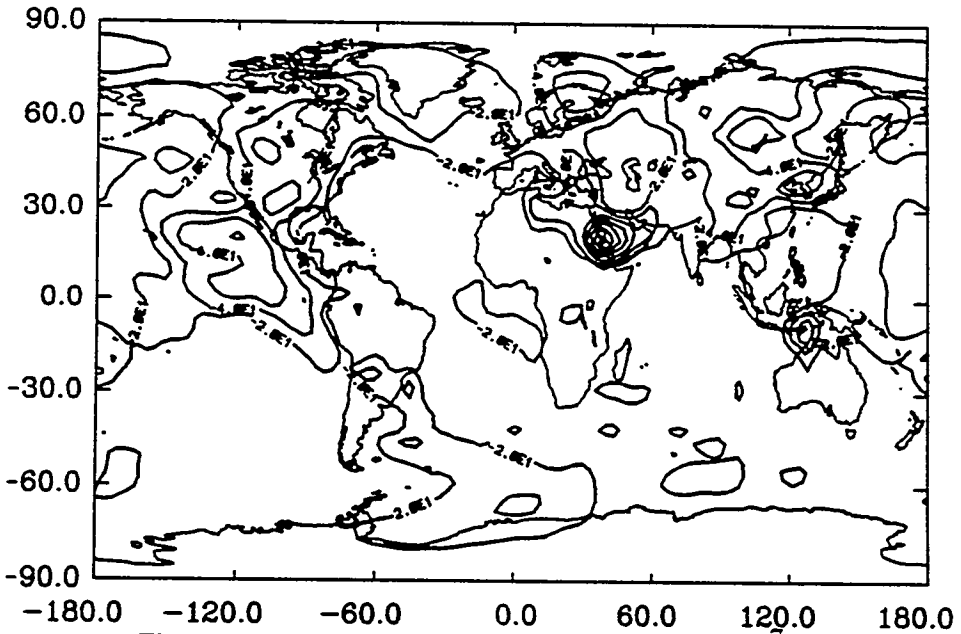

Figure 12.2(b) The difference between surface ^{7}Be concentrations predicted for the perpetual and seasonal July when the seasonal concentrations are greater Contours are 20, 40, 60, 80, 100, 120, and 140 fCi/sm^3.

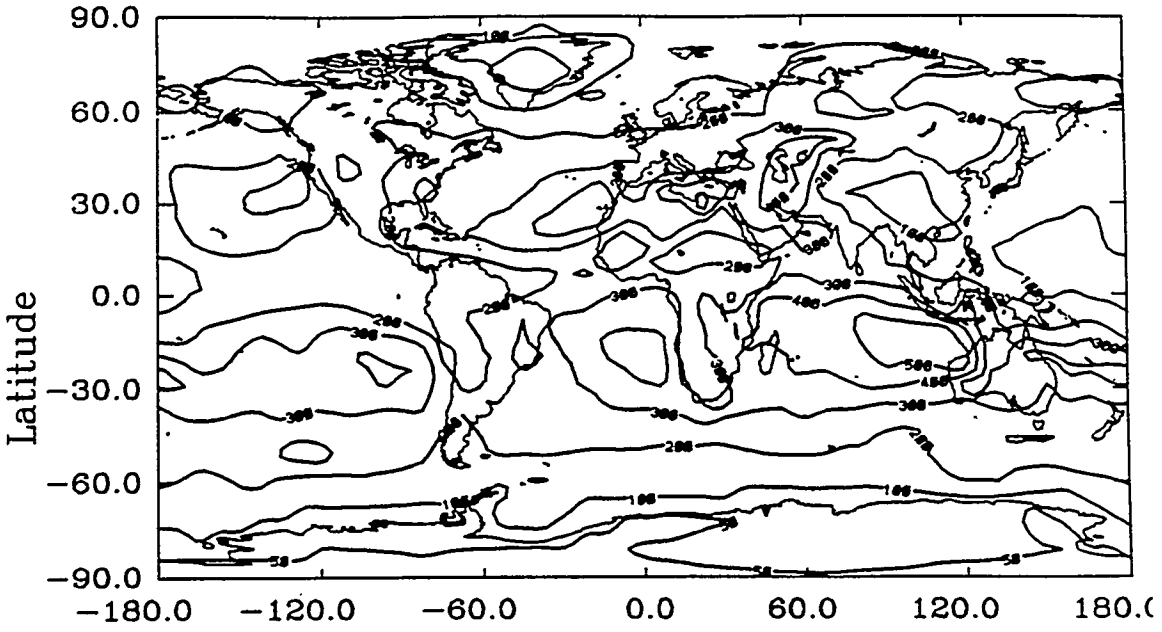

(a) Perpetual July

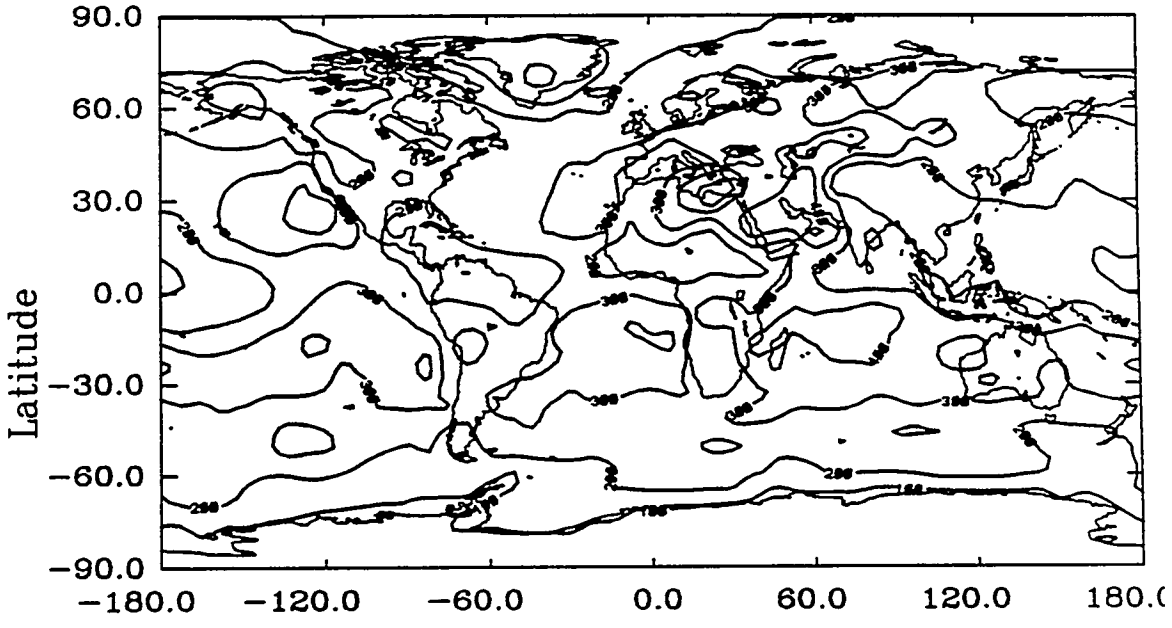

(b) Seasonal July

Figure 12.3 Predicted 800 mb ^{7}Be concentrations for the (a) perpetual and (b) seasonal July simulations. Contours are 50, 100, 200, 300, 400, and 500 femto-Curies/standard m^{3}.

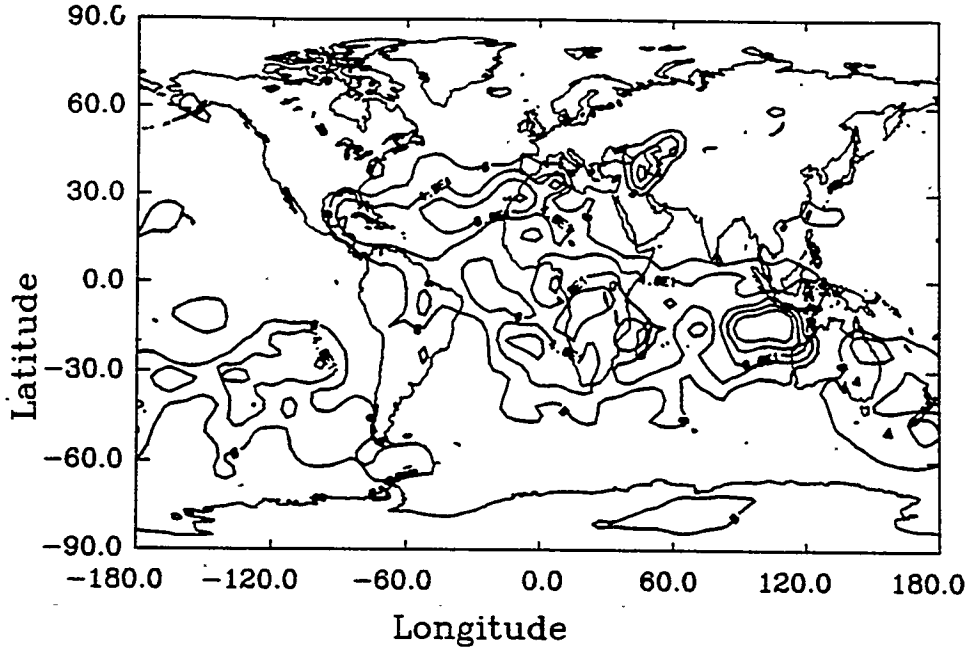

Figure 12.4 (a) The difference between the 800 mb ^{7}Be concentrations predicted for perpetual and seasonal July, where the perpetual concentrations are greater. Contours are 0, 40, 80, 120, 160, and 200 fCi/sm^3.

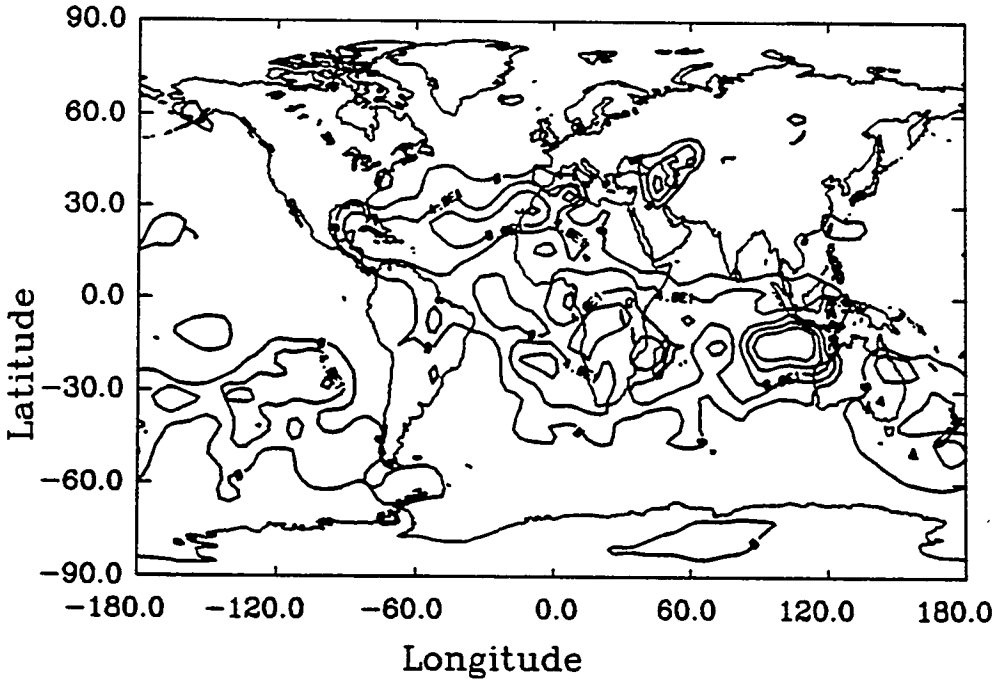

Figure 12.4 (b) The difference between the 800 mb ^{7}Be concentrations predicted for perpetual and seasonal July, where the seasonal concentrations are greater. Contours are 40, 80, 120, 160, 200, 240, and 280 fCi/sm^3.

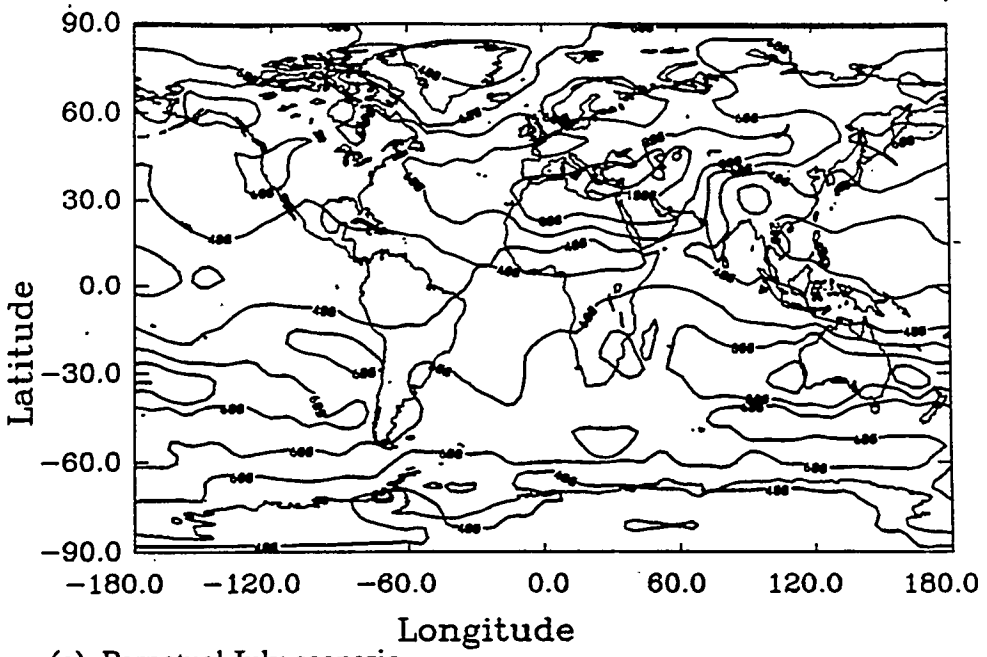

(a) Perpetual July scenario

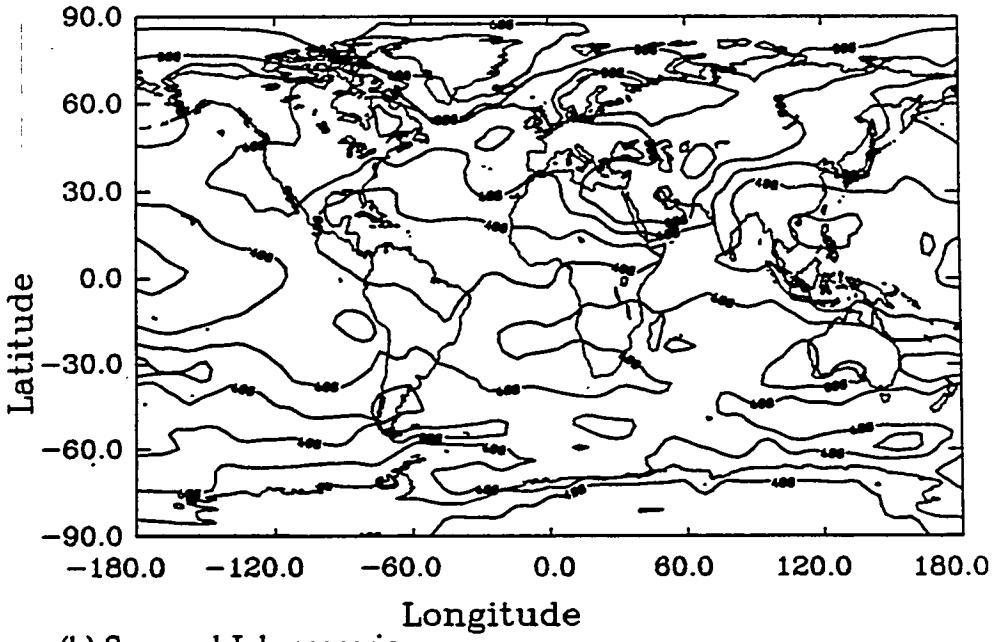

(b) Seasonal July scenario

Figure 12.5 Predicted 500 mb ^{7}Be concentrations for the (a) perpetual and (b) seasonal July simulations. Contours are 100, 200, 400, 600, 800, and 1000 fCi/sm^3.

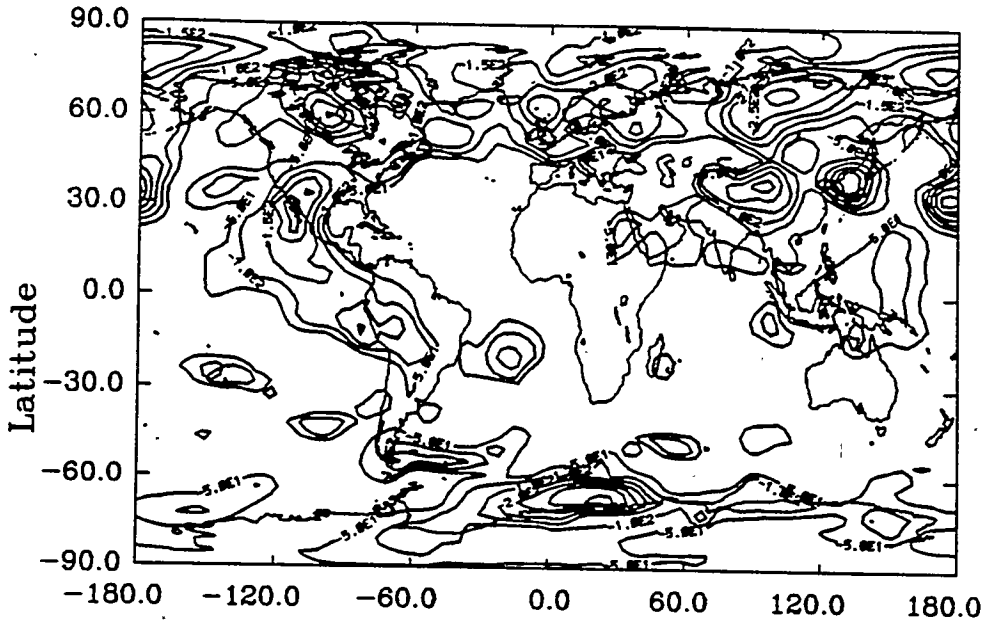

Figure 12.6(a) The difference between the 500 mb ^{7}Be concentrations predicted for perpetual and seasonal July, where the perpetual concentrations are greater. Contours are 0, 50, 100, 150, 200, 250, 300, 350, and 400 fCi/sm^3.

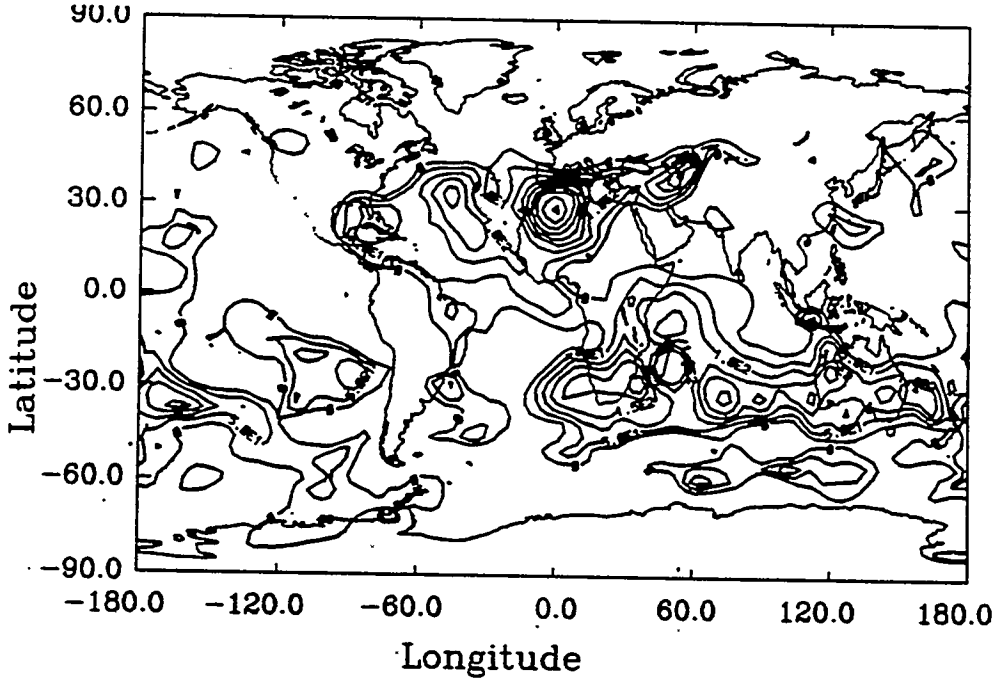

Figure 12.6 (b) The difference between the 500 mb 7Be concentrations predicte for perpetual and seasonal July, where the seasonal concentrations are greater. Contours are 50, 100, 150, 200, 250, 300, 350, and 400 fCi/sm^3.

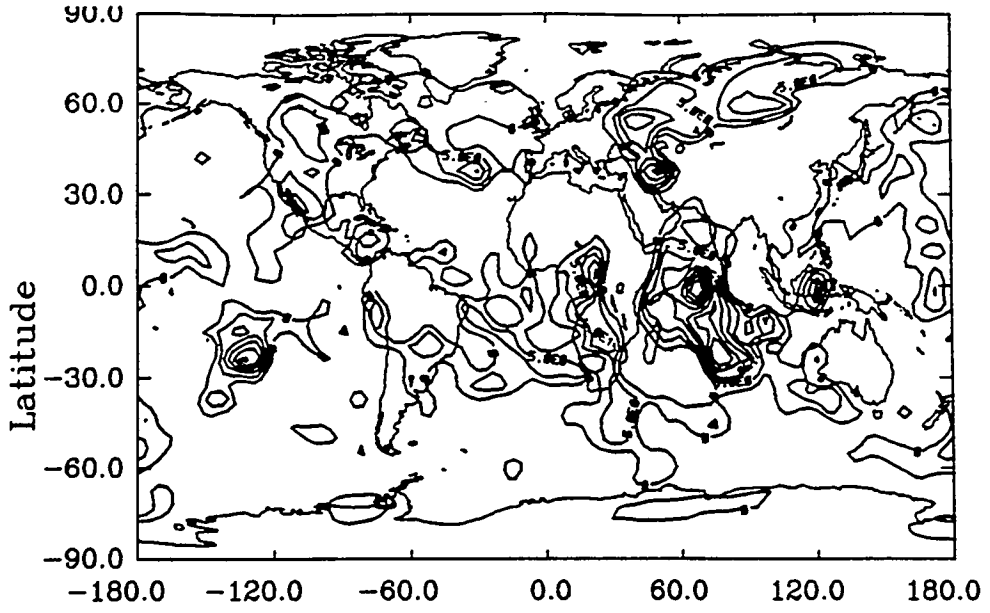

Figure 12.7 (a) Difference in the surface ^{7}Be concentrations for the two perpetual July scenarios. Contours are 5, 10, 15, 20, 25, and 30 fCi/sm^3.

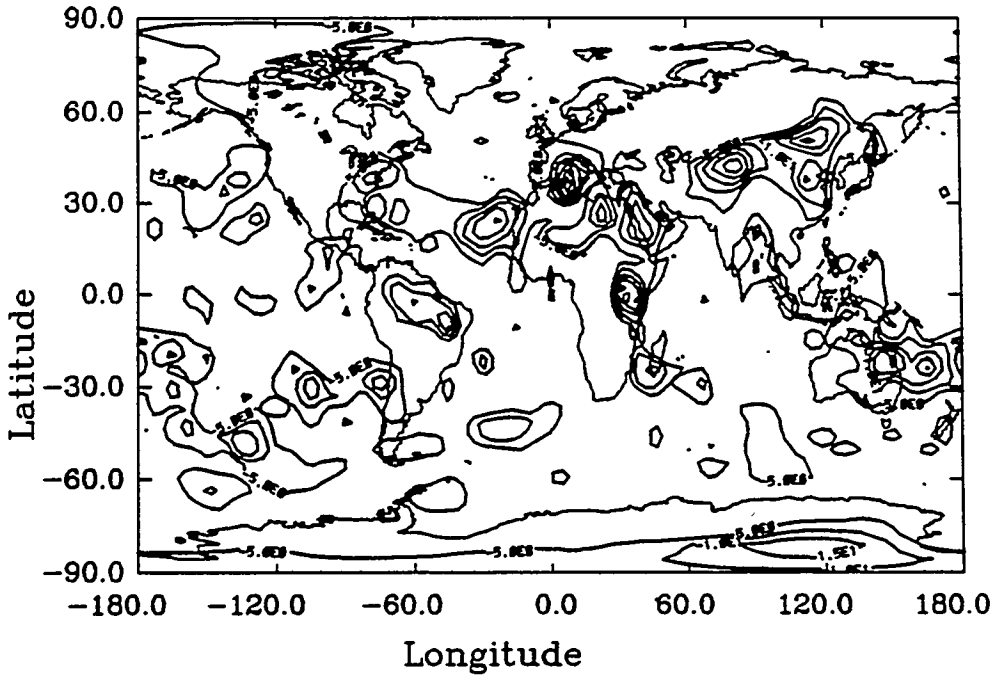

Figure 12.7 (b) Difference in the surface ^{7}Be concentrations for the two perpetual July scenarios (areas where the difference is of opposite as in (a)). Contours are 5, 10, 15, 20, 25, and 30 fCi/sm^3.

Table 12.1: Model predicted surface ^{7}Be, in fCi/sm^3

Site	Seasonal July	Perpetual July (1)	Perpetual July (2)
Barrow (71N, 157W)	53.3	33.6	37.6
Reykjavik (64N, 22E)	111.7	51.2	56.2
Mace Head (53N, 10W)	100.6	71.3	71.6
Niwot Ridge (40N, 106W)	123.2	76.8	74.6
Bermuda (32N, 65W)	99.2	89.4	99.2
Izania (28N, 17W)	125.7	164.0	180.4
Mauna Loa (20N, 156W)	105.3	80.1	84.5
Barbados (13N, 60W)	84.4	99.7	101.5
Samoa (14S, 171W)	114.2	89.8	97.0
South Pole (90S, 102E)	37.6	31.1	42.0

The values in the table reflect the differences shown in Figure 12.2. In the northern hemisphere, the perpetual values are generally 60 - 90% of the seasonal values for continental regions north of 20N. However, for the southern hemisphere tropics and subtropics, the perpetual values are greater than the seasonal. The regions in which the perpetual and seasonal simulations differ the most are regions in which the general circulation is expected to be strong. Reiter (1975) shows a strong downward motion for 5 - 30S and strong upward motion for 5S - 25N. This is consistent with the general circulation pattern being stronger for the perpetual meteorology than the seasonal. (Larger values 5-25S, smaller values for 5S-30N.) If this is the case, then similar results might be expected for the ozone simulation.

Several caveats apply, though. The ^{7}Be is strongly affected by wet removal and, therefore, local precipitation. The difference, therefore, between the perpetual and seasonal

may not be due entirely to general circulation patterns (see, e.g., Brost et al., 1991). Also, the tropospheric lifetime of ^{7}Be is shorter than for O_3, indicating the O_3 may be more affected by the meteorological history than ^{7}Be.

In conclusion, differences do exist between the perpetual and seasonal simulations and the surface, 800mb, and 500mb. These may be due to differences in general circulation of precipitation patterns.

CHAPTER 13 SUMMARY

Two of the most important chemically reactive tropospheric gases are ozone (O_3) and the hydroxyl radical (OH). Their photochemical cycles involve a complex, non-linear set of chemical reactions between atmospheric species that vary substantially in time and space. Their photochemistry is initiated when carbon monoxide (CO), methane (CH_4), and non-methane hydrocarbons (NMHCs) react with nitrogen oxides (NO_x) in the presence of sun. ıt.

In this work, I have developed two versions of a global, three-dimensional, chemistry-transport-deposition model that can simulate tropospheric O_3 and OH production. The first model version incorporated the chemistry necessary to model tropospheric O_3 production from the reactions of CO, CH_4, and NO_x. The second model version also included longer-lived alkane species and the biogenic hydrocarbon isoprene, which is emitted by live plants and trees.

The global model (GRANTOUR) has been used for other global cycles. Past model studies have included climatic response to large scale smoke injections (Ghan et al., 1988), the global reactive nitrogen cycles (Penner et al., 1991; Atherton et al., 1991), the global sulfur cycle (Erickson et al., 1990), and the global cycle of radon and lead (Dignon et al., 1989).

The development of a GRANTOUR version for photooxidant studies included choosing an appropriate chemical reaction mechanism (a subset of all possible chemical reactions) and a numerical solution technique for the chemistry integration. A predictor-corrector method was used in the $CO/CH_4/NOx$ model version. A tropospheric-specific technique (Sillman, 1991) was used in the $CO/CH_4/NMHC/NO_x$ model version. Numerical experiments were performed to further decrease the models' computational time.

Additionally, appropriate dry deposition velocities and wet deposition parameters were chosen. A number of source emission inventories were developed and/or obtained for NO_x and NMHCs. The important NO_x sources include: fossil fuel combustion, biomass burning, lightning, soil emissions, and transport from the stratosphere. The sources of NMHCs include biomass burning and industrial sources of alkanes and biogenic emissions of isoprene. The concentrations of CO and CH_4 were specified based on values published in the literature.

In Chapter 9, the first model version ($CO/CH_4/NOx$ cycle, solved using the predictor-corrector technique) was applied to three different scenarios for a perpetual July set of meteorology. The scenarios are shown in Table 13.1. The scenarios were used to understand the role of anthropogenic sources of NO_x on current O_3 and OH levels, and to understand the total changes in O_3 and OH that have occurred since preindustrial times.

Table 13.1: Three Perpetual July $CO/CH_4/NO_x/OH/O_3$ Scenarios Simulated

Scenario	[CO]	[CH_4]	NO_x emissions
1	Present day	Present day	Natural and Anthropogenic
2	Present day	Present day	Natural
3	Preindustrial	Preindustrial	Natural

The O_3 predicted by scenario 1 was compared to both O_3 surface observations and measured O_3 vertical profiles. In general, the model calculated surface O_3 concentrations are lower than observations. This may be because no NMHCs were included in the model, which would underestimate the O_3 actually produced. Also, several of the observational sites were at high elevations (over 2000 m), which may be influenced by free tropospheric air, which has higher levels of ozone. The GRANTOUR model output is for an average grid zone that is 7.5 degrees by 4.5 degrees, and doesn't resolve highly localized elevations.

The model simulated vertical profiles of O_3 generally overpredicted O_3 mixing ratios in the free troposphere. The O_3 levels specified by the model in the stratosphere were calculated by the LLNL 2D model. In general, the 2D fields are higher than actually observed at CMDL sites for the lowest layers of the stratosphere. Thus, the stratosphere-troposphere exchange of air would lead to higher levels of O_3 in the free troposphere.

Comparing scenarios 1 and 2 illustrates the role of anthropogenic NO_x on present day OH and O_3. Anthropogenic NO_x tends to increase O_3 by 10% on a global scale. Regional increases over continents tend to be higher--10 to 50%. Because OH formation is initiated by the photolysis of tropospheric O_3, concentrations of OH also increased by 10% on a global scale when anthropogenic NO_x was included.

Comparing scenarios 1 and 3 showed the changes in O_3 and OH since preindustrial times. Global tropospheric O_3 increased roughly 50% since preindustrial times because all precursors (NO_x, CO, and CH_4) increased. The hydroxyl radical, OH, however, decreased roughly 10% from preindustrial times. Because reaction with OH is the dominant sink for many tropospheric gases (such as CO and CH_4), as the concentrations of CO and CH_4 increase, OH is depleted.

In Chapter 10, the $CO/CH_4/NO_x$ (predictor-corrector) model version was applied to a seasonal cycle. Scenario 1 and 2 of Chapter 9 (see Table 13.1) were simulated to understand the role of anthropogenic NO_x on seasonal O_3 and OH. The results were similar to the perpetual July calculations. The predicted surface O_3 tended to be lower than observed, and predicted free tropospheric O_3 was higher than observed. The seasonality of surface O_3 measurements was reproduced at several sites. The anthropogenic NO_x tended to increase O_3 and decrease OH.

In Chapter 11, the $CO/CH_4/NMHC/NO_x$ version of the model was applied to three perpetual July scenarios. The scenarios, shown in Table 13.2, included a "background"

scenario (with $CO/CH_4/NO_x$ only), a scenario which also included two alkanes, and a scenario which included isoprene (an important biogenic hydrocarbon).

Table 13.2: Non-methane hydrocarbon simulations

Scenario	"Hydrocarbons"
Background	CO, CH_4
Alkane	CO, CH_4, ethane, propane
Isoprene	CO, CH_4, isoprene

When non-methane hydrocarbons are included in the calculations; peroxyacetyl nitrate (PAN), an important reservoir species of NO_x) is created.. PAN is thermally stable at lower temperatures and may travel long distances, then thermally dissociate, thereby acting as a source of NO_x in remote regions.

Again, both surface concentrations and vertical profiles of O_3 from the isoprene scenario were compared with observations. As discussed above, the surface O_3 concentrations tended to be lower than observed and free tropospheric O_3 mixing ratios higher than observed.

Comparing the background and alkane scenarios shows that with a total ethane source of 8 Tg/yr and propane source of 6 Tg/yr, O_3 is not appreciably affected on a global scale at the surface, or sigma = 0.811 and 0.500. At most, ozone concentrations increase 1 - 2 ppbv. Isoprene, however, does appreciably affect O_3 concentrations at the surface and in the free troposphere. The increases in surface O_3 are highest over the source regions (continents), where O_3 rises 5 - 20 ppbv. Over remote and marine locations the O_3 also increases by roughly 2 ppbv. The increase over remote regions may either be due to increased transport of O_3 to these areas, or the formation of PAN, which is then transported and acts as a reservoir of NO_x in remote locations.

Adding isoprene tends to decrease OH concentrations over the isoprene source

regions (continents) significantly. This phenomenon is constrained to the lowest 200 mb of the atmosphere, because isoprene is so reactive. Over remote marine locations, and possibly in the high northern latitudes, the addition of isoprene actually slightly increased the OH concentrations, perhaps because O_3 concentrations were increased, and its photolysis led to higher OH.

The simple $CO/CH_4/NO_x$ cycle does not produce PAN. If alkanes and/or isoprene are added, PAN is chemically produced. The alkane scenario showed that when alkanes are added, NO_x concentrations decreased over the continental source regions. The remote NO_x concentrations did not change appreciably. For the isoprene scenario, however, NO_x concentrations decreased over the source regions but increased over remote marine regions. The increase was presumably due to the long-range transport of PAN to remote locations, where it thermally decomposed and served as a source of NO_x. Consequently, the O_3 levels also increased over remote marine regions. This may be because the NO_x levels were increased enough to go from NO_x-poor (O_3 consumption) regions to NO_x-rich (O_3 production) regions.

In Chapter 12, the cycle of ^7Be was simulated using both perpetual July and seasonal July meteorology. ^7Be is a radioactive tracer produced by cosmic rays. It is produced primarily in the stratosphere. Concentrations from the two types of meteorology differed most in regions in which the general circulation is expected to be strong. This is consistent with the general circulation pattern being stronger for the perpetual meteorology than the seasonal. The differences may also be explained by differences in precipitation patterns.

References

Altshuller, A.P. 1983. Review: Natural volatile organic substances and their effect on air quality in the United States, Atmos. Env. 17, 2131-2166.

Altshuller, A.P. 1987. Estimation of the natural background of ozone present at surface rural locations, J. Air Poll. Cont. Assn. 37, 1409-1417.

Anderson, I.C., and Levine, J.S., 1987. Simultaneous field measurements of biogenic emissions of nitric oxide and nitrous oxides, J. Geophys. Res. 92, 965-976.

Anfossi. D., Sandroni, S., and Viarengo, S., 1991. Tropospheric ozone in the nineteenth century: The Moncalieri series, J. Geophys. Res. 96, 17,349 - 17,352.

Andreae, M.O., 1991. Biomass burning: Its history, use, and distribution and its impact on environmental quality and global climate, in Global Biomass Burning: Atmospheric, Climatic, and Biospheric Implications, J.S. Levine, ed., MIT Press, Cambridge, MA.

Bedi, J.F., Horvath, S.M., and Drechsler-Parks, D.M. 1988. Reproducibility of the pulmonary function response of older men and women to a 2-hour ozone exposure, J. Air Pollut. Cont. Assn. 38, 1016-1019.

Beloin, N.J. 1973. Test. Chem. Color. 5, 128-133.

Blake, D.R., Woo, V.H., Tyler, S.C. and Rowland, F.S. 1984. Methane concentrations and source strengths in urban locations, Geophys. Res. Lett. 11, 1211-1214.

Blake, D.R. and Rowland, F.S. 1986. World-wide increase in tropospheic methane, 1978-1983, J. Atmos. Chem. 4, 43-62.

Blake, D.R. and Rowland, F.S. 1988. Continuing worldwide increase in tropospheric methane, 1978 to 1987, Science 239, 1129-1131.

Bojkov, R.D. 1986. Surface ozone during the second half of the nineteenth century, J. Clim. Appl. Met. 25, 343-352.

Bonsang, B., Kanakidou, M., Lambert, G., and Monfray, P., 1988. The marine source of C_2-C_6 aliphatic hydrocarbons, J. Atmos. Chem., 6, 3-20.

Bonsang, B., Kanakidou, M., and Lambert, 1990. NMHC in the marine atmosphere: Preliminary resutls of monitoring at Amsterdam Island, J. Atmos. Chem. 11, 169-178.

Bonsang, B., G. Lambert, and C.C. Boissard, 1991. Light hydrocarbons emissions from African savanna burnings, in Global biomass burning: Atmospheric, climatic, and biospheric implications, J.S. Levine, ed., MIT Press, Cambridge, MA.

Bottenheim, J., Gallant, A., and Brice, K. 1986. Measurements of NO_y species and O_3 at 82 degrees N latitude, Geophys. Res. Lett. 13, 113-116.

Brasseur, G., Hitchman, M.H., Walter, S., Dymek, M., Falise, E., and Pirre, M., 1990 An interactive chemical dynamical radiative two-dimensional model of the middle atmosphere, J. Geophys. Res. 95, 5639-5655.

Brost, R.A., Feichter, J., and Heimann, M. 1991. Three-dimensional simulation of ^{7}Be in a global climate model, J. Geophys. Res. 96, 22,423-22,445.

Brown, P.N., Byrne, G.D., and Hindmarsh, A.C., 1989. VODE: A Variable Coefficient ODE solver, SIAM J. Sci. Stat. Comput. 10, 1038-1051.

Campbell, G.G., Schurr, G.G., Slawikowski, D.E., Spence, J.W. 1974. J. Paint Technol. 46, 59-71.

Cess, R.D., Potter, G.L., Blanchet, J.P., Boer, G.J., Ghan, S.J., Kiehl, J.T., Le Treut, H., Li, Z.-X., Liang, X.-Z., McAvaney, B.J., Meleshko, V.P., Mitchell, J.F.B., Morcrette, J.-J., Randall, D.A., Rikus, L., Roeckner, E., Schlese, U., Sheinin, D.A., Slingo, A., Sokolov, A.P., Taylor, K.E., Washington, W.M., Wetherald, R.T., and Yagai, I. 1989. Intercomparison and interpretation of climate feedback processes in sixteen atmospheric general circulation models, J. Geophys. Res. 95, 16,601-16,615.

Chameides, W. and Walker, J.C.G. 1973. A photochemical theory of tropospheric ozone, J. Geophys. Res. 78, 8751-8760.

Chameides, W.L. and Davis, D.D., 1982. Chemistry in the troposphere, Chem. Eng. News 60, 38-52.

Chameides, W.L., Lindsay, R.W., Richardson, J., and Kiang, C.S., 1988. The role of biogenic hydrocarbons in urban photochemical smog: Atlanta as a case study, Science 241, 1473-1475.

Chappellaz, J., Barnola, J.M., Raynaud, D., Korotkevich, Y.S., and Lorius, C. 1990. Ice core record of atmospheric methane over the past 160,000 years, Nature 354, 127-131.

Chung, Y.S. and Dann, T. 1985. Observations of stratospheric ozone at the ground level in Regina, Canada, Atmos. Env. 19, 157-162.

Coffin, D.L. and Stockinger, H.E. 1977. Biological effects of air pollutants, in "Air Pollution (Third Edition)", A.C. Stern (ed.), Academic Press, New York, 1977, p.233-263.

Condon, E.P., Danielsen, E.F., Sachse, G.W., and Hill, G.F. 1987. Carbon monoxide measurements over the eastern Pacific during GTE/CITE 1. J. Geophys. Res. 92, 2095-2102.

Craig, H. and Chou, C.C. 1982. Methane: The record in polar ice cores, Geophys. Res. Lett. 9, 1221-1224.

Crutzen, P. 1973. A discussion of the chemistry of some minor constituents in the stratosphere and troposphere, Pure Appl. Geophys. 106-108, 1385-1399.

Crutzen, P.J. 1979. The role of NO and NO_2 in the chemistry of the troposphere and stratosphere, Ann. Rev. Earth Planet. Sci. 7, 443-472.

Crutzen, P.J., Delany, A.C., Greenberg, J., Haagenson, P., Heidt, L., Lueb, R., Pollock, W., Seiler, W., Wartburg, A., and Zimmerman, P. 1985. Tropospheric chemical composition measurements in Brazil during the dry season, J. Atmos. Chem. 2, 233-256.

Crutzen, P.J. and L.T. Gidel, 1983. A two-dimensional photochemical model of the atmosphere 2: The tropospheric budgets of the anthropogenic chlorocarbons, CO, CH_4, CH_3Cl and the effect of various NO_x sources on tropospheric ozone, J. Geophys. Res., 88, 6641 - 6661.

Crutzen, P.J. and P.H. Zimmermann, The changing photochemistry of the troposphere, Tellus 43AB, 136-151, 1991.

Danielsen, E.F. and V. A. Mohnen, 1977. Project duststorm report: Ozone transport, in situ measurements, and meteorological analyses of tropopause folding, J. Geophys. Res. 82, 5867-5877.

Danielsen, E.F. 1968. Stratospheric-tropospheric exchange based on radioactivity, ozone and potential vorticity. J. Atmos. Sci. 25, 502-518.

Dasch, J.M., 1983. A comparison of surrogate surfaces for dry deposition collection, in Precipitation scavenging, dry depositon, and resuspension, Vol. 2 ; H.R. Pruppacher, R.G. Semonin, and W.G.N. Slinn, eds., pp. 883-902, Elsevier, New York.

Dasch. J.M., 1986. Measurement of dry deposition to vegetative surfaces, Water Air Soil Poll. 30, 205-210.

DeMore, W.B., S.P. Sander, D.M. Golden, R.F. Hampson, M.J. Kurylo, C.J. Howard, A.R. Ravishnkara, C.E. Kolb, and M.J. Molina, 1992. Chemical kinetics and photochemical data for use in stratospheric modeling, JPL Publication 92-20, Jet Propulsion Laboratory, California Institute of Technology, Pasadena, California.

Dickinson, R.E. and Cicerone, R.J. 1986. Nature 319, 109-115.

Dignon, J., Hameed, S., Penner, J.E., Walton, J.J., and Ghan, S. 1989. Global simulation of ^{222}Rn and ^{210}Pb in a 3-dimensional Lagrangian tracer model, EOS 70, 1025.

Dignon, J., Atherton, C.S., Penner, J.E., and Walton, J.J., 1991a. NO_x pollution from biomass burning: A global study, UCRL-JC-104735, presented at the 11th Conference on Fire and Forest Meteorology, Missoula, MT, April 16-19, 1991.

Dignon, J., Penner, J.E., Atherton, C.S., and Walton, J.J., 1991b. Atmospheric reactive nitrogen: A model study of natural and anthropogenic sources and the role of microbial soil emissions, presented at the CHEMRAWN VII World Conference on the CHemistry of the atmosphere, December, Baltimore, MD (also UCRL-JC-107393).

Dignon, J., 1992. NO_x and SO_x emissions from fossil fuels: A global distribution, Atmos. Environ. 26a, 1157-1163.

Dimitriades, B. 1981. The role of natural organics in photochemical air pollution, J. Air Pollut. Cont. Assn. 31, 229-235.

Dolske, D.A. and Gatz, D.F., 1985. A field intercomparison of methods for the measurement of particle and gas dry deposition, J. Geophys. Res. 90, 2076-2084.

Donahue, N.M. and Prinn, R.G., 1990. Nonmethane hydrocarbon chemistry in the remote marine boundary layer, J. Geophys. Res. 95, 18,387-18,411.

Eisele, F.L., and Tanner, D.J., 1991. Ion-assisted tropospheric OH measurements, J. Geophys. Res. 96, 9295-9308.

Erickson, D.J., Walton, J.J., Ghan, S.J., and Penner, J.E. 1989. Three-dimensional modeling of the global atmoshperic sulfur cycle: The origin of cloud condensation nuclei over the North Atlantic region, EOS 70, 1045.

Erickson, D.J., Ghan, S.J., and Penner, J.E. 1990. Global Ocean-to-Atmosphere Dimethyl Sulfide Flux, J. Geophys. Res. 95, 7543-7552.

Fahey, D.W., Hubler, G., Parrish, D.D., Williams, E.J., Norton, R.B., Ridley, B.A., Singh, H.B., Liu, S.C., and Fehsenfeld, F.D. 1986. Reactive nitrogen species in the troposphere: Measurements of NO, NO_2, HNO_3, particulate nitrate, peroxyacetyl nitrate (PAN), O_3, and total reactive odd nitrogen (NO_y) at Niwot Ridge, Colorado, J. Geophys. Res. 91, 9781-9793.

Fehsenfeld, F.D., Bollinger, M.J., Liu, S.C., Parrish, D.D., McFarland, M., Trainer, M., Kley, D., Murphy, P.C., Albritton, D.L., and Lenschow, D.H. 1983. A study of ozone in the Colorado Mountains, J. Atmos. Chem. 1, 87-105.

Felton, C.C., Sheppard, J.C., and Campbell, M.J. 1988. Measurements of the diurnal OH cycle by a ^{14}C-tracer method, Nature 335, 53-55.

Finlayson-Pitts, B.J. and Pitts, J.N. Jr. 1986. Atmospheric Chemistry: Fundamentals and Experimental Techniques, J. Wiley & Sons, New York.

Fishman, J., Gregory, G.L., Sachse, G.W., Beck, S.M., and Hill, G.F. 1987. Vertical profiles of ozone, carbon monoxide, and dew-point temperature obtained during GTE/CITE1, October-November 1983.

Fishman, J., Vukovich. F.M, Cahoon, D.R., Shipman, M.C. 1987. The characterization of an air pollution episode using satellite total ozone measurements, J. Clim. Appl. Met. 26, 1638-1654.

Fishman, J., Fakhruzzaman, K., Cros, B., and Nganga, D., 1991. Identification of widespread pollution in the southern hemisphere deduced from satellite analyses, Science 252, 1693 - 1696.

Fraser, P.J. and Hyson, P. 1986. Methane, carbon monoxide and methylchloroform in the southern hemisphere, J. Atmos. Chem. 4, 3-42.

Fung, I., John, J., Lerner, J., Matthews, E., Prather, M., Steele, L.P., and Fraser, P.J., 1991. Three-dimensional model synthesis of the global methane cycle, J. Geophys. Res. 96, 13,033-13,065.

Gauntner, D.J., Nyland, T., Tiefermann, M. and Dudzinski, T. 1979. Measurements of carbon monoxide, condensation nuclei, and ozone on a B 747SP aircraft flight around the world, Geophys. Res. Lett. 6, 167-170.

Ghan, S.J., MacCracken, M.C., and Walton, J.J. 1988. Climatic response to large atmospheric smoke injections: Sensitivity studies with a tropospheric general circulation model, J. Geophys. Res 93, 8315-8338.

Giorgi, F., and W.L. Chameides,1985. The rainout parameterization in a photochemical model, J.Geophys. Res., 90, 7872-7880.

Giorgi, F. and W.L. Chameides,1986. Rainout lifetimes of highly soluble aerosols and gases as inferred from simulations with a general circulation model, J. Geophys. Res., 91, 14,367-14,376.

Graedel, T.E. 1979. Terpenoids in the atmosphere, Rev. Geophys. Space Phys. 17, 937-947.

Greenberg, J.P., Zimmerman, P.R., Heidt, L., and Pollock, W., 1984. Hydrocarbon and carbon monoxide emissions from biomass burning in Brazil, J. Geophys. Res., 89, 1350-1354.

Greenberg, J.P., Zimmerman, P.R., and Haagenson, P., 1990. Tropospheric hydrocarbon and CO profiles over the U.S. West Coast and Alaksa, J. Geophys. Res. 95, 14,015-14,026.

Greenberg, J.P., Zimmerman, P.R., Pollock W.F., Lueb, R.A., and Heidt, L.E., 1992. Diurnal variability of atmospheric methane, nonmethane hydrocarbons, and carbon monoxide at Mauna Loa, J. Geophys. Res. 97, 10,395-10,413.

Grosjean, D. and Fung, K. 1984. Hydrocarbons and carbonyls in Los Angeles air, J. Air Poll. Cont. Assn. 34, 537-543.

Haagen-Smit, A.J. 1952. Chemistry and physiology of Los Angeles smog, Ind. Eng. Chem. 44, 1342-1346.

Hameed, S., Paidoussis, O.G., and Stewart, R.W., 1981. Implications of natural sources for the latitudinal gradients of NO_y in the unpolluted troposphere, Geophys. Res. Lett. 8, 591-594.

Handbook of Geophysics, 1960. United States Air Force Research and Development Command, The Macmillan Co., New York.

Hao, W.M., Liu, M.-H., and Crutzen, P.J., 1990. Estimates of annual and regional releases of CO2 and other trace gases to the atmosphere from fires in the tropics, based on the FAO statistics for the period 1975-1980, in Fire in the Tropical Biota (Ecological Studies, Vol. 84), J.G. Goldammer, ed., Springer-Verlag, New York, p.440-462

Hard, T.M., Chan, C.Y., Mehrabzadeh, A.A., Pan, W.H. and O'Brien, R.J. 1986. Diurnal cycle of tropospheric OH, Nature 322, 617-620.

Heck, W.W. and Brandt, C.S. 1977. Effects on vegetation: Native, crops, forests, in "Air Pollution (Third Edition)", A.C. Stern (ed.), Academic Press, New York, 1977, p.158-231.

Heck, W.W., Adams, R.M., Cure, W.W., Heagle, A.S., Heggestad, H.E., Kohut, R.J., Kress, L.W., Rawlings, J.O., and Taylor, O.C. 1983. A reassessment of crop loss from ozone, Environ. Sci. Tech. 17, 572A-581A.

Heidt, L.E., Krasnec, J.P., Lueb, R.A., Pollock, W.H., Henry, B.E., and Crutzen, P.J., 1980. Latitudinal distributions of CO and CH_4 over the Pacific, J. Geophys. Res. 85, 7329-7336.

Hewitt, C.N. and Harrison, R.M. 1985. Tropospheric concentrations of the hydroxyl radical--a review, Atmos. Env. 19, 545-554.

Hicks, B.B., 1986. Measuring dry deposition: A reassessment of the start of the art, Water Air Soil Poll. 30, 75-90.

Hicks, B.B. and D.R. Matt, 1988. Combining biology, chemistry, and meteorology in modeling and measuring dry deposition, J. Atmos. Chem. 6, 117-131.

Hindmarsh, A.C., 1974. Gear: Ordinary differential equation system solver, LLNL Report UCID-300001, Rev. 3, Livermore, CA.

Hough, A.M., 1991. Development of a two-dimensional global tropospheric model: Model chemistry, J. Geophys. Res. 96, 7325-7362.

Huebert, B.J. and Robert, C.H.,1985. The dry deposition of nitric acid to grass, J. Geophys. Res. 90, 2085-2090.

Isaksen, I.S.A. and O. Hov, 1987. Calculation of trends in the tropospheric concentration of O_3, HNO_3, CH_3CCl_3, O_3, CH_4,and NO_x, Tellus 39B, 271-285.

Isaksen, I.S.A., O. Hov, S.A. Penkett, and A.Semb, 1985. Model analysis of the measured concentration of organic gases in the Norwegian Arctic, J. Atmos. Chem. 3, 3-27.

Isaksen, I. and H. Rodhe, 1978. A two-dimensional model for the global distribution of gases and aerosol particles in the troposphere, Report AC-47, International Meteorological Institute, University of Stockholm.

Jacob, D.J., Sillman, S., Logan, J.A., and Wofsy, S.C. 1989. Least independent variables method for simulation of tropospheric ozone, J. Geophys. Res. 94, 8497-8509.

Jacob, D.J., Logan, J.A., Yevich R.M., Gardner, G.M., Spivakovsky, C.M., Wofsy, S.C., Munger, J.W., Sillman, S., Prather, M.J., Rodger, J.O., Westberg, H., and P.R. Zimmerman, 1993. Simulation of summertime ozone over North America, J. Geophys. Res. 98, 14,8797 - 14,816.

Janach, W.E. 1989. Surface ozone: Trend details, seasonal variations, and interpretation. J. Geophys. Res. 94, 18289-18295.

Junge, C.E. 1962. Global ozone budget and exchange between stratosphere and troposphere, Tellus 14, 363-377.

Kanakidou, M., H.B. Singh, K.M. Valentin, and P.J. Crutzen,1991. A two-dimensional study of ethane and propane oxidation in the troposphere, J. Geophys. Res. 96, 15,395 - 15,413.

Kanakidou, M. and Crutzen, P.J., 1993. Scale problems in global tropospheric chemistry modeling: comparison of results obtained with a three-dimensional model, adopting longitudinally uniform and varying emission of NO_x and NMHC, Chemosphere. 26. 787-801.

Kasibhatla, P.S., Levy, H. II, Moxim, W.J., and Chameides, W.L., 1991. The relative impact of stratospheric photochemical production on tropospheric NO_y levels: A model study, J. Geophys. Res. 96, 18,631-18,646.

Kasibhatla, P.S., Levy, H., II, and Moxim, W.J., 1993. Global NO_x, HNO_3, PAN, and NO_y distributions from fossil fuel combustion emissions: A model study, J. Geophys Res 98, 7165-7180.

Khalil, M.A.K., and Rasmussen, R.A., 1982. Secular trends of atmospheric methane. Chemosphere 11, 877-883, 1982.

Khalil, M.A.K. and Rasmussen, R.A. 1983. Sources, sinks, and seasonal cycles of atmospheric methane, J. Geophys. Res. 88, 5131-5144.

Khalil, M.A.K. and Rasmussen, R.A. 1984. Carbon monoxide in the Earth's atmosphere: Increasing trend, Science 224, 54-56.

Khalil, M.A.K. and Rasmussen, R.A. 1987. Atmospheric methane: Trends over the last 10,000 years, Atmos. Environ. 21, 2445-2452.

Khalil, M.A.K. and Rasmussen, R.A. 1988. Carbon monoxide in the Earth's atmosphere: indications of a global increase, Nature 332, 242-245.

Khalil, M.A.K., Rasmussen, R.A., and Shearer, M.J. 1989. Trends of atmospheric methane during the 1960s and 1970s. J. Geophys. Res. 94, 18279-18288.

Killus, J.P. and Whitten, G.Z. 1984. Isoprene: A photochemical kinetic mechanism, Environ. Sci. Tech. 18, 142-148, 1984.

Kirchhoff, V.W.J.H. 1984. Are northern hemisphere tropospheric ozone densities larger?, EOS Trans. AGU 65, 449-450.

Kirchhoff, V.W.J.H. 1988. Surface ozone measurements in Amazonia, J. Geophys. Res. 93, 1469-1476.

Kirchhoff, V.W.J.H., Browell, E.V. and Gregory, G.L. 1988. Ozone measurements in the troposphere of an Amazonian rain forest environment, J. Geophys. Res. 93, 15850-15860.

Komhyr, W.D., Oltmans, S.J., Franchois, P.R., Evans, W.F.J., and Matthews, W.A., 1989. The latitudinal distribution of ozone to 35 km altitude from ECC ozonesonde observations, 1985-1987, Proc. Quadrennial Ozone Symposium 1988 and Tropospheric Ozone Workshop, edited by R.D. Bojkov and P. Fabian, 147-150, A Deepak, Hampton, VA.

Komhyr, W.D., Oltmans, S.J., Lathrop, J.A., Kerr, J.B., and Matthews, W.A., 1992. The latitudinal distribution of ozone to 35 km altitude from ECC ozonesonde observations, 1982-1990, to appear in the Proc. Quadrennial Ozone Symposium 1992.

Lal, D., and Peters, B., 1967. Cosmic ray produced radioactivity on the earth, Handbuch der Physik, XLVI/2, 551-612, Springer-Verlag, New York.

Lamb, B., Westberg, H., Allwine, G., and Quarles, T. 1985. Biogenic hydrocarbon emissions from deciduous and coniferous trees in the United States, J. Geophys. Res. 90, 2380-2390.

Lamb, B., Guenther, A., Gay, D., and Westberg, H. 1987. A national inventory of biogenic hydrocarbon emissions, Atmos. Env. 21, 1695-1706.

Langner, J., and H. Rodhe, 1991. A global three-dimensional model of the tropospheric sulfur cycle, J. Atmos. Chem.13, 225-263.

Laursen, K., K., Hobbs, P.V., Radke, LF., and Rasmussen, R.A., 1992. Some trace gas emissions from North American biomass fires with an assessment of regional and global fluxes from biomass burning, J. Geophys. Res. 97, 20,687-20701.

Lefohn, A.S. and Pinkerton, J.E. 1988. High resolution characterization of ozone data from sites located in forested areas of the United States, J. Air Poll. Cont. Assn. 38, 1504-1511.

Levy, H. 1972. Photochemistry of the lower troposphere, Planet. Space Sci. 20, 919-935.

Levy, H. 1973. Photochemistry of minor constituents of the lower troposphere, Planet. Space Sci. 21, 575-591.

Levy, H., Mahlman, J.D., Moxim, W.J., and Liu, S.C. 1985. Tropospheric ozone: The role of transport, J. Geophys. Res. 90, 3753-3772.

Levy, H. and Moxim, W.J. 1987. Fate of US and Canadian combustion nitrogen emissions. Nature 328, 414-416.

Levy, H and Moxim, W.J. 1989. Influence of long-range transport of combustion emissi on the chemical variability of the background atmosphere, Nature 338, 326-328.

Lin, S., Trainer, M., and Liu, S.C., 1988. On the nonlinearity of the tropospheric ozone production, J. Geophys. Res., 93, 15,789-15,888.

Lindberg, S.E. and Lovett, G.M., 1983. Application of surffogate surface and leaf extraction methods to estimation of dry deposition to plant canopies, in Precipitation scavenging, dry depositon, and resuspension, Vol. 2 , H.R. Pruppacher, R.G. Semonin, and W.G.N. Slinn, eds., pp. 883-902, Elsevier, New York.

Liu, S.C., Trainer, M., Fehsenfeld, F.C., Parrish, D.D., Williams, E.J., Fahey, D.W., Hubler, G., and Murphy, P.C. 1987. Ozone production in the rural troposphere and the implications for regional and global ozone distributions, J. Geophys. Res. 92, 4191-4207.

Lloyd, A.C., Atkinson, R., Lurmann, F.W. and Nitta, B. 1983. Modeling potential ozone impacts from natural hydrocarbons--I. Development and testing of a chemical mechanism for the NO_x-air photooxidations of isoprene and alpha-pinene under ambient conditions, Atmos. Env. 17, 1931-1950.

Logan, J.A., Prather, M.J., Wofsy, S.C., and McElroy, M.B. 1981. Tropospheric chemistry: A global perspective, J. Geophys. Res. 86, 7210-7254.

Logan, J.A. 1983. Nitrogen oxides in the troposphere: Global and regional budgets, J. Geophys. Res. 88, 10785-10807.

Logan, J.A. 1985. Tropospheric ozone: Seasonal behavior, trends, and anthropogenic influence, J. Geophys. Res. 90, 10463-10482.

Logan, J.A. 1989. Ozone in rural areas of the United States, J. Geophys. Res. 94, 8511-8532.

Lonneman, W.A., Seila, R.L., and Bufalini, J.J. 1978. Ambient air hydrocarbon concentrations in Florida, Environ. Sci. Tech. 12, 459-463.

Lurmann, F.S., Lloyd, A.C., and Atkinson, R., 1986. A chemical mechanism for use in long-range transport/acid deposition computer modeling, J. Geophys. Res. 91, 10,095-10.936.

Mahlman, J.D., H. Levy II, and W.J. Moxim, 1980, Three-dimensional tracer structure and behavior as simulated in two ozone precursor experiments, J. Atmos. Sci. 37, 655-685.

Marenco, A. 1986, Variations of CO and O_3 in the troposphere: Evidence of O_3 photochemistry, Atmos. Env. 20, 911-918.

Marenco, A., Macaigne, M. and Prieur, S. 1989. Meridional and vertical CO and CH_4 distributions in the background troposphere from scientific aircraft measurements during the STRATOZ III experiment, Atmos. Env. 23, 185-200.

Matthews, E., 1983. Global vegetation and land use: New high-resolution data bases for climate studies, J. Clim. and Appl. Meteor., 22, 474-487.

Muller, J.-F., 1992. Geographical distibution and seasonal variation of surface emissoins and deposition velocities of atmospheric trace gases, J. Geophys. Res. 97, 3787-3804.

National Research Council, 1991. Rethinking the ozone problem in urban and regional air pollution, National Academy Press, Washington, D.C.

Newell, R.E., J.W. Kidson, D.C. Vincent and G.J. Boer, 1972. The general circulation of the tropical atmosphere and interactions with extratropical latitudes, Vol. 1., MIT Press, Cambridge, Mass.

Newell, R.E., J.W. Kidson, D.G. Vincent and G.J. Boer, 1974. The general circulation of the tropical atmosphere and interactions with extratropical latitudes, Vol. 2, MIT Press,Cambridge, Mass.

Newton, R.G. 1945. J. Rubber Res. 14, 27-39.

Oltmans, S.J. 1981. Surface ozone measurements in clean air, J. Geophys. Res. 86, 1174-1180.

Oltmans, S.J., and Levy, H. II, 1993. Surface ozone measurements from a global network, Atmos. Environ., accepted for publication, March, 1993.

Oort, A.H., 1983. Global atmospheric circulation satistics, 1958-1973, NOAA Professional Paper 14, U.S. Dept. of Commerce, Superintendent of Documents, U.S. Government Printing Office, Washington, D.C. 20402.

Parrish, D.D., J.S. Holloway, M. Trainer, P.C. Murphy, G.L. Forbes, F.C. Fehsenfeld, 1993. Export of North American ozone pollution to the North Atlantic Ocean, Science 259, 1436-1439.

Parrish, D.D., Fahey, D.W., Williams, E.J., Liu, S.C., Trainer, M., Murphy, P.C., Albritton, D.L. and Fehsenfeld, F.C. 1986a. Background ozone and anthropogenic ozone enhancement at Niwot Ridge, Colorado J. Atmos. Chem. 4, 63-80.

Parrish, D.D., Trainer, M., Williams, E.J., Fahey, D.W., Hubler, G., Eubank, C.S., Liu, S.C., Murphy, P.C., Albritton, D.L., and Fehsenfeld, F.C. 1986b. Measurements of the NO_x-O_3 photostationary state at Niwot Ridge, Colorado, J. Geophys. Res. 91, 5361-5370.

Paulson, S.E. and J.H. Seinfeld, 1992. Development and evaluation of a photooxidation mechanism for isoprene, J. Geophys. Res. 97, 20,703-20,715.

Penkett, S.A., Balke, N.J., Lightman, P., Marsh, A.R.W., Anwyl, P., and G. Butcher, 1993. The seasonal variation of nonmethane hydrocarbons in the free troposphere over the North Atlantic Ocean: Possible evidence for extensive reaction of hydrocarbons with the nitrate radical, J. Geophys. Res. 98, 2865-2885.

Penner, J.E., Atherton, C.S., Dignon, J., Ghan, S.J., Walton, J.J., and Hameed, S. 1990. Tropospheric nitrogen: A three-dimensional study of sources, distributions, and deposition, J. Geophys. Res.96, 959-990.

Perner, D., Platt, U., Trainer, M., Hubler, G., Drummond, J., Junkermann, W., Rudolph, J. Schubert, B., Volz, A., Ehhalt, D.H., Rumpel, K.J., and Helas, G. 1987. Measurements of tropospheric OH concentrations: A comparison of field data with model predictions, J. Atmos. Chem. 5, 185-216.

Piccot, S.D., J.J. Watson, and J.W. Jones, 1992. A global inventory of volatile organic compound emissions from antrhopogenic sources, J. Geophys. Res. 97, 9897-9912.

Pinto, J.P, Yung, Y.L., Rind, D., Russell, G.L., Lerner, J.A., Hansen, J.E., and Hameed, S. 1983. A general circulation model study of atmospheric carbon monoxide, J. Geophys. Res. 88, 3691-3702.

Pinto, J.P. and Khalil, M.A.K. 1991. The stability of tropospheric OH during ice ages, inter-glacial epochs and modern times, Tellus 43B, 347-352.

Platt, U., Rateike, M., Junkermann, W., Rudolph, J. and Ehhalt, D.H. 1988. New tropospheric OH measurements, J. Geophys. Res. 93, 5159-5166.

Prospero, J.M., and Savoie, D.L., 1989. Effect of continental sources on nitrate concentrations over the Pacific Ocean, Nature 339, 687-689.

Ramanathan, V., Cicerone, R.J., Singh, H.B., and Kiehl, J.T. 1985. J. Geophys. Res. 90, 5547-5566.

Rasmussen, R.A. 1972. What do the hydrocarbons from trees contribute to air pollution?, J. Air Pollut. Cont. Assn. 22, 537-543.

Rasmussen, R.A. and Khalil, M.A.K. 1984. Atmospheric methane in the recent and ancient atmospheres: Concentrations, trends, and interhemispheric gradient, J. Geophys. Res. 89, 11,599-11,605.

Rasmussen, R.A. and Khalil, M.A.K. 1988. Isoprene over the Amazon Basin, J. Geophys. Res. 1417-1421.

Reichle, H.G., Connors, V.S., Holland, J.A., Hypes, W.D., Wallio, H.A., Casas, J.C., Gormsen, B.B., Saylor, M.S., and Hesketh, W.D. 1986. Middle and upper tropospheric carbon monoxide mixing ratios as measured by a satellite-borne remote sensor during November 1981, J. Geophys. Res. 91, 10865-10887.

Reiter, E.R., 1975. Stratospheric-tropospheric exchange processes, Rev. Geophys. Space Phys., 13, 459 - 474.

Robinson, E., Clark, D., and Seiler, W. 1984. The latitudinal distribution of carbon monoxide across the Pacific from California to Antarctica, J. Atmos. Chem. 1, 137-149.

Rodhe, H., and J. Grandell, 1972. On the removal time of aerosol particles from the atmosphere by precipitation scavenging, Tellus, 24, 442-454.

Rodhe, H. and I. Isaksen, 1980. Global distribution of sulfur compounds in the troposphere estimated in a height/latitude transport model, J. Geophys. Res., 85, 7401-7409.

Routhier, F., Dennett, R., Davis, D.D., Wartburg, A., Haagenson, P. and Delany, A.C. 1980. Free tropospheric and boundary-layer airborne measurements of ozone over the latitude range of 58 degrees S to 70 degrees N, J. Geophys. Res. 85, 7307-7321.

Rudolph, J. and Khedim, A. 1985. Hydrocarbons in the non-urban atmosphere: Analysis, ambient concentrations and impact on the chemistry of the atmosphere, Intern. J. Environ. Anal. Chem. 20, 265-282.

Sachse, G.W., Harriss, R.C., Fishman, J. Hill, G.F., and Cahoon, D.R. 1988. Carbon monoxide over the Amazon Basin during the 1985 dry season, J. Geophys. Res. 93, 1422-1430.

Sandroni, S., Anfossi. D., and Viargeno, 1992. Surface ozone levels at the end of the nineteenth century in South America, J. Geophys. Res. 97, 2535 - 2539.

Sehmel, G.A. , 1980. Particle and gas dry depostion: A review, Atmos. Env. 14, 983-1011.

Seila, R.L., Arnts, R.R., and Buchanan, J.W., 1984. Atmospheric volatile hydrocarbon composition at five remote sites in Northwestern North Carolina, in Environmental Impact of Natural Emissions, V. Aneja, ed., Air Pollution Control Association, Pittsburgh, PA.

Seiler, W. 1974. The cycle of atmospheric CO, Tellus 26, 117-135.

Seiler, W., and Crutzen, P.J., 1980. Estimates of gross and net fluxes of carbon between the biosphere and the atmosphere from biomass burning, Climatic Change, 2, 207-247.

Seiler, W. and Fishman, J. 1981. The distribution of carbon monoxide and ozone in the free troposphere, J. Geophys. Res. 86, 7255-7265.

Seiler, W., Giehl, H., Brunke, E.-G., and Halliday, E. 1984. The seasonality of CO abundance in the southern hemisphere, Tellus 36B, 219-231.

Seinfeld, J.H. 1986. Atmospheric chemistry and physics of air pollution. John Wiley & Sons, New York.

Sexton, K. and Westberg, H. 1984. Nonmethane hydrocarbon composition of urban and rural atmospheres, Atmos. Environ. 18, 1125-1132.

Shaver, C.L., Cass, G.R., and Druzik, J.R. 1983. Ozone and the deterioration of works of art, Environ. Sci. Technol. 17, 748-752.

Sickles, J.E., Bach, W.D., and Spiller, L.L., 1983. Comparison of several techniques for determining dry deposition flux, in Precipitation scavenging, dry depositon, and resuspension, Vol. 2 , H.R. Pruppacher, R.G. Semonin, and W.G.N. Slinn, eds., pp. 883-902, Elsevier, New York.

Sillman, S., Logan, J.A., and Wofsy, S.C. 1990. The sensitivity of ozone to nitrogen oxides and hydrocarbons in regional ozone episodes, J. Geophys. Res. 95, 1837-1851.

Sillman, S., 1991. A numerical solution for the equations of tropospheric chemistry based on an analysis of sources and sinks of odd hydrogen, J. Geophys. Res., 96, 20,736-20,744.

Singh, H.B., Viezee, W., Johnson, W.B. and Ludwig, F.L. 1980. The impact of stratospheric ozone on tropospheric air quality. J. Air Pollut. Cont. Assn. 30, 1009-1017.

Singh, H.B., and Salas, L.J., 1983a. Peroxyacetyl nitrate in the free troposphere, Nature 302, 326-328.

Singh, H.B., and Salas, L.J., 1983b. Methodology for the analysis of peroxyacetyl nitrate (PAN) in the Unpolluted atmosphere, Atmos. Environ. 17, 1507 - 1516.

Singh, H.B., Viezee, W., Johnson, W.B. and Ludwig, F.L. 1980. The impact of stratospheric ozone on tropospheric air quality. J. Air Pollut. Cont. Assn. 30, 1009-1017.

Singh, H.B., and Salas, L.J., 1989. Measurements of peroxyacetyl nitrate (PAN) and peroxypropionyl nitrate (PPN) at selected urban, rural, and remote sites, Atmos. Environ., 231-238.

Singh, H.B., Herlth, D., O'Hara, D.O., Salas, L., Torres, A.L., Gregory, G.L., Sachse, G.W., and Kasting, J.F.,1990. Atmospheric peroxyacetyl nitrate measurements over the Brazilian Amazon Basin during the wet season: Relationships with nitrogen oxides and ozone, J. Geophys. Res., 95, 16,945-16,954a.

Singh, H.B., Condon, E., Vedder, J., O'Hara, D., Ridley, B.A., Gandrud, B.W., Shetter, J.D., Salas, L.J., Huebert, B., Hubler, G., Carroll, M.A., Albritton, D.L., Davis, D.D., Bradshaw, J.D., Sandholm, S.T., Rodgers, M.O., Beck, S.M., Gregory, G.L., and Lebel, P.J., 1990b. Peroxyacetyl nitrate measurements during CITE 2: Atmospheric distribution and precursor relationships, J. Geophys. Res. 95, 10,163-10178

Singh, H.B., O'Hara, D., Herlth, D., Bradshaw, J.D., Sandholm, S.T., Gregory, G.L., Sachse, G.W., Balke, D.R., Crutzen, P.J., and M.A. Kanakidou, 1992. Atmospheric measurements of peroxyacetyl nitrate and other organic nitrates at high latitudes: Possible sources and sinks, J. Geophys. Res. 97, 16,511-16522.

Singh, H.B. and P.B. Zimmerman, 1992. Atmospheric distribution and sources of nonmethane hydrocarbons, Chapter 5 in Gaseous Pollutants: Characterization and Cycling, J.O. Nriagu, ed., John Wiley & Sons, New York.

Slemr, K.R., and Seiler, W., 1984. Field measurements of NO and NO_2 emissions from fertilized and unfertilized soils, J. Atmos. Chem., 2, 1-24.

Spivakovsky, C.M., Wofsy, S.C., and Prather, M.J., 1990a. A numerical method for paramerization of atmospheric chemistry: Computation of tropospheric OH, J. Geophys. Res. 95, 18,433-18,439.

Spivakovsky, C.M., Yevich, R., Logan, J.A., Wofsy, S.C., McElroy, M.B., and Prather, M.J., 1990b. Tropospheric OH in a three-dimensional chemical tracer model: An assessment based on observations of CH_3CCl_3.

Stauffer, B., Fischer, G., Neftel, A., and Oeschger, H. 1985. Increase of atmospheric methane recorded in Antarctic Ice Core, Science 229, 1386-1388.

Stauffer, B., Lochbronner, E., Oeschger, H., and Schwander, J. 1988, Methane concentration in the glacial atmosphere was only half that of the preindustrial Holocene, Nature 332, 812-814.

Steele, L.P., Dlugokencky, E.J., Lang, P.M., Tans, P.P., Martin, R.C., and Masarie, K.A. 1992. Slowing down of the global accumulation of atmospheric methane during the 1980s, Nature 358, 313-316.

Steele, L.P., Fraser, P.J., Rasmussen, R.A., Khalil, M.A.K., Conway, T.J., Crawford, A.J., Gammon, R.H., Masarie, K.A., and Thoning, K.W. 1987. The global distribution of methane in the troposphere, J. Atmos. Chem. 5, 125-171.

Stewart, R.W.,1988. The effect of random precipitation times on the scavenging rate for tropospheric NO2, Tellus, 40B, 285-296.

Stewart, R.W., A.M. Thompson, M.A. Owens, and J.A. Herwehe, 1989. Comparison of parameterized nitric acid rainout rates using a coupled stochastic-photochemical tropospheric model, J. Geophys. Res. 94, 5219 - 5226.

Taylor, J.A., Brasseur, G., Zimmerman, P. and Cicerone, R. 1991. A study of the sources and sinks of methane and methyl chloroform using a global 3-D Lagrangian tropospheric tracer transport model, J. Geophys. Res.96, 3013-3044.

Tie, S., Alyea, F.N., Dunnold, D.M., and Kao, C.-Y. J., 1991. Atmospheric methane: A global three-dimensional model study, J. Geophys. Res. 96, 17,339-17,348.

Tingey, D.T., Manning, M., Gorthaus, L.C., and Burns, W.F. 1979. The influence of light and temperature on isoprene emission rates from live oak, Physiol. Plant. 47, 112-118.

Tingey, D.T., Manning, M., Grothaus, L.C., and Burns, W.F. 1980. Influence of light and temperature on monoterpene emission rates from slash pine, Plant. Physiol. 65, 797-801.

Trainer, M., Williams, E.J., Parrish, D.D., Buhr, M.P., Allwine, E.J., Westberg, H.H., Fehsenfeld, F.C., and Liu, S.C. 1987. Models and observations of the impact of natural hydrocarbons on rural ozone, Nature 329, 705-707.

Turco, R.P. and R.C. Whitten, 1978. A note on the diurnal averaging of aeronomical models, J. Atmos. and Terres. Physics, 40, 13 - 20.

Vaghjiani, G.L., and Ravishankara, A.R., 1991. New measurements of the rate coefficient for the reaction of OH with methane, Nature 360, 406-409.

Van Valin, C.C. and Luria, M. 1988. O_3, CO, hydrocarbons and dimethyl sulfide over the western Atlantic Ocean, Atmos. Env. 22, 2401-2409.

Voldner, E.C., Barrie, L.A., and Sirois, A., 1986. A literature review of dry deposition of oxides of sulphur and nitrogen with emphasis on long-range transport modeling in North America, Atmos. Env. 20, 2101-2123.

Volz, A. and Kley, D. 1988. Evaluation of the Montsouris series of ozone measurements made in the nineteenth century, Nature 332, 240-242.

Vukovich, F.M., Fishman, J., and Browell, E.V. 1985. The reservoir of ozone in the boundary layer of the eastern United States and its potential impact on the global tropospheric ozone budget, J. Geophys. Res. 90, 5687-5698.

Walcek, C.J., Brost, R.A., Chang, J.S., and Wesely, M.L., 1986. SO_2, sulfate and HNO_3 deposition velocities computed using regional landuse and meteorological data, Atmos. Environ. 20, 949-964.

Walega, J.G., Ridley, B.A., Madronich, S., Grahek, F.E., Shetter, J.D., Sauvain, T.D., Hahn, C.Jn, Merill, J.T., Bodhaine, B.A., and E. Robinson, 1992. Observations of peroxyacetyln itrate, peroxypropionyl nitrate, methyl nitrate and ozone during the Mauna Loa observatory photochemistry experiment, J. Geophys. Res. 97, 10,311-10,330.

Walton, J.J., MacCracken, M.C., and Ghan, S.J. 1988. A global-scale Lagrangian trace species model of transport, transformation, and removal processes, J. Geophys. Res. 93, 8339-8354

Warneck, P., 1988. Chemistry of the Natural Atmosphere, Academic Press, New York, 753pp.

Warren Spring Laboratory, 1989. The global distribution of aircraft air pollutant emissions, Stevenage, Hertfordshire, United Kingdom.

Watson, J.J., J.A. Probert, and S.D. Piccot, 1991. Global inventory of volatile organic compound emissions from anthropogenic sources, EPA-600/8-91-002 (NTIS PB91-161687), U.S. Environ. Prot. Agency, Air and Energy Eng. Res. Lab., Research Triangle Park, N.C.

Wayne, W.S., Wehrle, P.F., and Carroll, R.E. 1967. Oxidant Air Pollution and Athletic Performance, J. Amer. Med. Assn. 199, 151-154.

Wesely, M.L. and Hicks, B.B., 1977. Soome factors that affect the deposition rates of sulfur dioxide and similar gases on vegetation, J. Air Poll. Cont. Assoc. 27, 1110-1116.

Williams, E.J., Parrish, D.D., and Fehsenfeld, F.C., 1987. Determination of nitrogen oxides emissions from soils: Results from a grassland site in Colorado, United States. J. Geophys. Res. 92, 2173-2179.

Williams, E.J., Parrish, D.D., Buhr, M.P., and Fehsenfeld, F.C., 1988. Measurement of soil NO_x emissions in central Pennsylvania, J. Geophys. Res. 93, 9539-9546.

Williams, E.J. and Fehsenfeld, F.C., 1991. Measurement of soil nitrogen oxides emissions at three North American ecosystems, J. Geophys. Res. 96, 1033-1042.

Winkler, P. 1988. Surface ozone over the Atlantic Ocean, J. Atmos. Chem. 7, 73-91.

World Meteorological Organization, Atmospheric Ozone 1985, Global Ozone Research and Monitoring Project--Report No. 16, Geneva, Switzerland.

Wuebbles, D.J., Connell, P.S., Grant, K.E., Tarp, R., and Taylor, K.E., 1987. Initial results with the LLNL 2D chemical-radiative-transport model of the troposphere and stratosphere, LLNL Internal Rep. UCID-21178, LLNL, Livermore, CA.

Wuebbles, D.J., Grant, K.E., Connell, P.S., and Penner, J.E. 1989. The role of atmospheric chemistry in climate change, J. Air Poll. Cont. Assn. 39, 22-28.

Zimmerman, P.R. 1979a. Testing for hydrocarbon emissions from vegetation leaf litter and aquatic surfaces, and development of a methodology for compiling biogenic emission inventories. EPA-450/4-4-79-004.

Zimmerman, P.R. 1979b. Determination of emission rates of hydrocarbons from indigenous species of vegetation in the Tampa/St. Petersburg, Florida area. EPA-904/9-77-028.

Zimmerman, P.R., Greenberg, J.P., and Westberg, C.E., 1988. Measurements of atmospheric hydrocarbons and biogenic emission fluxes in the Amazon Boundary Layer, J. Geophys. Res. 93, 1407-1416.

Technical Information Department · Lawrence Livermore National Laboratory
University of California · Livermore, California 94550